# Electronic excitations and rational design of novel light sensitisers for photovoltaics

Marina Rucsandra Filip

St Cross College
University of Oxford

Thesis submitted for the Degree of
Doctor of Philosophy in Materials

July 2, 2015

# Abstract


**Electronic excitations and rational design of novel light sensitisers for photovoltaics**

**Marina Rucsandra Filip**
**St. Cross College, University of Oxford**

**Thesis submitted for the Degree of Doctor of Philosophy in Materials**
**Hillary Term, 2015**

The development of scalable and cost-efficient solar cell technologies constitutes a priority in the field of photovoltaics research. Semiconductor sensitised solar cells (SSSC) and hybrid organic-inorganic perovskite solar cells (HOPSC) are two emerging technologies that have been actively pursued in the search for the most efficient, cost-competitive, stable and non-toxic photovoltaic devices. The HOPSCs have been polarising the attention of the photovoltaics community in the past three years due to their ever-increasing efficiencies, currently exceeding 20% while SSSCs have increased in popularity in the last decade, showing a steady increase of their efficiency and emergence of new materials implemented as light sensitisers. Improvement of these novel technologies relies on understanding of the physical properties of the materials components and on efficient strategies towards the discovery of novel compounds. In this thesis, we address these requirements by modelling the electronic structures of novel light sensitisers from first principles. We focus on the analysis of two groups of materials, the hybrid organic-inorganic lead-iodide perovskites and the metal chalcogenides of the stibnite family. We study the electronic structure of $CH_3NH_3PbI_3$ within density functional theory and obtain the quasiparticle band gap for this material within the *GW* method in good agreement with experiment. Further, we conduct a systematic study of the interplay between the electronic properties of hybrid organic-inorganic perovskites and the structure of the inorganic perovskite network. As a result, we obtain a simple strategy for tuning the band gap of perovskite light absorbers by changing the size of the central cation, and propose $AsH_4PbI_3$ and $SbH_4PbI_3$ as potential novel light sensitisers for HOPSC. The second part of the thesis is dedicated to the study of the electronic structure of four isostructural metal chalcogenides of the stibnite family, stibnite, antimonselite, bismuthinite and guanajuatite. A study of the quasiparticle band gaps of these materials is conducted, similar to the approach used for $CH_3NH_3PbI_3$. By using the Shockley-Queisser analysis, we obtain that all four materials are promising for application as light sensitisers.

# Contents

**Abstract** **i**

**Contents** **iii**

**1 Introduction** **1**

1.1 Solar cells - general principles . . . . . 3

1.1.1 Basic parameters . . . . . 4

1.1.2 Maximum attainable efficiency . . . . . 6

1.2 Emerging solar cells . . . . . 8

1.2.1 Dye-sensitised solar cells . . . . . 8

1.2.2 Semiconductor sensitised solar cells . . . . . 10

1.2.3 Hybrid organic-inorganic perovskite solar cells . . . . . 11

1.3 Summary and organisation of the thesis . . . . . 13

**2 Density Functional Theory and the *GW* method** **15**

2.1 Density functional theory . . . . . 16

2.1.1 Many-body Schrödinger equation . . . . . 16

2.1.2 Hohenberg and Kohn theorem . . . . . 17

2.1.3 Kohn-Sham equations . . . . . 18

2.1.4 Local density approximation . . . . . 19

2.1.5 Spin-orbit coupling . . . . . 20

2.2 The *GW* approximation . . . . . 22

2.2.1 The many-body Hamiltonian in second quantisation . . . . . 23

2.2.2 The single-particle Green's function . . . . . 24

2.2.3 The quasiparticle self-energy . . . . . 25

2.2.4 Dyson's equation . . . . . 26

2.2.5 Hedin's equations . . . 28
2.2.6 Screened Coulomb interaction . . . 29
2.2.7 Self-consistency . . . 30
2.2.8 $G_0W_0$ approximation including spin-orbit coupling . . . 31
2.3 Practical calculations . . . 32
2.3.1 Convergence in DFT . . . 33
2.3.2 Convergence in GW . . . 38
2.3.3 Summary of convergence parameters . . . 42
2.4 Summary . . . 42

**3 Metal-halide perovskite absorbers: An overview of recent literature 45**
3.1 General properties of perovskites . . . 47
3.1.1 Crystal structure and symmetry properties . . . 47
3.1.2 Tolerance factor . . . 48
3.2 Properties of $CH_3NH_3PbI_3$: insight from experimental and computational studies . . . 50
3.2.1 Synthesis of $CH_3NH_3PbI_3$ . . . 50
3.2.2 Structural properties of $CH_3NH_3PbI_3$ . . . 51
3.2.3 Electronic and Optical properties of $CH_3NH_3PbI_3$ . . . 54
3.3 Tuning optical properties . . . 58
3.3.1 Mixed-metal perovskites . . . 58
3.3.2 Mixed-halide perovskites . . . 59
3.3.3 Mixed-cation perovskites . . . 60
3.4 Summary . . . 61

**4 Electronic properties of the hybrid $CH_3NH_3PbI_3$ perovskite 63**
4.1 Density functional theory calculations . . . 64
4.1.1 Crystal structure optimisation . . . 64
4.1.2 Scalar relativistic calculations . . . 65
4.1.3 Effect of spin-orbit coupling . . . 67
4.1.4 Effective masses: scalar vs. fully relativistic . . . 69
4.2 *GW* calculations . . . 71
4.2.1 Effect of the semicore electrons . . . 71
4.2.2 Effect of self-consistency . . . 74
4.3 Summary . . . 79

**5 Rational design of novel perovskite absorbers with tunable optical properties 81**

5.1 Platonic model of metal-halide perovskites . . . . . 82
5.1.1 The Platonic octahedron . . . . . 82
5.1.2 The construction . . . . . 83
5.1.3 The metal-halide-metal bond angles in the Platonic model . . . 88
5.2 Electronic structure and the metal-halide metal bond angles . . . . . 89
5.2.1 Band gaps . . . . . 89
5.2.2 Effective masses . . . . . 95
5.2.3 Excitons . . . . . 96
5.3 Electronic structure and the metal-halide-metal bond length . . . . . 99
5.4 Controlling the metal-halide-metal bond angles via the steric size of the cation . . . . . 100
5.4.1 Structural optimisations . . . . . 102
5.4.2 Correlation of the band gap with the maximum unit cell bond angle . . . . . 106
5.4.3 Stability against structural distortions . . . . . 108
5.5 Experimental validation . . . . . 110
5.6 Summary . . . . . 112

**6 Electronic and optical properties of hypothetical $APbI_3$ perovskites: A = $NH_4$, $PH_4$, $AsH_4$, $SbH_4$ 115**
6.1 Density functional theory calculations . . . . . 116
6.1.1 Crystal structure . . . . . 116
6.1.2 Electronic structure . . . . . 118
6.2 Quasiparticle *GW* band gaps and effect of self consistency . . . . . 121
6.3 Summary . . . . . 126

**7 The $A_2B_3$ metal chalcogenides (A = Sb, Bi; B = S, Se): An overview of recent literature 129**
7.1 Structure and synthesis . . . . . 131
7.2 Electronic and optical properties: insight from experimental and computational studies . . . . . 133
7.2.1 Experimental studies . . . . . 133
7.2.2 Computational studies . . . . . 135
7.3 Summary . . . . . 138

**8 Electronic properties of light sensitisers of the $A_2B_3$ metal chalcogenide semiconductors (A = Sb, Bi; B = S, Se) 139**
8.1 Crystal structure . . . . . 140

8.1.1 Structural relaxations . . . . . 140
8.1.2 Cohesive energies . . . . . 142
8.2 Electronic properties . . . . . 143
8.2.1 DFT/LDA band structures . . . . . 143
8.2.2 Quasiparticle corrections . . . . . 145
8.2.3 Relativistic corrections . . . . . 149
8.2.4 Band gaps . . . . . 150
8.3 Summary . . . . . 154

**9 Conclusions** **157**
9.1 Summary . . . . . 157
9.2 Outlook . . . . . 159

**Appendix A Computational details** **161**
A.1 Computational setup for Chapter 4 . . . . . 161
A.1.1 DFT calculations . . . . . 161
A.1.2 *GW* calculations . . . . . 162
A.2 Computational setup for Chapter 5 . . . . . 165
A.2.1 DFT calculations . . . . . 165
A.3 Computational setup for Chapter 6 . . . . . 166
A.4 Computational setup for Chapter 8 . . . . . 167
A.4.1 DFT calculations . . . . . 167
A.4.2 *GW* calculations . . . . . 168

**References** **171**

**Acknowledgements** **I**

**List of published papers** **III**

# Chapter 1

# Introduction

In a recent speech at the 2014 World Economic Forum in Davos, Lord Nicholas Stern left the audience with a compelling message: *"The last time we had a change in global temperatures of this order of magnitude it was in the other direction. It was called the Ice Age"* [1]. The alarming global warming rate in conjunction with the global energy crisis have put the development of clean renewable energy technologies high on the international policy agenda. This year in Davos, Lord Stern also made a strong case for the economic benefits brought forth by the lowering costs of renewable energies [2], encouraging leading global economies to compete in the "green race" [1]. Regardless of the motivation, it has become apparent that the global focus on energy resources is shifting from fossil fuels to clean sustainable energy sources.

The search for renewable energy solutions has been the focus of the scientific community long before policy makers have recognised its importance. Solar power has proved to be one of the most promising avenues for renewable energy sources, showing fast development of scalable, efficient and cost-competitive solutions. The most successful solar cell technology thus far is based on silicon photovoltaic (PV) devices. Owing to the vast technological advances in semiconductor applications, solar cells employing single junction crystalline or amorphous silicon currently hold 90% of the

global market share [3], delivering consistent 17-18% efficiencies, long guaranteed lifetimes of up to 20 years and cost efficiency (1$/W) [3]. Despite these successes, academic and industrial research alike are focusing tremendous efforts toward the development of the next generation photovoltaic devices.

Most recent records of the National Renewable Energy Laboratory (NREL) [4] show the multi-junction solar cells leading the power conversion efficiency tables. The champion multi-junction cell is the InGaP/GaAs/InGaAs device, recording a staggering 44.4% efficiency [5]. While very competitive from an efficiency point of view, manufacturing costs of these devices still remains a challenge.

The dye sensitised solar cell (DSSC) proposed in 1991 by Brian O'Regan and Michael Grätzel [6] is currently one of the most popular emerging photovoltaic technologies. Although it does not boast such impressive efficiency figures (the highest certified efficiency is of 11.9% according to the most recent NREL report) it attracts through the simplicity of the manufacturing process, which does not require high temperature or high vacuum conditions [3, 7]. In addition, control of colour and transparency of these devices is now available, making them attractive for commercialisation [8, 9]. Further development of the DSSC has seen the emergence of semiconductor sensitised solar cells (SSSC) [10] and the recent unprecedented success of hybrid organic-inorganic perovskite solar cells (HOPSC) [11–14]. The latter combines low-cost fabrication and high power-conversion efficiencies, promising to deliver the next generation PV technologies that could compete with the current market leaders.

This thesis will be focused on the computational study of the physical properties of hybrid organic-inorganic perovskite absorbers in HOPSC as well as the properties of metal chalcogenide semiconductors of the stibnite family, which have been employed in SSSC devices. The goal of this introductory chapter is to outline some of the basic concepts behind the functionality of these types of solar cells and give a brief summary of their recent developments.

## 1.1 Solar cells - general principles

The basic role of a solar cell is to convert absorbed visible light into an electric current. This is achieved by photogenerating negative and positive charges and transporting them to conducting electrodes. When a photon is absorbed by a material, an electron is promoted to a higher energy level, such that the photon energy is equal to the difference between the final and initial energies of the electron. This photoexcitation process generates an excited electron and leaves behind an empty electronic state, or a hole (Figure 1.1). Before the electron and hole can recombine, the charges must be separated by a driving force which is built into the photovoltaic device in order to create a current [15].

The efficiency with which this process is carried out depends on several factors such as the electronic and optical properties of the light absorbing material, the mechanism for charge separation, and the charge conductors that collect the photogenerated charges [15].

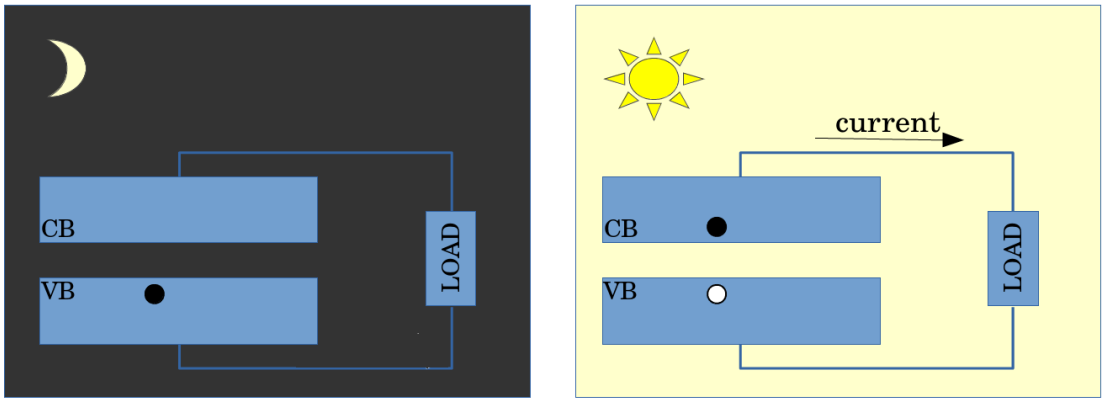


Figure 1.1: Schematic representation of the basic solar cell operation principles. In the dark, there is no current flowing through the circuit. Under illumination, photogenerated electron (black disk) and hole (white disc) generate a current in the presence of a load [15].

### 1.1.1 Basic parameters

In the dark, a solar cell behaves like an ideal diode. If a forward bias $V$ is applied, then the current density flowing through the circuit is given by [15]:

$$J_{\text{dark}}(V) = -J_0\Big(e^{eV/k_{\text{B}}T} - 1\Big). \tag{1.1}$$

where $J_0$ is a temperature dependent parameter, $e$ is the electronic charge, $k_{\text{B}}$ is the Boltzmann constant and $T$ is the temperature of the cell. Upon illumination, a photocurrent is produced which flows in the opposite direction to $J_{\text{dark}}$. Therefore, the total current density through the circuit could be expressed as [15]:

$$J(V) = J_{\text{SC}} - J_0\Big(e^{eV/k_{\text{B}}T} - 1\Big). \tag{1.2}$$

where $J_{\text{SC}}$ is the short circuit current density. Furthermore, the open circuit voltage, $V_{\text{OC}}$, can be calculated from $J(V_{\text{OC}}) = 0$:

$$V_{\text{OC}} = \frac{k_{\text{B}}T}{e}\log\Big(\frac{J_{\text{SC}}}{J_0} + 1\Big). \tag{1.3}$$

The open circuit voltage is smaller than the band gap of the light absorber, $E_g$ [15, 16] and in the limit of T approaching 0 K $V_{\text{OC}}$ approaches $E_g$.

In Figure 1.2 we plot $J(V)$ for a solar cell, highlighting the open circuit voltage and the short-circuit current density. Another key parameter in the characterization of a solar cell is the fill factor, $FF$, defined as the ratio between the area under the $J(V)$ curve and the product $J_{\text{SC}}V_{\text{OC}}$ [15].

The short circuit current density can be calculated using the following expression [15]:

$$J_{\text{SC}} = \int_0^\infty t_s(1 - R(E))a(E)\frac{S(E)}{E}dE. \tag{1.4}$$

where $S(E)$ is power radiated by the sun on Earth per unit of surface area and per unit of energy, $a(E)$ is the probability that a photon with energy $E$ is absorbed by the cell, $R(E)$ is the probability that a photon with energy $E$ is reflected by the cell and $t_s$ is

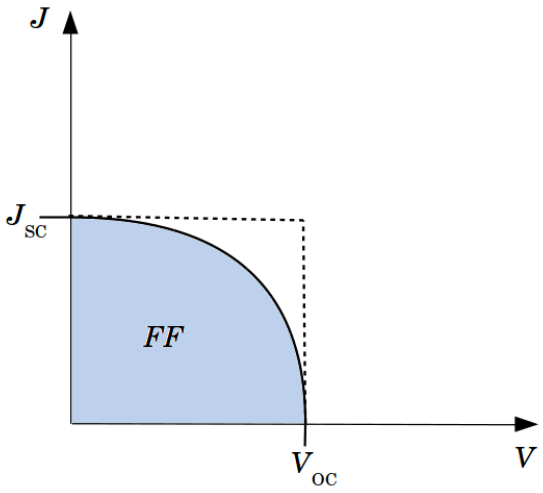


Figure 1.2: $J(V)$ plot for an ideal solar cell. The short circuit current $J_{SC}$, open-circuit voltage $V_{OC}$ and fill factor $FF$ are marked on the diagram [15].

the probability that the absorbed photon will promote an electron to an unoccupied state [15, 16]. We can simplify the expression in Eq. 1.4 by assuming the ideal case in which the $a(E) = 1$ and $t_s = 1$ for any photon energy above $E_g$ and $R(E) = 0$, obtaining [15, 16]:

$$J_{SC} = \int_{E_{gap}}^{\infty} \frac{S(E)}{E} \mathrm{d}E. \tag{1.5}$$

The efficiency of a solar cell is defined as the ratio between the electric power produced by the solar cell (the area under the $J(V)$ curve) and the power received from the sun ($P_{sun}$), and can be expressed as [15]:

$$\eta = \frac{FF \times J_{SC} V_{OC}}{P_{sun}}. \tag{1.6}$$

The total solar power can be calculated by integrating the solar spectrum, typically reported at air mass coefficient of 1.5 (AM1.5). The spectral data are readily available from the NREL website [4], and the denominator of Eq. (1.6) can be evaluated as:

$$P_{sun} = \int_{0}^{\infty} S(E) \mathrm{d}E. \tag{1.7}$$

### 1.1.2 Maximum attainable efficiency

Using Eq 1.5, the power generated by an ideal solar cell can be expressed as [15]:

$$P = FF \times V_{\mathrm{OC}} \int_{E_g}^{\infty} \frac{S(E)}{E} dE. \tag{1.8}$$

Knowing that $FF < 1$ and $V_{\mathrm{OC}} < E_g$, it follows that $\eta < \eta_{ult}$. $\eta_{ult}$ is the so-called ultimate effiency [16] and can be defined as the efficiency of an ideal solar cell at 0 K which absorbs all photons with energy above $E_g$, and produces an electron-hole pair for each absorbed photon [16]:

$$\eta_{ult}(E_g) = \frac{E_g \int_{E_g}^{\infty} \frac{S(E)}{E} dE}{\int_0^{\infty} S(E) \mathrm{d}E}. \tag{1.9}$$

In order to estimate a more realistic limiting efficiency for DSSCs, HOPSCs and SSCs one can reintroduce the fill factor, the open circuit voltage into the expression of the limiting efficiency, as well as a factor accounting for the probability that an incident photon would be absorbed and would produce an electron-hole pair upon absorption, called the incident photon to converted electron efficiency (IPCE) [17]. The IPCE is in general dependent on the energy of the incident photon. However, for the purpose of estimating a limit efficiency achievable by a solar cell, we approximate the IPCE by a step function, which is 0 for energies below the band gap, and a constant lower than 1 for energies above $\mathrm{E}_g$. Moreover, the open circuit voltage can be expressed, as it was shown in the case of the DSSC in terms of the band gap of the light absorber as [17]:

$$V_{\mathrm{OC}} = E_g - E_{\mathrm{loss}}. \tag{1.10}$$

where $E_{\mathrm{loss}}$ has been defined in the case of the DSSC as the 'loss-in-potential', due to the energy level mismatch between the dye and electron and hole conductor. In principle, regardless of the solar cell setup, open circuit voltage and the band gap of the light absorber are measurable quantities, and the parameter $E_{\mathrm{loss}}$ can always be defined [17].

Based on the discussion above, we can rewrite this limiting efficiency for a solar cell, which we henceforth call the maximum attainable efficiency in Eq. 1.10 as [15–17]:

$$\eta(E_g) = FF \times IPCE \times \frac{(E_g - E_{\text{loss}}) \int_{E_g}^{\infty} \frac{S(E)}{E}}{\int_0^{\infty} S(E)\mathrm{d}E} dE. \tag{1.11}$$

In Figure 1.3 we show the calculated maximum attainable efficiency as a function of the band gap, for an increasing loss-in-potential. As it is pointed out in Ref. [17], the efficiency reaches its maximum for increasing band gaps as the loss-in-potential increases. Moreover, as the loss-in-potential increases, the maximum attainable efficiency decreases in magnitude. In the inset of Figure 1.3 we also show the plot of the ultimate effeciency as reported in the original paper by Shockley and Queisser. The

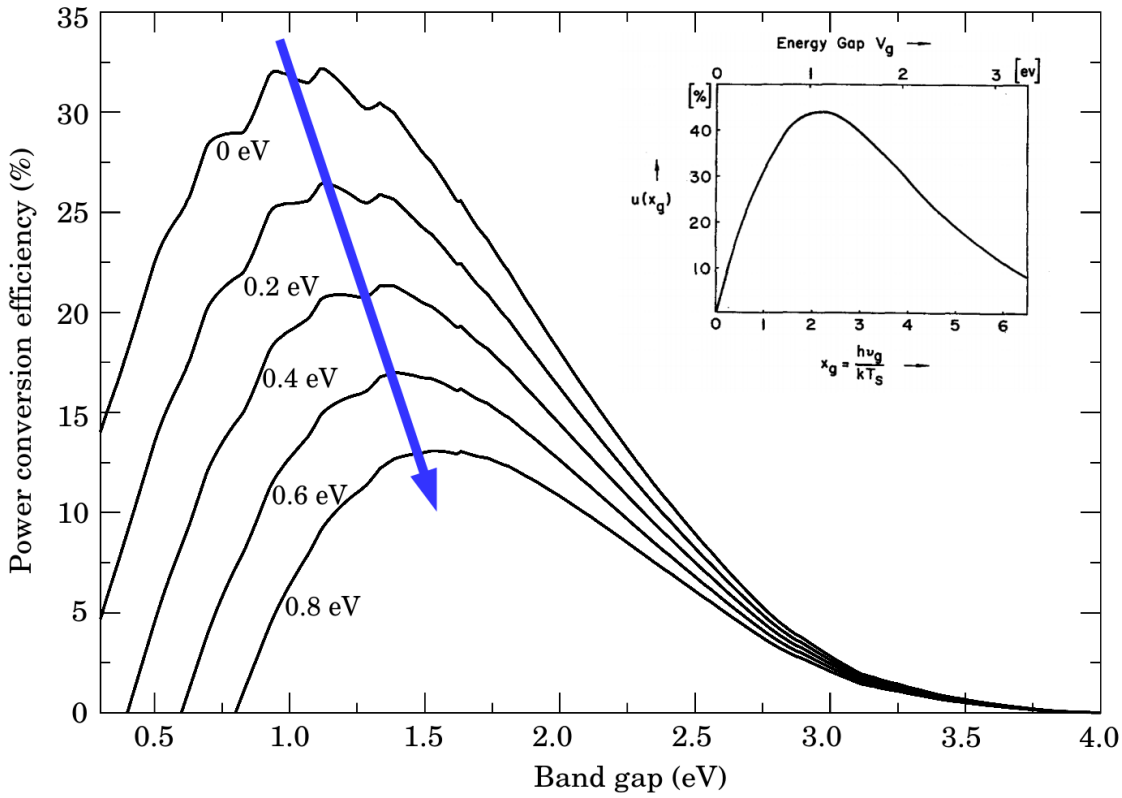


Figure 1.3: Plot of the maximum attainable efficiency as a function of the band gap of the light absorber and loss-in-potential. The blue arrow shows that the band gap corresponding to the maximum efficiency increases as the loss in potential increases. The curves were obtained taking into account a 73% fill factor and $IPCE = 0.9$, for photons with energies higher than $E_g$, in order to reproduce the results shown in Ref [17]. The inset shows the original plot of the ultimate power conversion efficiency, reported in Ref [16]. The efficiency is calculated as a function of $x_g = h\nu_g/kT_s$, where $h\nu_g$ is the band gap, $k$ is the Boltzmann constant and $T_s$ is the temperature of the Sun. Picture taken from ref. [16] with permission.

ultimate power conversion efficiency is directly comparable to the curve corresponding to 0 eV loss-in potential in Figure 1.3. Indeed, if the loss-in-potential vanishes, the expression for the efficiency in Eq. 1.11 becomes equivalent to Eq. 1.10 up to the $FF$ and $IPCE$ factors, which for the purpose of this discussion are considered constant scaling factors. Indeed, we can see from Figure 1.3 that the maximum of the ultimate efficiency curve shown in the inset is achieved around 1.1 eV, as it is the case for the curve corresponding to $V_{\text{loss}} = 0$ eV. The ratio between the maxima of the two curves is approximately 0.7, which is very close to the product $FF \times IPCE$ of 0.66. Moreover, the inset plot is obtained using the black-body radiation spectrum to represent the light source, while our calculations are performed using the direct solar spectrum irradiance, as available from the NREL website [18]

## 1.2 Emerging solar cells

In the NREL records of the best efficiency solar cells, the DSSC, SSSC and HOPSC are listed in the "Emerging PV" category, among organic and quantum dot solar cells [4]. In the following we will sketch the basic characteristics of the DSSC, SSSC and HOPSC along with the recent best efficiency figures.

### 1.2.1 Dye-sensitised solar cells

The DSSC introduces a novel photovoltaic architecture by which the light absorption and charge transport are undertaken by different materials within the solar cell [8, 19]. In Figure 1.4 we show a schematic representation of the DSSC, taken from Ref. [19]. In the device shown in Figure 1.4, dye molecules are deposited onto the porous surface of the electron conductor in order to facilitate charge injection [6, 19]. A photon absorbed by the dye excites an electron into the higher energy levels of the dye. The excited electron is injected into the conduction band of the electron conductor [19]. This is achieved if the lowest unoccupied molecular orbital of the dye molecule is

higher than the conduction band minimum of the electron conductor. The charge equilibrium is ensured by the liquid or solid-state hole transporting material (HTM), supplying the dye with an electron via a red-ox process [8]. From the energy diagram in Figure 1.4 it is clear that a photogenerated current can only be obtained if the electron conductor, hole conductor and the dye have energy levels aligned in this configuration, also known as a type-II hetero-junction [20]. In an ideal situation

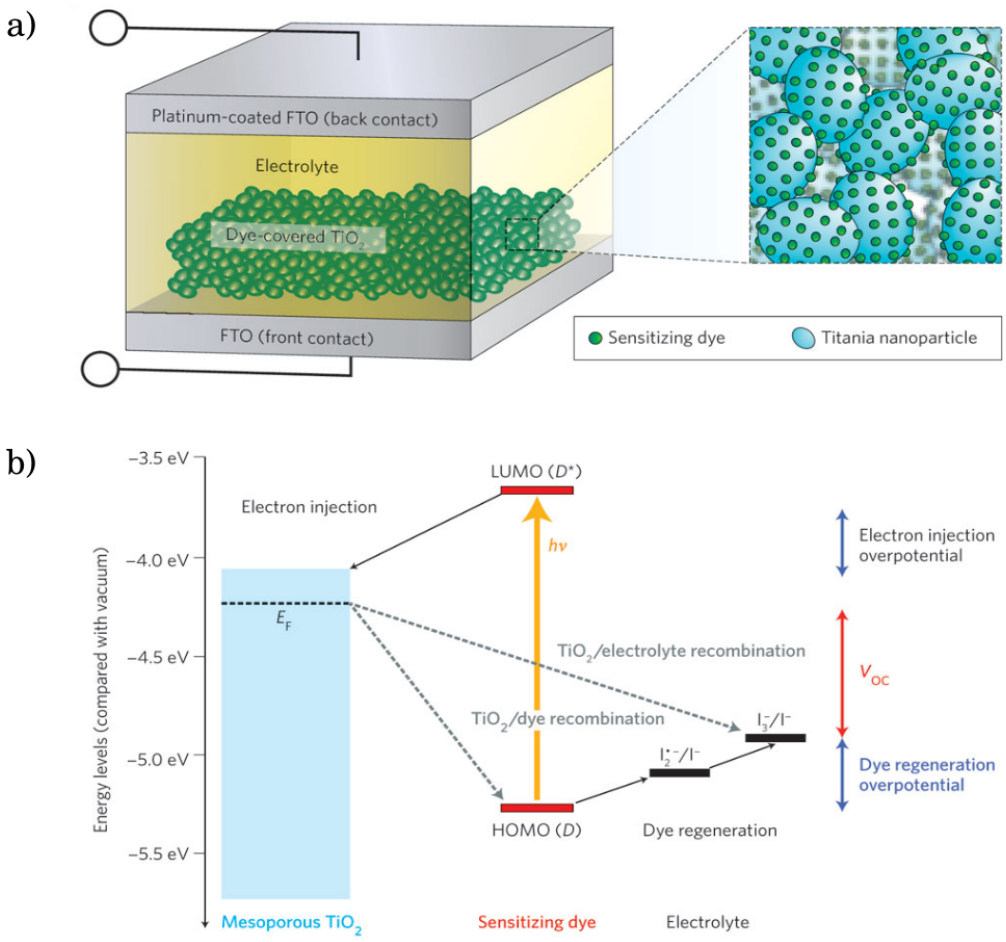


Figure 1.4: Schematic representation of the dye-sensitised solar cell (a) and the energy diagram corresponding to the components of the dye-sensitised solar cell (b). The dye-sensitized solar cell constitutes of a junction between the electron conductor, mesoporous $TiO_2$, a sensitizing dye, and an iodide based electrolyte. Photons ($h\nu$) are absorbed by the dye and the electron-hole pair is separated at the junction with the $TiO_2$ and the electrolyte respectively. The highest occupied molecular orbital of the dye [HOMO (D)] has a lower energy than the ionization potential of the electrolyte, and the lowest unoccupied molecular orbital of the dye [LUMO ($D^*$)] is higher in energy than the Fermi level of the mesoporous $TiO_2$, facilitating the dye regeneration and electron injection respectively. The current generation is achieved via electrical contacts which are based on fluorine doped tin oxide (FTO). Picture taken from Ref. [19] with permission.

the photogenerated charges are instantaneously transferred to the charge conductors, which means that the open-circuit voltage has the same value as the optical absorption onset. As pointed out by Ref. [17] electron and hole transfer to the electron and hole conductor require energy, and reduce the open-circuit voltage. The difference between the energy gap and the open-circuit voltage is referred to as a loss-in-potential [17]. Ref. [19] identifies two main ways to improve the performance of a DSSC: either by extending the absorption range of the dye, or by improving the electrolyte so that the dye regeneration over-potential is reduced (Figure 1.4b).

The originally proposed DSSCs are based on a ruthenium dye as light absorber [3, 6], $TiO_2$ electron conductor and an I-based electrolyte, as shown in Figure 1.4a, achieving efficiencies up to 11% [3]. The highest efficiency (uncertified) to date for the DSSC is obtained for a setup containing a porphyrin dye (SM315) with $TiO_2$ as an electron absorber and a cobalt-based electrolyte [9]. An efficiency of 13% is obtained with this device, with 0.91 V open-circuit voltage, 18.1 $mA/cm^{-2}$ short circuit current density, and a 78% fill factor [9].

### 1.2.2 Semiconductor sensitised solar cells

The SSSC is closely related to the DSSC given that it employs an almost identical architecture. The main difference between the SSSC and the DSSC lies in the nature of the light absorber: in the former the molecular dye is replaced by a solid semiconducting light sensitiser [10]. One of the advantages of replacing the molecular dye by semiconductor nanoparticles is that the absorption ranges can be easily tuned via quantum size effects [10].

Similar to the DSSC, the SSSC setup requires also that the band alignment of the electron conductor, light absorber and hole conductor form a type-II hetero-junction [21]. Typically, the light sensitiser is deposited in a very thin layer onto the surface of the electron conductor (for example $TiO_2$ or ZnO), in order to minimise recombination

rates [21].

Semiconducting metal chalcogenides have been implemented successfully in an SSSC architecture as light absorbers [22–26]. The highest efficiency was recently obtained for SSSCs employing stibnite ($Sb_2S_3$) as a light sensitiser, reaching 7.5% [27]. A recent computational study of photovoltaic interfaces for SSSC points out that the other members of the stibnite mineral family [bismuthinite ($Bi_2S_3$), antimonselite ($Sb_2Se_3$) and guanajuatite ($Bi_2Se_3$ in the orthorhombic phase)] exhibit optical properties similar to stibnite and should be considered as potential candidates for novel semiconductor sensitisers [20]. In addition to this, Ref [20] points out that while stibnite and antimonselite form a type-II hetero-junction with $TiO_2$, the conduction band bottom of $Bi_2S_3$ aligns below the conduction band bottom of $TiO_2$ thereby preventing charge transfer. The computational predictions made in Ref. [20] are validated by Refs [25, 28–31] which report antimonselite-sensitised solar cells, so far reaching 3.7% efficiency [32]. In addition, Ref. [28] also confirms the unfavourable alignment between $TiO_2$ and $Bi_2S_3$. However, efficiencies of up to 4.8% were reported for solar cells employing bulk nano-hetero-junctions of $Bi_2S_3$ nano-crystals and PbS quantum dots [24].

### 1.2.3 Hybrid organic-inorganic perovskite solar cells

Solar cells based on hybrid organic-inorganic perovskites (HOP) are the most recent of the emerging PV technologies appearing in the NREL charts. The first report of photovoltaic devices based on $CH_3NH_3PbI_3$ and $CH_3NH_3PbBr_3$ perovskites dates back to 2006 [33]. Ref [34] presents a DSSC-type cell in which the perovskites are used as light absorbers, achieving a 3.9% efficiency (for the iodide perovskite) but very short term lifetimes due to the quick degradation of the perovskite by the iodide based liquid hole transporter [34]. Refs [35, 36], which were published almost simultaneously in 2012, show that upon replacement of the liquid electrolyte by solid-state spiro-MeOTAD the solar cell based on $CH_3NH_3PbI_3$ reaches an efficiency of up to 10.9%, as

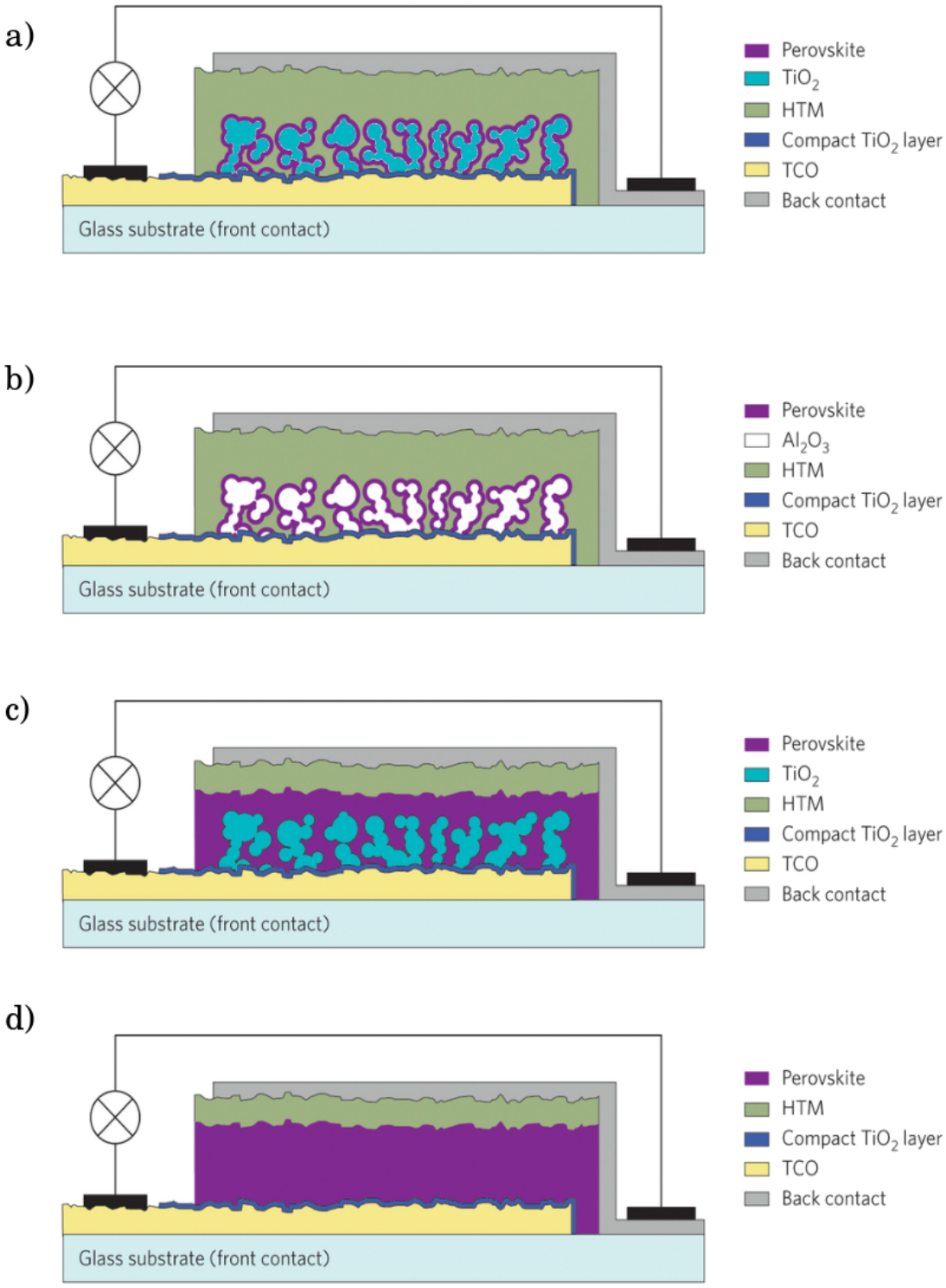


Figure 1.5: Sketch of experimental stack of the four possible HOPSCs: a) $TiO_2$/HOP/HTM, b) a solar cell based on $Al_2O_3$/HOP/HTM hetero-junction without the electron conductor, c) a solar cell based on $TiO_2$/HOP hetero-junction, without the hole conductor and d) the planar HOPSC. Figures b)-d) are taken from Ref. [11] with permission and figure a) is adapted from Figure 2 of Ref. [11].

well as long term stability. These two publications mark the beginning of an unprecedented progress for HOPSCs, with three NREL certified efficiency records added just last year. The highest certified efficiency is currently of 20.1%, achieved at the Korean Institute of Chemical Technology [4]. This rapid increase in efficiency is due to continuous improvement in the fabrication process [37–39]. Moreover, HOPSCs are rapidly becoming attractive due to recent development of partially transparent [40, 41], flexible [42–45], multi-coloured [40, 46, 47] and low-temperature processed devices[48].

Given the unusually long lifetimes of the photoexcited carriers [49, 50] and the relatively low gap, it was proposed that the perovskite layer could act as light absorber as well as electron and hole transporter [12]. In the diagram shown in Figure 1.5 (adapted from Ref [11]) we sketch the types of HOPSCs reported so far. In Figure 1.5a), the perovskite is deposited on mesoporous $TiO_2$, in a setup identical to the DSSC [35, 36]. In Ref. [36] the authors present a comparison between structures using either $TiO_2$ or $Al_2O_3$ as the mesoporous scaffold, obtaining superior performance for the cells employing $Al_2O_3$ (Figure 1.5b). Interestingly, the energy diagrams of the perovskite layer and $Al_2O_3$ do not align in a type-II hetero-junction, suggesting that in fact the photogenerated electrons are transported through the perovskite. [36]. Similarly, by exploiting the high hole mobilities, HOPSCs without hole-transporting materials are also possible (Figure 1.5c) [51–53]. Finally, Figure 1.5d shows the composition of the planar hetero-junction solar cells, where the photogeneration and transport of the charge carriers occur in the perovskite layer [54, 55]. Increasing efficiencies are reported for all four setups shown in Figure 1.5 with values over 10% routinely published.

## 1.3 Summary and organisation of the thesis

In this chapter we aimed to set a context and provide motivation for the studies about to be presented in this thesis. To this end, we have briefly described some of the ba-

sic characteristic of the dye-sensitised, semiconductor-sensitised and hybrid organic-inorganic perovskite solar cells, and outlined the most recent development for each of these technologies. In the following chapters we will present the computational research performed during this DPhil project, which was aimed at understanding and predicting the electronic properties of hybrid organic-inorganic perovskites and metal chalcogenides for semiconductor-sensitised solar cells.

This thesis is organised in 9 chapters, including this introduction. Chapter 2 will summarise the theoretical background of the computational methods used throughout the studies presented in this thesis, covering density functional theory and the *GW* method, and technical details needed for practical calculations. Chapters 3, 4, 5 and 6 will be dedicated to hybrid organic-inorganic perovskites. Chapter 3 will present a summary of the general properties of metal-halide perovskites from the most recent experimental and computational literature, while Chapters 4, 5 and 6 will present results of computational studies performed during this DPhil project. Chapter 7 and 8 will cover metal-chalcogenide semiconductor sensitisers, presenting a literature review of the properties of this class of materials (Chapter 7) and a computational study of their electronic structure (Chapter 8). Technical details involved in all calculations are given in the Appendix. Finally, Chapter 9 will present the conclusions of this thesis.

# Chapter 2

## Density Functional Theory and the *GW* method

In this chapter we discuss the two computational methods used throughout this thesis: Density Functional Theory and the *GW* method. The main purpose of this chapter is to briefly describe these two approaches used in the study of the electronic structure of $N$ interacting particle systems. While this chapter touches on the mathematical derivations which are most relevant to the computational studies presented in this thesis, it does not pretend to be an exhaustive description of the DFT or *GW* methodologies. Ample reviews of these methodologies can be found in Refs. [56–58] for DFT and Refs. [59–67] for *GW*.

Aside from the mathematical derivations, this chapter includes a discussion on the main convergence parameters to be taken into consideration in a DFT and *GW* study. While convergence for DFT calculations is reasonably straight forward and generally unproblematic for the materials presented in this thesis, *GW* calculations involve many more convergence parameters which should be analysed carefully.

## 2.1 Density functional theory

### 2.1.1 Many-body Schrödinger equation

In order to calculate the electronic structure of a system of $M$ nuclei and $N$ electrons we must solve the many-body Schrödinger equation shown below (in atomic units) [57]:

$$\begin{aligned}\Big[-\sum_{i=1}^{N}\frac{1}{2}\nabla_i^2-\sum_{I=1}^{M}\frac{1}{2M_I}\nabla_I^2+\sum_{I}^{M-1}\sum_{J=I+1}^{M}\frac{Z_I Z_J}{|\mathbf{R}_I-\mathbf{R}_J|}- \\ -\sum_{i=1}^{N}\sum_{I=1}^{M}\frac{Z_I}{|\mathbf{r}_i-\mathbf{R}_I|}+\sum_{i}^{N-1}\sum_{j=i+1}^{N}\frac{1}{|\mathbf{r}_i-\mathbf{r}_j|}\Big]\Psi(\mathbf{r}_1,\ldots,\mathbf{r}_N;\mathbf{R}_1,\ldots,\mathbf{R}_M)= \\ =\mathscr{E}_{tot}\Psi(\mathbf{r}_1,\ldots,\mathbf{r}_N;\mathbf{R}_1,\ldots,\mathbf{R}_M),\end{aligned} \tag{2.1}$$

where the $I$ and $J$ indices are used to indicate nuclei and $i$ and $j$ are used for electrons. $M_I$ are the atomic masses, $Z_I$ are the atomic numbers, $\mathbf{R}_I$ are the atomic positions and $\mathbf{r}_i$ are the positions of the electrons. $\Psi$ is the total many body wave function and $\mathscr{E}_{tot}$ is the total energy.

Working in the approximation of fixed nuclei [57], we can rewrite Eq. (2.1) for the electrons. In this approximation, the masses of the nuclei are considered much larger than the masses of the electrons, $M_I=\infty$ [57]:

$$\begin{aligned}\Big[-\sum_{i=1}^{N}\frac{1}{2}\nabla_i^2-\sum_{i=1}^{N}\sum_{I=1}^{M}\frac{Z_I}{|\mathbf{r}_i-\mathbf{R}_I|}+\sum_{i=1}^{N-1}\sum_{j=i+1}^{N}\frac{1}{|\mathbf{r}_i-\mathbf{r}_j|}\Big]\psi(\mathbf{r}_1,\ldots,\mathbf{r}_N)= \\ =E_{(\mathbf{R}_1,\ldots,\mathbf{R}_M)}\psi(\mathbf{r}_1,\ldots,\mathbf{r}_N),\end{aligned} \tag{2.2}$$

where $E_{(\mathbf{R}_1,\ldots,\mathbf{R}_M)}$ is the total electronic energy, when the nuclei are in the configuration $(\mathbf{R}_1,\ldots,\mathbf{R}_M)$, and it is defined as [57]:

$$E_{(\mathbf{R}_1,\ldots,\mathbf{R}_M)}=\mathscr{E}_{tot}-\sum_{I}^{M-1}\sum_{J=I+1}^{M}\frac{Z_I Z_J}{|\mathbf{R}_I-\mathbf{R}_J|}. \tag{2.3}$$

The positions of the frozen ions are fixed parameters in this case. If these positions change, the total energy of the electrons in the system also changes [57].

### 2.1.2 Hohenberg and Kohn theorem

The electronic total energy is, in general, a functional of the electronic wave function, $E[\psi(\mathbf{r}_1,\ldots,\mathbf{r}_N)]$:

$$E = \int \mathrm{d}\mathbf{r}_1,\ldots,\mathrm{d}\mathbf{r}_N \psi^*(\mathbf{r}_1,\ldots,\mathbf{r}_N)\hat{H}\psi(\mathbf{r}_1,\ldots,\mathbf{r}_N), \tag{2.4}$$

where $\hat{H} = -\sum_i \frac{1}{2}\nabla_i^2 - \sum_i \sum_{I=1}^{M} \frac{Z_I}{|\mathbf{r}_i-\mathbf{R}_I|} + \frac{1}{2}\sum_{i\neq j} \frac{1}{|\mathbf{r}_i-\mathbf{r}_j|}$ is the many-body hamiltonian. The theorem of Hohenberg and Kohn states that if the system is in the ground state, the total energy is in fact a functional of the electron density, $E[n]$ [68]. The electronic charge density is a function of a single position variable and can be defined as follows [57]:

$$n(\mathbf{r}) = N \int \mathrm{d}\mathbf{r}_2 \ldots \mathrm{d}\mathbf{r}_N \psi^*(\mathbf{r},\mathbf{r}_2,\ldots,\mathbf{r}_N)\psi(\mathbf{r},\mathbf{r}_2,\ldots,\mathbf{r}_N). \tag{2.5}$$

Furthermore, the ground state energy of a system can be found by minimising the total energy functional with respect to the charge density [68]:

$$\frac{\delta E[n]}{\delta n} = 0. \tag{2.6}$$

In practice, one of the main challenges behind solving Eq. 2.6 lies in finding an accurate approximation for the kinetic energy functional of the charge density [69] which constitutes the core focus of the 'Orbital Free Density Functional Theory'. Details of this methodology go beyond the scope of the research presented in this thesis and will not be discussed further. An alternative method to solve Eq. 2.6 is to rewrite the total energy as a sum of separate kinetic and potential energy terms, and express them as functionals of the charge density.

The total energy functional $E[n]$ can be written as:

$$E = \int \mathrm{d}\mathbf{r}_1, \ldots, \mathrm{d}\mathbf{r}_N \psi^*(\mathbf{r}_1, \ldots, \mathbf{r}_N)\Big(-\sum_i \frac{1}{2}\nabla_i^2 + V_{\mathrm{N}}(\mathbf{r}_1, \ldots, \mathbf{r}_N)\Big)\psi(\mathbf{r}_1, \ldots, \mathbf{r}_N) + V_{\mathrm{Coulomb}}[n], \tag{2.7}$$

where $V_{\mathrm{N}}(\mathbf{r}_1, \ldots, \mathbf{r}_N) = \sum_i \sum_{I=1}^{M} \frac{Z_I}{|\mathbf{r}_i - \mathbf{R}_I|}$ is the interaction between electrons and nuclei, and $V_{\mathrm{Coulomb}}[n]$ is a functional approximating the Coulomb interaction between electrons, $\frac{1}{2}\sum_{i \neq j} \frac{1}{|\mathbf{r}_i - \mathbf{r}_j|}$. In the following section, we will show how the problem can be further simplified by applying the Kohn-Sham equations [70].

### 2.1.3 Kohn-Sham equations

The complexity of Eq. (2.2) lies in the Coulomb interaction between electrons, [57]. Without this term, the many-body Schrödinger equation becomes:

$$\Big[-\sum_{i=1}^{N} \frac{1}{2}\nabla_i^2 - \sum_{i=1}^{N}\sum_{I=1}^{M} \frac{Z_I}{|\mathbf{r}_i - \mathbf{R}_I|}\Big]\psi(\mathbf{r}_1, \ldots, \mathbf{r}_N) = E_{(\mathbf{R}_1, \ldots, \mathbf{R}_M)}\psi(\mathbf{r}_1, \ldots, \mathbf{r}_N). \tag{2.8}$$

If we express the many-body wave function as a product of independent single particle wave functions: $\psi(\mathbf{r}_1, \ldots, \mathbf{r}_N) = \phi_1(\mathbf{r}_1) \ldots \phi_N(\mathbf{r}_N)$ then the problem can be reformulated as a set of independent single-particle Schrödinger equations.

The goal of the Kohn-Sham equations is to reformulate the many-body problem in a similar form to Eq. (2.8) but without sacrificing the information included in the electron-electron Coulomb term [70]. In the Kohn-Sham equations, the electron-electron Coulomb interaction is rewritten as a sum of two potentials which are functionals of the electron density: $V_{\mathrm{H}}(\mathbf{r})$ and $V_{\mathrm{xc}}(\mathbf{r})$ [70]. The Hartree potential, $V_{\mathrm{H}}(\mathbf{r})$, accounts for the classical electrostatic interaction between a single electron and the charge density of all the other electrons, $\nabla^2 V_{\mathrm{H}}(\mathbf{r}) = -4\pi n(\mathbf{r})$ [71]. The exchange-correlation potential $V_{\mathrm{xc}}(\mathbf{r})$ accounts for the difference between the electron-electron Coulomb interaction and the Hartree potential, and it is also a functional of the electron density. The local exchange potential is an approximation to the non-local Hatree-Fock potential [72], and arises from the Pauli exclusion principle [57]. Furthermore,

expressing the many-body wave function as a product of single particle wave functions implies that the probability of finding electron $i$ at position $\mathbf{r}_i$ is independent of the probability of finding electron $j$ at $\mathbf{r}_j$, which is not accurate. The correlation potential is the term that corrects this approximation [70]. The exchange-correlation potential has no known analytic form, and it is approximated numerically in practical applications.

The set of independent-particle equations obtained after rewriting the electron-electron Coulomb interaction as the sum of the Hartree and exchange-correlation potentials is known as the Kohn-Sham equations [70]:

$$\begin{aligned}
\Big[-\frac{1}{2}\nabla^2 \;+\; & V_{\mathrm{N}}(\mathbf{r}) + V_{\mathrm{H}}(\mathbf{r}) + V_{\mathrm{xc}}(\mathbf{r})\Big]\phi_n(\mathbf{r}) = \epsilon_n \phi_n(\mathbf{r}), \qquad (2.9)\\
V_{\mathrm{N}}(\mathbf{r}) &= -\sum_I \frac{Z_I}{|\mathbf{r}-\mathbf{R}_I|},\\
\nabla^2 V_{\mathrm{H}}(\mathbf{r}) &= -4\pi n(\mathbf{r}),\\
V_{\mathrm{xc}}(\mathbf{r}) &= \frac{\delta E_{\mathrm{xc}}[n]}{\delta n},\\
n(\mathbf{r}) &= \sum_n |\phi_n(\mathbf{r})|^2,
\end{aligned}$$

where $\epsilon_n$ are the energy eigenvalues (also known as Kohn-Sham eigenvalues), and $\phi_n(\mathbf{r})$ are the corresponding single particle eigenfunctions [57]. The sequence of equations shown in Eq. (2.9) is solved iteratively until the change in the charge density calculated at two consecutive steps is smaller than a chosen threshold.

### 2.1.4 Local density approximation

The premise of local density approximation (LDA) [73, 74] is that the exchange and correlation interactions between electrons in a system may be approximated locally with the exchange and correlation interactions between electrons in a homogeneous electron gas [73, 74].

The exchange energy functional of the homogeneous electron gas can be expressed

analytically as [57, 75]:

$$E_{\mathrm{x}}^{\mathrm{hom}}[n(\mathbf{r})] = -\frac{3}{4}\Big(\frac{3}{\pi}\Big)^{1/3} n^{4/3}(\mathbf{r}). \tag{2.10}$$

The correlation energy for the homogeneous electron gas has no known analytic form. It has been calculated numerically [73] and parametrized as [74]:

$$E_{\mathrm{c}}^{\mathrm{hom}} = \begin{cases} -0.0480 + 0.0311\ \ln r_s - 0.0116\ r_s + 0.002\ r_s \ln r_s & \text{if } r_s < 1, \\ -0.1423(1 + 1.0529\sqrt{r_s} + 0.3334\ r_s)^{-1} & \text{if } r_s \geq 1, \end{cases} \tag{2.11}$$

where $r_s = \Big(\frac{3}{4\pi n}\Big)^{1/3}$ is the Wigner-Seitz radius [76].

Furthermore, the exchange-correlation functional can also be approximated by taking into account both the charge density and the charge density gradient, $E_{\mathrm{xc}}[n, \nabla n]$. This formulation is known as the generalized gradient approximation (GGA) [77].

Both the LDA and GGA are popular approximation methods for the exchange correlation functional in DFT. While, both LDA and GGA are generally similar in performance, it has been shown in some benchmarking tests that lattice constants, bulk moduli and phonon frequencies obtained within LDA are in better agreement to experiment than those obtained from GGA [78], while GGA calculations of cohesive energies are in better agreement with experiment than those claculated within LDA [78]. Due to these observation, throughout the calculations presented in this thesis we choose the local density approximation for the calculation of the ground state electronic properties of metal-halide perovskites and metal chalchogenides of the stibnite family.

### 2.1.5 Spin-orbit coupling

In broad terms, the spin-orbit coupling is the interaction between the intrinsic angular momentum of an electron and the magnetic field created by its movement around the nucleus [79]. If we consider the simple case of a single electron moving around a nucleus under the effect of a spherical potential $V(r)$, the spin-orbit interaction

introduces the following additional term into the Hamiltonian (in atomic units) [79]:

$$\hat{H}_{\mathrm{SO}} = \frac{1}{2c^2}(\boldsymbol{l}\cdot\boldsymbol{s})\frac{1}{r}\frac{\mathrm{d}V}{\mathrm{d}r}, \tag{2.12}$$

where $\boldsymbol{l}$ is angular momentum, and $\boldsymbol{s}$ is the intrinsic angular momentum of the electron and $c$ is the speed of light in vacuum expressed in atomic units.

The spin-orbit coupling is a relativistic effect [79, 80]. In order to describe it in the many-body context a treatment involving the Dirac equation must be employed [81]. In the relativistic case, the single-particle Kohn-Sham wave functions are replaced by two-component spinors [70, 82]. This implies that the charge density function shown in Eq. (2.9) now becomes an electron density matrix [57]:

$$n_{\alpha\beta}(\mathbf{r}) = \sum_n \phi_n^*(\mathbf{r};\alpha)\phi_n(\mathbf{r};\beta), \tag{2.13}$$

where $\alpha, \beta$ indicate the two spinor components [57]. In this case the total energy will have to be minimised with respect to this electron density matrix, or equivalently with respect to the charge density and the spin density, both defined below [57]:

$$n(\mathbf{r}) = \sum_\alpha n_{\alpha\alpha}(\mathbf{r}), \tag{2.14}$$

$$\mathbf{s}(\mathbf{r}) = \frac{1}{2}\sum_{\alpha\beta} n_{\alpha\beta}(\mathbf{r})\boldsymbol{\sigma}_{\alpha\beta}, \tag{2.15}$$

where the vector $\boldsymbol{\sigma}_{\alpha\beta} = \sigma^x_{\alpha\beta}\hat{\mathbf{x}} + \sigma^y_{\alpha\beta}\hat{\mathbf{y}} + \sigma^z_{\alpha\beta}\hat{\mathbf{z}}$ with:

$$\sigma^x = \begin{pmatrix} 0 & 1 \\ 1 & 0 \end{pmatrix},\ \sigma^y = \begin{pmatrix} 0 & -i \\ i & 0 \end{pmatrix},\ \sigma^z = \begin{pmatrix} 1 & 0 \\ 0 & -1 \end{pmatrix},$$

the Pauli matrices [79]. The Kohn-Sham equations in this case can be rewritten as [57]:

$$\Big[-\frac{1}{2}\nabla^2 + V_{\rm N}(\mathbf{r}) + V_{\rm H}(\mathbf{r})\Big]\phi_n(\mathbf{r};\alpha) + \sum_\beta v^{\rm xc}_{\alpha\beta}(\mathbf{r})\phi_n(\mathbf{r};\beta) = \epsilon_n\phi_n(\mathbf{r};\alpha), \quad (2.16)$$

$$\begin{aligned} V_{\rm N}(\mathbf{r}) &= -\sum_I \frac{Z_I}{|\mathbf{r}-\mathbf{R}_I|}, \\ \nabla^2 V_{\rm H}(\mathbf{r}) &= -4\pi\sum_n n_{\alpha\alpha}(\mathbf{r}), \\ v^{\rm xc}_{\alpha\beta}(\mathbf{r}) &= V_{\rm xc}(\mathbf{r})\mathbf{1} + \mu_{\rm B}\boldsymbol{\sigma}\cdot\mathbf{B}_{\rm xc}(\mathbf{r}), \\ n_{\alpha\beta}(\mathbf{r}) &= \sum_n \phi^*_n(\mathbf{r};\alpha)\phi_n(\mathbf{r};\beta), \end{aligned}$$

where the exchange-correlation potential has been replaced by an exchange correlation matrix, which includes the contribution from the $V_{\rm xc}(\mathbf{r})$ described for the spin unpolarised case [57, 83]. The $B_{\rm xc}(\mathbf{r})$ component is called the exchange-correlation magnetic field, and can be intuitively regarded as an effective contribution of the non-collinear spins of all electrons in the system [57].

## 2.2 The *GW* approximation

One of the well known limitations of density functional theory is the "band gap problem" for semiconductors and insulators [74, 84], by which the band gaps calculated within DFT are systematically underestimated with respect to experiment. In Figure 2.1 we show a plot of the DFT/LDA calculated band gaps and the experimental band gaps for a range of materials, taken from Ref. [85]. From this plot, we can see that all DFT/LDA data points lie under the diagonal, i.e. they underestimate the experimental band gaps. Despite the consistent underestimation of band gaps for semiconductors and insulators, band gap trends are generally captured within DFT, and they are considered a good starting point for more sophisticated methodologies.

More generally, the band gap is defined as the difference between the electron affinity and the ionisation potential [84]. In other words it is the difference between the minimum energy required to add an electron to a system and the minimum energy

required to remove an electron from the system [84]:

$$E_g = \Big[E(N+1) - E(N)\Big] - \Big[E(N) - E(N-1)\Big], \tag{2.17}$$

where $E(N+1)$ is the total energy of the system with one extra electron, $E(N)$ is the total energy of the system in its ground state and $E(N-1)$ is the total energy of the system missing one electron. This definition shows that a quantum mechanical description of the addition or removal of an electron from the system is necessary for the correct calculation of the band gap. Therefore, to calculate band gaps we need a formalism which can describe quantum systems with a variable number of particles.

### 2.2.1 The many-body Hamiltonian in second quantisation

The many-body Hamiltonian in the fixed nuclei approximation discussed in the previous section can be rewritten in the second quantisation as [59]:

$$H = \int \psi^\dagger(\mathbf{r}) h(\mathbf{r}) \psi(\mathbf{r}) \mathrm{d}\mathbf{r} + \int \psi^\dagger(\mathbf{r}) \psi^\dagger(\mathbf{r}') v(\mathbf{r}, \mathbf{r}') \psi(\mathbf{r}') \psi(\mathbf{r}) \mathrm{d}\mathbf{r} \mathrm{d}\mathbf{r}', \tag{2.18}$$

where $\mathbf{r}$ and $\mathbf{r}'$ are the position variables and the electronic spin is ignored in this discussion for simplicity. The following notations have been employed [59]:

1. $h(\mathbf{r}) = \sum_i^N \Big[\Big(-\frac{1}{2}\nabla_i^2\Big) + V_{\mathrm{N}}(\mathbf{r}_i)\Big]$ is the single particle hamiltonian.
2. $v(\mathbf{r}, \mathbf{r}') = \dfrac{1}{|\mathbf{r} - \mathbf{r}'|}$ is the Coulomb interaction between electrons.
3. $\psi^\dagger(\mathbf{r})$ and $\psi(\mathbf{r})$ are the creation and annihilation field operators in second quantisation.

Furthermore, the time-dependent field operators in the Heisenberg picture have the following form [59]:

$$\begin{aligned} \psi(\mathbf{r}, t) &= \exp(iHt)\psi(\mathbf{r})\exp(-iHt), \\ \psi^\dagger(\mathbf{r}, t) &= \exp(iHt)\psi^\dagger(\mathbf{r})\exp(-iHt). \end{aligned} \tag{2.19}$$

The time-dependent field operator $\psi(\mathbf{r},t)$ verifies the Heisenberg equation of motion [59]: $-i\frac{\partial}{\partial t}\psi(\mathbf{r},t) = [\psi(\mathbf{r},t), H]$. Therefore, we can write the Heisenberg equation of motion for the field operator in the following form [59]:

$$\left[h(\mathbf{r}) + \int v(\mathbf{r},\mathbf{r}')\psi^{\dagger}(\mathbf{r}',t)\psi(\mathbf{r}',t)\mathrm{d}\mathbf{r}'\right]\psi(\mathbf{r},t) = -i\frac{\partial}{\partial t}\psi(\mathbf{r},t). \tag{2.20}$$

### 2.2.2 The single-particle Green's function

In order to understand the addition or removal of an electron to a system of $N$ electrons, we define the single particle Green's function [59]:

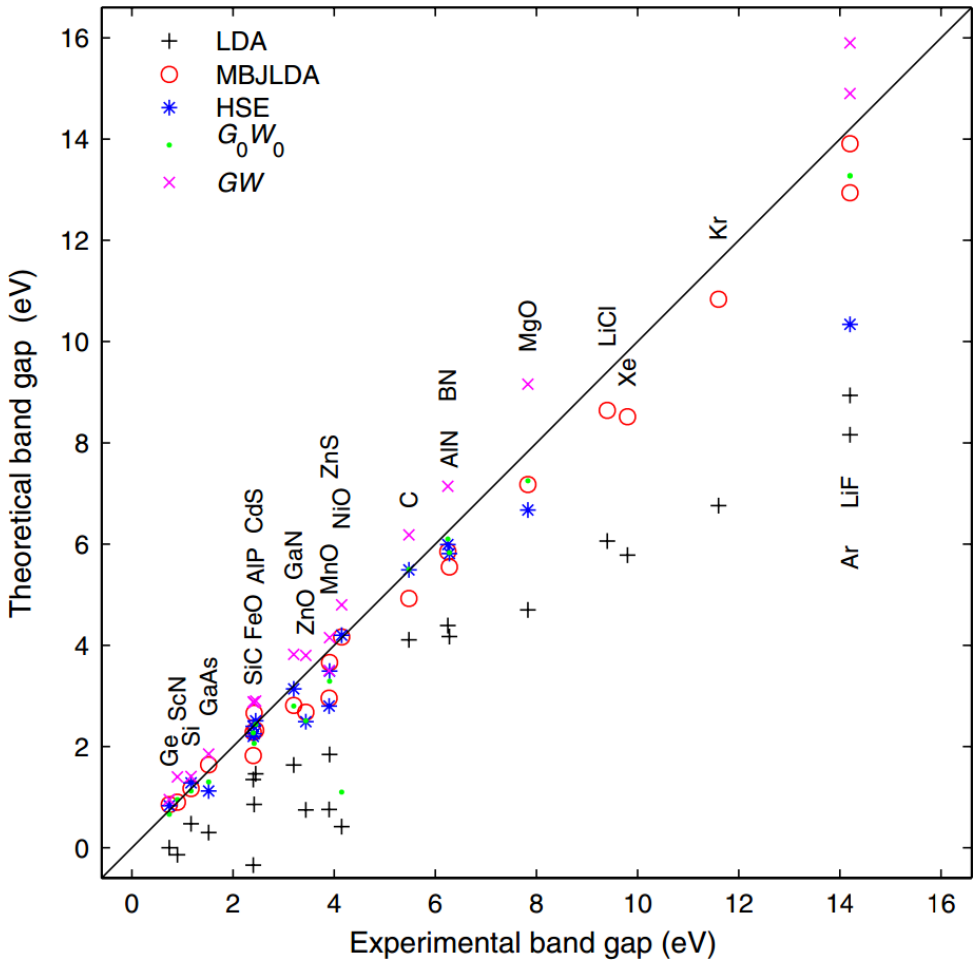


Figure 2.1: Comparison between experimental band gaps and band gaps calculated within local density approximation (LDA), the modified Becke-Johnson local density aproximation (MBJLDA) [85], the Heyd - Scuseria - Erzenhof [86] screened functional hybrid exchange functional (HSE) the $G_0W_0$ method and self-consistent $GW$. Only the comparison between LDA and the $GW$ methods are relevant to the discussion in this chapter. The figure is taken from Ref. [85] with permission.

$$G(\mathbf{r}t;\mathbf{r}'t') = -i\langle N|T[\psi(\mathbf{r},t)\psi^{\dagger}(\mathbf{r}',t')]|N\rangle, \tag{2.21}$$

where $|N\rangle$ is the ground state of an $N$-electron system with corresponding energy $E(N)$, and $T$ is the time-ordering operator [59]. The Green function describes the propagation of an electron added at position $\mathbf{r}'$ and moment $t'$ (if we assume that $t > t'$). Furthermore, the time-dependent field operator $\psi(\mathbf{r},t)$ has the following property [59]:

$$\langle N|\psi(\mathbf{r},t)|N+1,s\rangle = f_s(\mathbf{r})\exp(-iE_s t), \tag{2.22}$$

where $f_s(\mathbf{r}) = \langle N|\psi(\mathbf{r})|N+1,s\rangle$, $|N+1,s\rangle$ is an eigenstate of the $(N+1)$-electron system with energy $E(N+1,s)$ and $E_s = E(N+1,s) - E(N)$. Using Eq. (2.22) and the completeness relation for the eigenstates of the $(N+1)$-electron system we obtain the Fourier transform of the Green's function in the following form [59]:

$$G(\mathbf{r},\mathbf{r}';\omega) = \sum_s \frac{f_s(\mathbf{r})f_s^*(\mathbf{r})}{\omega - E_s - i\delta}, \tag{2.23}$$

where $\delta$ is a small constant which is generally positive when $s$ is an occupied state and negative when $s$ is an unoccupied state of the $N$-particle system.

### 2.2.3 The quasiparticle self-energy

Using the definition of the Green's function, we can Fourier transform the Heisenberg equation of motion as [Eq. (2.20)] [59]:

$$\Big[\omega - h(\mathbf{r}) - V_H(\mathbf{r})\Big]G(\mathbf{r},\mathbf{r}';\omega) - \int \Sigma(\mathbf{r},\mathbf{r}'';\omega)G(\mathbf{r}'',\mathbf{r}';\omega)\mathrm{d}\mathbf{r}'' = \delta(\mathbf{r}-\mathbf{r}'), \tag{2.24}$$

where $V_H(\mathbf{r})$ is the Hatree potential defined in the previous section. The "self energy" $\Sigma(\mathbf{r},\mathbf{r}';\omega)$ is defined so that the following expression is valid for its Fourier transform [59]:

$$i\int \mathrm{d}\mathbf{r}''v(\mathbf{r},\mathbf{r}'')\langle N|T[\psi^{\dagger}(\mathbf{r}'',t)\psi(\mathbf{r}'',t)\psi(\mathbf{r},t)\psi^{\dagger}(\mathbf{r}',t')]|N\rangle = \tag{2.25}$$
$$-V_H(\mathbf{r})G(\mathbf{r}t;\mathbf{r}'t')-\int \Sigma(\mathbf{r}t;\mathbf{r}''t'')G(\mathbf{r}''t'';\mathbf{r}'t')\mathrm{d}\mathbf{r}''\mathrm{d}t''.$$

Furthermore, if we use the expression in Eq. (2.23) for the Green's function and replace it in Eq. (2.24), we can rewrite the equation of motion in a form that resembles the Kohn-Sham equations [59]:

$$\Big[h(\mathbf{r})+V_H(\mathbf{r})\Big]f_s(\mathbf{r},\omega)+\int \Sigma(\mathbf{r},\mathbf{r}'';\omega)f_s(\mathbf{r}'',\omega)\mathrm{d}\mathbf{r}''=E_sf_s(\mathbf{r},\omega), \tag{2.26}$$

where $f_s(\mathbf{r})$ is reminiscent of a single particle wave function. In comparison with the Kohn-Sham equations, the exchange-correlation potential is now replaced by the more complicated self-energy operator, $\Sigma$. The self energy operator is non-local, non-Hermitian and frequency-dependent, and describes the quasiparticle self-interaction [62, 64]. Intuitively, by using the concept of quasiparticles we translate the problem of many-interacting electrons into a problem of weakly interacting quasiparticles. The quasiparticle represents a bare electron screened by a surrounding positive charge [62, 64]. The remaining question is how the self-energy and the Green's function can be calculated in practice.

### 2.2.4 Dyson's equation

In the simplified case of non-interacting electrons the second term from the left hand side of Eq. 2.24 vanishes, leading to an expression for the non-interacting Green's function [63]: $\delta(\mathbf{r}-\mathbf{r}')=[\omega-h(\mathbf{r})-V_H(\mathbf{r})]G_0(\mathbf{r},\mathbf{r}',\omega)$. If we introduce this expression in the equation of motion we readily obtain the Dyson's equation, written schematically as [59, 63, 64]:

$$G=G_0+G_0\Sigma G. \tag{2.27}$$

According to this expression the Green's function can in principle be calculated self-

consistently [63, 64]. We will come back to the the idea Dyson's equation for a fully self-consistent *GW* calculation later on in this chapter. In practice, the Green's function is approximated by the non-interacting Kohn-Sham Green's function $G_0$ and has the following expression [63]:

$$G_0(\mathbf{r},\mathbf{r}';\omega) = \sum_n \frac{\phi_n(\mathbf{r})\phi_n^*(\mathbf{r}')}{\omega - \epsilon_n - i\delta}, \tag{2.28}$$

where $\phi_n$ are the Kohn-Sham single particle wave functions obtained from a DFT/LDA calculation, and $\epsilon_n$ are the corresponding Kohn-Sham eigenvalues [63].

If we compare Eq. (2.28) with Eq. (2.23), we can use this analogy to rewrite Eq. (2.26) using the Kohn-Sham single particle wave functions instead of the functions $f_s(\mathbf{r};\omega)$ [63]:

$$\Big[h(\mathbf{r}) + V_{\mathrm{H}}(\mathbf{r})\Big]\phi_n(\mathbf{r}) + \int \Sigma(\mathbf{r},\mathbf{r}';E_n)\phi_n(\mathbf{r}')\mathrm{d}\mathbf{r}' = E_n\phi_n(\mathbf{r}). \tag{2.29}$$

Furthermore, the Kohn-Sham eigenvalues satisfy the Kohn-Sham equations, therefore the first term of the left hand side is equivalent to $\Big[\epsilon_n - V_{\mathrm{xc}}(\mathbf{r})\Big]\phi_n(\mathbf{r})$, where $\epsilon_n$ are the Kohn-Sham eigenvalues corresponding to $\phi_n(\mathbf{r})$, and $V_{\mathrm{xc}}(\mathbf{r})$ is the exchange and correlation potential. Finally, after rearranging terms and taking advantage of the orthonormality of the Kohn-Sham wave functions, Eq. (2.29) can be rewritten as [62–64]:

$$E_n = \epsilon_n + \langle\phi_n|\Sigma(E_n) - V_{\mathrm{xc}}|\phi_n\rangle. \tag{2.30}$$

The dependence of the self energy on the quasiparticle energy $E_n$ can be taken into account by retaining only the first order term in the Taylor expansion of the self energy around the Kohn-Sham eigenvalues, obtaining: $\Sigma(E_n) = \Sigma(\epsilon_n) + \frac{\partial\Sigma}{\partial\omega}\Big|_{\omega=\epsilon_n}(E_n - \epsilon_n)$. Using this approximation we obtain the final expression for the quasiparticle energy as [64]:

$$E_n = \epsilon_n + Z(\epsilon_n)\langle\phi_n|\Sigma(\epsilon_n) - V_{\mathrm{xc}}|\phi_n\rangle, \tag{2.31}$$

where $Z(\epsilon_n) = \left(1 - \frac{\partial \Sigma}{\partial \omega}\Big|_{\omega=\epsilon_n}\right)^{-1}$ is called the "quasiparticle renormalisation" constant [64].

Eq. (2.31) is the main expression which will be used for the calculation of the quasiparticle energies throughout this thesis. The quasiparticle energies are therefore calculated using a first order perturbation theory approach, with the Kohn-Sham eigenvalues and eigenfunctions as a starting point for the calculation of the non-interacting Green's function [62–65]. The remaining ingredient needed for the calculation is an expression for the quasiparticle self energy.

### 2.2.5 Hedin's equations

The quasiparticle self energy can be calculated, in principle, by solving Hedin's equations self-consistently [59]. Hedin's equations involve a large number of position and time variables for which we use the following notation: $1 = (\mathbf{r}, t)$ and $1^+ = (\mathbf{r}, t+\delta)$, where $\delta$ is a small positive constant, and different numbers mark different variable sets. With these notations Hedin's equations have the following form [59]:

$$\begin{aligned}
\Sigma(1,2) &= i\int W(1^+,3)G(1,4)\Gamma(4,2;3)\mathrm{d}(34), \qquad (2.32)\\
W(1,2) &= v(1,2) + \int W(1,3)P(3,4)v(4,2)\mathrm{d}(3,4),\\
P(1,2) &= -i\int G(2,3)G(4,2)\Gamma(3,4;1)\mathrm{d}(3,4),\\
\Gamma(1,2;3) &= \delta(1,2)\delta(1,3) + \int \frac{\partial \Sigma(1,2)}{\partial G(4,5)} G(4,6)G(7,5)\Gamma(6,7;3)\mathrm{d}(4,5,6,7).
\end{aligned}$$

The three new quantities in this set of equations are described below:

1. $P(1,2) = \frac{\delta n(1)}{\delta V(2)}$ is the irreducible polarisability and it is defined as the response of the charge density, $\delta n(1)$, to a small external perturbation, $\delta V(2)$.

2. $W(1,2)$ is the screened Coulomb interaction.

3. $\Gamma(1,2;3) = -\frac{\delta G^{-1}(1,2)}{\delta V(3)}$ is the vertex function, defined as the response of the

Green's function to the external perturbation, $\delta V(3)$ [59, 60, 64].

In this form, solving Hedin's equations is too challenging and approximations are required. The first approximation is to set $\Gamma(1,2;3) = \delta(1,2)\delta(1,3)$, obtaining the following simplified equations [59, 64]:

$$\Sigma(1,2) = iG(1,2)W(1^+,2), \tag{2.33}$$

$$W(1,2) = v(1,2) + \int W(1,3)P(3,4)v(4,2)\mathrm{d}(3,4), \tag{2.34}$$

$$P(1,2) = -iG(1,2)G(2,1). \tag{2.35}$$

The first equation leads to the name of the "$GW$ approximation", and provides an expression for the calculation of the self energy.

### 2.2.6 Screened Coulomb interaction

Using the non-interacting Green's function $G_0(\mathbf{r},\mathbf{r}';\omega)$, the non-interacting polarisability $P_0(\mathbf{r},\mathbf{r}';\omega)$ can be calculated as shown in Eq. (2.35). The expression for the polarisability in the absence of the vertex $\Gamma$ is also known as the Random Phase Approximation (RPA) [87, 88]. $P_0$ is then used to calculate the Screened Coulomb interaction, $W_0(\mathbf{r},\mathbf{r};\omega)$ and obtain the self energy. In practical calculations, the self energy is written as a sum of an energy-independent term (exchange) and an energy-dependent term (correlation) [89]:

$$\Sigma(\mathbf{r},\mathbf{r}';\omega) = \Sigma_x(\mathbf{r},\mathbf{r}') + \Sigma_c(\mathbf{r},\mathbf{r}';\omega), \tag{2.36}$$

where $\Sigma_x = iGv$ and $\Sigma_c = iG(W-v)$.

The $G_0W_0$ method is an approximation of the $GW$ method. The $G_0$ notation suggests that the Green's functions considered in the calculation are non-interacting and are calculated without iterating the Dyson's equation. Furthermore, the non-interacting Green's functions are used to calculate the irreducible RPA polarisability $P_0$ and the screened Coulomb interaction $W_0$.

### 2.2.7 Self-consistency

The $G_0W_0$ quasiparticle energies can be sensitive to the Kohn-Sham eigenvalues and eigenstates used as a starting point to calculate the perturbative corrections [90–96]. It is now well established that this sensitivity can be mitigated by employing a self-consistent approach in the many-body perturbation theory [90–96].

In Figure 2.2 we show a schematic representation of the various routes to calculate the quasiparticle energies starting from the approximations made to Hedin's equations. Within the *GW* approximation two types of approaches can be distinguished: the perturbative and the fully self-consistent approach [96].

The fully self-consistent *GW* method implies the use of the interacting Green's functions, calculated from the Dyson's equation. In practice, this approach is computationally very demanding, and has so far been implemented only for finite systems, using

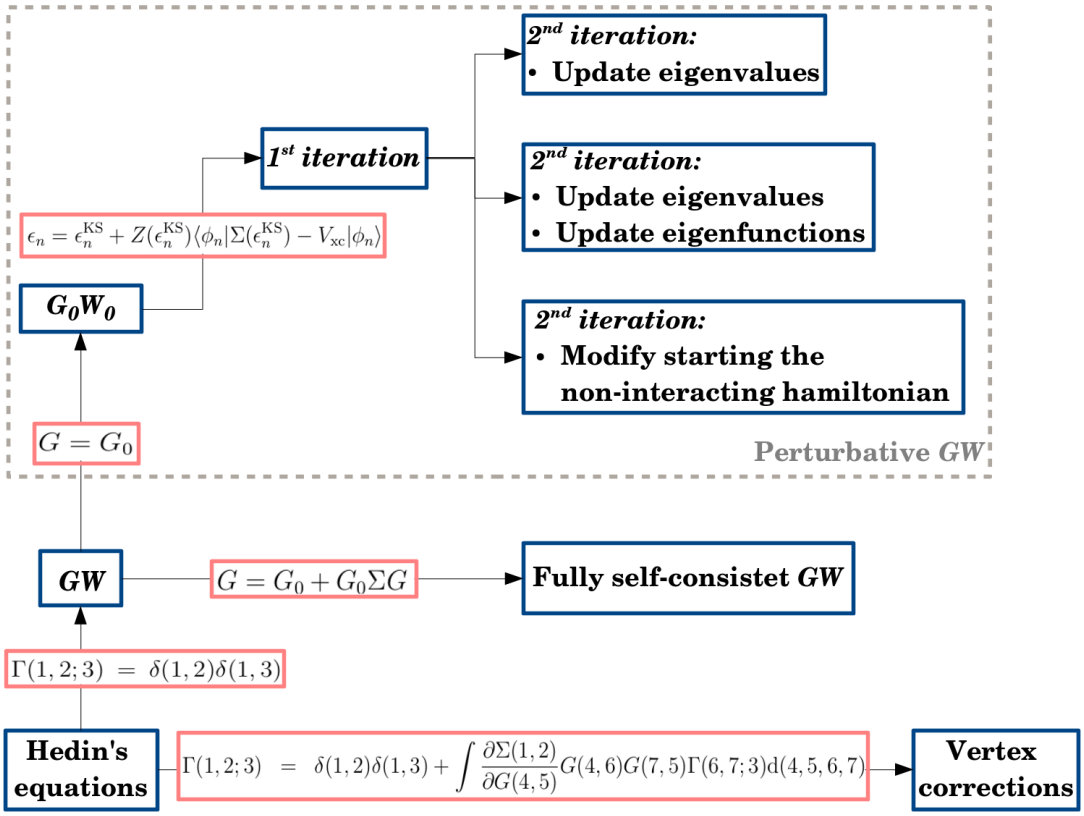


Figure 2.2: Schematic summary of possible routes for self-consistency in the *GW* approximation.

localised basis sets [96].

In perturbative *GW* the quasiparticle eigenvalues can be obtained within 1st ($G_0W_0$) or higher orders perturbation theory. Higher order iterations are performed either by updating only the single-particle eigenvalues with the $G_0W_0$ eigenvalues, or both the eigenvalues and eigenfunctions and recalculating the quasiparticle eigenvalues using Eq. (2.30). An alternative approach is to use the quasiparticle eigenvalues and eigenfunctions calculated at the first iteration to construct a modified single particle Hamiltonian and repeat the $G_0W_0$ process. This basic approach has been implemented in methods such as the quasiparticle self-consistent *GW* (QS*GW*) [90], or *GW*+U [91, 92]. Since the higher order iterations in perturbative *GW* are generally repeated until the quasiparticle eigenvalues are converged within a chosen threshold, these approaches are often referred to in literature as self-consistent approaches. In Chapter 4 we will discuss a simplified iterative method for perturbative *GW*, which we call SS-*GW* (self-consistent scissor *GW*) [97]. Using this new method, we are able to address the self-consistency requirement for the calculation of the quasiparticle band gaps of $CH_3NH_3PbI_3$ with the computational cost of a single $G_0W_0$ calculation [97].

### 2.2.8 $G_0W_0$ approximation including spin-orbit coupling

In order to include the spin-orbit contribution to the quasiparticle eigenvalues, the independent particle wave functions used to construct the non-interacting Green's functions have to be spin-dependent. Therefore, the non-interacting green's function $G_0$ can now be put in a 2×2 matrix form, in order to account for the two-component spinors [98]:

$$G_0^{\alpha\beta}(\mathbf{r},\mathbf{r}';\omega) = \sum_n \frac{\phi_n(\mathbf{r},\alpha)\phi_n^*(\mathbf{r},\beta)}{\omega - \epsilon_n \pm i\delta}, \tag{2.37}$$

where $\phi_n(\mathbf{r},\alpha)$ are the single particle spinors. The irreducible RPA polarisability can then be calculated as [98]:

$$P_0(\mathbf{r},\mathbf{r}';\omega) = -\frac{i}{2\pi}\sum_{\alpha\beta}\int G_0^{\alpha\beta}(\mathbf{r},\mathbf{r}';\omega+\omega')G_0^{\beta\alpha}(\mathbf{r}',\mathbf{r};\omega)\mathrm{d}\omega' \tag{2.38}$$

It follows that the screened Coulomb interaction $W_0(\mathbf{r},\mathbf{r}';\omega)$ will be influenced by the spin-orbit interaction due to the spin-dependent non-interacting Green's function. Consequently, we can write the 2×2 matrix form for the self energy [98–100]:

$$\Sigma_{\alpha\beta}(\mathbf{r},\mathbf{r}';\omega) = -\frac{i}{2\pi}\int G_0^{\alpha\beta}(\mathbf{r},\mathbf{r}';\omega+\omega')W_0(\mathbf{r},\mathbf{r}';\omega)\mathrm{d}\omega'. \tag{2.39}$$

The quasiparticle energies in the $G_0W_0$ approximation are obtained for non-magnetic materials as [98–100]:

$$E_n = \epsilon_n + \sum_{\alpha\beta}\langle\phi_{n,\alpha}|\Sigma_{\alpha\beta}(E_n) - V_{\mathrm{xc}}|\phi_{n,\beta}\rangle. \tag{2.40}$$

## 2.3 Practical calculations

In this section we attempt to bridge the theoretical details described so far and the practical calculations within DFT and *GW* for crystalline solids in a plane-wave representation. The goal is to highlight the principal convergence parameters involved in these methodologies.

All DFT calculations discussed throughout this thesis are performed using the `Quantum Espresso` [101] suite. *GW* calculations discussed here are performed with the `Yambo` [102] and `SaX` [89] codes. The convergence tests for all calculations shown in the results Chapters 4 - 6 and 8 are discussed in the Appendix.

For the case of crystalline solids, both the DFT and *GW* formalisms discussed so far can be rewritten taking advantage of the crystal periodicity. In particular, the Kohn-Sham eigenfunctions which are involved throughout both methodologies can be rewritten as [57]:

$$\phi_{n\mathbf{k}}(\mathbf{r}) = \mathrm{e}^{i\mathbf{k}\cdot\mathbf{r}}u_{n\mathbf{k}}(\mathbf{r}), \tag{2.41}$$

where $u_{n\mathbf{k}}(\mathbf{r})$ is periodic with the same unit of repetition as the crystal lattice. In practical applications, the Bloch functions $u_{n\mathbf{k}}(\mathbf{r})$ have to be expanded in a basis set. In the data presented throughout this thesis, we use a plane-wave representation, as implemented in `Quantum Espresso`, `Yambo` and `SaX`. Combining the Bloch's theorem with the expansion in a plane wave basis set we obtain the Kohn-Sham wave functions as [89]:

$$\psi_{n\mathbf{k}}(\mathbf{r}) = \frac{1}{\sqrt{\Omega}} \sum_{\mathbf{G}} c_{n\mathbf{k}+\mathbf{G}} e^{i(\mathbf{k}+\mathbf{G})\cdot\mathbf{r}}, \tag{2.42}$$

where $\Omega$ is the unit cell volume and $\mathbf{G}$ represents a vector in the reciprocal lattice space.

### 2.3.1 Convergence in DFT

#### Plane waves

Using the Bloch theorem, the charge density can be rewritten as [57]:

$$n(\mathbf{r}) = \sum_{n} \int_{BZ} \frac{d\mathbf{k}}{\Omega} |u_{n\mathbf{k}}(\mathbf{r})|^2, \tag{2.43}$$

where the sum is performed only for occupied states and the integration is performed in the first Brillouin zone. In practice, this integral is performed numerically by sampling the first Brillouin zone using a discrete grid of $\mathbf{k}$-points. The denser the grid, the more accurate the calculation of the electron density. The density of the $\mathbf{k}$-point grid is one of the parameters which must be converged in the DFT calculation. Furthermore, by combining Eq. (2.42) and (2.43) we obtain:

$$n(\mathbf{r}) = \sum_{n} \int_{BZ} \frac{d\mathbf{k}}{\Omega} \sum_{\mathbf{G}\mathbf{G}'} c^*_{n\mathbf{k}+\mathbf{G}} c_{n\mathbf{k}+\mathbf{G}'} \exp[i(\mathbf{G}'-\mathbf{G})\mathbf{r}]. \tag{2.44}$$

The summations over the $\mathbf{G}$ and $\mathbf{G}'$ vectors in Eq. (2.42) and (2.44) are truncated by setting the cutoffs $\mathbf{G}_{\text{cut}}$ and $\mathbf{G}'_{\text{cut}}$. The plane wave cutoffs are set by cutoff energy parameters so that $E_{\text{cut}} = \frac{1}{2}|\mathbf{G}_{\text{cut}}|^2$. The two cutoff energies required for the calculation

of the charge density are the kinetic and the charge density cutoff. For calculations using norm conserving pseudopotentials (see discussion below) the required charge density cutoff is exactly 4 times the kinetic cutoff and does not need to be converged separately. Separate convergence tests are required for calculations using ultrasoft pseudopotentials.

**Pseudopotentials**

In the case of an isolated atom, we can calculate the electronic eigenvalues and eigenfunctions using the Kohn-Sham equations[103]:

$$\left[\hat{T}_{\text{rad}} + V_{\text{N}}(r) + \hat{V}_{\text{H}}[n] + \hat{V}_{\text{xc}}[n]\right]\psi_{nl}(r) = \epsilon_{nl}\psi_{nl}(r), \tag{2.45}$$

where the equation is written only for the radial part of the wave function, and the kinetic energy term in Eq. (2.9) is replaced by the operator notation $\hat{T}_{\text{rad}}$ (for the radial coordinate). The indexes $n$ and $l$ are the principal and angular momentum quantum numbers (not to be confused with the electron density in $V_{\text{xc}}[n]$), $V_{\text{N}}(r) = -Z/r$ in the case of the isolated atom, $\psi_{nl}(r)$ is the radial component of the all-electron eigenfunction with corresponding eigenvalue $\epsilon_{nl}$. The most intuitive way to reduce the computational cost of Eq. (2.9) is to separate the valence electrons from the localised core electrons in an atom. This way we would effectively replace the system containing $Z$ electrons, by a "pseudo-atom" containing only the valence electrons. The Kohn-Sham equations for the pseudo-atom can be written as [57, 103]:

$$\left[\hat{T}_{\text{rad}} + V^{l}_{\text{ps}}(r) + \hat{V}_{\text{H}}[n_{ps}] + \hat{V}_{\text{xc}}[n_{ps}]\right]\phi_{l}(r) = \epsilon_{l}\phi_{l}(r), \tag{2.46}$$

where here $V^{l}_{\text{ps}}(r)$ is the pseudopotential describing the core of the pseudo-atom, $n_{ps}$ is the electron density for the pseudo-atom, $\phi_l(r)$ are the radial component of the eigenfunctions of the pseudo-atom and $\epsilon_l$ the corresponding eigenvalues. The eigenfunctions of the pseudo-atom are required to be identical to the all-electron wave functions for the same angular momentum beyond a chosen cutoff radius, $r_{\text{c},l}$, and

to be nodeless (if possible), as shown in Figure 2.3. Furthermore, for each angular momentum the eigenvalues calculated for the all-electron and the pseudised system must be identical, $\epsilon_l = \epsilon_{nl}$ [103]. The pseudopotential will then have the following form [103]:

$$V_{ps}^{l}(r) = \epsilon_l - \frac{1}{\phi_l(r)}\Big[\hat{T}_{\text{rad}} + \hat{V}_{\text{H}}[n_{ps}(r)] + \hat{V}_{\text{xc}}[n_{ps}(r)]\Big]\phi_l(r). \tag{2.47}$$

Useful pseudopotentials must be transferable (from calculations on an isolated atom to molecular or crystalline systems) and efficient from a computational point of view [56, 103]. In this thesis we discuss calculations using norm-conserving and ultrasoft pseudopotentials, scalar and fully relativistic pseudopotentials and pseudopotentials with and without semicore. In the following we briefly describe all of these types of pseudopotentials.

1. **Norm conserving and ultrasoft pseudopotentials.**

   Norm conserving pseudopotentials have the requirement that the pseudised charge density up to the cutoff radius must be equal to the all-electron charge

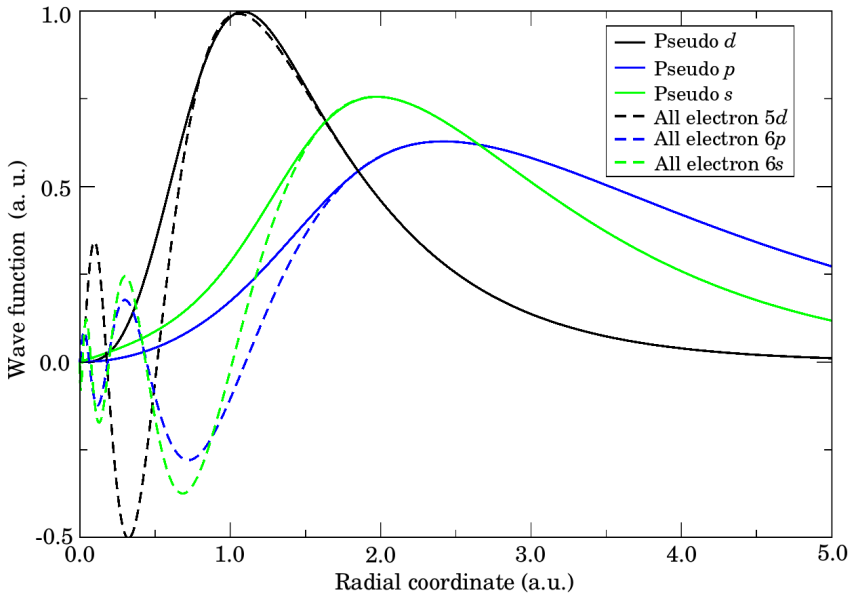


Figure 2.3: Comparison between the all electron (all dashed lines) and pseudised (all continuous lines) wave functions for the case of Pb. The black lines correspond to the $d$ electrons, the blue lines correspond to the $p$ electrons and the green lines to the $s$ electrons.

density [104]. Given that the all-electron and the pseudised wave-functions are required to be identical beyond $r_{c,l}$ for all $l$ it follows that [103]:

$$\int_0^{r_{c,l}} |\phi_l(r)|^2 \mathrm{d}r - \int_0^{r_{c,l}} |\psi_{nl}(r)|^2 \mathrm{d}r = 0. \tag{2.48}$$

In the case of ultrasoft pseudopotentials, this condition is not required and the valence charge density of the pseudo-atom is compensated as [105]:

$$n_{ps}(\mathbf{r}) = \sum_l \Big[ |\phi_l(\mathbf{r})|^2 + \sum_{ij} Q_{ij}(\mathbf{r}) \langle \phi_l | \beta_i \rangle \langle \beta_j | \phi_l \rangle \Big], \tag{2.49}$$

where the pseudo-wave functions now include the angular coordinates $\phi_l(\mathbf{r})$, $|\beta_{i,j}\rangle$ are projector functions which vanish beyond the $r_{c,l}$ and $Q_{ij}(\mathbf{r}) = \psi^*_{ni}(\mathbf{r})\psi_{nj}(\mathbf{r}) - \phi^*_i(\mathbf{r})\phi_j(\mathbf{r})$ are called augmented functions and also vanish beyond $r_{c,l}$ [105, 106]. This construction allows larger cutoff radii than the ones required for norm conservation.

Calculations involving norm-conserving pseudopotentials require up to double the kinetic cutoff energy than those performed using ultrasoft pseudopotentials. However, while most of the functionalities employed in this thesis are implemented within DFT for ultrasoft pseudopotentials, in current *GW* implementations they are not supported, and norm-conserving pseudopotentials will be used.

2. **Scalar- and fully-relativistic pseudopotentials**

Relativistic effects can be included in the construction of a pseudopotential either "fully" by starting the construction from the relativistic Kohn-Sham equation [107] or approximately by starting from the Koelling-Harmon equation [107, 108], obtaining "scalar"-relativistic pseudopotentials.

For scalar relativistic pseudopotentials, the spin orbit coupling terms in the relativistic Kohn-Sham equations are averaged over and the relativistic effects are taken into account only for the kinetic term [103]. In the scalar-

relativistic approach the radial potential corresponding to the angular momentum $l$ is [109, 110]:

$$V_l^{\mathrm{SR}}(r) = \frac{l+1}{2l+1} V_{l+1/2}(r) + \frac{l}{2l+1} V_{l-1/2}(r), \tag{2.50}$$

where $V_{l\pm1/2}(r)$ are obtained from the Dirac equation in a similar approach to the one described above for the spin-independent case.

For fully-relativistic pseudopotentials, the starting point for the construction of the pseudopotential is the relativistic Kohn-Sham equations [107]. The radial potential correspondent to the $l$ angular momentum in this case contains the additional spin-orbit coupling component, $V_l^{\mathrm{FR}} = V_l^{\mathrm{SR}} + V_l^{\mathrm{SO}}$, which has the following expression [109, 110]:

$$V_l^{\mathrm{SO}}(r) = \frac{2}{2l+1}\Big[V_{l+1/2}(r) - V_{l-1/2}(r)\Big]. \tag{2.51}$$

3. **Semicore electrons in pseudopotentials**

When a pseudopotential is constructed, one of the choices to be made is the valence configuration of the atom under study, which sets how many angular momenta $l$ will be included in the pseudopotential. This configuration can either consist in the top-most electronic shell of the atom or it can include "semicore" electrons, which are the core electrons in the outermost shell. In general, semicore states are required when outer core energy levels are closer to the valence energies than to the core states, or when the core and valence wave functions have a large spatial overlap.

Formally, the requirement to include semicore electrons originates in the derivation of the pseudopotential in Eq. (2.47), which implies a linear dependence of the exchange correlation energy on the electron density: $V_{\mathrm{xc}}[n] = V_{\mathrm{xc}}[n_{core}] + V_{\mathrm{xc}}[n_{ps}]$, where $n = n_{core} + n_{ps}$, $n_{core}$ is the electron charge density of the core electrons, and $n_{ps}$ is the charge density of the valence electrons. This linearity is an approximation, and it does not always hold when only the outermost valence

electrons are included in the pseudopotential [111].

The contribution of the core electrons to the exchange-correlation energy can be introduced either partially through the nonlinear core-correction [111], or by including an additional electronic shell from the core to the valence part of the total charge density.

In Figure 2.3 we show the comparison between all electron wave-functions of Pb and the pseudised norm-conserving wave functions within the LDA. In this case, we have constructed the pseudopotential for the $6s^2$ and $6p^2$ valence electrons of Pb, but we have also included the semicore $5d$ states. The $6s$ and $6p$ bound states have energies of $-11.5$ and $-3$ eV respectively, while the energy level of the $5d$ electrons is at $-20$ eV. For reference, the second highest core electronic states ($5p$) is at $-86$ eV. Furthermore, in Figure 2.3 it can be seen that the semicore $d$ electrons are localised much closer to the core than the valence electrons. In this case a smaller cutoff radius is necessary to ensure norm-conservation, with a larger plane wave kinetic cutoff required for calculations performed with this pseudopotential.

### 2.3.2 Convergence in GW

The quasiparticle equation for a periodic system is [89]:

$$E_{n\mathbf{k}} = \epsilon_{n\mathbf{k}} + Z(\epsilon_{n\mathbf{k}})\langle n\mathbf{k}|\Sigma(\epsilon_{n\mathbf{k}}) - V_{\mathrm{xc}}|n\mathbf{k}\rangle. \tag{2.52}$$

To highlight the convergence parameters in a *GW* calculation we can express both the exchange and correlation self energy matrix elements in a plane-wave basis sets.

#### Exchange self energy

The exchange term has the following form [89]:

$$\langle n\mathbf{k}|\Sigma_x|n\mathbf{k}\rangle = -\frac{1}{N\Omega}\sum_{m}\sum_{\mathbf{q}}\sum_{\mathbf{G}} M^{*}_{m\mathbf{k}-\mathbf{q},n\mathbf{k}}(\mathbf{G})v_{\mathbf{q}}(\mathbf{G})M_{m\mathbf{k}-\mathbf{q},n\mathbf{k}}(\mathbf{G}), \tag{2.53}$$

where $N$ is the number of unit cells, the summations run over all occupied states ($m$), all $\mathbf{q}$ points in the grid sampling first Brillouin zone, and all $\mathbf{G}$ vectors within a set cutoff. The density of the $\mathbf{q}$-point grid and the plane wave exchange cutoff require convergence. Here, the Fourier transform of the Coulomb potential is used: $v_{\mathbf{q}}(\mathbf{G}) = \dfrac{4\pi\delta_{\mathbf{GG'}}}{|\mathbf{G}+\mathbf{q}|^2}$.

The matrix elements $M_{m\mathbf{k}-\mathbf{q},n\mathbf{k}}(\mathbf{G})$ are defined in reciprocal space as [64, 89]:

$$M_{m\mathbf{k}-\mathbf{q},n\mathbf{k}}(\mathbf{G}) = \sum_{\mathbf{G'}} c^*_{m\mathbf{k}-\mathbf{q}}(\mathbf{G'}-\mathbf{G}) c_{n\mathbf{k}}(\mathbf{G'}). \tag{2.54}$$

The calculation of these matrix elements requires convergence with an additional plane wave cutoff, which truncates the sum over the $\mathbf{G}'$ vectors shown above.

**Correlation self energy**

The frequency-dependent correlation self energy has the following expression [89]:

$$\begin{aligned}\langle n\mathbf{k}|\Sigma_c(\omega)|n\mathbf{k}\rangle = -\frac{1}{N\Omega}\sum_m\sum_{\mathbf{q}}\sum_{\mathbf{GG'}} M^*_{m\mathbf{k}-\mathbf{q},n\mathbf{k}}(\mathbf{G}) M_{m\mathbf{k}-\mathbf{q},n\mathbf{k}}(\mathbf{G'}) \times \\ \times \int \mathrm{d}\omega' \frac{\exp(i\omega'\delta)}{-2\pi i} \frac{W_{\mathbf{GG'}}(\mathbf{q}) - v_{\mathbf{q}}(\mathbf{G})}{\omega+\omega'-\epsilon_{n\mathbf{k}-\mathbf{q}} \pm i\delta},\end{aligned} \tag{2.55}$$

where this time the summations are performed with respect to the index $m$ which runs over occupied and unoccupied states, all $\mathbf{q}$ points in the grid sampling of the first Brillouin zone and all $\mathbf{G}$ and $\mathbf{G}'$ vectors within a set cutoff called the polarisability cutoff. For the calculation of the correlation self energy, it is necessary to perform convergence tests with respect to the total number of states (number of bands), the polarisability cutoff and the number of $\mathbf{q}$-points in the Brillouin zone sampling. Generally, the exchange and correlation self energies are calculated for the same $\mathbf{q}$-point sampling, and convergence tests are performed only for the exchange self energy to reduce computational cost.

The most computationally expensive quantity to be evaluated is the screened Coulomb interaction $W_{\mathbf{GG'}}(\mathbf{q},\omega)$. The complexity of this quantity lies in the frequency depen-

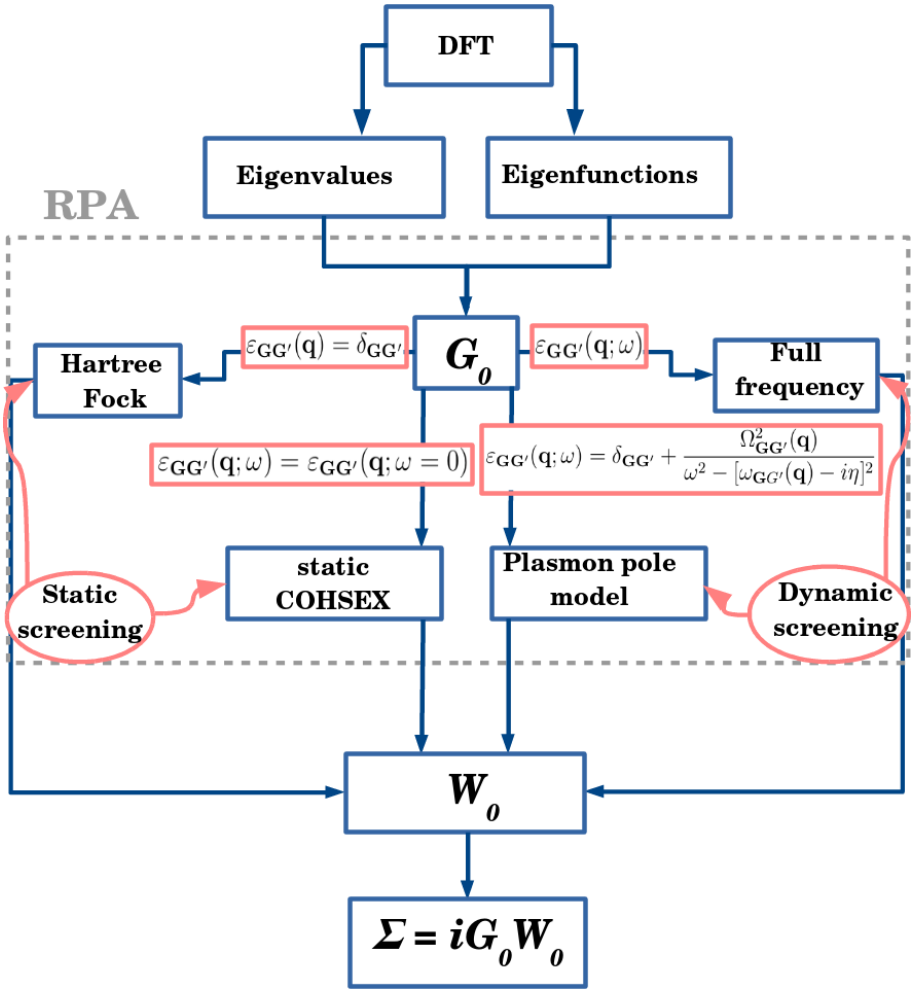


Figure 2.4: Schematic representation of the classification of the *GW* calculations based on the approximation employed for the dielectric function.

dence. The integral in Eq. 2.55 may be performed numerically ("Full frequency" in Figure 2.4), however this poses computational challenges and further approximations are required [89].

The screened Coulomb interaction can be expressed using the inverse dielectric matrix $\varepsilon^{-1}_{GG'}(\mathbf{q};\omega)$ as [89]:

$$W_{GG'}(\mathbf{q};\omega) = \varepsilon^{-1}_{GG'}(\mathbf{q};\omega)v_{\mathbf{q}}(\mathbf{G}). \tag{2.56}$$

In this form, we can distinguish three approximate methods commonly used in *GW* calculations:

1. **No screening**. Neglecting the polarisability, we obtain the dielectric function $\varepsilon_{GG'}(\omega) = \delta_{GG'}$. In this approximation the screened Coulomb interaction be-

comes $W = v$, recovering the Hartree-Fock self-energy. The Hartree-Fock self-energy is known to significantly overestimate band gaps due to the absence of the correlation interaction [112].

2. **Static screening**. In this case we consider that the dielectric matrix is not frequency dependent, $\varepsilon_{\mathbf{GG'}}(\mathbf{q};\omega) = \varepsilon_{\mathbf{GG'}}(\mathbf{q};\omega = 0)$. Within this approximation the integral in the expression of the correlation self-energy disappears leaving the following expression [89]:

$$\langle n\mathbf{k}|\Sigma_c(\omega)|n\mathbf{k}\rangle = -\frac{1}{N\Omega}\sum_m\sum_{\mathbf{q}}\sum_{\mathbf{GG'}} M^*_{m\mathbf{k}-\mathbf{q},n\mathbf{k}}(\mathbf{G})M_{m\mathbf{k}-\mathbf{q},n\mathbf{k}}(\mathbf{G'})\times \\ \times v_{\mathbf{q}}(\mathbf{G})[\varepsilon^{-1}_{\mathbf{GG'}}(\mathbf{q}) - \delta_{\mathbf{GG'}}]. \tag{2.57}$$

This approximation is known as the static Coulomb-Hole Screened Exchange (COHSEX) approximation [65]. It has been shown that due to the absence of the dynamic screening effects, this approximation renders band gaps which are overestimated with respect to experiment by over 1 eV [113].

3. **Dynamic screening within the generalised plasmon pole model**. In the *GW* calculations detailed in this thesis we use the Godby-Needs generalized plasmon pole model [62, 63, 114]. In this model the dynamical dielectric matrix is modelled by the following function [89]:

$$\varepsilon_{\mathbf{GG'}}(\mathbf{q};\omega) = \delta_{\mathbf{GG'}} + \frac{\Omega^2_{\mathbf{GG'}}(\mathbf{q})}{\omega^2 - [\omega_{\mathbf{GG'}}(\mathbf{q}) - i\eta]^2}, \tag{2.58}$$

where the plasmon-pole parameters $\Omega_{\mathbf{GG'}}$ and $\omega_{\mathbf{GG'}}$ are obtained by evaluating the RPA dielectric matrix at $\omega = 0$ and $i\omega_p$; $\omega_p$ should have a value close the plasma frequency [62, 63, 114]. If the plasmon-pole model is suitable for the representation of the dielectric function in a given system, the quasiparticle band gap should be insensitive to the variation of the $\omega_p$ parameter.

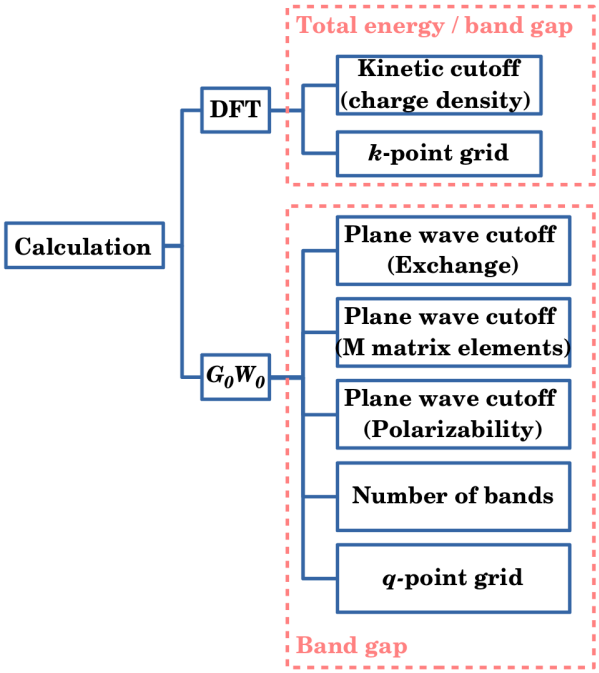


Figure 2.5: Schematic summary of the parameters that need to be converged in a DFT + *GW* calculation. The parameters are listed on the right hand side of the diagram. The two pink dashed boxes enclose the parameters that are converged in the DFT and the *GW* calculation, and the target quantities to be converged are marked within each box.

### 2.3.3 Summary of convergence parameters

In Figure 2.5 we show a schematic summary of all parameters that need to be converged in a DFT and *GW* calculation. For all DFT calculations discussed in this thesis, the target quantity which is converged with respect to the plane wave cutoff and the **k**-point grid is either the total energy or the Kohn-Sham band gap. In all *GW* calculations we converge the band gap with respect to all parameters shown in Figure 2.5.

## 2.4 Summary

In this chapter we have presented the background theory involved in the computational studies to be discussed in this thesis. The discussion of density functional theory showed how the problem of many interacting electrons in the ground state can be transformed into single-particle problems using the theorem of Hohenberg and Kohn and the Kohn-Sham equations. The second section of this chapter was dedicated to the

methods for studying excited states, in particular the *GW* method. Furthermore, we have shown how the Kohn-Sham and quasiparticle equations can be rewritten for periodic system using a plane wave basis set for the eigenfunctions. Finally, we discussed practical calculations and the convergence requirements for both methodologies.

In the next chapters we will apply the DFT and *GW* methods to the study of the electronic structures of hybrid organic-inorganic metal-halide perovskites as well as $A_2B_3$-type semiconductors of the stibnite family.

# Chapter 3

# Metal-halide perovskite absorbers: An overview of recent literature

In 1839 the German mineralogist Gustav Rose identified the mineral $CaTiO_3$ during a scientific expedition in the Russian Ural Mountains [115]. This mineral was named after the Russian nobleman and mineralogist Lev Aleksevich Perovski [115]. Later on, the perovskite denomination was extended to the entire family of materials which exhibit a similar crystal structure to $CaTiO_3$. Pioneering crystallography research on materials in the perovskite family date as far back as 1926, when Victor Goldschmidt first described this structure and introduced the concept of tolerance factor [116].

The general chemical formula of a perovskite material is $AMX_3$. Ref. [117] presents a useful classification of perovskite materials (Figure 3.1). The first classification criterion is the X anion, which binds to both cations A and M. Based on the X anion we can split the perovskite family into oxide and halide perovskites [117].

The oxide perovskites form a very widely explored family of materials, in which the X anion is the oxygen atom. They have been famously associated with remarkable breakthroughs in fields such as superconductivity, ferroelectricity, piezoelectricity, colossal magneto-resistance [118]. While oxide perovskites are actively investigated also in relation to photovoltaic applications [119], they will not be discussed in this thesis.

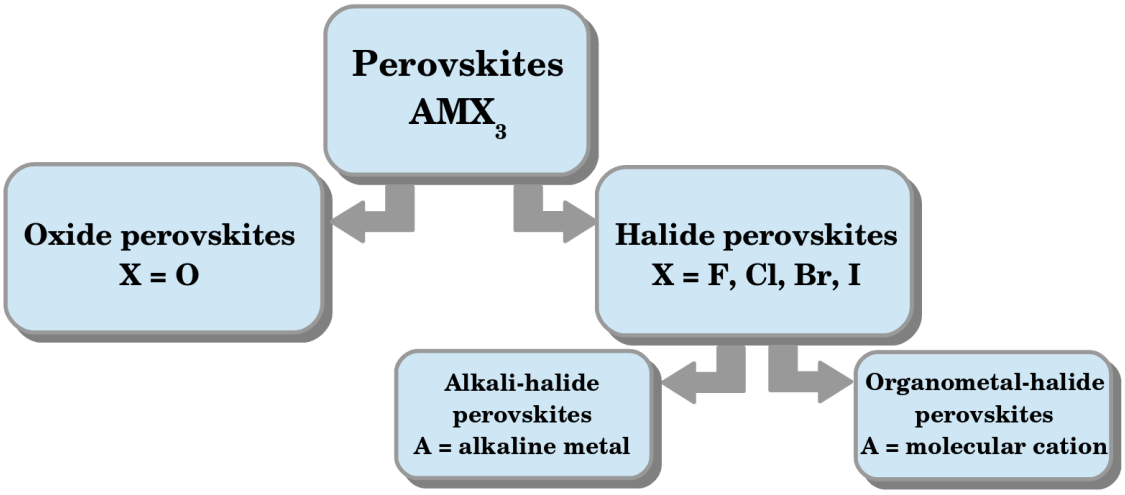


Figure 3.1: Classification of the perovskite materials based on the chemical composition. The figure is reproduced from Fig.3 of Ref. [117].

The focus of a large part of this thesis is on the electronic and optical properties of halide perovskites in the context of solar cell research. According to the classification shown in Figure 3.1 [117] a further sub-hierarchy can be made within the halide perovskite family, subdividing them into alkali-halide and organo-metal halide perovskites. Both of these categories assume that the M cation is a divalent metal atom and X is a halogen atom. For the alkali-halide perovskites the cation A belongs to the alkaline series. In the case of organometal-halide perovskites, the cation A is an organic molecular cation.

In the rest of this chapter we will focus on the main experimental and theoretical results reported on halide perovskites. In particular, a large part of this review will be dedicated to methylammonium lead iodide ($CH_3NH_3PbI_3$), but reports on other halide perovskites will also be summarised here. The main purpose of this chapter is to give a flavour of the main experimental and theoretical results reported to date. Given the large number of publications on halide perovskites, particularly in the last two years, this chapter is does not pretend to be a comprehensive review of the existing literature.

## 3.1 General properties of perovskites

### 3.1.1 Crystal structure and symmetry properties

The simplest, most symmetric perovskite crystal structure is the cubic perovskite, represented schematically in Figure 3.2. In this configuration, the metallic cation M is 6-fold coordinated and the nearest X atoms form an octahedron with the centre at the M atom [120–122]. The M atoms in the lattice form the corners of a perfect cube and along with the octahedra, a cuboctahedral cavity. The cation A is located at the centre of this cuboctahedral cavity. The cubic perovskite structure belongs to the $Pm\bar{3}m$ symmetry space group and carries the octahedral $O_h$ symmetry [120–122]. In this structure the octahedra are regular, meaning that their diagonals are respectively perpendicular and they intersect in a single point at the centre of the octahedron.

However, not all perovskite structures follow such a symmetric configuration. From the first few crystallographic studies on $BaTiO_3$ and $SrTiO_3$ it is known that the crystal structure is in fact distorted with respect to the perfect cubic structure [123]. The perovskite unit cell can distort due to the displacement of the A or M cation, or due

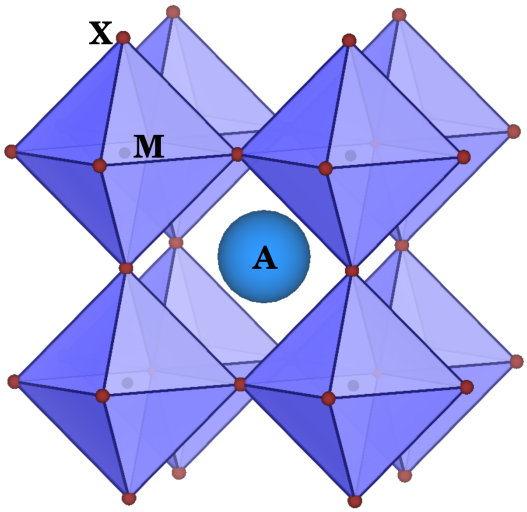


Figure 3.2: Polyhedral representation of the cubic perovskite structure $AMX_3$. The small red spheres represent the X atoms, the small blue spheres at the centre of the blue octahedra represent the M atoms and the large blue central sphere at the centre of the cuboctaheral cavity is the A cation.

to the octahedral tilting or distortions [120, 124]. The displacements of cations A and M do not impact the unit cell size significantly and they are linked directly to ferroelectric and antiferroelectric effects [120–122, 124]. By contrast, the tilting and distortions of the octahedra have a far greater impact on the size and symmetry of the crystal lattice. In particular, the tilting of the octahedra can be used to classify possible perovskite structures [120–122, 124].

In 1972 Glazer identified 23 possible tilting patterns for the octahedra and characterised the symmetry of all structures [120]. In this work he introduced a simple notation which characterises a perovskite system based on the tilting of the octahedra around the axes of the lattice vectors of the most symmetric cubic lattice [120]. For example, the notation $a^+b^-c^0$ specifies that the octahedra are tilted in phase (+) along the $a$ axis, out of phase (—) along the $b$ axis and are not tilted (0) along the $c$ axis of the crystal. The use of different letters for $a$ and $b$ signifies that the tilting angles are not necessarily equal in magnitude [120, 121]. In principle, any tilting pattern for a perovskite structure can be obtained as a linear combination of 6 basic tilting systems: $a^+b^0b^0$, $a^-b^0b^0$, $b^0a^+b^0$, $b^0a^-b^0$, $b^0b^0a^+$, $b^0b^0a^-$ [125]. The list of 23 possible tilting patterns was reduced later on to 15 possible structures based on symmetry considerations [125]. These structures were further classified in a group-subgroup hierarchy and linked to structural phase transitions associated to perovskite crystals, as shown in Figure 3.3 [124, 125]. Interestingly most of the possible phases shown in Figure 3.3 exhibit distortions of the octahedra and displacements of the A and M cations as a secondary effect [125].

### 3.1.2 Tolerance factor

The perovskite distortions are closely linked to the size of the A, M and X components [14, 116, 126, 127]. Intuitively, if the cation A is very large (for example, a large molecule of the type R-$NH_3^+$, where R could be an alkyl chain or an aromatic group)

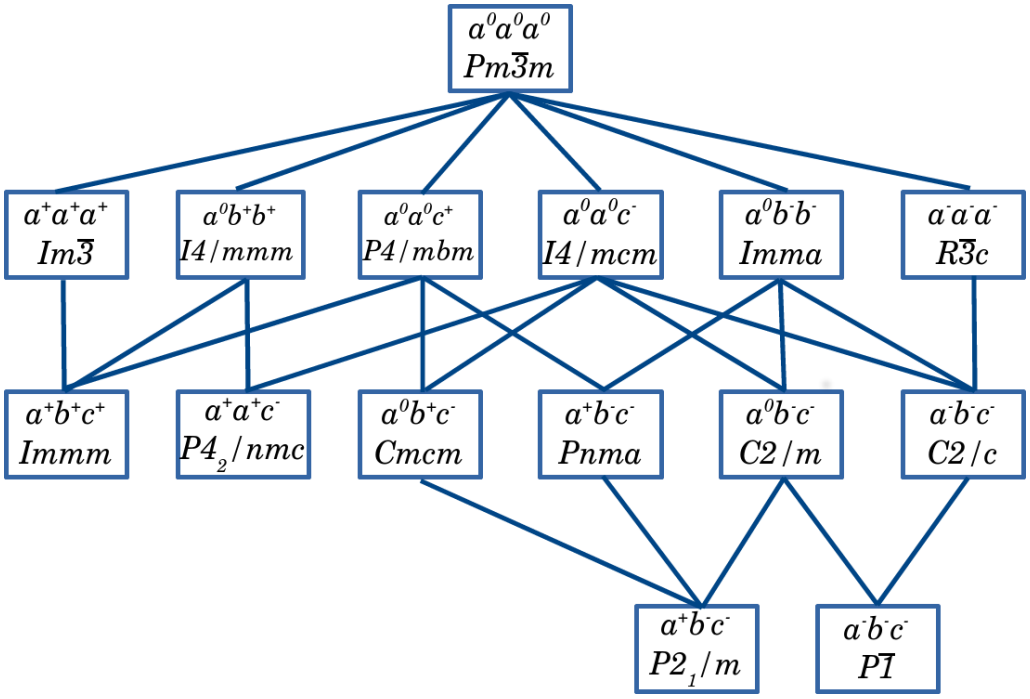


Figure 3.3: Group-subgroup hierarchy of perovskite systems based on the octahedral tilting configuration. This diagram is reproduced from Ref. [124].

the perovskite structure reorganises into the a two-dimensional layered structure, alternating organic and inorganic layers [126, 128].

The Goldschmidt tolerance factor is an empirical criterion used to determine whether a perovskite structure is likely to form a 3D, 2D or 1D structure based on the ionic radii of the chemical components. The tolerance factor is given by $t = (R_A + R_X)/\sqrt{2}(R_M + R_X)$, with $R_A$, $R_M$ and $R_X$ the ionic radii of the elements in $AMX_3$ perovskites [116]. It is found empirically that 3D perovskites are formed when $t$ is in the range of 0.7 to 1.1 [14, 116, 126, 127]. The lower bound corresponds to a situation where the cation is close enough to the halogen component to form a bond. In this case the 3D perovskite structure is more likely to collapse into a 1D needle-like structure. $KPbI_3$ is a good example of such occurrence [129]. The upper bound describes the case of the closed packed cubic perovskite structure. For values of $t$ larger than 1 the perovskite structure is expected to distort or even form a layered two-dimensional perovskite structure [126]. For the rest of this thesis we will focus our attention to three-dimensional perovskites only.

## 3.2 Properties of $CH_3NH_3PbI_3$: insight from experimental and computational studies

### 3.2.1 Synthesis of $CH_3NH_3PbI_3$

$CH_3NH_3PbI_3$ is a solution-processable semiconductor. Broadly described, the synthesis of $CH_3NH_3PbI_3$ involves the reaction between two precursor solutions of $CH_3NH_3I$ and $PbI_2$. Based on the method that facilitates this reaction, there are four main fabrication processes for $CH_3NH_3PbI_3$ [117]. In the one-step deposition method [34] the perovskite thin film is obtained by spin-coating or drop-casting the reaction product of the two precursors in solution form followed by annealing [34, 40, 130–134]. In the sequential deposition method, a pre-coated thin film of $PbI_2$ is exposed to a $CH_3NH_3I$ solution and subsequently annealed [39, 135–137]. Alternatively, the reaction of the precursors can be obtained through vapour deposition [138]. Similarly to the solution case, one can facilitate a reaction in vapour form (dual source chemical vapour deposition [54]) or at the solid-vapour interface (vapour assisted solution processing [139, 140]). In the solution deposition processes the initial product is a yellow (needle-like) hydrated structure and requires further annealing at high temperature in order to obtain the 3D perovskite. This intermediate phase is bypassed in the vapour-assisted methods [54, 139, 140].

The principal goal of any synthesis methodology is to achieve control over the coverage, crystallinity and morphology of the final product, in order to ensure reproducibility [139]. The vapour-assisted methodologies are advantageous with respect to the solution deposition methods from this point view. Active research on the synthesis of these materials focuses now on achieving a low cost fabrication protocol which ensures large scale reproducibility, in view of commercial production [117, 139].

### 3.2.2 Structural properties of $CH_3NH_3PbI_3$

Depending on stoichiometry, methylammonium lead iodide can be synthesised in various dimensionalities [141]. The layered two-dimensional perovskite structure is of the form $(CH_3NH_3)_2PbI_4$ [142] and the zero-dimensional structure has the chemical formula $(CH_3NH_3)_4PbI_6{\cdot}2H_2O$ [143]. In principle, the $CH_3NH_3^+$ in various stoichiometries acts as a "spacer" for the inorganic components and can determine the structural reorganisation of the inorganic $PbI_6$ network [141]. In the following we will summarise some of the recent research on the 3D $CH_3NH_3PbI_3$.

#### Experimental studies

The crystal structure of $CH_3NH_3PbI_3$ is strongly dependent on temperature and undergoes two phase transitions. At low temperature, the crystal structure is orthorhombic. The octahedra in the inorganic Pb-I cavity are tilted with respect to each other and the organic cation has a fixed orientation within the cavity (although it is free to rotate around its own axis) [144–148]. Around 160 K the crystal transitions to a tetragonal phase and around 330 K the crystal structure becomes cubic. As the temperature increases, the orientation of the cation within the inorganic perovskite cage becomes disordered [144–151].

XRD experiments performed at various temperatures report data describing the structure and symmetry of the crystal at each phase (see Table 3.1). However, given that the crystal structure could be dependent on the sample preparation, there is some level of variation between reports belonging to different research groups [145, 146]. The overall consensus confirms that due to the high orientational disorder of the organic cation at high temperature, intermediate phases and crystalline domains are likely to form during the phase transition from higher to lower symmetry phases [145, 146]. For example, Ref. [146] reports a spurious phase found from measurements at 152 K with symmetry corresponding to the $Ibam$ space group. Moreover, some of the crystal

| Phase | Temperature | Symmetry | Unit cell | Lattice Parameters |
|---|---|---|---|---|
| | | Ref. [145] | | |
| $\alpha$ | N/A | $P4mm$ | Tetragonal | $a = 6.3115$ Å<br>$c = 6.3161$ Å |
| $\beta$ | N/A | $I4cm$ | Tetragonal | $a = 8.8490$ Å<br>$c = 12.6420$ Å |
| | | Ref. [146] | | |
| $\alpha$ | T > 330 K | $Pm\bar{3}m$ | Cubic | $a = 6.2800$ Å |
| $\beta$ | 161 K < T < 330 K | $I4/m$, $I4/mcm$ | Tetragonal | $a = 8.8510$ Å<br>$b = 12.4440$ Å |
| $\gamma$ | T < 161 K | $Pnma$ | Orthorhombic | $a = 8.8490$ Å<br>$b = 12.5804$ Å<br>$c = 8.5551$ Å |
| | | Ref. [144] | | |
| $\alpha$ | T > 327 K | $Pm\bar{3}m$ | Cubic | $a = 6.3285$ Å |
| $\beta$ | 162 K < T < 327 K | $I4/mcm$ | Tetragonal | $a = 8.8550$ Å<br>$b = 12.6590$ Å |
| $\gamma$ | 162 K < T | $Pna2_1$ | Orthorhombic | $a = 8.8360$ Å<br>$b = 8.5810$ Å<br>$c = 12.6210$ Å |

Table 3.1: Comparison between crystal structure and phase transition data reported for $CH_3NH_3PbI_3$ in three experimental studies. Data from Refs [144–146]

symmetries obtained from XRD experiments do not follow the group-subgroup hierarchy devised by Howard and Stokes [124], due to a combination between the effect of tilting for the octahedra and ferroelectric distortions [145]. Finally, in the orthorhombic case Ref. [146] reports ellipsoidal shaped atomic dynamic displacements around the apical and equatorial I, which can be assigned either to soft transverse acoustic phonons or to anharmonic modes [146, 152].

**Computational studies**

Computational studies of the structure of $CH_3NH_3PbI_3$ confirm that the structural energetic landscape is characterised by multiple local minima. Consequently, changes in the structural geometry of the crystal lattice only induce variations of the total energy of the order of meV per formula unit [153–157]. Due to this effect, the structural relaxation of $CH_3NH_3PbI_3$ can be dependent on the starting tilting configuration of the $PbI_6$ [154, 158] octahedra or the orientation of the $CH_3NH_3^+$ cations [155, 156]. These observations confirm that the crystal structure of $CH_3NH_3PbI_3$ is characterised by substantial disorder associated with both the orientation of the cation and the octahedral tilting.

Molecular dynamics studies performed on $CH_3NH_3PbI_3$ focus particularly on the rotationally disordered $CH_3NH_3^+$ cation in the high temperature cubic and tetragonal phases [159–161]. Ref. [159, 160] report the formation of ferroelectric domains due to a reorganisation of the $CH_3NH_3^+$ cations at room temperature, associating this effect to the hysteresis exhibited in photovoltaic devices implementing $CH_3NH_3PbI_3$. However, Ref. [161] point out that molecular dynamics simulations are sensitive to the size of the simulation cells. They show that the long range electrostatic interactions could be enhanced in smaller simulation cells, and therefore reduce the dynamic disorder of the cations as an artefact of the computational setup [161]. Additionally, Ref. [161] points out the band gap fluctuation with time calculated within the density functional theory and showing variations around the value of 1.51 eV with a standard deviation of 0.1 eV. The description of the dynamically disordered character of the $CH_3NH_3^+$ is important particularly in the interpretation of experimental Raman spectra [162] as well as UV/VIS absorption spectra [163].

### 3.2.3 Electronic and Optical properties of $CH_3NH_3PbI_3$

#### Experimental studies

The earliest spectroscopic studies of $CH_3NH_3PbI_3$ show that the three-dimensional $CH_3NH_3PbI_3$ structure exhibits a weakly bound exciton [164–168]. Room-temperature optical absorption spectra cannot resolve this feature, suggesting the possible thermal dissociation of the exciton. Refs. [169, 170] describe this phenomenon in detail for $CH_3NH_3PbI_3$ and the mixed halide $CH_3NH_3PbI_{3-x}Cl_x$ reporting optical absorption spectra measured at gradually increasing temperatures starting from 4 K, as shown in Figure 3.4.

The Wannier-like excitons reported in Ref. [169] have binding energies around 55±30 meV, as estimated by applying the law of mass action. Moreover, Ref. [169] establishes that free carriers are likely to dominate over bound excitons in working photovoltaic conditions, for example at room temperature or above. These results are in agreement with previous reports on the excitonic properties of $CH_3NH_3PbI_3$ [164–169]. A recently published study on the dielectric properties of $CH_3NH_3PbI_3$ challenges the estimation of the exciton binding energies in the Wannier model [171] on

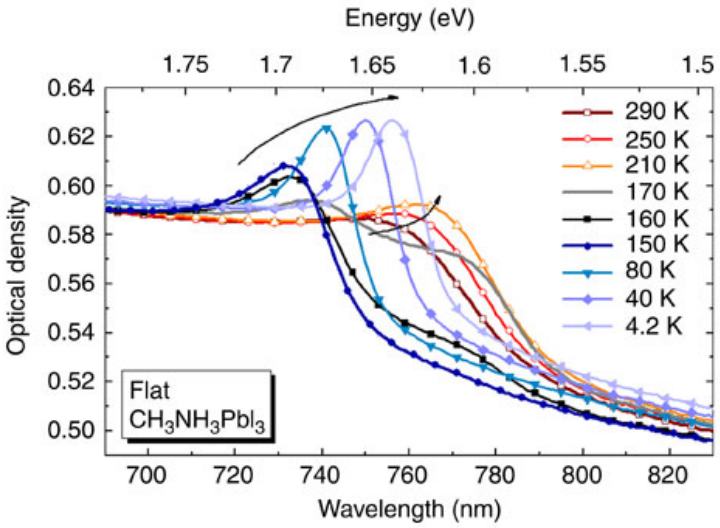


Figure 3.4: Optical absorption spectra obtained at various temperatures for $CH_3NH_3PbI_3$. The figure is reproduced from Ref. [169] with permission.

the basis of the static dielectric constant approximating the electron-hole screening. Indeed, Ref. [172] use the low-frequency ($10^0$ Hz) dielectric constant ($\sim$70) instead of the high-frequency dielectric constant ($\sim$ 6) to approximate the dielectric screening in the calculation of exciton binding energy, which is one order of magnitude higher than the values reported in previous experimental studies [169]. Consequently, Ref. [172] obtains an exciton binding energy of 2 meV. Regardless of the conceptual difference in the approach for calculating the Wannier exciton binding energy, Refs. [172] and [169] reach the same conclusion, that is at room temperature free electrons and holes are created upon the absorption of photons. Indeed, a direct spectroscopic measurement of the exciton binding energy for $CH_3NH_3PbI_3$ published recently [173] obtains an exciton binding energy of 16 meV.

It is now understood that electron and holes have very long diffusion lengths reaching up to 1 $\mu$m [49, 50, 174–176]. Moreover, Ref. [49] points out that $CH_3NH_3PbI_xCl_{3-x}$ exhibits electron and hole diffusion lengths one order of magnitude higher than the pure iodide [50]. The reason for this large difference has not yet been clarified [141]. Moreover, the photogenerated electrons and holes have long lifetimes and exhibit up to four times lower bi-molecular recombination rate than predicted by Langevin theory as well as high mobilities [174]. These properties make these perovskites highly attractive for lasing applications [177, 178]. In Refs. [179] it is shown that nonradiative pathways are created due to defects which form trap states within the band gap. The reduction of nonradiative pathways is desirable for achieving power conversion efficiencies close to the Shockley-Queisser limit [16]. Further reduction of charge recombination can be obtained in the presence of electron and hole transporting materials such as $TiO_2$ and $spiro$-OMeTAD [175]. In this case, however excess holes are likely to form in the perovskite layer due to an imbalance between the electron and hole transport to the $TiO_2$ and $spiro$-OMeTAD respectively, leading to a lowering of the short circuit current [180, 181].

**Computational studies**

Computational studies of the electronic structure of $CH_3NH_3PbI_3$ were reported using various methodologies ranging from the semi-empirical Hückel theory [182] to *ab initio* methods within the Hartree-Fock theory [182], density functional theory [154, 156, 157, 164, 183–190] and beyond [191, 192]. The band gap of $CH_3NH_3PbI_3$ is direct, centred at different high symmetry points in the Brillouin zone depending of the structure of the system (R [0.5,0.5,0.5] for the cubic system, and Γ in the case of the tetragonal and orthorhombic system.) [185, 188]. As discussed in more detail in Chapter 4, the valence band top is primarily of I-5*p* character with a small Pb-6*s* contribution at the valence band edge. The conduction band bottom is of Pb-6*p* and I-5*p* character and the states localised on the $CH_3NH_3^+$ only have a significant contribution to electronic states within 5 eV from the band edges [155, 185, 193]. For this reason, the electronic states localised on the $CH_3NH_3^+$ cation do not contribute significantly to the optical absorption [155, 185, 193]. In fact, the principal role of the $CH_3NH_3^+$ besides the obvious charge balancing, is to act as a "spacer" for the $PbI_6$ perovskite cage, and implicitly determine its structure [158, 194].

Within scalar relativistic (SR) density functional theory, the calculated band gap is in surprisingly good agreement to the experimental band gaps reported from optical absorption measurements [154, 186, 189, 191]. However, given the presence of the Pb and I atoms, the contribution of the spin-orbit coupling effect is likely to be very large in this system. Indeed, upon inclusion of relativistic (FR) effects, Refs. [186, 189] report a band gap which is approximately 1 eV smaller than the measured optical gaps. Refs. [186, 189] report not only a large band gap change upon inclusion of spin-orbit coupling, but also a significant change in the topology of the conduction band [184, 186, 189, 191].

The significant discrepancy between FR-DFT band gaps and experimental optical gaps provided motivation for carrying out more sophisticated hybrid exchange calcula-

tions [188] and *GW* quasiparticle calculations [191, 192]. So far two studies addressed the quasiparticle band gap of $CH_3NH_3PbI_3$ within the *GW* approximation, using different approaches [191, 192]. Ref. [191] reported a quasiparticle band gap of 1.67 eV obtained within the $G_0W_0$ approximation. In this approximation the authors used a scalar relativistic approximation for the screened Coulomb interaction $W_0$ and spin-orbit effects were included only in the Green's function $G_0$ as a correction term. Ref. [192] reported a $G_0W_0$ quasiparticle gap of 1.27 eV when spin-orbit coupling was fully included in the calculation of both $G_0$ and $W_0$. Ref. [192] also calculated the quasiparticle band gap using the quasiparticle self-consistent *GW* (QS*GW*) approach [90]. Surprisingly they report a QS*GW* band gap of 1.67 eV which matches the $G_0W_0$ results obtained in Ref. [191]. In Chapter 4 we discuss a simple self-consistent "scissor" *GW* method which nicely reconciles the results of Refs. [191, 192].

To the best of our knowledge, there are two published computational studies of the optical absorption spectrum of $CH_3NH_3PbI_3$ [195] calculated within the Bethe-Salpeter (BSE) formalism. Ref. [195] obtains a sharp peak in the optical absorption spectrum at the absorption onset, in agreement with experimental data. They define the exciton binding energy as difference between the optical absorption onset calculated within BSE and the quasiparticle *GW* band gap and obtain a value of 40 meV, in good agreement with experimental results published in Ref. [169]. By contrast, Ref. [196] finds an exciton binding energy of 200 meV, and obtains excitonic wave functions which are highly delocalised. However, there are very few essential computational details given in Refs. [195, 196] regarding convergence at both the *GW* and BSE level. As such it is difficult to comment on the discrepancy between their results.

Other computational studies extend the DFT analysis of photovoltaic interfaces, such as the interface with between $TiO_2$ and the perovskite [193, 197, 198] or to understanding the impact of the electronic structure on the recombination processes or on the short circuit current [153, 155].

## 3.3 Tuning optical properties

### 3.3.1 Mixed-metal perovskites

The optical band gap of metal-halide perovskites can be broadly tuned by manipulating their chemical composition and crystal structure [27, 47, 137, 145, 158, 194, 199, 200]. The gap can be tuned from 1.17 eV to 1.55 eV by controlling the mixing fraction of Pb and Sn in $CH_3NH_3Pb_xSn_{1-x}I_3$ [145, 201]. Interestingly, Ref. [201] report an anomalous dependence on the band gap as a function of the $x$ fraction of Sn in the componence of the perovskite, shown in Figure 3.5. This dependence is associated in Ref. [201] with the similar effect observed in the topological insulator $Pb_{1-x}Sn_xTe$ [202] due to the band inversion appearing with increasing $x$.

However, a recent computational study of mixed Sn-Pb perovskites shows that the band gap decreases monotonously with the increase in the concentration of Sn [203]. Moreover, Ref. [203] shows that the electron effective masses have almost constant values for increasing values of the Sn concentration. By contrast the hole effective masses are more than halved as the Sn concentration is increased from 0 to 100% [203].

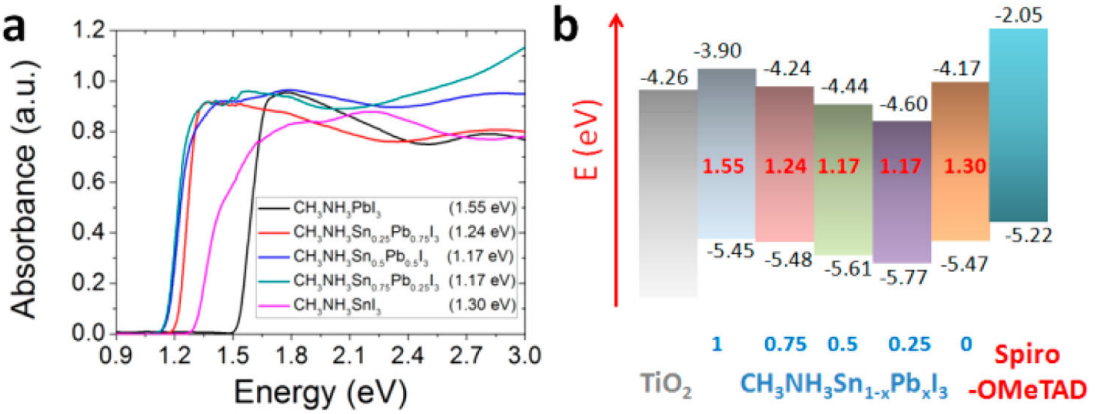


Figure 3.5: (a) Absorption spectra and (b) and alignment of mixed $CH_3NH_3Pb_xSn_{1-x}I_3$ perovskites for various concentrations $x$. Figure reproduced from Ref. [201] with permission.

### 3.3.2 Mixed-halide perovskites

The electronic properties of metal-halide perovskites can also be tuned by exchanging the halide I for Cl or Br. Early studies of metal-halide perovskites show that the absorption onset blue shifts upon halogen I substitution by Br or Cl [166, 204]. Interestingly, the gradual substitution of I with Br or Br with Cl induces a gradual increase of the band gap [46, 204]. However there is no clear effect on the band gap noticed upon gradual substitution of I with Cl [117]. The substitution of I with Br achieves a broad tunability of the band gap over a range of 1.5 to 2.3 eV, obtaining samples which vary in colour [46]. The band gap tunability of I-Br and Br-Cl mixed halides is shown in Figure 3.6. The Cl substitution in $CH_3NH_3PbI_3$ appears to have a substantial effect on the enhancement of the electron and hole diffusion lengths and mobilities [49, 50]. The role of Cl is yet unclear in the electronic properties of this mixed halide [11]. Ref. [154] finds that the Cl atoms increase the binding energy between the perovskite and the surface of $TiO_2$, which could lead to an increase in stability of solar cells in this configuration. XRD studies of this mixed halide have not

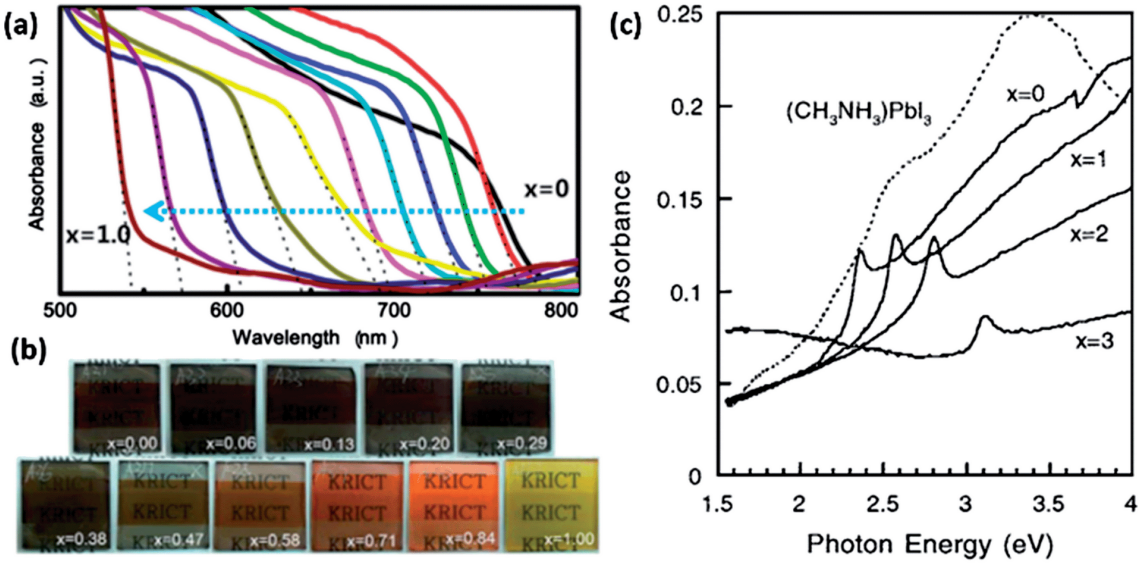


Figure 3.6: (a) Absorption spectra of I-Br mixed halides, $CH_3NH_3PbI_xBr_{3-x}$ of different concentrations obtaining samples of various colours (b) Original figures from Ref [46]. (c) Absorption spectra of $CH_3NH_3PbI_3$ (dotted line) and Br-Cl mixed halides for different concentrations. Original figure from Ref. [204]. This collage of figures is reproduced from Ref. [117] with permission.

confirmed the existence of Cl atoms in the composition of the crystal, speculating that the $CH_3NH_3Cl$ product sublimates during the temperature treatment in the synthesis process [42, 49, 117, 132, 205, 206].

### 3.3.3 Mixed-cation perovskites

Lead-iodide perovskite based on alternative cations to $CH_3NH_3^+$ [formamidinium $HC(NH_2)_2^+$ or $Cs^+$] have band gaps varying from 1.45 to 1.72 eV, as shown in Figure 3.7 [145, 200]. This effect is a consequence of the steric interaction between the central cation and the inorganic Pb-I network. Increasing the size of the cation at the centre of the cuboctahedral cavity determines the increase of the volume of the cavity, which is achieved by stretching the Pb-I bonds or bending the Pb-I-Pb bond angles. In Chapter 5 we show that the bond angles are the principal drivers for the change in the volume of the cuboctahedral cavity, and the bond stretching is a secondary effect. The first few studies observing the steric interaction between the molecular cation and the metal-halide cavity assume that the metal-halide bond length stretch in order to make space for the given cation [190, 207, 208] and obtain an incorrect dependence of the

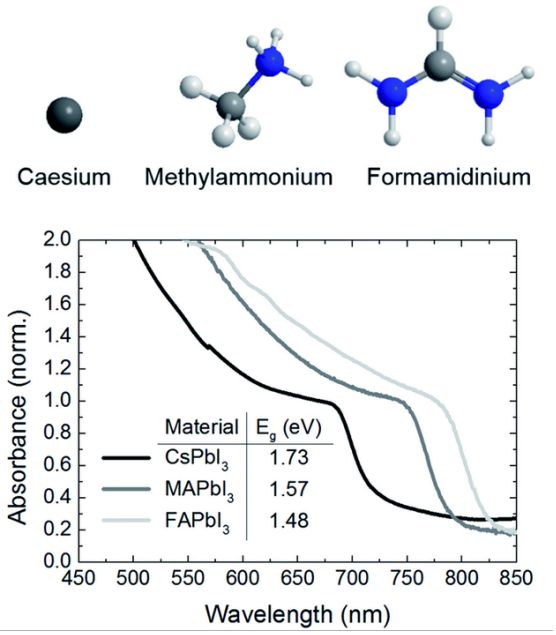


Figure 3.7: Optical absorption spectra for $CsPbI_3$, $CH_3NH_3PbI_3$ and $HC(NH_2)_2PbI_3$. Figure reproduced from Ref [200] with permission.

band gap with cation size when compared to experimental observations [145, 200]. By contrast, an increase in the Pb-I-Pb bond angles determines an increasing volume of the cuboctahedral cavity but also a decreasing band gap [158, 194, 199] as expected from experimental observations. This effect is described in detail in Chapter 5. Experimental studies published in Refs [27, 137] show that the gradual cation replacement while keeping the same composition for the Pb-I network is also possible. Combinations of $CH_3NH_3PbI_3$ and $HC(NH_2)_2PbI_3$ [137] and of $CH_3NH_3PbI_3$ and $CsPbI_3$ [27] show a continuous variation of the band gap as a function of concentration. Moreover, using this rationale it is possible to stabilise perovskite species in crystalline structures which are not favourable at a given temperature. In Ref. [158] such a continuous dependence of band gap on the concentration is shown for $Rb_xCs_{1-x}PbI_3$, even though $RbPbI_3$ is known to crystallise in a one-dimensional needle-like structure [209].

## 3.4 Summary

Perovskite photovoltaic devices have shown unprecedented progress in the last three years. In parallel with these rapid technological advances of device configuration and performance, significant efforts are devoted to understanding the microscopic mechanisms which are responsible for the exceptional performance of these materials. Experimental and computational studies alike are focused on elucidating the electronic and optical properties of metal-halide perovskites and the routes to improving for these already remarkable materials.

From a computational point of view the study of these relatively new materials requires a systematic understanding of the sensitivity of the results on the computational setup in order to reach correct and reliable conclusions. Alongside tackling open fundamental questions such as the effect of the structural disorder on the electronic properties, the excitonic properties or recombination phenomena, smart materials design strategies could accelerate the development of novel perovskites.

In Chapter 4 we address the requirement for a systematic computational analysis of these materials by performing a careful study of the quasiparticle band structure of $CH_3NH_3PbI_3$ within the *GW* approximation. In Chapter 5, we move to an analysis of the effect of the structural changes. Based on our findings we propose a design route for novel perovskites which will be analysed in more detail in Chapter 6.

# Chapter 4

# Electronic properties of the hybrid $CH_3NH_3PbI_3$ perovskite

As described in the previous chapter, the crystal structure of $CH_3NH_3PbI_3$ is highly dependent on temperature and undergoes two phase transitions [144–146]. In addition to that, as the temperature increases, the structural determination is complicated by the orientational disorder of the cation. Results reported in Ref. [155] show that the total energy landscape of the crystal structure of $CH_3NH_3PbI_3$ is possibly characterised by a multitude of local minima within energy differences less than the thermal energy at room temperature (25 meV). Moreover, the position of the atoms in the Pb-I inorganic cage as well as the disordered character of the $CH_3NH_3^+$ can trigger changes in the band structure of $CH_3NH_3PbI_3$ [158, 194]

The interplay of the structural and electronic properties of this material is the cause for much debate in the computational study of the electronic properties of $CH_3NH_3PbI_3$. For this reason, a systematic computational investigation is required. In this chapter we focus our attention purely on the electronic properties of $CH_3NH_3PbI_3$. The principal goal is to analyse the electronic structure properties of a single crystal structure within scalar and fully relativistic density functional theory and within the *GW* approximation. We focus on highlighting both physical properties as well as techni-

cal computational details important for a correct study of the electronic properties, particularly in the context of the *GW* approximation. Finally we devise a simple computational "recipe" to use for calculating the quasiparticle band gaps of other Pb-I perovskite structures.

## 4.1 Density functional theory calculations

### 4.1.1 Crystal structure optimisation

In this chapter we study the low-temperature orthorhombic phase of $CH_3NH_3PbI_3$. The unit cell of $CH_3NH_3PbI_3$ in this case contains 48 atoms, corresponding to four $PbI_6$ octahedra and four cations. The space group of this system is *Pnma* and the orientation of the $CH_3NH_3^+$ is well understood in this case [146]. A polyhedral representation of the orthorhombic $CH_3NH_3PbI_3$ crystal structure is shown in Figure 4.1. We use the experimental lattice parameters and atomic positions reported by Baikie et

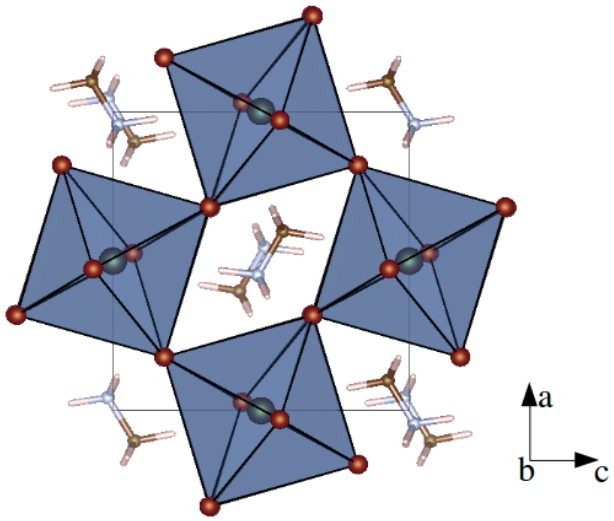


Figure 4.1: Polyhedral representation of the crystal structure of $CH_3NH_3PbI_3$. The Pb atoms are represented by the large blue spheres at the centre of each octahedron. The small red spheres located at the shared corners of the octahedra are the I atoms. The $CH_3NH_3^+$ atoms are shown using ball-and-stick models at the centre of the cuboctahedral cavities. (C is light blue, N is brown and H is pink). The structure is viewed along the *b* axis.

al [146] as a starting point for our calculations. We optimise this structure by minimising the total energy and forces within the unit cell, allowing the atomic positions and lattice parameters to relax. Finally, we obtain an optimised structure which preserves the *Pnma* symmetry within a threshold of 0.14 Å. In Table 4.1 we show a comparison between the experimental and optimised lattice parameters and in Table 4.2 we show the atomic positions in the asymmetric experimental and optimised unit cells. It is worth noting at this point that the positions of the hydrogen atoms have not been determined experimentally, therefore the starting point positions are chosen in order to comply with the symmetry of the system. For this reason, their atomic positions are not given in Table 4.2.

Unless otherwise specified, the calculations presented in this chapter are performed for the optimised structure of $CH_3NH_3PbI_3$.

| Lattice parameter (Å) | Experimental [146] | Optimised |
|---|---|---|
| *a* | 8.836 | 8.682 |
| *b* | 12.580 | 12.366 |
| *c* | 8.555 | 8.301 |

Table 4.1: Comparison between structurally optimised lattice parameters and the experimental lattice parameters Ref.[146] of $CH_3NH_3PbI_3$ in the orthorhombic phase. The experimental lattice parameters listed in this table are used as a starting point for the structural optimisation calculations.

### 4.1.2 Scalar relativistic calculations

We calculate the electronic band structure and the partial density of states of $CH_3NH_3PbI_3$ without including the relativistic spin-orbit coupling effect at this initial stage. In Figure 4.2a we show the scalar relativistic band structure along the U(0.5,0,0.5) - Γ - Y(0.0,0.5,0.0) high symmetry path (in crystal units). This path corresponds to the directions of the straight lines connecting the neighbouring Pb atoms in the unit cell, as shown in Figure 4.1.

| Atom | Experimental [146] | | | Optimised | | |
|---|---|---|---|---|---|---|
| | x | y | z | x | y | z |
| Pb | 0.5000 | 0.0000 | 0.0000 | 0.5000 | 0.0000 | 0.0000 |
| I1 | 0.4900 | 0.2500 | 0.9500 | 0.4700 | 0.2500 | 0.9350 |
| I2 | 0.1900 | 0.0200 | 0.1900 | 0.1800 | 0.0200 | 0.1750 |
| C | 0.9300 | 0.7500 | 0.0300 | 0.9550 | 0.7500 | 0.0150 |
| N | 0.9100 | 0.2500 | 0.0600 | 0.9000 | 0.2500 | 0.0700 |

Table 4.2: Comparison between structurally optimised atomic positions and the experimental atomic positions Ref.[146] of $CH_3NH_3PbI_3$ in the orthorhombic phase. The experimental atomic positions are used as a starting point for the structural optimisation calculations. Upon optimisation, the atomic position in the unit cell of $CH_3NH_3PbI_3$ follow the symmetry transformations of the *Pnma* space group within a threshold of 0.14 Å. All coordinates are listed in crystal units.

In Figure 4.3 we show the total and projected density of states. In the vicinity of the valence band top the electron occupation is predominantly of I-*p* character, while the top of the valence band has a small contribution from the Pb-*s* type states. The conduction band appears to be predominantly of Pb-*p* and I-*p* type in the energy range close to the conduction band bottom. Moreover, the states localised on the $CH_3NH_3^+$ cation have energies which are almost 5 eV away from the valence band top and conduction band bottom, suggesting that there is no charge transfer between the $PbI_6$ perovskite network and the organic cation. This observation is in line with previous computational reports on $CH_3NH_3PbI_3$ [184, 193].

Given that the central $CH_3NH_3^+$ cations appear to not influence the conduction and valence band edges, we can perform a simple exercise by which we remove the cations from the unit cell and replace them with a compensating background charge. We calculate the band structure for such a fictitious system and compare it to the $CH_3NH_3PbI_3$ band structure shown in Figure 4.4, along the Γ-Y direction. It can be easily seen that the topology of the bands remains unchanged upon removal of the cation. There is a small difference in band gap of 0.1 eV and a slight widening of the highest valence band width of the same order.

We obtain a band gap of 1.49 eV, direct at the Γ point. This value is in surprisingly

good agreement with the reported experimental band gaps of 1.55 eV. As it was pointed out in literature [186, 189, 191], we will show in the following that this agreement is fortuitous and it is due to a cancellation between the negative spin-orbit coupling correction and the positive quasiparticle correction.

### 4.1.3 Effect of spin-orbit coupling

In Figure 4.2b we show the band structure of $CH_3NH_3PbI_3$ in the orthorhombic phase including the relativistic spin-orbit coupling effects. From Figure 4.2 we observe the large spin-orbit coupling effect on the electronic structure in the vicinity of the band

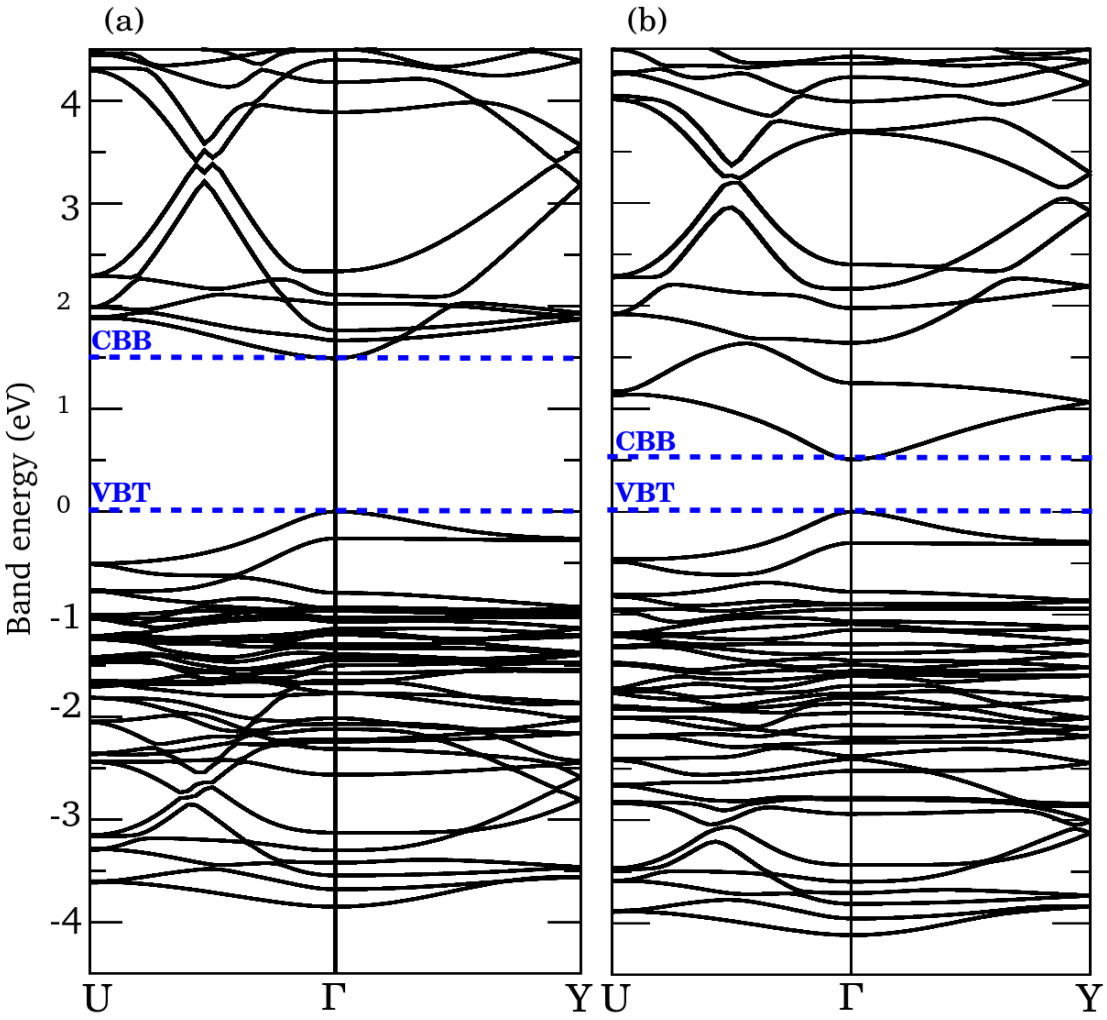


Figure 4.2: Scalar relativistic (a) and fully relativistic (b) band structure of $CH_3NH_3PbI_3$ along the high symmetry path U - Γ - Y. The dashed blue lines highlight the top of the valence band (VBT) and the bottom of the conduction band (CBB).

edges. The direct band gap is reduced by approximately 1 eV due to the spin-orbit interaction, in agreement with previous computational results [186, 189, 191]. Moreover, the topology of the conduction band edge changes drastically when the spin-orbit interaction is taken into account in the electronic structure calculation. Indeed, in the scalar relativistic case the lower conduction bands are crossing and they are nearly degenerate at the Γ point (the difference between the lowest and second lowest energy level at the Γ point is less than 0.2 eV). This small deviation from the degenerate state is due to symmetry considerations and caused by the tilted octahedra in the orthorhombic phase (a detailed discussion of this effect is found in the next chapter). On the other hand, in the fully relativistic case, the difference between the first and second lowest energy level in the conduction band at the Γ point is of almost 1 eV.

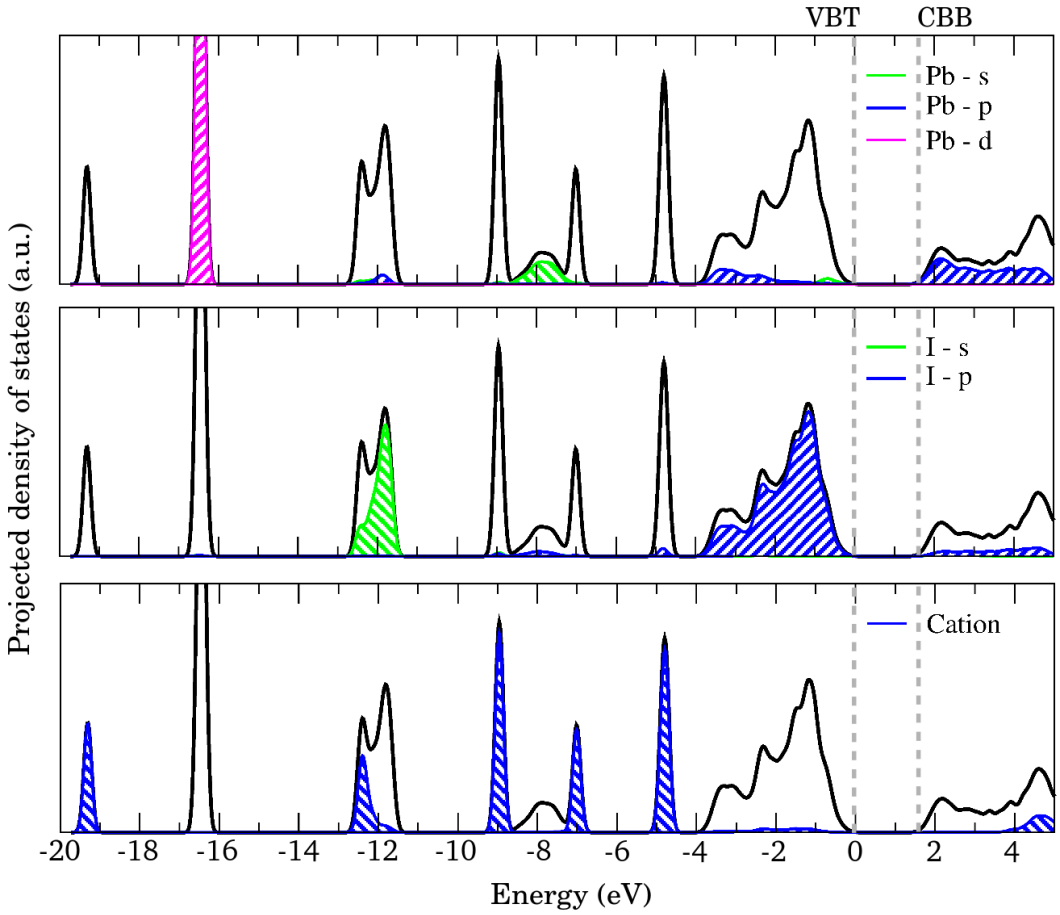


Figure 4.3: Projected density of states for $CH_3NH_3PbI_3$. The black plotted line is the total density of states. The contributions from the Pb, I orbitals and the total contribution of the cations are represented separately.

Moreover the lowest band crossing point is approximately 0.5 eV away from the conduction band bottom, in agreement with Ref. [184]. By contrast, the shape of the valence band edge does not appear to change significantly due to the spin-orbit interaction.

Since the topology of the conduction band suffers such a drastic change upon the inclusion of spin-orbit interaction, we expect that the effective masses calculated within the scalar and fully relativistic calculations are drastically different.

### 4.1.4 Effective masses: scalar vs. fully relativistic

We calculate the effective mass tensor by approximating the second derivatives of the relativistic Kohn-Sham eigenvalues at the Γ point:

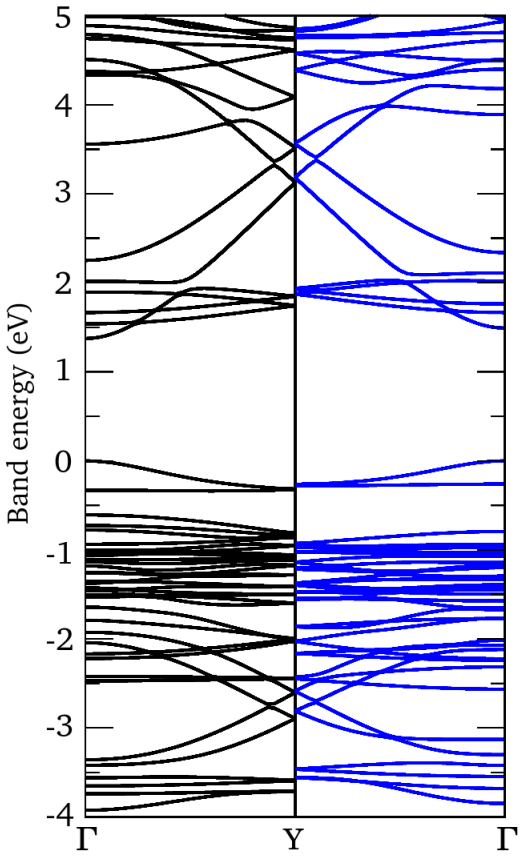


Figure 4.4: Comparison between the scalar relativistic band structure along the Γ-Y direction for the Pb-I perovskite structure with the cation replaced by a background charge (black line) and the full $CH_3NH_3PbI_3$ structure.

$$m^*_{ij} = \hbar^2(\epsilon_{ij})^{-1}. \tag{4.1}$$

where $\epsilon_{ij} = \partial^2\epsilon/\partial k_i \partial k_j$ is the second partial derivative of the Kohn-Sham eigenvalues with respect to the wave vector $\mathbf{k}$ along the three crystallographic directions, $i$ and $j$ index the crystallographic directions. We calculate these derivatives numerically using the finite-difference method.

We obtain the electron and hole effective masses by diagonalising the effective mass tensor $m^*_{ij}$ for the valence and conduction band respectively, and taking the isotropic average.

Table 4.3 shows the comparison between the three components of the eigenvalues of the effective mass tensor $m^*_{ij}$, $(m_1, m_2, m_3)$, for the electrons and holes. In the scalar relativistic case, the three eigenvalues of the electron effective mass tensor are strongly anisotropic. This is not the case for the fully-relativistic calculations, where the calculated effective masses are almost isotropic. This discrepancy is due to the effect of the spin-orbit interaction on the topology of the conduction band bottom, suggesting that the electron effective mass cannot be calculated correctly without including relativistic effects. In the case of the valence band the effective mass is isotropic in both the scalar and fully relativistic case, in agreement with the observations made for Figure 4.2.

| | Scalar relativistic | | Fully relativistic | |
|---|---|---|---|---|
| | Holes | Electrons | Holes | Electrons |
| $m_1$ | 0.25 | 0.08 | 0.17 | 0.10 |
| $m_2$ | 0.25 | 0.54 | 0.15 | 0.14 |
| $m_3$ | 0.19 | 0.87 | 0.12 | 0.16 |
| $m_{\text{eff}}$ | 0.23 | 0.50 | 0.15 | 0.13 |

Table 4.3: Eigenvalues of the hole and electron effective mass tensor calculated for the scalar and fully relativistic case and their isotropic average $m_{\text{eff}}$. All effective masses are expressed in atomic units.

An alternative route for calculating the effective mass is using the so called '$\mathbf{k}\cdot\mathbf{p}$ method', by which the energy dispersion relation is extrapolated using the band ener-

gies at the Brillouin zone center. Using the $\mathbf{k}\cdot\mathbf{p}$ one obtains that the electron effective mass is proportional to the band gap for a direct gap semiconductor [171].

## 4.2 *GW* calculations

The direct band gap of $CH_3NH_3PbI_3$ calculated within fully relativistic DFT is approximately 1 eV smaller than reported optical band gaps [146]. In the following we describe the calculation of the quasiparticle band gap within the *GW* approximation.

### 4.2.1 Effect of the semicore electrons

The effect of semicore electrons on the calculation of quasiparticle energies is well documented in the literature [210–212]. This effect arises from an additional exchange contribution to the self-energy which results from the spatial overlap of diffuse semicore states with the valence states at the band edges. The correlation self energy is generally less affected by the inclusion of semicore states, since their contribution is damped by the energy dependence. In Figure 4.5 we show a comparison between the radial wave functions for Pb and I as obtained in the pseudopotential method. From

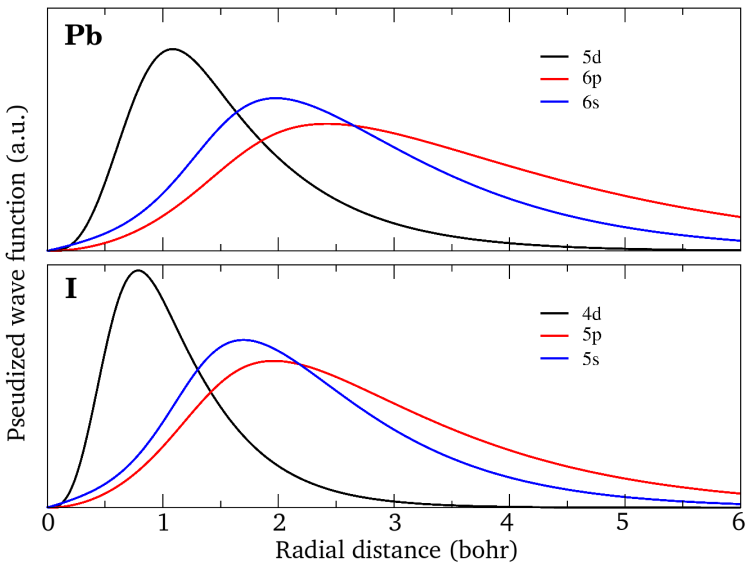


Figure 4.5: Wave function overlap for the orbitals explicitly included in the valence configurations for Pb and I.

Figure 4.5 it is clear that both Pb and I $d$ wave functions have a significant overlap with the valence $s$ and $p$ wave functions. As such, it is likely that the inclusion of the semicore $d$ electrons for both Pb and I would impact the quasiparticle eigenvalues.

In the case of $CH_3NH_3PbI_3$ we analyse the effect of semicore electrons on the quasiparticle eigenvalues by including the $d$ semicore electrons in the pseudopotentials of Pb and I. We compare four cases with different valence electronic configurations included in the pseudopotentials of Pb and I: i) Pb without semicore states ($6s^26p^2$) and I without semicore ($5s^25p^3$), ii) Pb with semicore ($5d^{10}6s^26p^2$) and I without semicore, iii) Pb without semicore and I with semicore ($4d^{10}5s^25p^3$), and iv) Pb and I with semicore states. The inclusion of the semicore states has a small impact on the DFT band gaps of $CH_3NH_3PbI_3$. In Table 4.4 we show that the DFT band gap changes by less than 0.04 eV when semicore states are included in both the scalar and fully relativistic calculations. By contrast, the quasiparticle band gap appears to be sensitive to the Pb-5$d$ and I-4$d$ semicore states. Upon inclusion of semicore states the quasiparticle band gap increases by up to 0.3 eV.

| | Pb: w/o s<br>I: w/o s | Pb: w s<br>I: w/o s | Pb: w/o s<br>I: w s | Pb: w s<br>I: w s |
|---|---|---|---|---|
| | | DFT/LDA | | |
| SR | 1.43 | 1.42 | 1.51 | 1.50 |
| FR | 0.54 | 0.52 | 0.60 | 0.58 |
| Difference | 0.89 | 0.90 | 0.91 | 0.92 |
| | | $G_0W_0$ | | |
| SR | 2.20 | 2.18 | 2.61 | 2.55 |
| FR | 1.08 | 0.98 | 1.41 | 1.32 |
| Difference | 1.12 | 1.20 | 1.20 | 1.23 |

Table 4.4: DFT/LDA Kohn-Sham and $G_0W_0$ quasiparticle band gaps. We report the results of scalar relativistic calculations (SR) and fully relativistic calculations (FR) for all combinations of Pb and I pseudopotentials considered in this work ('w s'/'w/o s' indicates that semicore electrons are included/not included). All values are in eV. The last row reports the difference between the SR and the FR gap for each case considered.

In Figure 4.6 we show the comparison of the quasiparticle eigenvalues calculated in the cases i)-iv). From Figure 4.6 we can see that the quasiparticle band gap change is mostly associated with a red-shift of the valence band top upon inclusion of semicore states. For clarity, we compare the exchange and correlation terms of the self energy in each of these four cases. We can see that the effect of the semicore states is most pronounced in the exchange term of the self-energy, approximately of the order of 1 eV (Figure 4.7a), while for the correlation part this effect is smaller (approximately 0.5 eV), as shown in Figure 4.7b.

In the exchange part of the self energy (Figure 4.7a) the bottom of the conduction band is mostly affected by the Pb-5*d* electrons. This is consistent with the predominant Pb-6*p* character of those states, shown in Figure 4.3. Similarly, the corrections near the top of the valence band are affected both by Pb-5*d* and I-4*d* semicore states, in line with the observation that those states carry both Pb-6*s* and I-5*p* character. Taken together, these results indicate that $G_0W_0$ quasiparticle corrections are sensitive to the explicit inclusion of semicore electrons in the valence. This sensitivity results in a band gap variation of around 25%. In the following section we show the effect of self

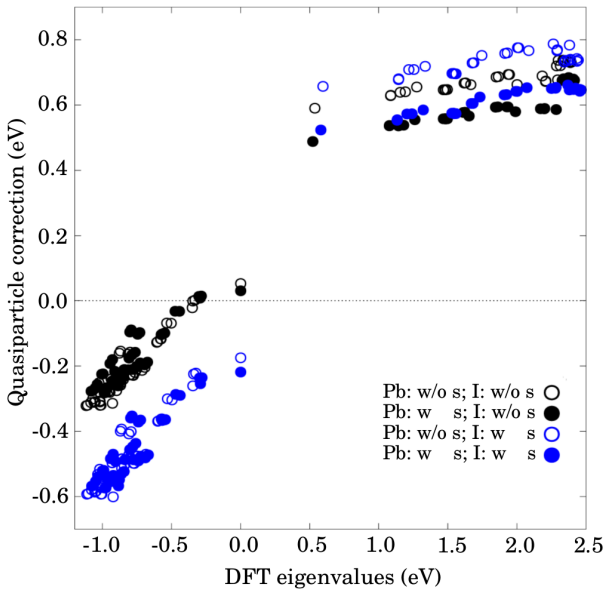


Figure 4.6: Fully relativistic quasiparticle corrections of the DFT/LDA band gap near the band edges and throughout the Brillouin zone as a function of the DFT/LDA eigenvalues.

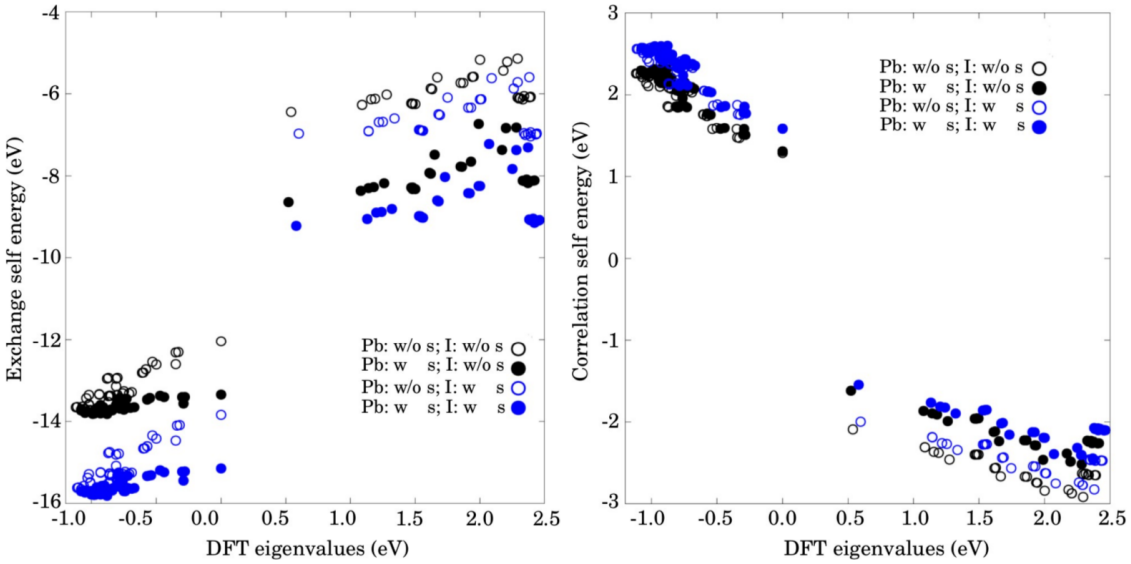


Figure 4.7: The exchange (a) and correlation (b) self energy of the state near the band edges and throughout the Brillouin zone as a function of the DFT/LDA eigenvalues.

consistency of $G_0W_0$ calculations only for the calculations which include the semicore *d* states for both Pb and I, which we consider our most accurate calculations.

### 4.2.2 Effect of self-consistency

#### The self-consistent scissor *GW* method

As discussed in Chapter 2 $G_0W_0$ quasiparticle energies can be sensitive to the Kohn-Sham eigenvalues and eigenstates used as the starting point to calculate the perturbative corrections [90–96].

In this chapter we propose a simple scissor correction approach in order to study the impact of self-consistency on the quasiparticle band gap of $CH_3NH_3PbI_3$. The scissor correction is particularly appropriate for $CH_3NH_3PbI_3$ since the optical absorption onset results from transitions between two parabolic bands which are well separated from other bands, therefore the effects of band-mixing via off-diagonal matrix elements of the self-energy are expected to be very small.

In this approach, the idea is to determine the $G_0W_0$ band gap using Eq. (2.52) of

Chapter 2, reproduced here for convenience. The quasiparticle eigenvalues at the initial iterative step, $E^{(1)}_{n\mathbf{k}}$ are calculated as:

$$E^{(1)}_{n\mathbf{k}} = \epsilon_{n\mathbf{k}} + Z(\epsilon_{n\mathbf{k}})\langle n\mathbf{k}|\Sigma(\epsilon_{n\mathbf{k}}) - V_{xc}|n\mathbf{k}\rangle. \tag{4.2}$$

In particular, for the case of $CH_3NH_3PbI_3$ we are interested in the band gap at the zone center. The quasiparticle correction at this step is calculated as:

$$\Delta^{(1)} = E_{n\mathbf{k}} - \epsilon_{n\mathbf{k}}. \tag{4.3}$$

with $\mathbf{k} = (0,0,0)$. We apply a scissor correction of magnitude $\Delta^{(1)}$ to the Kohn Sham conduction bands and repeat this process until $\Delta^{(i)}$ and $\Delta^{(i+1)}$ are within a set tolerance. The scissor correction modifies both the Green's function $G_0$ and the screened Coulomb interaction $W_0$ via the RPA polarisability. In the remainder of this thesis we will refer to this approach as "SS-*GW*" (self-consistent scissor *GW*).

The effect of the scissor correction can be seen as if obtained by adding a non-local exchange and correlation potential to the original Kohn-Sham Hamiltonian, $V^{(i)}_{\mathrm{nl}} = \Delta^{(i)} P_{\mathrm{c}}$, with $P_{\mathrm{c}}$ being the projector on the manifold of unoccupied states. In order to avoid double-counting, this extra potential must be removed from Eq. (4.2). Therefore, the calculation of the quasiparticle eigenvalues at the iterative step $(i)$ can be written as:

$$E^{(i)}_{n\mathbf{k}} = \epsilon_{n\mathbf{k}} + Z(\epsilon_{n\mathbf{k}})\langle n\mathbf{k}|\Sigma(\epsilon_{n\mathbf{k}}) - V_{xc} - V^{(i)}_{\mathrm{nl}}|n\mathbf{k}\rangle. \tag{4.4}$$

In practical calculations using the `Yambo` code the problem of the double counting is resolved by adding the correction $-Z(\epsilon_{n\mathbf{k}})\Delta^{(i)}$ to the quasiparticle band gap obtained as the result of iteration $(i)$.

The SS-*GW* approach is similar in spirit to other more sophisticated techniques such as *GW*+U [91, 92] or quasiparticle self-consistent *GW* [90]. The main difference between SS-*GW* and these approaches is that Eq. (4.4) can be implemented as a post-processing operation following the initial $G_0W_0$ step described in Eq. (4.2). The scissor

correction has no impact on the exchange self energy, since the scissor correction only acts on the unoccupied states. The scissor correction affects only the correlation self-energy and acts to improve the description of the screening via a modulation of the band gap.

### SS-*GW* calculation on $CH_3NH_3PbI_3$

Figure 4.8 shows the convergence of the quasiparticle correction to the band gap at each iteration of the SS-*GW* procedure for both optimised and experimental crystal structure of $CH_3NH_3PbI_3$. The SS-*GW* procedure converges after five iterations, at which point the band gap correction becomes smaller than 20 meV. Figures 4.8a and b show visual representations of the SS-*GW* calculations, plotting the quasiparticle band gap against the scissor-corrected gap of the previous iteration in both cases. These pictures are similar to those obtained in previous *GW*+U calculations on different systems [91].

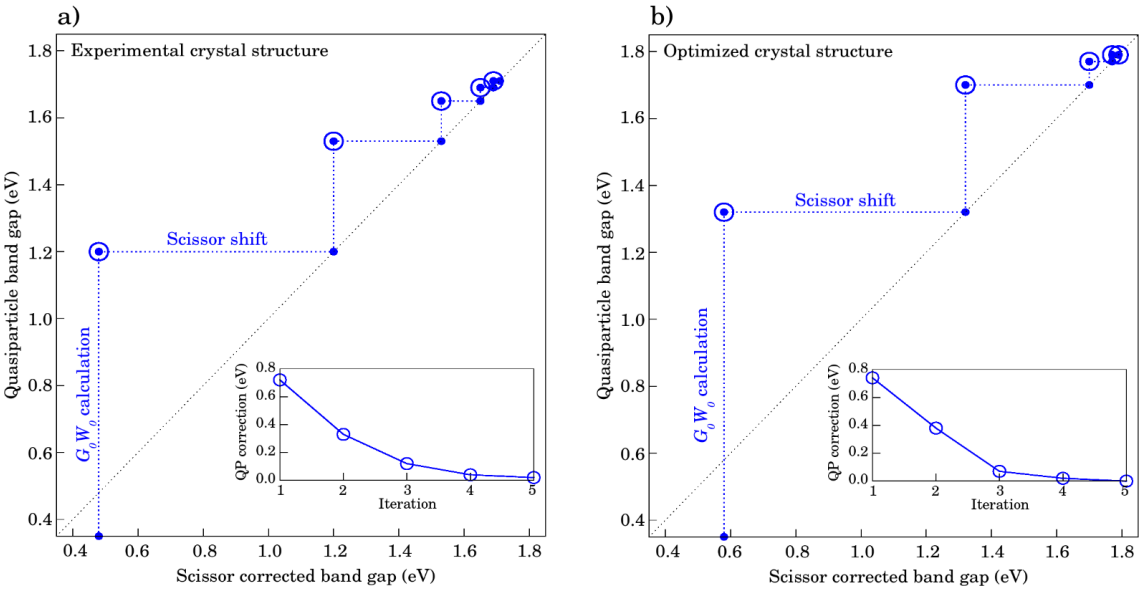


Figure 4.8: Evolution of the quasiparticle band gap throughout the SS-*GW* iterative procedure for the experimental (a) and optimised (b) crystal structure of $CH_3NH_3PbI_3$. The blue dotted lines show the progression of the calculation at each iteration: the vertical blue lines represent the $G_0W_0$ calculation performed at each iteration, while the horizontal blue lines are the scissor shifts applied at each iteration. The iterative procedure stops when the $G_0W_0$ correction vanishes, that is when the small and large circle coincide on the black line. The inset of both (a) and (b) represents the convergence of the self-consistent scissor correction to the band gap of $CH_3NH_3PbI_3$ with the number of iterations.

**Quasiparticle band gaps of $CH_3NH_3PbI_3$**

Table 4.5 reports DFT and quasiparticle band gaps of the optimised and experimental crystal structures of $CH_3NH_3PbI_3$ obtained by including semicore *d* states for both Pb and I. For the optimised crystal structure we also show the DFT and $G_0W_0$ results for the scalar and fully relativistic case, and the SS-*GW* results in the fully relativistic case only. The $G_0W_0$ scalar relativistic band gaps are in good agreement with previously reported calculations [191, 192]. This data overestimates the band gap with respect to experiment by up to 1 eV due to the neglect of relativistic corrections. As expected, the overestimation of the quasiparticle band gap in the scalar relativistic case is of the same magnitude as the relativistic spin-orbit coupling effect calculated from DFT. This observation nicely explains the surprising agreement between the scalar-relativistic DFT band gap and the experimental band gap of $CH_3NH_3PbI_3$.

For the fully relativistic case we report the DFT, $G_0W_0$ and SS-*GW* band gaps for both the optimised and experimental structures of $CH_3NH_3PbI_3$. The band gaps calculated for the optimised crystal structure are larger than the ones calculated for the experimental structure by at least 0.1 eV at all levels of theory (DFT, $G_0W_0$ and SS-*GW*). This difference is in line with experimental and computational observations that the crystal structure has a strong influence on the electronic properties of metal-halide perovskites [158, 169, 170, 194].

The fully relativistic $G_0W_0$ gaps reported in Table 4.5 for the experimental and optimised structures are 0.3-0.5 eV smaller than the fully relativistic $G_0W_0$ band gap reported in Ref. [191], while the SS-*GW* band gaps are much closer to this value. This apparently puzzling situation can be rationalised by noting that in Ref. [191] the Green's function is fully relativistic, but the screened Coulomb interaction is calculated at the scalar relativistic level. This choice implies that the $W_0$ of Ref. [191] was obtained starting from a DFT/LDA gap which was artificially increased by the neglect of spin-orbit effects. In doing so the $W_0$ of Ref. [191] was obtained using a DFT/LDA

| | Present work | | | Previous *GW* | |
|---|---|---|---|---|---|
| | DFT | $G_0W_0$ | SS-*GW* | $G_0W_0$ | QS*GW* |
| | | | Optimised crystal structure | | |
| SR | 1.50 | 2.55 | | 2.68 [191], 2.73 [192] | |
| FR | 0.58 | 1.32 | 1.79 | 1.67 [191], 1.27 [192] | 1.67 [192] |
| | | | Experimental crystal structure | | |
| FR | 0.48 | 1.20 | 1.71 | | |

Table 4.5: Comparison between our calculated quasiparticle band gaps of $MAPbI_3$, obtained here within the $G_0W_0$ or the self-consistent scissor (SS-*GW*) approach, for both the optimised and experimental crystal structure and previously reported values (in eV).

band gap which is close to our scissor-corrected gap. In order words the choice of Ref. [191] of neglecting spin-orbit effects in $W_0$ acts as an "effective scissor correction". This observation also nicely reconciles the apparent discrepancy between the results of Refs. [192] and [191].

Our fully-relativistic $G_0W_0$ band gaps are in good agreement with the $G_0W_0$ band gap reported in Ref. [192]. This agreement is somewhat fortuitous since in Ref. [192] the quasiparticle renormalisation (which in our case is $Z = 0.8$) was not taken into account. We speculate that the agreement may be due to the fact that in Ref. [192] a cubic $CH_3NH_3PbI_3$ structure is considered, which is known to have a smaller band gap than the orthorhombic counterpart.

Both the SS-*GW* band gaps calculated for the experimental and optimised structures are within 0.1 eV from the quasiparticle self consistent *GW* (QS*GW*) band gap reported in Ref. [192] (1.67 eV). The large band gap corrections introduced by the "self-consistent" scissor correction are not too surprising since the energy dependence of the quasiparticle corrections for $CH_3NH_3PbI_3$ is very smooth (Figure 4.6). The agreement with the more sophisticated QS*GW* methodology is encouraging and indicates that the simple SS-*GW* should be able to mimic more elaborate self-consistent procedures.

The small differences between our SS-*GW* results and the results of Ref. [191, 192] can be explained by the difference in the structures employed in the two studies. Indeed, in Ref. [192], the structure under study is cubic. On the other hand, Ref. [191] analyses the orthorhombic structure of $CH_3NH_3PbI_3$, obtaining the structural parameters from a geometry optimisation within the Generalised Gradient Approximation (GGA).

**Comparison with experiment**

Our calculations do not include electron-phonon interactions or effects which are dependent on temperature. Therefore, we compare the final quasiparticle band gap obtained from SS-*GW* with the experimental band gap of $CH_3NH_3PbI_3$ measured at 4.2 K [169]. The exciton binding energy is estimated at $55 \pm 22$ meV in Ref. [169], and the measured optical band gap is 1.62-1.64 eV. These values are in very good agreement with our calculated band gaps, and in particular with the SS-*GW* band gaps calculated for the experimental structure of 1.71 eV. Moreover, this value is in very good agreement with recent data obtained from photoemission experiments, reporting a band gap of 1.7 eV for $CH_3NH_3PbI_3$ [213, 214]. The final SS-*GW* band gap calculated for the fully optimised crystal structure is larger than the experimental gap by just over 0.1 eV. The difference in the two SS-*GW* band gaps reflects exactly the difference in their DFT band gaps (0.48 vs 0.58 eV) which can be assigned to the crystal structure differences. This difference hints at the interplay between the structural and electronic properties of Pb-I perovskites, which will be analysed in detail in the next chapter.

## 4.3 Summary

In this chapter we have presented a systematic study of the quasiparticle band gap of $CH_3NH_3PbI_3$ using the *GW* many-body perturbation theory. We showed that the explicit inclusion of semicore Pb-5*d* and I-4*d* electrons in the valence manifold is important in order to obtain a quantitatively accurate band gap. The neglect of semicore states induced errors in the gap of the order of 25%. We showed that the $G_0W_0$ band

gap including semicore electrons and spin-orbit coupling underestimates the band gap by 0.3-0.4 eV with respect to the experimental optical band gap. In order to address this deficiency we tested a simple self-consistent scissor correction approach (SS-*GW*). We demonstrated that this simple method can achieve very good agreement with experiment and the more elaborate self-consistent *GW* schemes.

The validity of the SS-*GW* approach is interesting in the wider context of predicting the band gap of hybrid perovskites. This approach is simple, transparent and at no higher computational cost than a single $G_0W_0$ calculation. Moreover, the SS-*GW* procedure could also be used to gauge the reliability of the perturbative treatment, by simply comparing the initial $G_0W_0$ gap with the final SS-*GW* gap. A significant discrepancy between these values generally indicates the need to go beyond $G_0W_0$ theory. These observations can be important in the development of automated high-throughput computational screening strategies that rely on *GW* calculations.

Based on the calculations presented in this chapter we can devise a schematic computational strategy for Pb-I perovskites, which will be used for hypothetical compounds in Chapter 6: (i) Calculate the fully relativistic DFT/LDA eigenvalues including spin orbit coupling and semicore *d* electrons for Pb and I. (ii) Calculate the quasiparticle $G_0W_0$ energies using the eigenvalues calculated at the previous step. (iii) Repeat the SS-*GW* procedure presented in this chapter until the quasiparticle correction is smaller than a set threshold.

Finally, we have showed that small changes in the crystal structure of the perovskite can have a significant influence on the calculated band gap at the DFT, *GW* and SS-*GW* level. In the next chapter we will explore this observation further by analysing the interplay of the structural and electronic properties of lead-iodide perovskites in a systematic way.

# Chapter 5

# Rational design of novel perovskite absorbers with tunable optical properties

An attractive feature of perovskite absorbers is the possibility of tailoring their band gaps by changing the elemental composition through the chemical precursors. Several computational and experimental studies have reported various approaches in the optimisation of solar cells by modifying the metal-halide network or the organic cation of the perovskite absorber [27, 46, 137, 145, 146, 191, 194, 199, 200].

From a computational point of view the idea of tuning the band gap of metal-halide perovskites by changing the cation is particularly interesting due to the separation between the electronic charges localised on the cation and on the metal-halide network [155, 158, 207]. Indeed, in Figure 6.3 we show that the electronic states associated with the cation are located almost 5 eV from the band edges. These observations suggest that the electronic structure of these metal-halide perovskites may be described by removing the cation from the structural model and compensating the negative charge of the $PbI_3$ network using a positive background. However, given that the optical absorption onsets of $CsPbI_3$ and $CH_3NH_3PbI_3$ differ by 0.2 eV, it appears that the cation indirectly influences the electronic structure of perovskite through the steric interaction between the cations and the Pb-I network.

These observations open two important questions which we set to answer in the present chapter: i) How does the electronic structure of metal-halide perovskite depend on the structural properties of the metal-halide network? ii) How does the central cation change the structure of the metal-halide network?

## 5.1 Platonic model of metal-halide perovskites

### 5.1.1 The Platonic octahedron

In the most symmetric case, the cubic perovskite structure is formed by corner-sharing, identical rigid octahedra with centres equally spaced along the three lattice vectors (See Figure 5.1) [120]. The unit cell of this structure contains therefore a single octahedron. Due to the periodicity constraints and the condition that all octahedra in the structure must share their corners, we readily observe that the orientation of the rigid octahedron within the cubic unit cell is fixed. Tetragonal and orthorhombic perovskite structures maintain the corner sharing octahedra as the basic building block, but distortions appear in order to allow the structural changes. These distortions were classified in an early work by Glazer [120, 121, 125] in three main categories: rotations of individual octahedra, flattening or elongations of octahedra and the displacements of the central atom within the octahedra. In real perovskite systems the crystal structure

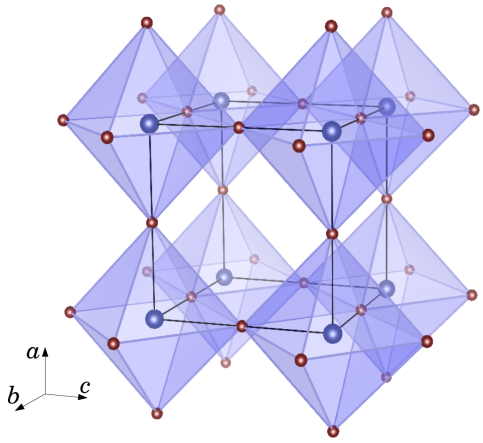


Figure 5.1: Polyhedral model of the cubic perovskite structure.

is a result of a linear combination of all three distortions. Consequently the parameter space describing the structure of all possible three-dimensional perovskite structures is extremely large, and they can be classified based on their symmetry, as shown in Refs. [120, 121, 125].

In the case of lead-iodide perovskites and indeed metal-halide perovskites, some of the degrees of freedom introduced by these possible distortions can be ruled out or ignored momentarily by observing some of the available experimental evidence for the structural geometry of this group of materials. The most important observation can be made from X-Ray diffraction data [145, 146] reported for $MAPbI_3$, revealing that the Pb-I bond lengths are extremely regular throughout the perovskite crystal structure, and that the diagonals of the $PbI_6$ octahedra are almost perpendicular to one another. Moreover, in the least symmetric phase, $MAPbI_3$ exhibits an orthorhombic structure, with four corner sharing rotated octahedra in the unit cell. Therefore, as an initial approximation, we can represent the $PbI_6$ octahedra as rigid and regular, more specifically with diagonals equal in magnitude, perpendicular with one another and all intersecting at the centre of the octahedron (Figure 5.2).

A rigid, regular octahedron carries full $O_h$ symmetry, falling in the commonly referred to category of *Platonic solids*. Consequently, we set to build a *Platonic model* of metal-halide peroskites consisting of four regular corner-sharing octahedra in the unit cell and no cation.

### 5.1.2 The construction

Given that the construction of the Platonic model for the unit cell of a perovskite structure is not dependent on the exact chemical components, the system will be referred to generally as $ABX_3$ and the octahedra as $BX_6$. The cation A is absent from the representations in this model, the atom B occupies the centre of the $BX_6$ octahedron and the atoms X occupy the corners. Furthermore, for the purpose of this construction the

four octahedra in the unit cell will be labelled as $O_1$-$O_4$ as indicated in Figure 5.2 (c). The corners of each octahedron are labelled as $X_i^j$, with the superscript $j$ identifying the octahedron and the subscript $i$ identifying a corner of the octahedron as shown in Figure 5.2 (a). The centre of each octahedron are labelled as $B^j$, with the subscript $j$ identifying the octahedron.

At the start of the construction we set out three initial constraints which are based at the experimental observations discussed in the previous sections:

- The $BX_6$ octahedra are regular. All B-X distances are equal to a given parameter $d$, and all diagonals are perpendicular to one another.
- The final structure must be at least orthorhombic. The lattice vectors of the unit cell must be orthogonal to one another, but the lattice parameters must not necessarily be equal.
- The octahedra remain corner sharing upon rotation.

**Construction steps**

1. **Octahedron $O_1$**

   We start by defining the octahedron $O_1$ and the system of reference in which we will build our unit cell as shown in Figure 5.2a. The octahedron $O_1$ has the centre at the origin of the reference system and the corners at the following coordinates: $(1,1,0)d/\sqrt{2}$, $(-1,-1,0)d/\sqrt{2}$, $(-1,1,0)d/\sqrt{2}$, $(1,-1,0)d/\sqrt{2}$, $(0,0,1)d$ and $(0,0,-1)d$.

   In order to generate the most general structural model for the unit cell we perform a rotation of $O_1$ according to the three Euler angles $\psi$, $\theta$ and $\phi$. These angles define a a sequence of spin, tilt and precession around the $c$ axis. The tilt $\theta$ is performed via a rotation around $a$, as illustrated in Figure 5.2b. Mathematically, this can be expressed by the matrix defining the rotation of the octahedron [215]:

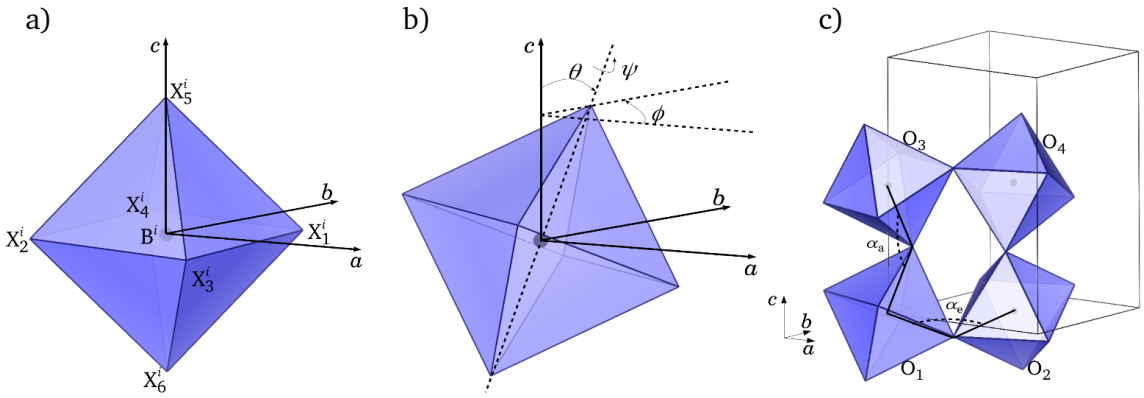


Figure 5.2: a) The straight Platonic octahedron. The centre and corners of the octahedron are labelled on the figure. b) The rotated Platonic octahedron. The rotational angles $\psi$, $\theta$ and $\phi$ are labelled on the figure. c) Polyhedral model of the orthorhombic unit cell built as described by the Platonic model. The four octahedra of the are labelled $O_1$ - $O_4$.

$$\begin{pmatrix} \cos\psi\cos\phi - \cos\theta\sin\phi\sin\psi & -\sin\psi\cos\phi - \cos\theta\sin\phi\cos\psi & \sin\theta\sin\phi \\ \cos\psi\sin\phi + \cos\theta\cos\phi\sin\psi & -\sin\psi\sin\phi + \cos\theta\cos\phi\cos\psi & -\sin\theta\cos\phi \\ \sin\theta\sin\psi & \sin\theta\cos\psi & \cos\theta \end{pmatrix}.$$

By applying this rotation to the initial coordinates of $O_1$ we obtain the positions of the corners $X_i^1$ $(i = 1, ..., 6)$ in their final orientation. These new coordinates are used to locate the centres and orientation of the remaining octahedra.

The centres of the remaining three octahedra $O_2$ - $O_4$ are denoted by $(x, y, 0)$, $(0, 0, z)$ and $(x, y, z)$ respectively. The coordinates $x$, $y$ and $z$ must be different from zero and they will be determined by imposing the constraints listed at the beginning of this section. The lattice parameters are expressed in terms of the centres of the octahedra as $a = 2x$, $b = 2y$ and $c = 2z$. The coordinates of each corner $X_i^j$ are referred to as $(x_i^j, y_i^j, z_i^j)$.

2. **Octahedron $O_2$**

In order to the determine the centre $(x, y, 0)$ of the octahedron $O_2$ we request that the distance between the centre $(B^j)$ of each octahedron and each corner is $d$ in all cases along with the following additional observations.

- $O_1$ shares the corner $X_1^1 = X_2^2$ with $O_2$:

$$\mathrm{B}^1\mathrm{X}_1^1 = \mathrm{B}^2\mathrm{X}_1^1 : \quad x^2 + y^2 - 2xx_1^1 - 2yy_1^1 = 0. \tag{5.1}$$

- $\mathrm{O}_2$ shares the corner $\mathrm{X}_3^2 = \mathrm{X}_4^{1'}$ with $\mathrm{O}_{1'}$, the periodic replica of $\mathrm{O}_1$ along the $b$ axis. The coordinates of $\mathrm{X}_4^{1'}$ can be expressed in terms of the coordinates of $\mathrm{X}_4^1$ as $(x_4^1, y_4^1 + 2y, z_4^1)$.

$$\mathrm{B}^{1'}\mathrm{X}_4^{1'} = \mathrm{B}^2\mathrm{X}_4^{1'} : \quad x^2 + y^2 - 2xx_4^1 + 2yy_4^1 = 0. \tag{5.2}$$

- $\mathrm{O}_2$ must be a regular octahedron, with its diagonals perpendicular to one another.

$$\mathrm{B}^2\mathrm{X}_4^{1'} \perp \mathrm{B}^2\mathrm{X}_1^1 : \quad x^2 - y^2 - x(x_4^1 + x_1^1) + y(y_1^1 - y_4^1) = 0. \tag{5.3}$$

After we express all coordinates $x_i^j$ appearing in Eqs. (5.1), (5.2) and (5.3) in terms of the Euler angles $\psi$, $\theta$ and $\phi$ we obtain that the above relations are verified simultaneously only if the spinning angle vanishes: $\psi = 0$. In this case, the coordinates of the centre of $\mathrm{O}_2$ are given by $x = d\sqrt{2}\cos\phi$ and $y = d\sqrt{2}\cos\theta\cos\phi$. The coordinates of the corners of the octahedron $\mathrm{O}_2$ are determined using the condition that the octahedron must be regular and that its corners are shared with neighbouring octahedra:

$$\begin{array}{lll} \mathrm{X}_1^2\colon (2x - x_1^1, 2y - y_1^1, -z_1^1), & \mathrm{X}_2^2\colon (x_1^1, y_1^1, z_1^1), & \mathrm{X}_3^2\colon (x_4^1, y_4^1 + 2y, z_4^1), \\ \mathrm{X}_4^2\colon (2x - x_4^1, -y_4^1, -z_4^1), & \mathrm{X}_5^2\colon (x + p, y + q, r), & \mathrm{X}_6^2\colon (x - p, y - q, -r). \end{array}$$

where the auxiliary variables $p$, $q$, $r$ are given by:

$$\begin{aligned} p &= \frac{(y_4^1 + y)z_1^1 - z_4^1(y_1^1 - y)}{d}, \\ q &= \frac{(x_1^1 - x)z_4^1 - z_1^1(x_4^1 - x)}{d}, \\ r &= \frac{(x_4^1 - x)(y_1^1 - y) - (y_4^1 + y)(x_1^1 - x)}{d}. \end{aligned}$$

From the location of $\mathrm{O}_2$ we can also determine the lattice parameters as: $a = 2d\sqrt{2}\cos\phi$ and $b = 2d\sqrt{2}\cos\theta\cos\phi$.

3. **Octahedron $O_3$ and $O_4$**

   Octahedron $O_3$ shares the corner $X_5^1$ =$X_6^3$ with $O_1$. From this condition we can readily deduce the position of $B^3$, $(0, 0, 2d\cos\theta)$ and the lattice parameter $c = 4d\cos\theta$. The position of $B^4$ is further given by $(d\sqrt{2}\cos\phi, d\sqrt{2}\cos\theta\cos\phi, 4d\cos\theta)$.

   The positions of the corners of $O_3$ and $O_4$ are obtained by taking into account the regularity of the octahedra, and by observing the corners shared between $O_1$ - $O_3$, $O_2$ - $O_4$ and $O_3$ - $O_4$.

**Summary of the construction**

In general, for a system of four identical, regular octahedra in the unit cell which can rotate freely we can have 12 degrees of freedom, 3 angular degrees of freedom for each. By imposing the constraints that the unit cell must be orthorhombic, that the system must be periodic, and that the octahedra must be regular and corner sharing, we reduce the number of angular parameters to two, $\theta$ and $\phi$.

Intuitively , we distinguish two particular cases for the angles $\theta$ and $\phi$ which can immediately be related to XRD data on $MAPbI_3$ [146] or to the classification of Glazer [125].

If $\theta = 0$ the lattice parameters $a$ and $b$ are equal in magnitude and $c = a\sqrt{2}$. In this case, the pair of parameters (0,$\phi$) may define two possible structures, as shown in Figure 5.3. When $\theta = 0$ the octahedra rotate only around the $c$ axis. However, the pairs of octahedra ($O_1$, $O_2$) and ($O_3$, $O_4$) can rotate either in our out of phase as shown in the diagram in Figure 5.3. The in-phase case can be associated with the $a^0a^0c^+$ case in the Glazer notation [120]. The structure obtained in this case is a supercell of the tilt system #21 shown in Ref. [125]. The out-of-phase case is the $a^0a^0c^-$ in the Glazer notation [125] and corresponds to the tilt system #22.

In the case of $\theta = \phi = 0$ we obtain a perovskite unit cell in which the octahedra do

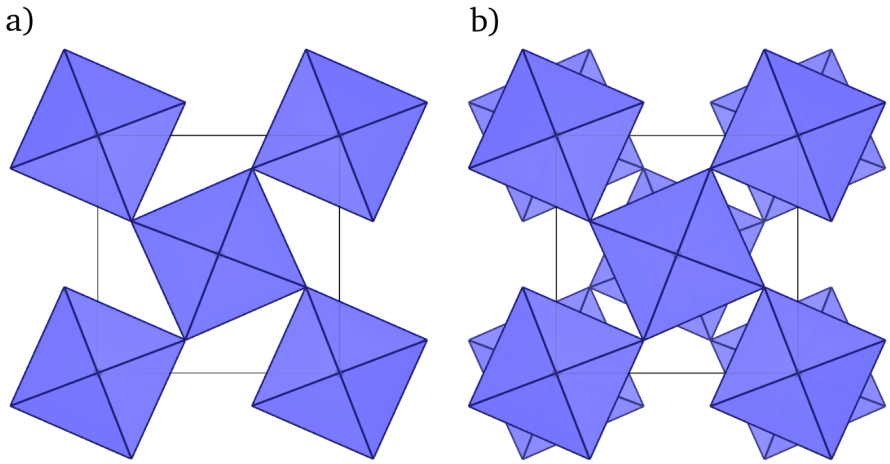


Figure 5.3: Model perovskite structures obtained from the Platonic model in the case of $\theta = 0$ and $\phi \neq 0$. The diagrams depict the two possible structures that can be constructed in this case: in phase (a) and out of phase (b) tilting around the $c$ axis. Both structures are shown as viewed along the $c$ axis.

not exhibit any tilting ($a^0a^0a^0$). In fact, the unit cell formed by four such *straight* octahedra is a supercell of the simplest, most symmetric cubic perovskite structure [120, 125].

### 5.1.3 The metal-halide-metal bond angles in the Platonic model

The two independent angular parameters $\theta$ and $\phi$ and the fixed bond length $d$ are a system of spherical coordinates which is clamped on the crystallographic unit cell. It is more convenient to change this system of coordinates to variables which are not dependent of the choice of unit cell but rather intrinsic parameters of the structure. Therefore, we express $\theta$ and $\psi$ in terms of the metal-halide-metal bond angles $\alpha_a$ and $\alpha_e$.

The equatorial bond angle, $\alpha_e$, is defined, for example as the $B^1X^1_1B^2$ angle. Similarly, the apical bond angle, $\alpha_a$, corresponds to the $B^1X^1_5B^3$ angle. Using the expression of the coordinates of the centres and corners of the octahedra $O_1$, $O_2$ and $O_3$ we find:

$$\begin{aligned} \cos\alpha_a &= 1-2\cos^2\theta, \\ \cos\alpha_e &= 1-\cos^2\phi(1+\cos^2\theta). \end{aligned} \tag{5.4}$$

The structure of the Platonic model is completely defined once we specify the values of two angles and the B-X bond length. This property simplifies considerably the task of rationalising the physics of metal-organic halide perovskites. Furthermore the model illustrated here carries general validity and it can easily be adapted to describe other idealised perovskite structures. In the following section, we will discuss the role of the two inequivalent bond angles in the electronic and optical properties of these ideal perovskite structures.

## 5.2 Electronic structure and the metal-halide metal bond angles

In this section we perform a series of electronic structure calculations on a large set of model structures with different values of $\alpha_a$ and $\alpha_e$ in the absence of the cation for Pb-I systems. The goal of these calculations is to demonstrate the structurally dependent electronic properties of three-dimensional lead-iodide perovskites.

To this end we construct a set of structures using the Platonic model described in the previous section by uniformly varying the parameters $\theta$ and $\phi$. Consequently, we obtain a set of structures for which the angles $\alpha_a$ and $\alpha_e$ vary uniformly. For definiteness, we set the Pb-I bond length to the average value measured in Ref. [146] of 3.18 Å. The effect of the variation of the Pb-I bond length is discussed separately in the next section. For each structure we perform scalar and fully relativistic DFT calculations.

### 5.2.1 Band gaps

#### Scalar relativistic calculations

In Figure 5.4 we show the band gap of the Platonic model calculated using DFT as a function of the apical and equatorial bond angles $\alpha_a$ and $\alpha_e$ without including the

relativistic spin-orbit coupling effects. Each point on the map shown in Figure 5.4 represents a perovskite structure identified by the two angles $\alpha_a$ and $\alpha_e$, and the colour of the point indicates the calculated band gap as it can be read on the colour scale.

The incomplete coverage of the parameter space in Figure 5.4 reflects the fact that only certain pairs of apical and equatorial angles are compatible with the corner-sharing connectivity. The relations shown in Eq. (5.4) combined with the condition that $\cos^2\phi \leq 1$ it follows that $\cos(\pi-\alpha_a) \geq 2\cos(\pi-\alpha_e)-1$. For all angles considered in Figure 5.4 the expansion of this inequality to first order is accurate within 3% and reads $\pi-\alpha \geq (\pi-\alpha_a)/\sqrt{2}$. As a result, the Platonic model does not admit solutions with continuous corner-sharing connectivity in a region of the map bound by a straight line of slope $1/\sqrt{2}$, as shown Figure 5.4. The extremal parameters of this map are, on the one side $\alpha_a = \alpha_e = 180°$ (bottom left corner). On the other side we have $\alpha_a = \alpha_e = 120°$ (top right corner), which we have chosen by considering

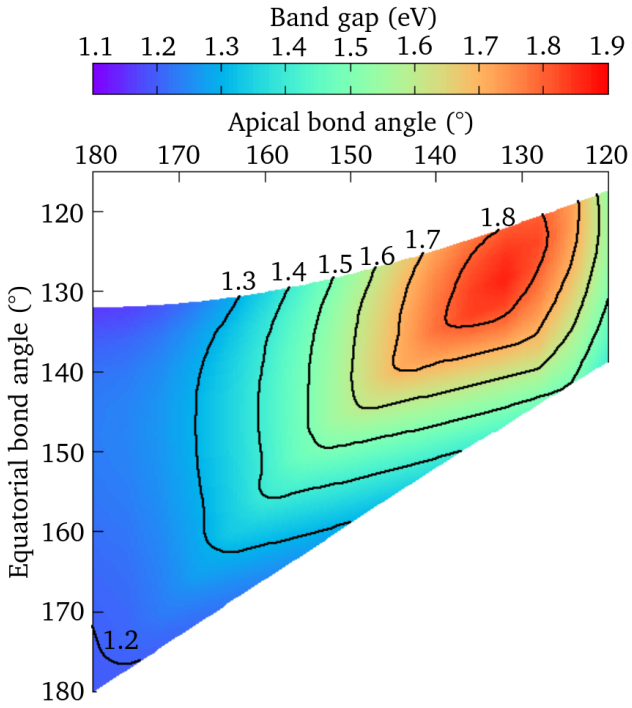


Figure 5.4: Two dimensional map of the variation of the band gap with respect to the apical and equatorial bond angles of ideal perovskite structures in the absence of the cation, obtained from the Platonic model. The calculated band gaps do not include the relativistic spin orbit coupling.

a limiting structure where the shortest distance between iodine atoms belonging to different octahedra matches the $I_2$ bond length ($\alpha_a = 0$ and $\alpha_e = 120°$).

The variation of the angular coordinates in Figure 5.4 clearly induces a substantial modulation of the band gap, from the top of the mid-infrared (1.1 eV) to the beginning of the visible spectrum (1.9 eV). This trend is in line with earlier calculations of simpler two-dimensional Sn-I perovskites for solution-processable electronics [199].

The qualitative trend shown in Figure 5.4 can be interpreted using elementary tight-binding arguments. For definiteness, we focus on the bottom of the conduction band at Γ, which is most affected by bond angles. In the case of $\alpha_a = \alpha_e = 180°$ there are three degenerate electronic states derived from the $6p$ orbitals of Pb (without considering spin-orbit coupling at this initial stage), as shown in the wave function plot in Figure 5.5a. As observed qualitatively from the wave function plots in Figure 5.5a, the energy of these states results mainly from $pp\sigma$ bonding integrals since all the Pb-I bonds are collinear [216]. By moving away from the bottom left corner of the band gap map the degeneracy at the bottom of the conduction band is lifted. In particular, from the band structure comparison shown in Figure 5.5b we can see that the lower conduction band is lifted by 0.5 eV. At the Γ point, this energy state corresponds to the $p$ orbital of Pb along the apical direction of the octahedron (Figure 5.5b). As it can be seen the $p$ orbital is no longer oriented along the Pb-I bond. In this case the bond integrals acquire components weighted by the bond angle $\alpha_a$, tending to raise the energy levels. The same can be observed for the second and third lowest conduction band states, where the bond integrals are weighted by the bond angle $\alpha_e < \alpha_a$ and cause the energy of the state to increase even further. Intuitively, the increase in the band gap with the decrease in the Pb-I-Pb bond angles can be seen as a competition between the energy states correspondent to bond integrals weighted by the bond angles $\alpha_e$ or $\alpha_a$. Therefore, the we can expect that the band gap will be dictated by the maximum of the two Pb-I-Pb bond angles in the unit cell.

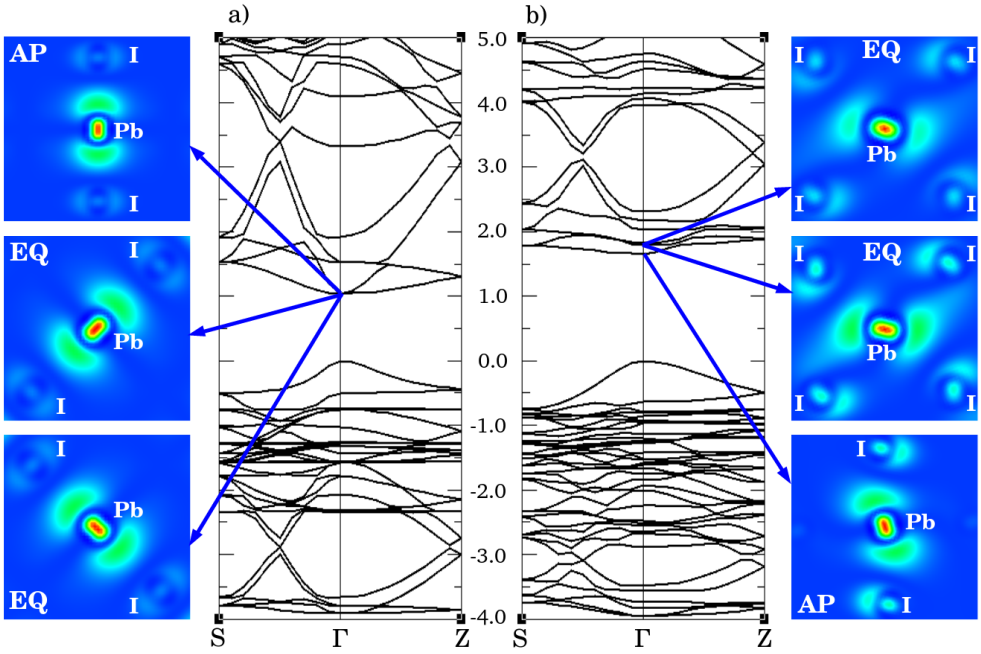


Figure 5.5: Comparison between the band structures obtained for Platonic model structures in the $\alpha_a = \alpha_e = 180°$ (left) and $\alpha_a = 140°$, $\alpha_e = 131°$ (right) cases. The blue arrows connect the state in the conduction band at the Γ point with the plot of the corresponding wave function plot. The wave functions are represented as surface plots by cutting through the apical (AP) or equatorial (EQ) plane of one of the octahedra in the unit cell. The corresponding positions for each atom are directly labelled on the surface plots. The energy scale in the band structure plots is in units of eV.

### Fully relativistic calculations including spin-orbit coupling

The relation between band gap and bond angles holds unchanged when considering fully relativistic calculations including spin-orbit coupling. As shown in Figure 5.6, the relativistic effects induce a large but slowly varying red-shift of the band gap of 0.8 to 1.1 eV for the majority of this family of structures. Notably, the region beyond $\sim 165°$ on the bottom left corner should not be considered as reliable in the fully relativistic case, since the DFT band gap closes in this range, causing an unphysical swap of the electronic states at the band edges. The band gap maps calculated with (Figure 5.4) and without (Figure 5.6a) spin-orbit coupling exhibit different isoline shapes due to the slight modulation of the spin-orbit correction with the Pb-I-Pb bond angle.

A similar rationale can be made for the band gap variation as in the scalar relativistic case. In Figure 5.7 we show the comparison of the band structures of perovskite model

structures with $\alpha_a = 180°$, $\alpha_e = 140°$ and $\alpha_a = 140°$, $\alpha_e = 131°$, along with the surface plots of electronic wave function corresponding to the first, second and third lowest energy electronic states. Similar to the scalar relativistic case, upon tilting in the apical plane, the Pb-*p* electronic wave function corresponding to the lowest conduction band energy is no longer directed along the direction of the bond, causing the corresponding energy to increase by up to 0.5 eV. A comparative analysis of Figure 5.5 and 5.7 shows that the mechanism of band gap variation with the Pb-I-Pb bond angles is similar in both the scalar in fully relativistic pictures.

Ref. [194] reported a similar study of the scalar relativistic and fully relativistic band gap with the tilting angle, by building a structural model considering only one parameter in the description of the perovskite structure. The structural model presented in Ref. [194] represents the particular case of $\alpha_a = 180°$, $\alpha_e < 180°$ of our Platonic model. Accordingly, Ref. [194] concludes that the scalar relativistic band gap is insensitive to the variations of the single angular parameter, while the spin-orbit coupling decreases as this parameter increases. Indeed, in can be observed in the maps shown

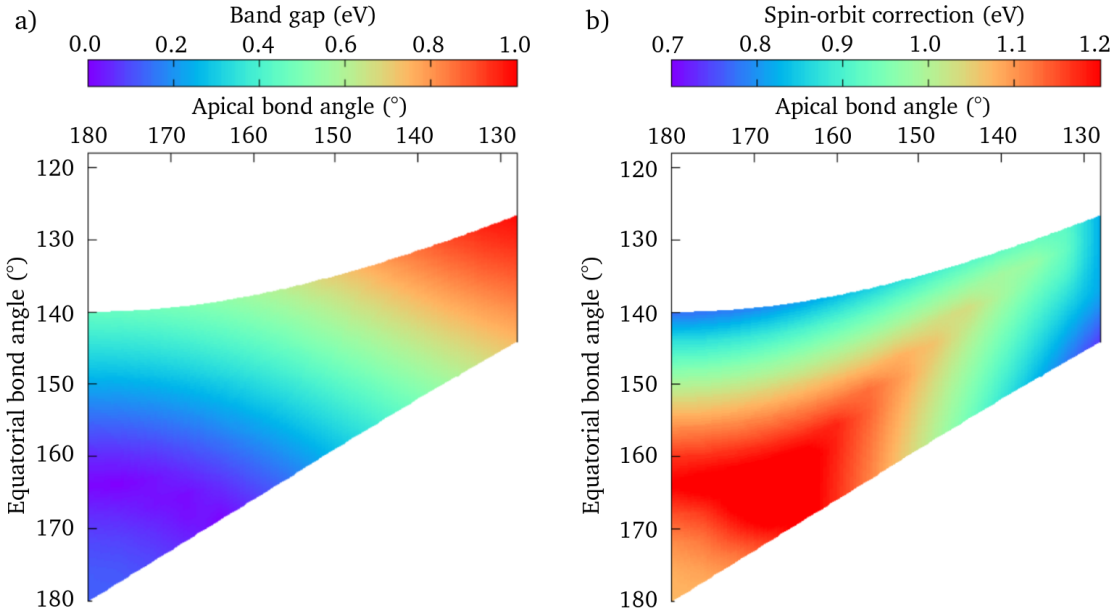


Figure 5.6: Two dimensional map of the variation of the spin-orbit band gap (a) and spin-orbit correction (b) with respect to the apical and equatorial bond angles of ideal perovskite structures in the absence of the cation obtained from the Platonic model.

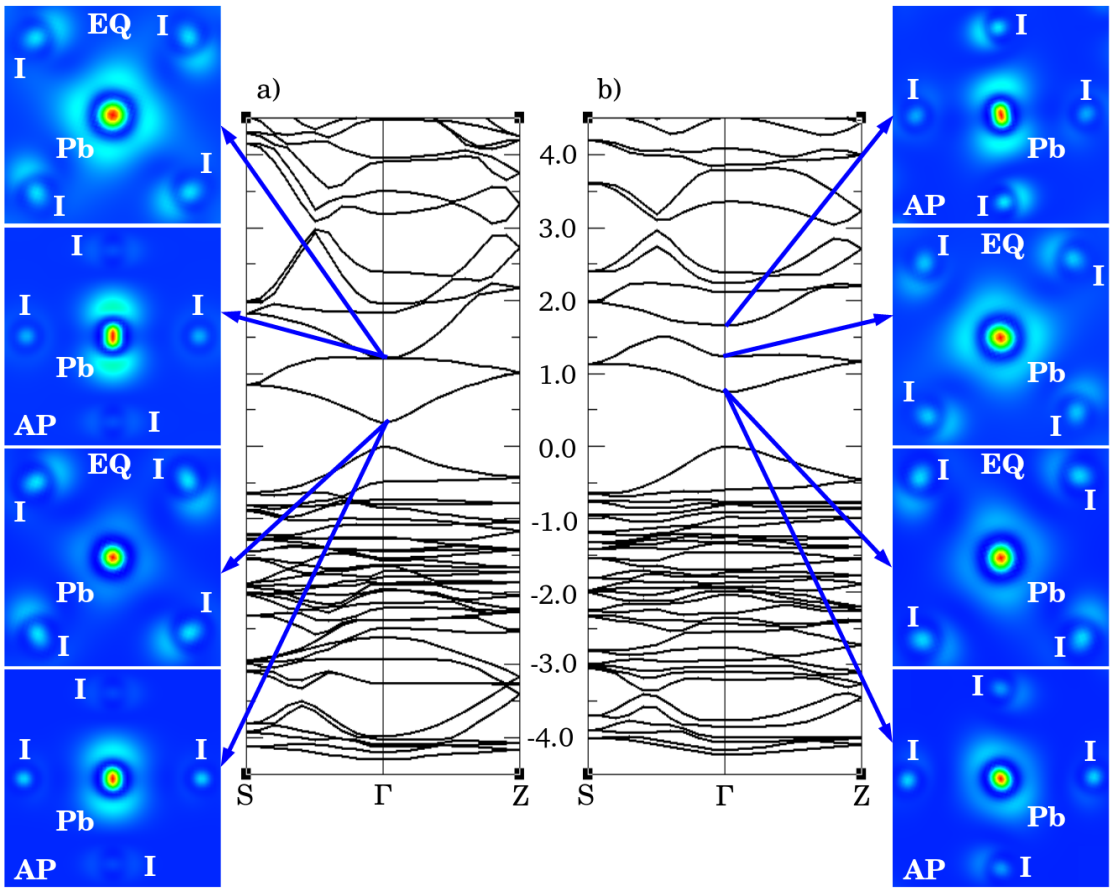


Figure 5.7: Comparison between the band structures obtained for Platonic model structures in the $\alpha_a = 180°$, $\alpha_e = 140°$ (left) and $\alpha_a = 140°$, $\alpha_e = 131°$ (right) cases. The blue arrows connect the state in the conduction band at the Γ point with the plot of the corresponding wave function plot. The wave functions are represented as surface plots by cutting through the apical (AP) or equatorial (EQ) plane of one of the octahedra in the unit cell. The correspondent atoms for each atom are directly labelled on the surface plots. The energy scale in the band structure plots is in units of eV. The calculations are including fully relativistic spin-orbit coupling corrections.

in Figure 5.4 and 5.6b that when $\alpha_a = 180°$, the scalar relativistic band gaps vary by up to 0.1 eV with the parameter $\alpha_e$, while in the fully relativistic case the band gap changes by 0.4 eV when $\alpha_e$ varies from 140° to 180°. While the conclusion of Ref. [194] holds for the case of $\alpha_a = 180°$, this observation is no longer valid for more general values of $\alpha_a$ and $\alpha_e$. In fact, we note that when the apical bond angle decreases from 180° the variation of the scalar relativistic the band gap varies more significantly with the equatorial bond angle. This is in agreement with our observation that the band gap of the lead-iodide perovskite structures are governed by the value of the largest Pb-I-Pb bond angle.

### 5.2.2 Effective masses

Given that the spin-orbit coupling modifies the topology of the band structure, as shown in the previous chapter, we calculate the effective masses for each of the model structure from fully relativistic calculations. We calculate the effective mass tensor using the same procedure described for the case of $CH_3NH_3PbI_3$ in Chapter 4.

Figure 5.8 shows the hole and electron effective masses obtained for the Platonic perovskite model, as a function of $\alpha_a$ and $\alpha_e$ as well as the reduced effective masses. For comparison, in Table 5.1 we show values of the effective masses reported in literature for $CH_3NH_3PbI_3$ and $CsPbI_3$. The values of the hole, electron and reduced effective masses calculated for the model structures are in the same range as the previously reported values listed in Table 5.1. As expected from the variation of the band gap with bond angles, the electron and hole masses decrease when increasing the Pb-I-Pb bond angle. Since the effective masses were obtained from fully relativistic calculations including spin-orbit coupling, we make a similar observation as in the spin-orbit band gaps case. Indeed, also for the effective masses the data shown in the region with bond angles larger than $\sim 165^\circ$ is unreliable.

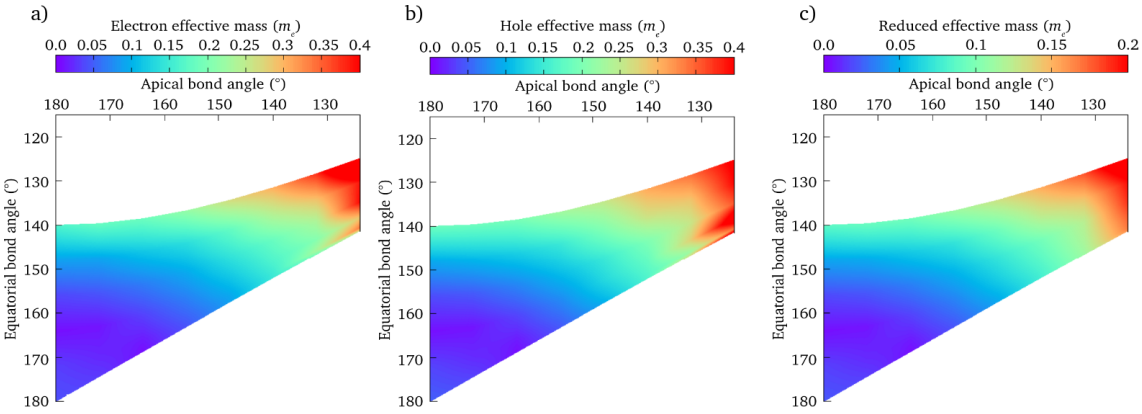


Figure 5.8: Two dimensional map of the variation of electron (a), hole (b) and reduced effective mass (c) with respect to the apical and equatorial bond angles of ideal perovskite structures. The effective masses were calculated via the finite difference method using the eigenvalues calculated including fully relativistic spin-orbit correction.

| | Holes | Electrons | Reduced |
|---|---|---|---|
| $CsPbI_3$ (cubic) | 0.12 [186] | | |
| $CH_3NH_3PbI_3$ (cubic) | 0.29 [187] | 0.23 [187] | |
| $CH_3NH_3PbI_3$ (orthorhombic) | 0.28 [191]<br>0.25 [191] | 0.19 [191]<br>0.19 [191] | 0.10 [191]<br>0.11 [191] |

Table 5.1: Calculated effective masses in atomic units reported in literature. The first three rows shows effective masses obtained from DFT calculations including spin-orbit coupling in Ref. [186, 187, 191] and the last row shows the effective masses obtained from *GW* calculations including spin-orbit coupling, shown in Ref [191]. All reported values are in atomic units

### 5.2.3 Excitons

#### The Wannier exciton model

Optical absorption experiments on $CH_3NH_3PbI_3$ at low temperature highlight a strong excitonic feature [164–166, 169] associated with a weakly bound exciton (Refs. [164–166, 169] report excitonic binding energies of 40-55 meV and Ref. [173] obtained an exciton binding energy of 16 meV). Given this data, we can estimate the excitonic effect of these materials by the Wannier-Mott model.

In the Wannier-Mott model the exciton is assumed to be localised over distances of the same order or larger than the lattice spacing of the crystal [171]. In this assumption, the dielectric screening between the electron and hole can be approximated by the dielectric constant of the material, $\varepsilon_0$, and the Schrödinger equation for the electron-hole pair can be written as [171]:

$$\Big[-\frac{1}{2m_c}\nabla^2_{\mathbf{r}_e}-\frac{1}{2m_v}\nabla^2_{\mathbf{r}_h}-\frac{1}{\varepsilon_0|\mathbf{r}_e-\mathbf{r}_h|}\Big]\Phi(\mathbf{r}_e,\mathbf{r}_h)=E\ \Phi(\mathbf{r}_e,\mathbf{r}_h). \tag{5.5}$$

where $m_e$ and $m_h$ are the electron and hole effective masses, $\mathbf{r}_e$ and $\mathbf{r}_h$ are the positions of the electron and hole, and $\Phi(\mathbf{r}_e,\mathbf{r}_h)$ is the excitonic wave function corresponding to the energy $E$ [171]. If we change the variables $\mathbf{r}_e$ and $\mathbf{r}_h$ to the position of centre of mass, $\mathbf{R}=(m_e\mathbf{r}_e+m_h\mathbf{r}_h)/M$ and the relative position $\mathbf{r}=\mathbf{r}_e-\mathbf{r}_h$ then Eq. 5.5 becomes [171]:

$$\Big[-\frac{1}{2M}\nabla^2_{\mathbf{R}}-\frac{1}{2\mu}\nabla^2_{\mathbf{r}}-\frac{1}{\varepsilon_0 r}\Big]\Phi(\mathbf{R},\mathbf{r})=E\ \Phi(\mathbf{R},\mathbf{r}). \tag{5.6}$$

where $M = m_h + m_e$ and $\mu = m_e m_h/(m_e + m_h)$ are the total and the reduced mass of the exciton. If we rewrite the total excitonic wave function as $\Phi(\mathbf{R},\mathbf{r}) = \Psi(\mathbf{R})\psi(\mathbf{r})$ and separate the equations, we obtain the Schrödinger equation in the reference frame tied to the centre of mass of the exciton [171]:

$$\Big[-\frac{1}{2\mu}\nabla_{\mathbf{r}}-\frac{1}{\varepsilon_0 r}\Big]\psi(\mathbf{r})=E_{\mathbf{r}}\psi(\mathbf{r}). \tag{5.7}$$

The solutions Eq. 5.7 are a product of radial wave functions and spherical harmonics, similar to the electronic wave functions of the hydrogen atom, and the corresponding eigenvalues are calculated as $E_n = -\frac{\mu}{2\varepsilon_0^2 n^2}$, with $n$ = 1,2,... (in atomic units). The absolute value of the lowest energy eigenvalue is the exciton binding energy in the Wannier-Mott model, $E_b = \frac{\mu}{2\varepsilon_0^2}$13.6 eV. Similar to the hydrogen atom, we can calculate a Bohr radius for the exciton, $a_0 = \varepsilon_0/\mu$ bohr.

**Exciton binding energies**

In order to calculate the exciton binding energy for the model perovskite structures we use the reduced effective masses shown in Figure 5.8. For the evaluation of $\varepsilon_0$ we perform finite-electric field calculations using the Berry phase technique [217, 218]. In this technique we calculate the macroscopic polarization for a given system with and without applying a finite electric field. The dielectric constant is evaluated as:

$$\varepsilon_0 = 1 + 4\pi\frac{P(\delta\epsilon)-P(0)}{\delta\epsilon}, \tag{5.8}$$

where $\delta\epsilon$ is the finite electric field (in this case we use a finite electric field of 0.001 a.u. directed along the $c$ axis), $P$ is the macroscopic polarization. For this direction of the electric field we show that $\varepsilon_0$ does not depend strongly on the bond angles in the majority of the structures represented on the map, exhibiting values of 5.5-6.0 (Figure 5.9a). We therefore do not evaluate the isotropic average in order to contain

the computational cost and we conclude that the variation of the dielectric constant with respect to the apical and equatorial bond angles is not significant.

Finally, we estimate the excitonic effects as detailed above and obtain excitonic binding energies that do not exceed 80 meV within the family of Platonic structures represented in the map (as shown in Figure 5.9 b). This is in line with previous optical absorption studies reporting exciton binding energies in the range of 16-55 meV [164–166, 169, 173]. Given the small variations of the dielectric constant with the apical and equatorial bond angles, we note that the exciton binding energy shows a similar dependence on the Pb-I-Pb bond angles as the effective mass and the band gap.

While the Wannier-Mott model is a very rough approximation for the calculation of the excitonic properties of materials, our calculations agree well with experimental results, suggesting that this methodology is suited for the case of lead-iodide perovskites. Indeed, in order to confirm and have a more detailed understanding of the excitonic properties of these materials, a more sophisticated analysis based on the Bethe-Salpeter formalism is required [61].

The general trend identified with the aid of the Platonic model suggests that in order

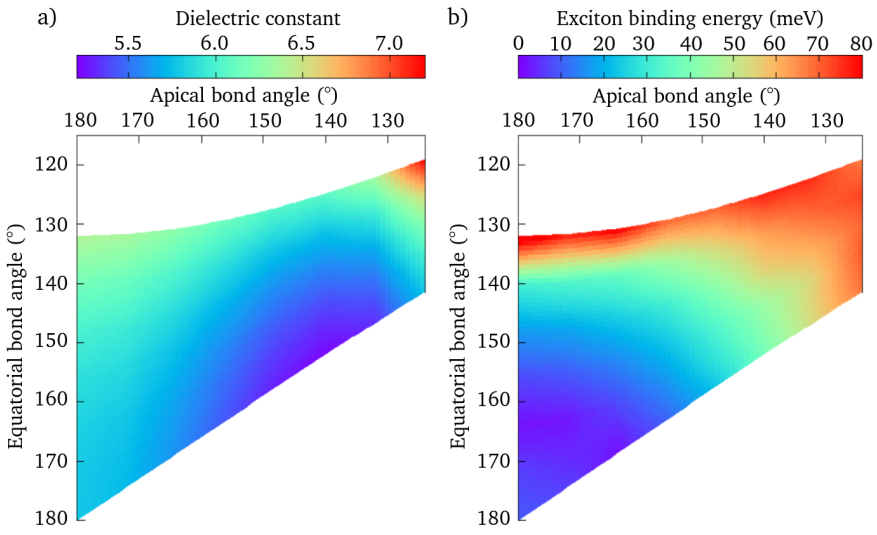


Figure 5.9: Two dimensional map of the variation of the dielectric constant calculated along the *c* direction (a) and exciton binding energy calculated within the Wannier model (b) with respect to the apical and equatorial bond angles of ideal perovskite structures.

to make low-gap perovskites for optimum photovoltaic efficiency we need to engineer structures with minimal octahedral tilt. On the other hand, in order to make large-gap perovskites we need to design structures with a maximum tilt.

## 5.3 Electronic structure and the metal-halide-metal bond length

For completeness we analyse the variation of the band gap with respect to the Pb-I bond length. We calculate the band gap of a cubic perovskite structure for different values of the Pb-I bond length in the absence of the cation. In Figure 5.11 we show the variation of the band gap (calculated without including the spin-orbit coupling correction) with Pb-I bond length varying from 3.1 to 3.2 Å. We show that within this range the band gap varies approximately linearly over a range of 0.3 eV. From the linear fit of the data we estimate the rate of the band gap increase with the bond stretching at 3 eV/Å. This trend is in line with previous studies for Sn-I perovskites [207, 208].

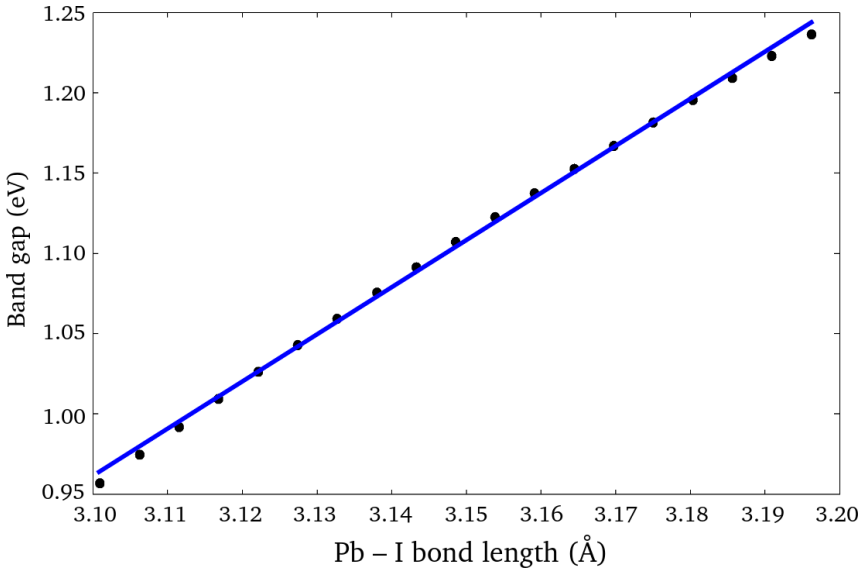


Figure 5.10: Variation of the band gap with bond length. The blue straight line is a linear fit of the calculated data. The fitting parameters are $a = 2.94$ eV/Å and $b = -8.14$ eV (for $f(x) = ax + b$).

As mentioned in Section 7.2 it is expected that real perovskite structures exhibit a combination of octahedral tilting and bond stretching due to the steric interaction between the central cation and the metal-halide network. The separate analyses of the effect of bond angle bond length variation on the band gap of these structure are an attempt to decouple these distortion with the goal of predicting the overall steric effect on the electronic structure. The variation of the bond angle induces an increase of the band gap as the volume of the unit cell decreases due to the tilting of the perfect octahedra. On the other hand, the band gap tends to increase as the volume of the unit cell increases due to a uniform bond stretching. It is therefore expected that the steric interaction of the cation with the metal-halide network will be the result of a competing effect between bond bending and bond stretching. In the following section we will analyse the extent of this effect by proposing a range of new Pb-I perovskites with cations of increasing size at the centre of the cuboctahedral cavity.

## 5.4 Controlling the metal-halide-metal bond angles via the steric size of the cation

The Pb-I-Pb bond angles and Pb-I bond lengths define the volume of the cuboctahedral cavity. For a given Pb-I bond length the largest volume is obtained for Pb-I-Pb angles of 180°. Therefore, it is intuitive that the use of larger cations may lead to values of $\alpha_a$ and $\alpha_e$ closer to straight angles [126]. In search for such cations we perform DFT calculations for existing structures as well as for many hypothetical structures not considered hitherto. We perform full structural optimisations (with variable atomic positions and lattice parameters) and electronic structure calculations including spin-orbit interactions in the presence of the cations. We note at this point that the apical direction in these structures is along the $b$ axis, due to the labelling of the lattice vectors of the starting geometrical configuration, as reported in Ref. [146]. However, the comparison of the structures with the Platonic model is straightforward, since

the angular parameters $\alpha_a$ and $\alpha_e$ are intrinsic to the cell. In order to relate these structures and their properties to the predictions of the Platonic model, we consider the average values of the Pb-I-Pb bond angles and the Pb-I bond length over a crystalline unit cell. These values are used as the coordinates needed for locating each structure on a map such as the one shown in Figure 5.4.

In addition to the previously reported cations: methylammonium ($CH_3NH_3^+$), formamidinium ($CH_2(NH_2)_2^+$), caesium ($Cs^+$) (synthesised) [145, 200] and ammonium ($NH_4^+$) (proposed) [190, 192] we consider four different families of cations generated therefrom. The first family consists of secondary, tertiary and quaternary ammonium cations, namely di-, tri- and tetra-methylammonium. These are large molecules obtained by replacing hydrogen atoms bonded to the N atom with methyl groups. The second family is generated from ammonium by descending the pnictogen column in the periodic table, that is by substituting N for P, As and Sb. Members of this family include phosphonium ($PH_4^+$), arsonium ($AsH_4^+$) and stibonium ($SbH_4^+$). Similarly, for methylammonium analogues we obtain $CH_3PH_3^+$, $CH_3AsH_3^+$ and $CH_3SbH_3^+$. The third family of cations that we consider is obtained by replacing the hydrogen in ammonium by halogen atoms, and possibly N by another pnictogen. In this group analyse the cases of $NF_4^+$, $NCl_4^+$, $PF_4^+$ and $PCl_4^+$. The fourth and final family simply consists of the alkali metals $Li^+$, $Na^+$, $K^+$ and $Rb^+$. In total we consider 21 structures, including 18 hypothetical compounds not reported to date. In order to quantify the steric size of each cation, we use the radius of the sphere which contains 95% of the DFT electron density. This choice ensures that the steric radii of the alkali metals are in agreement with their standard ionic radii [219]. Table 5.2 summarises all the families of cations summarised in this paragraph and their calculated steric radii.

| Cation | Steric radius (Å) | Cation | Steric radius (Å) |
|---|---|---|---|
| $Li^+$ | 0.67 | $SbH_4^+$ | 2.36 |
| $Na^+$ | 0.85 | $CH_3NH_3^+$ | 2.03 |
| $K^+$ | 1.31 | $CH_3PH_3^+$ | 2.38 |
| $Rb^+$ | 1.50 | $CH_3AsH_3^+$ | 2.49 |
| $Cs^+$ | 1.77 | $CH_3SbH_3^+$ | 2.72 |
| $NH_4^+$ | 1.56 | $CH_2N_2H_4^+$ | 2.24 |
| $NCl_4^+$ | 2.72 | $C_2H_6NH_2^+$ | 2.42 |
| $PH_4^+$ | 2.04 | $C_2H_6PH_2^+$ | 2.68 |
| $PF_4^+$ | 2.14 | $C_3H_9NH^+$ | 2.58 |
| $PCl_4^+$ | 2.92 | $C_4H_{12}N^+$ | 2.65 |
| $AsH_4^+$ | 2.14 | | |

Table 5.2: Table summarising the cations proposed for tuning the band gap of lead-iodide perovskites and their calculated steric radii.

### 5.4.1 Structural optimisations

An initial observation of the structural optimisations indicates that for certain cations the octahedra are distorted significantly while for others the octahedra are approximately regular. While it is difficult to distinguish rigorously between “very distorted“ and “less distorted“ structures, the variation of the Pb-I bond length within the unit cell could be a qualitative criterion for this distinction. For each of the relaxed structures we calculate an average Pb-I bond length $d$. Moreover, we can calculate the variation of the bond length $\Delta d$ as the difference between the maximum and the minimum value of the Pb-I bond length within the unit cell. The parameter $\Delta d$ can be thought of as a measure of the match of the relaxed structure to the Platonic model. In principle, if $\Delta d$ is small with respect to $d$, then a comparison between the relaxed structure and the model structure is meaningful. In Figure 5.11 we plot $d$ and $\Delta d$ as an error bar for all the considered structures. The data associated with this picture is given in more detail in Table 5.3.

Figure 5.11 and Table 5.3 indicate that for some of the large cations the three-

| Cation | $d$ (Å) | $d_{max}$ (Å) | $d_{min}$ (Å) | $\Delta d$ (Å) |
|---|---|---|---|---|
| $Li^+$ | 3.16 | 3.20 | 3.13 | 0.07 |
| $Na^+$ | 3.14 | 3.20 | 3.11 | 0.09 |
| $K^+$ | 3.15 | 3.16 | 3.15 | 0.01 |
| $Rb^+$ | 3.14 | 3.15 | 3.13 | 0.02 |
| $Cs^+$ | 3.13 | 3.14 | 3.12 | 0.02 |
| $NH_4^+$ | 3.13 | 3.14 | 3.13 | 0.01 |
| $NCl_4^+$ | 3.17 | 3.24 | 3.09 | 0.15 |
| $PH_4^+$ | 3.13 | 3.16 | 3.11 | 0.05 |
| $PF_4^+$ | 3.20 | 3.35 | 3.09 | 0.26 |
| $PCl_4^+$ | 3.30 | 3.63 | 3.03 | 0.60 |
| $AsH_4^+$ | 3.12 | 3.16 | 3.10 | 0.06 |
| $SbH_4^+$ | 3.12 | 3.16 | 3.09 | 0.07 |
| $CH_3NH_3^+$ | 3.14 | 3.15 | 3.13 | 0.02 |
| $CH_3PH_3^+$ | 3.13 | 3.14 | 3.11 | 0.03 |
| $CH_3AsH_3^+$ | 3.17 | 3.22 | 3.13 | 0.09 |
| $CH_3SbH_3^+$ | 3.16 | 3.23 | 3.11 | 0.12 |
| $CH_2N_2H_4^+$ | 3.15 | 3.23 | 3.06 | 0.17 |
| $C_2H_6NH_2^+$ | 3.15 | 3.19 | 3.11 | 0.08 |
| $C_2H_6PH_2^+$ | 3.18 | 3.26 | 3.12 | 0.14 |
| $C_3H_9NH^+$ | 3.19 | 3.32 | 3.08 | 0.24 |
| $C_4H_{12}N^+$ | 3.30 | 3.69 | 3.02 | 0.67 |

Table 5.3: The average, maximum, minimum and variation of the Pb-I bond length throughout the unit cell for each proposed cation.

dimensional perovskite network is significantly distorted. This is in line with previous studies showing that large molecular cations determine a reorganisation of the three-dimensional perovskite network into a two-dimensional layered structure [199, 220]. In Figure 5.12 we compare the optimised crystal structures of $AsH_4PbI_3$ for which the Pb-I bond length is approximately regular throughout the unit cell ($\Delta d = 0.06$ Å) and $PCl_4PbI_3$, for which the Pb-I bond lengths vary over 0.6 Å. From Figure 5.12a and c we observe that the Pb-I-Pb bond angles become larger due to the larger $PCl_4$ cation. While this is the desired effect, we also observe from Figure 5.12b and d that for $PCl_4$ the structure has the tendency to reorganise into a two-dimensional layered structure while in the case of $AsH_4$ the structure remains three-dimensional. The same

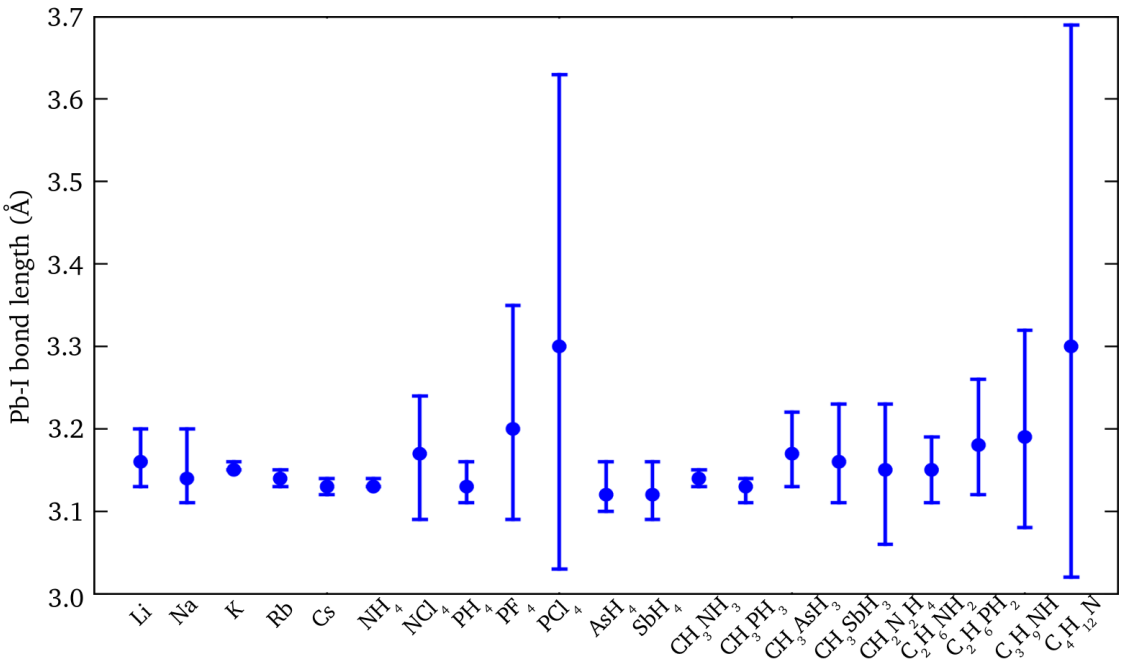


Figure 5.11: Average Pb-I bond length over the relaxed structures obtained for the case of each cation. The error bars mark the minimum and maximum Pb-I bond length in the unit cell. The large error bars appearing for $PCl_4$ and $C_4H_{12}N$ are due to the significant distortions of the $PbI_6$ octahedral network, caused by the steric interaction between the large cations and the inorganic network.

observation can be made for all other cations for which $\Delta d$ is larger than 0.2 Å, such as the tertiary and quaternary methylammonium cations and nitrogen and phosphorus tetrafluorides. As these structures depart substantially from the three-dimensional metal-halide network that we aim to analyse, we do not consider them any further.

For each of the other proposed structures which preserve the three-dimensional metal-halide network we calculate the average apical and equatorial bond angles within the unit cell. In Figure 5.13 we plot the maximum of the equatorial and apical angle for each structure against the calculated steric size of the cation. Figure 5.13 shows that the largest Pb-I-Pb angles correlate strongly with the steric size of the cation (calculated Spearmann correlation of 88%), in line with our initial expectation. The newly proposed structures span a range of angles from 130° to 170°, thereby they should cover a much wider portion of the band gap map than presently possible.

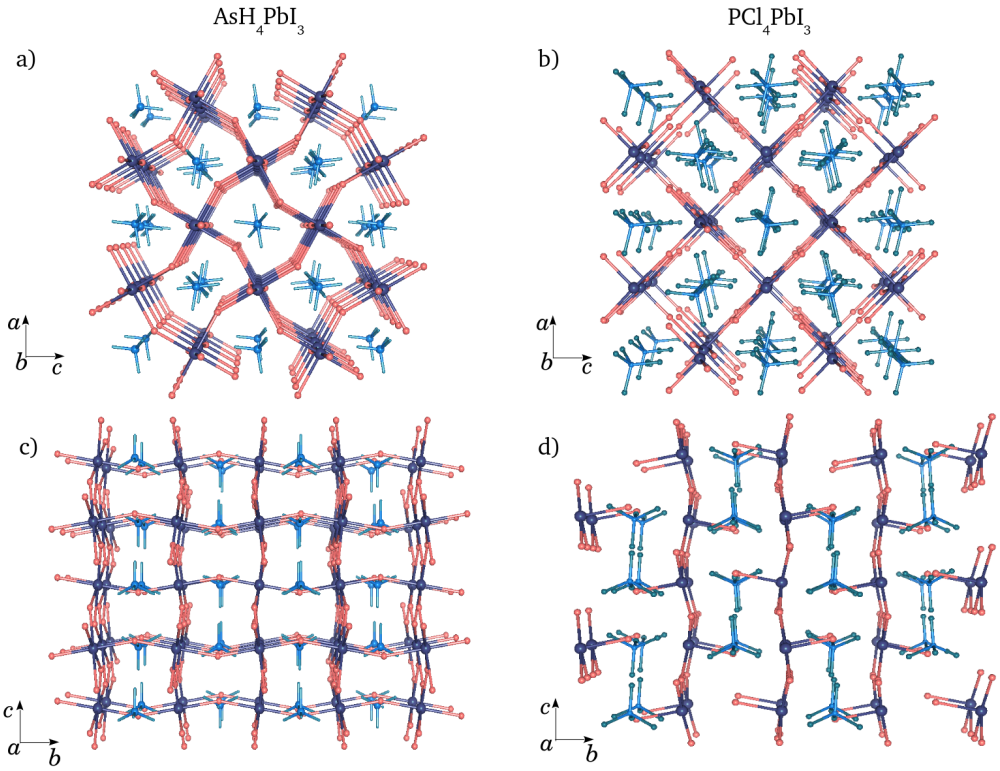


Figure 5.12: Ball and stick models of the proposed lead-iodide perovskites with $AsH_4^+$ (a,c) and $PCl_4^+$ (b,d) cations at the centre. We represent the view along the *b* and *a* axis for both $AsH_4PbI_3$ (a and c respectively) and $PCl_4PbI_3$ (b and d respectively). The red spheres represent the I atoms and the dark blue spheres the Pb atoms. The central cations at the centre of the Pb-I cavity are represented in light blue.

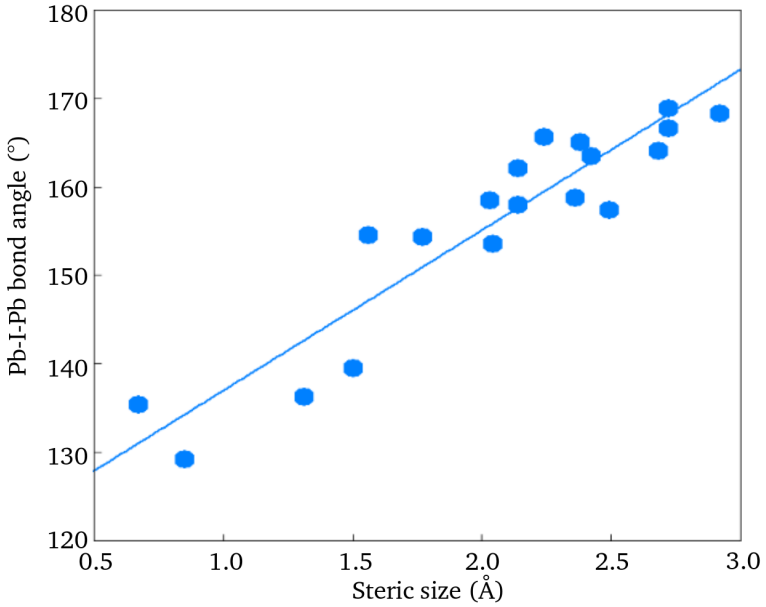


Figure 5.13: Correlation between the maximum bond angle in the Pb-I perovskite network and the steric radius of the cation (blue circles). The straight line is a linear fit of the data with a slope of 18°/Å.

### 5.4.2 Correlation of the band gap with the maximum unit cell bond angle

The structures corresponding to the previously reported cations $CH_3NH_3^+$, $CH_2(NH_2)_2^+$, $Cs^+$ and $NH_4^+$ represented by the white circles on the map in Figure 5.14 cluster around the centre of the map. As it can be seen in Figure 5.14, they do not yield a significant modulation of the band gap. Indeed, for these structures we obtain scalar-relativistic band gaps ranging over only 0.16 eV. Optical absorption spectra reported in literature indicate that the absorption onsets of these compounds should vary over a range of 0.25 eV [27, 137, 145, 200], in agreement with our calculations.

In Figure 5.14 we show that by expanding the choice of cations at the centre of the cuboctahedral cavity, a much wider surface of the map can be explored. Using their average apical and equatorial bond angles as "coordinates" we locate each structure on the band gap map (black circles). The size of each of the circles represents the deviation of the Pb-I bond length from 3.18 Å. As a reference, for the same angular coordinates the difference between the band gap corresponding to the largest and the smallest circle in the figure is 0.2 eV.

In Figure 5.15 we show that the band gaps of all the relaxed structures correlate strongly with the largest Pb-I-Pb bond angle in the unit cell. We calculate a Spearmann correlation coefficient of 91%. This correlation is in agreement with the band gaps predicted by the Platonic model, and it is also exhibited for the band gaps calculated within fully-relativistic DFT calculations including spin-orbit coupling. There is substantial scatter of the data from the linear fit, which can be observed in Figure 5.15. We associate this scatter with the variation of the Pb-I bond lengths in the metal-halide network. In order to verify that the band gap tuning is primarily due to the bond angle variation we calculate the Spearmann correlation coefficient of the band gap with respect to the average bond lengths of the unit cell and obtain a very

weak correlation (9%). This test indicates that the role of bond lengths represents a second-order effect. Finally, the main message of the plot shown in Figure 5.15 is that by suitably choosing the cation, it is possible in principle to fine-tune the band gap almost continuously over a very wide range of photon energy.

In Table 5.4 we summarise the calculated band gaps for all the perovskite structures proposed in this section. We list both the scalar-relativistic and fully-relativistic band gaps. From the data shown in Table 5.4 we observe that the substantial spin-orbit coupling effect appears in all of the proposed cases. In the case of $CH_3NH_3PbI_3$ it has been established that the spin-orbit interaction tends to reduce the scalar-relativistic

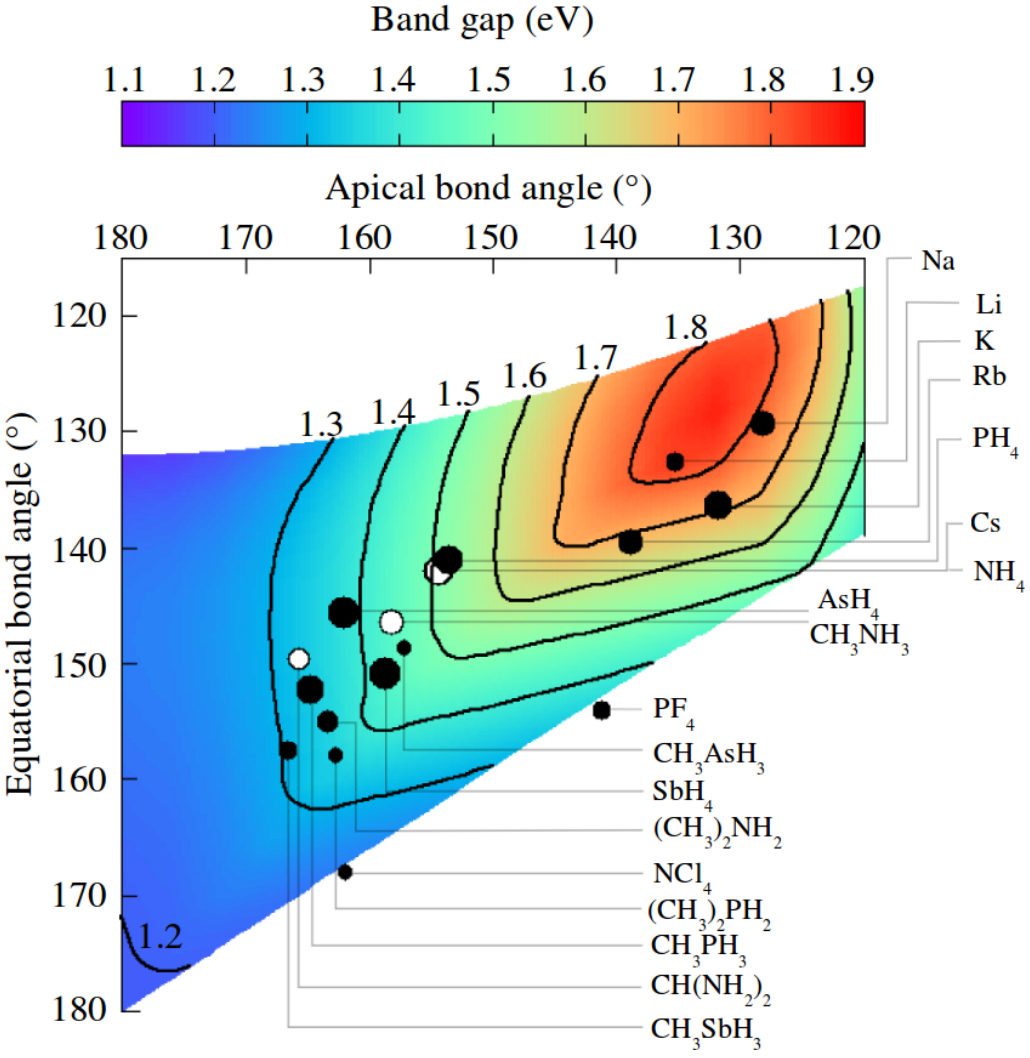


Figure 5.14: Two dimensional map of the scalar relativistic band gaps of the Platonic model structures as a function of the apical and equatorial bond angles completed with the relaxed structures obtained for the new proposed cations.

band gap by approximately 1-1.1 eV [186, 189, 191, 192]. The spin-orbit correction for the band gaps of the perovskites proposed in Table 5.4 ranges from 0.8 to 1.1 eV.

### 5.4.3 Stability against structural distortions

In order to evaluate the practical feasibility of the hypothetical perovskites identified in this chapter we searched for possible dynamical instabilities in one of the structures with the smallest band gap, $AsH_4PbI_3$. This structure is especially interesting since the preparation could proceed in principle in a similar way as for $CH_3NH_3PbI_3$, through the corresponding iodide [221].

We calculate the vibrational density of states of $AsH_4PbI_3$ within density functional perturbation theory [222] using the tetrahedron method [223] and a $q$-point grid of 2×2×2 centred at the Γ point. In Figure 5.16 we can see that the vibrational density of states does not exhibit any soft modes, indicating that the 3D perovskite structure of $AsH_4PbI_3$ considered in this analysis should be stable against distortions.

The analysis of the vibrational spectrum and density of states is a reliable methodol-

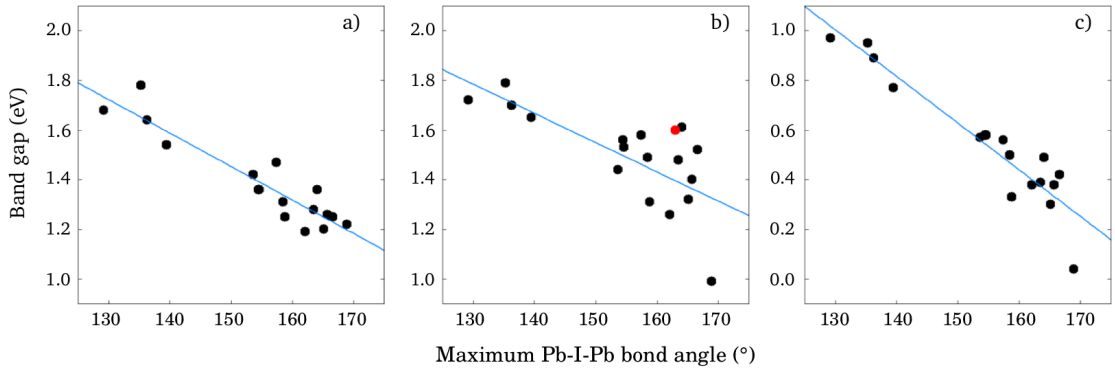


Figure 5.15: a) Correlation of the band gap with the magnitude of the maximum Pb-I-Pb bond angle in the unit cell for the Pb-I structures obtained from the Platonic model. The structures are constructed using the average Pb-I-Pb bond angles and Pb-I bond lengths of the structurally optimise Pb-I perovskites with different cations. b) Correlation of the band gap with the maximum bond angle obtained for the relaxed structures. The red point corresponds to the experimental band gap of $CH_3NH_3PbI_3$ [146] and the experimental maximum Pb-I-Pb bond angle as obtained from the experimental crystal structure reported in Ref. [146]. The band gaps plotted in a) and b) are scalar-relativistic. c) Correlation of the spin-orbit band gap with the Pb-I-Pb bond angles for the relaxed structures. The straight blue lines in all three plots represent linear fits of the plotted data.

ogy for assessing the structural stability of proposed crystal structures. It is, however a very computationally time consuming methodology, particularly for systems with a large number of atoms in the unit cell. In this case, the proposed unit cells contain a minimum of 20 atoms and a maximum of 60 atoms. The evaluation of the vibrational spectrum of all of the proposed structures would be computationally impractical. In addition, these calculations would not provide information about the thermodynamic stability, which represents an even greater challenge from a computational perspective. Given these arguments, in order to assess the stability of the proposed structures we adopt the semi-empirical methodology based on the Goldschmidt tolerance factor [116], described in Chapter 3.

Figure 5.17 shows the tolerance factors derived from our calculated steric sizes as well

| Cation | SR Band gap(eV) | FR Band gap (eV) | Experimental band gap(eV) (optical) |
|---|---|---|---|
| $Li^+$ | 1.79 | 0.95 | |
| $Na^+$ | 1.72 | 0.97 | |
| $K^+$ | 1.70 | 0.89 | |
| $Rb^+$ | 1.65 | 0.77 | |
| $Cs^+$ | 1.56 | 0.58 | 1.72 [200] |
| $NH_4^+$ | 1.53 | 0.58 | |
| $NCl_4^+$ | 0.99 | 0.04 | |
| $PH_4^+$ | 1.44 | 0.57 | |
| $AsH_4^+$ | 1.26 | 0.38 | |
| $SbH_4^+$ | 1.31 | 0.33 | |
| $CH_3NH_3^+$ | 1.49 | 0.50 | 1.6 [169] |
| $CH_3PH_3^+$ | 1.32 | 0.30 | |
| $CH_3AsH_3^+$ | 1.58 | 0.56 | |
| $CH_3SbH_3^+$ | 1.52 | 0.42 | |
| $CH_2N_2H_4^+$ | 1.40 | 0.38 | 1.48 [200] |
| $C_2H_6NH_2^+$ | 1.48 | 0.39 | |
| $C_2H_6PH_2^+$ | 1.61 | 0.49 | |

Table 5.4: The calculated scalar relativistic (SR) and fully relativistic (FR) DFT band gaps for each of the proposed structures as well as experimental optical band gaps for $CH_3NH_3PbI_3$, $CH_2N_2H_4PbI_3$ and $CsPbI_3$ for reference.

as the tolerance factors derived from ionic radii reported in literature where available [14, 219]. The tolerance factors fall within the range of 0.7 to 1.1 for most of the structures proposed in this section. In particular, it appears that all of the structures except $LiPbI_3$, $NaPbI_3$ and $KPbI_3$ should form 3D perovskite structures according to this criterion, while $NH_4^+PbI_3$ and $RbPbI_3$ lie at the edge of instability.

## 5.5 Experimental validation

In order to test our predicted band gap tunability of lead-iodide perovskites with different cations at the centre of the cuboctahedral cavity we requested the expertise of our experimental collaborators at the Department of Physics, University of Oxford, Giles Eperon and Prof. Henry Snaith. They attempted the synthesis of the perovskites based on elemental cations.

Their approach to the demonstration of the band gap tunability was to explore the idea of cation mixtures in lead-iodide perovskites as suggested in Ref. [209]. As proof-

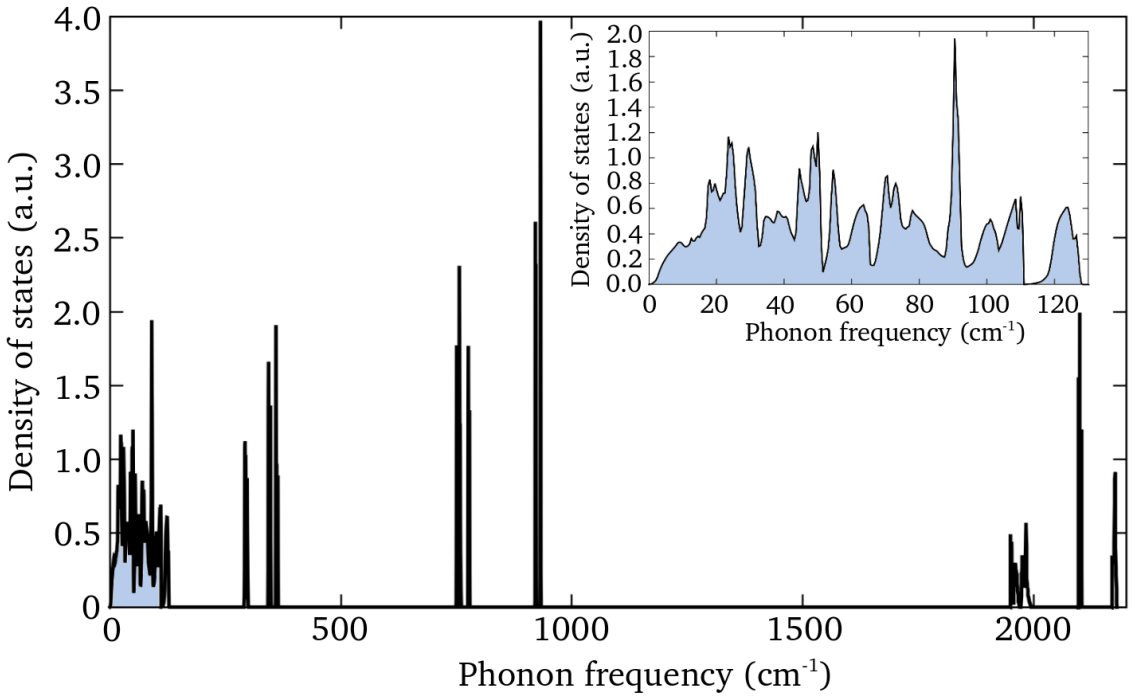


Figure 5.16: Calculated vibrational density of states for $AsH_4PbI_3$. The inset shows a close up of the low-energy region of the spectrum.

of-concept they explored the Rb/Cs mixtures of the type $Rb_xCs_{1-x}PbI_3$ with $x = 0$, $x = 0.1$ and $x = 0.2$. The as-deposited films were annealed at temperatures above 400° C in order to obtain the three-dimensional perovskite phase (this was achieved when the thin film changed colour from yellow to a dark phase upon annealing). A detailed description of the synthesis process is presented in Ref. [158].

Optical characterisation of $Rb_xCs_{1-x}PbI_3$ with $x = 0$, $x = 0.1$ and $x = 0.2$ is shown in Figure 5.18. The optical absorption spectra indicate that the absorption edge blue-shifts from 720 nm to 690 nm in going from Cs to Rb. This result is in good agreement with our calculations, which predict a corresponding blue shift of 40 nm. Moreover, our findings are also in line with other results presented in literature (which appeared while the research presented in this chapter was already completed) where the authors demonstrated band gap tunability via mixing of $CH_3NH_3^+$ and $Cs^+$ [27] or $CH_2(NH_2)_2^+$

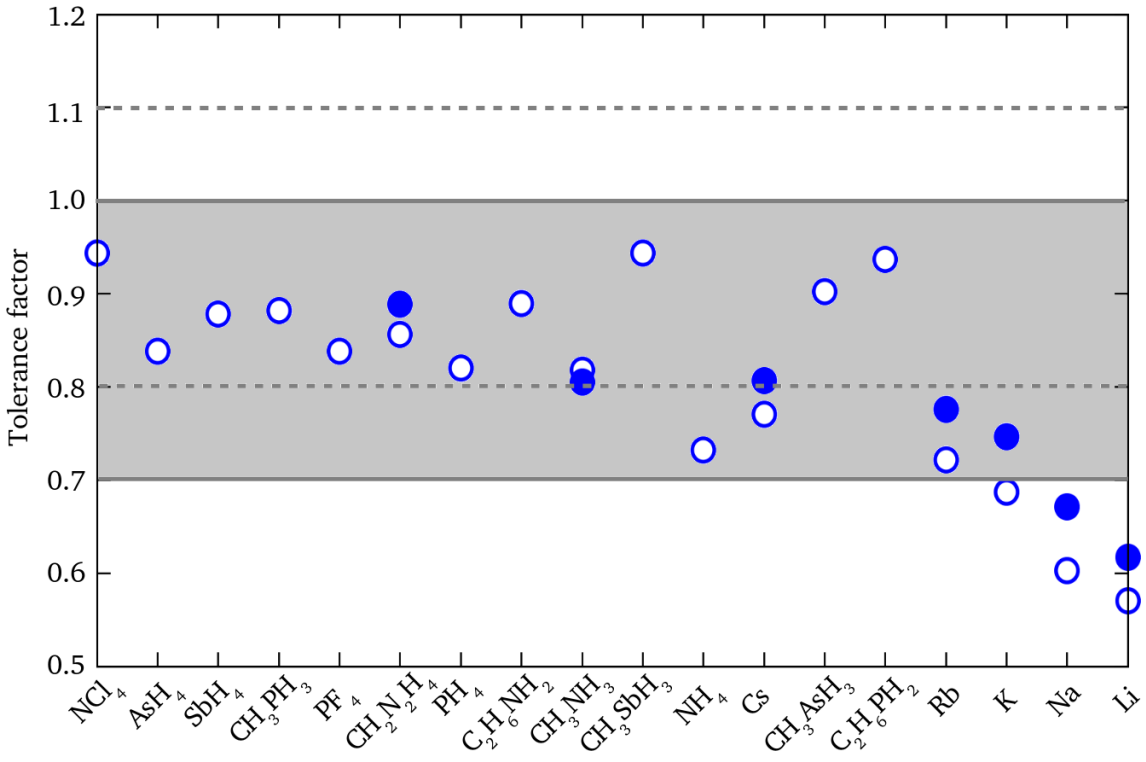


Figure 5.17: Calculated Goldschmidt tolerance factors for all the perovksite structures considered in this chapter. The open circles are obtained using the steric sizes calculated from DFT. The filled circles are the tolerance factors obtained using the ionic radii reported in Ref.[14, 219]. The grey area bound by solid grey lines corresponds to the empirical range proposed in Ref. [116, 127], while the dashed lines correspond to the empirical range proposed in Ref. [14]

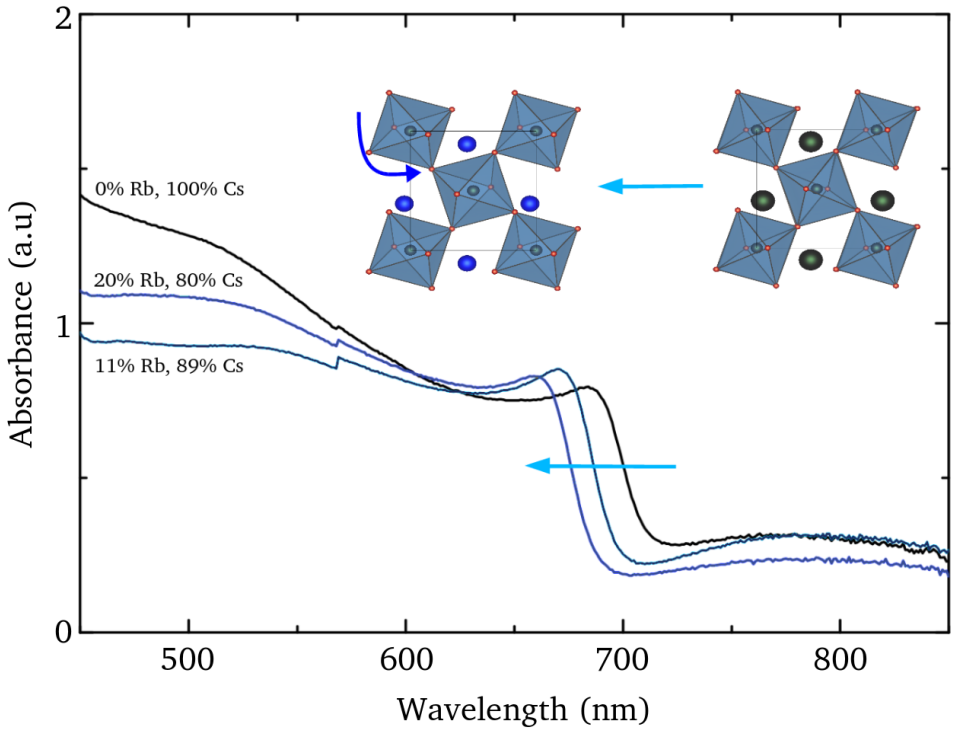


Figure 5.18: Measured absorbance spectra of the $Rb_xCs_{1-x}PbI_3$ perovskite thin films, with $x = 0$, $x = 0.1$, $x = 0.2$. The blue shift corresponds to an increase in band gap, and is assigned to the more pronounced octahedral tilt in the $PbI_3$ network as illustrated in the inset.

and $CH_3NH_3^+$ [137]. Putting together experimental studies in literature, along with the experiments performed by our collaborators, all results confirm the tunability of the band gap via the steric size of the cation over almost half of our predicted range, thereby providing strong support to our theory.

## 5.6 Summary

In this chapter we have constructed a model for metal-halide perovskite structures based on simple geometric arguments. In this model we have shown that an ideal orthorhombic perovskite structure can be uniquely identified by the metal-halide bond length and the apical and equatorial metal-halide-metal bond angle. Moreover, we have shown that the electronic properties of lead-iodide ideal perovskites constructed within this model are strongly dependent on these geometric parameters. In particular, we were able to establish that the fundamental band gap of lead-iodide perovskites

is dictated by the largest Pb-I-Pb bond angle in the unit cell. By changing the cation component of the Pb-I perovskite we have shown that the Pb-I-Pb bond angles in the unit cell are dependent on the size of the central cation. These angles increase with the size of the cation due to the steric interaction of the cation and the Pb-I perovskite network. We proposed 18 cations with increasing steric sizes and performed structural optimisations of the perovskite network for each case. Fourteen of these proposed structures are hypothetical, having not been reported to date to the best of our knowledge. We showed that the band gap of these structures correlates strongly with the size of the central cation and obtained a band gap modulation of almost 1 eV for the entire range of cations.

The construction of the Platonic perovskite structures allows a systematic approach to the study of the interplay of the structural and electronic properties of lead-iodide perovskites identifies a route for the proposal of new hypothetical compounds. The results presented in this chapter provide a useful guide for the design of new perovskite materials for photovoltaic applications by identifying the steric size of the cation as a potential tool for controlling the band gap of novel perovskite materials. Taking these results as a starting point, we can envision the next theoretical steps in the process of design and discovery of new 3D lead-iodide perovskites:

- Identification of the most promising hypothetical structures;
- Analysis of the electronic properties within the *GW* approximation for the hypothetical structures;
- Analysis of the excitonic properties of the hypothetical structures;
- Analysis of the structural and thermodynamic stability of the hypothetical structures, including stability with respect to phase segregation;
- Analysis of the temperature dependent electronic properties and electron-phonon interactions.

Only the first two steps will be addressed in this thesis. In the next chapter we will identify the most promising hypothetical structures proposed in this chapter, perform a more detailed analysis of their electronic properties and obtain their quasiparticle band gaps, using the methodology described in Chapter 4.

# Chapter 6

## Electronic and optical properties of hypothetical $APbI_3$ perovskites: A = $NH_4$, $PH_4$, $AsH_4$, $SbH_4$

Out of the perovskite structures proposed in the previous chapter we identify two hypothetical compounds which could be promising from the point of view of applicability as light absorbers in photovoltaic devices: $AsH_4PbI_3$ and $SbH_4PbI_3$. $AsH_4PbI_3$ is particularly interesting due to the possibility of obtaining the perovskite structure from $AsH_4I$ [221]. These two structures exhibit bond angles which approach 180°, and should have band gaps close to the ideal Shockley-Queisser limit [16], as pointed out in the Chapter 5. Furthermore, due to the tetrahedral symmetry of the cations, potential devices are expected not to suffer from the hysteresis issues which arise in the presence of cations with a net dipole moment.

The predictions made in Chapter 5 are so far based on density functional theory calculations, assuming that the spin-orbit coupling and the quasiparticle corrections cancel out for all the hypothetical structures in the same way as for $CH_3NH_3PbI_3$. It is important to verify that the trend predicted in Chapter 5 holds for higher levels of theory, such as the *GW* method, including spin-orbit coupling. For this reason, we calculate the $G_0W_0$ quasiparticle band gaps for $AsH_4PbI_3$ and $SbH_4PbI_3$. We extend the study to the related cases of $NH_4PbI_3$ and $PH_4PbI_3$, for which the cations have the same

tetrahedral symmetry. This ensemble of structures covers approximately half of the band gap range shown in Figure 5.14. Finally, we apply the SS-*GW* method to all four structures and calculate the corresponding quasiparticle band gap, including self consistency on the eigenvalues.

## 6.1 Density functional theory calculations

### 6.1.1 Crystal structure

In Table 6.1 we show the atomic positions in the irreducible lattice of each of the four hypothetical atomic positions. The unit cells obtained from structural relaxations preserve the *Pnma* symmetry. The positions of the hydrogen atoms are chosen so that they satisfy the symmetry relations of this space group, in the same way it was done for the case of $CH_3NH_3PbI_3$. In Table 6.2 we present the lattice parameters and the volume of the unit cell for each of the four hypothetical perovskites. We

| Atom | $x$ | $y$ | $z$ | Atom | $x$ | $y$ | $z$ |
|---|---|---|---|---|---|---|---|
| | $NH_4PbI_3$ | | | | $PH_4PbI_3$ | | |
| Pb | 0.5000 | 0.0000 | 0.0000 | Pb | 0.5000 | 0.0000 | 0.0000 |
| I(1) | 0.5465 | 0.2500 | 0.9320 | I(1) | 0.5192 | 0.2500 | 0.9170 |
| I(2) | 0.1702 | 0.0320 | 0.1706 | I(2) | 0.1721 | 0.0446 | 0.1774 |
| N | 0.4701 | 0.2500 | 0.5197 | P | 0.4715 | 0.2500 | 0.5148 |
| | $AsH_4PbI_3$ | | | | $SbH_4PbI_3$ | | |
| Pb | 0.5000 | 0.0000 | 0.0000 | Pb | 0.5000 | 0.9986 | 0.0000 |
| I(1) | 0.5045 | 0.2500 | 0.9415 | I(1) | 0.5161 | 0.2500 | 0.9338 |
| I(2) | 0.1790 | 0.0294 | 0.1789 | I(2) | 0.2000 | 0.0404 | 0.2005 |
| As | 0.4890 | 0.2500 | 0.5005 | Sb | 0.4884 | 0.2500 | 0.5044 |

Table 6.1: Atomic positions for the asymmetric unit cell of the four hypothetical perovskites in crystal units.

| | $NH_4PbI_3$ | $PH_4PbI_3$ | $AsH_4PbI_3$ | $SbH_4PbI_3$ |
|---|---|---|---|---|
| $a$ (Å) | 8.358 | 8.145 | 8.379 | 8.462 |
| $b$ (Å) | 12.223 | 12.284 | 12.470 | 12.418 |
| $c$ (Å) | 8.400 | 8.480 | 8.381 | 8.536 |
| Volume(Å$^3$) | 858.14 | 848.45 | 875.70 | 896.97 |

Table 6.2: Lattice parameters obtained from the structural optimisation for each of the four hypothetical perovskites. The initial geometry of the Pb-I network is obtained from the experimental atomic positions and lattice parameters of the $CH_3NH_3PbI_3$ structure in all four cases. The cations are placed in the centre of the cuboctahedral cavity so that they satisfy the symmetry relations of the *Pnma* space group.

observe that the volume of the unit cell increases in order to accommodate a cation of increasing size, in agreement to the results shown in Chapter 5. $NH_4PbI_3$ departs from this assumption slightly in that its unit cell volume is marginally higher than that of $PH_4PbI_3$. $NH_4PbI_3$ also lies very close to the stability limit, according to the analysis of the tolerance factor shown in Figure 5.17. In fact, hydrated $NH_4PbI_3$ is reported to form quasi 1D structures [129, 224]. Moreover, it was speculated that due to the hydrogen interactions associated with the $NH_4^+$, a 3D $NH_4PbI_3$ could be unstable [225]. In that sense, cations such as $PH_4^+$ or larger are desirable, since such interactions are suppressed [225].

The unit cell obtained for $NH_4PbI_3$ from our structural relaxations is orthorhombic and has a 3D perovskite structure similar to the ones analysed in Chapter 5. Given the complexity of the total energy landscape of the perovskite systems, we check the sensitivity of the structural minimisation with respect to the choice of initial configuration. We perform structural optimisations starting from four Pb-I network structures, which can be described using the Pb-I-Pb bond angles $\alpha_a$ and $\alpha_e$ defined in Chapter 5: $(i)$ $\alpha_a = \alpha_e = 0$, (ii) $\alpha_a = 0$ and $\alpha_e \neq 0$, with octahedra tilted in phase along the apical direction, (iii) same as in (ii) but with octahedra tilted out of phase. In Table 6.3 we show the lattice parameters obtained in each structure and the difference in total energy

| | $\alpha_a \neq 180°$ $\alpha_e \neq 180°$ | $\alpha_a = 180°$ $\alpha_e \neq 180°$ | In phase $\alpha_a = 180°$ $\alpha_e \neq 180°$ | Out of phase $\alpha_a = 180°$ $\alpha_e \neq 180°$ |
|---|---|---|---|---|
| $a$ (Å) | 8.358 | 8.794 | 8.299 | 8.341 |
| $b$ (Å) | 12.225 | 11.618 | 12.221 | 12.295 |
| $c$ (Å) | 8.399 | 7.992 | 8.464 | 8.474 |
| Total energy (meV/atom) | 0 | -3 | -0.02 | 6 |

Table 6.3: Lattice parameters obtained from the structural optimisation of $NH_4PbI_3$ for four starting point configurations of the Pb-I network, defined by the bond angles $\alpha_a$ and $\alpha_e$ as described in Chapter 5. The total energy is referred to the total energy obtained for the structure reported in Tables 6.1 and 6.2.

with respect to the structure presented in Table 6.3. We can see that the optimised structures have total energies within 6 meV/atom. In order to ascertain the impact of the structural changes we calculate the scalar relativistic band gaps in each case. The highest deviation from the band gap for the structures shown in Table 6.3 is of 0.2 eV, and reflects the differences in the bond angles following the trend predicted by the Platonic model in Chapter 5. For simplicity, in the rest of this chapter we show results obtained for the four structures presented in Tables 6.1 and 6.2.

### 6.1.2 Electronic structure

Figure 6.1 shows a comparison between the band structures of $NH_4PbI_3$, $PH_4PbI_3$, $AsH_4PbI_3$ and $SbH_4PbI_3$ obtained from DFT/LDA including relativistic spin-orbit coupling corrections. All band gaps are direct with the lowest transition at the centre of the Brillouin zone; the valence and conduction band edges exhibit parabolic profiles in each case.

In Figure 6.2 we show the projected density of states for all four structures. Interestingly, the bands corresponding to the states which are localised on the Pb-I perovskite network maintain the same relative energy with respect to the valence band top. By

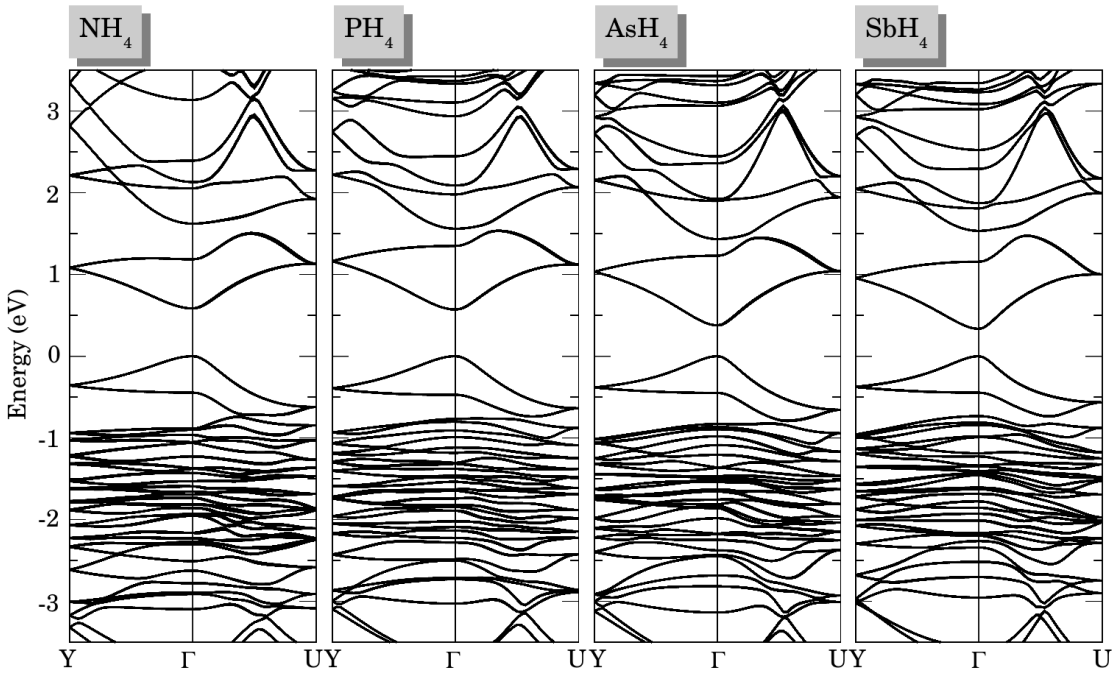


Figure 6.1: Comparison between the DFT/LDA band structures of $NH_4PbI_3$, $PH_4PbI_3$, $AsH_4PbI_3$, $SbH_4PbI_3$ along the high symmetry paths Y-Γ-U, including spin-orbit coupling.

contrast, the energy levels associated with the states localised on the cation have different positions in the valence and conduction bands with respect to the valence band top. It appears that with the increase in the cation size the energy bands correspondent to the cation become closer in energy to the valence and conduction band edges. Nevertheless, the band edges remain predominantly of either I-$p$ or Pb-$p$ character, and the energy states localised on the cations should not have significant effect on the optical absorption in the vicinity of the absorption edge.

In Table 6.4 we show the eigenvalues of the electron and hole effective mass tensors calculated for all four structures. The average effective masses for electrons and holes decrease as the size of the cation increases, in agreement with the predictions made from the Platonic model presented in Chapter 5. Moreover, $AsH_4PbI_3$ appears to have similar average electron and hole effective masses as the ones calculated for $CH_3NH_3PbI_3$, while for $SbH_4PbI_3$ we obtain values which are 33% lower. The carrier mobility can be expressed as $\mu_{e,h} = \frac{q\tau}{m_{e,h}}$, where $q$ is the charge of the carrier and $\tau$ is

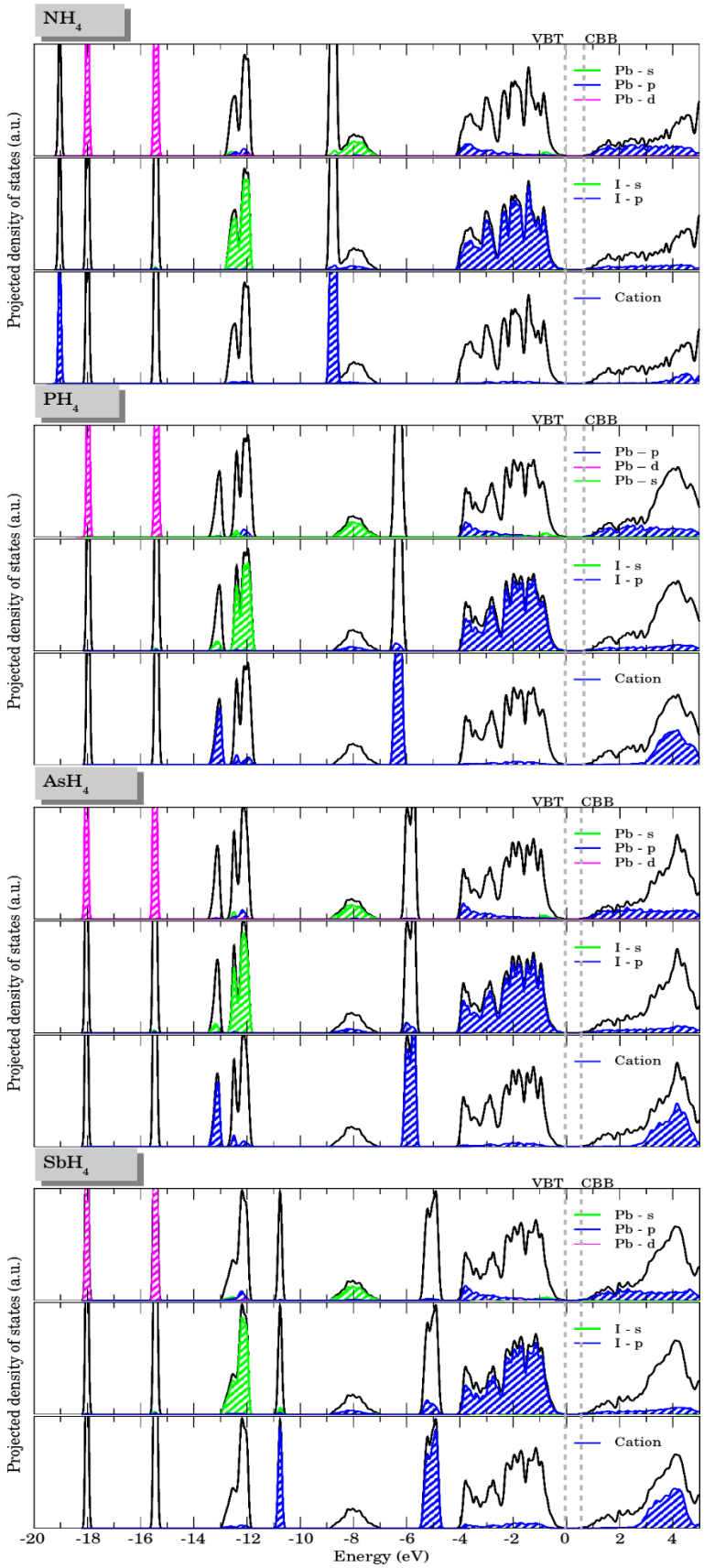


Figure 6.2: Comparison between the projected densities of states of $NH_4PbI_3$, $PH_4PbI_3$, $AsH_4PbI_3$, $SbH_4PbI_3$, from DFT/LDA calculations including spin-orbit coupling.

| | $NH_4PbI_3$ | $PH_4PbI_3$ | $AsH_4PbI_3$ | $SbH_4PbI_3$ |
|---|---|---|---|---|
| | | Holes | | |
| $m_1$ | 0.19 | 0.22 | 0.14 | 0.12 |
| $m_2$ | 0.19 | 0.19 | 0.12 | 0.09 |
| $m_3$ | 0.17 | 0.14 | 0.08 | 0.09 |
| $m_h$ | 0.18 | 0.18 | 0.12 | 0.10 |
| | | Electrons | | |
| $m_1$ | 0.14 | 0.11 | 0.07 | 0.08 |
| $m_2$ | 0.27 | 0.24 | 0.18 | 0.09 |
| $m_3$ | 0.40 | 0.25 | 0.19 | 0.11 |
| $m_e$ | 0.27 | 0.20 | 0.14 | 0.09 |

Table 6.4: Eigenvalues $(m_1, m_2, m_3)$ for the electron and hole effective mass tensors and average electron $(m_e)$ and hole $(m_h)$ effective masses calculated for all four structures. All values are expressed in atomic units.

the average recombination lifetime [171]. If we assume that recombination lifetimes are similar for all Pb-I perovskites, regardless of cation, then we could expect an increase in the electron and hole mobilities of up to 33% for $SbH_4PbI_3$, while $AsH_4PbI_3$ should have a similar charge carrier mobility to $CH_3NH_3PbI_3$.

## 6.2 Quasiparticle *GW* band gaps and effect of self consistency

In order to test that the band gap trend calculated within DFT/LDA holds for higher levels of theory, we perform $G_0W_0$ calculations on the four hypothetical compounds. In Figure 6.3 we show a comparison between the $G_0W_0$ band gaps of $NH_4PbI_3$, $PH_4PbI_3$, $AsH_4PbI_3$ and $SbH_4PbI_3$. In addition we compare these results with $G_0W_0$ quasiparticle band gaps for $CsPbI_3$ and the structurally optimised $CH_3NH_3PbI_3$ (as described in Chapter 5). In the same figure we also show the band gap trends obtained at the DFT/LDA level for all these structures. From Figure 6.3 we can conclude that the trend identified in Chapter 5 and predicted by the Platonic model is robust and holds

within the *GW* approximation. This confirms, that the effect of band gap modulation via the size of the cation is purely an effect of the crystal structure geometry.

As it was pointed out in the previous chapter for $CH_3NH_3PbI_3$, $G_0W_0$ band gaps underestimate the experimental values. The same conclusion can be drawn also for $CsPbI_3$. Indeed, the experimental band gap of $CsPbI_3$ is reported to be in the range of 1.67-1.73 eV, while our calculated $G_0W_0$ quasiparticle band gap is of 1.45 eV. It is reasonable to assume that $G_0W_0$ band gaps calculated for the four hypothetical perovskites would also be underestimated with respect to experimental band gaps.

For this reason we employ the SS-*GW* method described in Chapter 4 for the case of $CH_3NH_3PbI_3$. As already pointed out, a significant difference between the SS-*GW* band gap an the $G_0W_0$ is an indication that a self-consistent *GW* technique is required for the calculation of the quasiparticle band gaps. In Figure 6.4 we show the convergence of the SS-*GW* band gap for each of the four hypothetical perovskites. In all four cases the SS-*GW* gap converges within 5 or 6 iterations, after which the quasiparticle correction is below 10 meV. As it can be seen in Figure 6.4, the SS-*GW* procedure increases the quasiparticle band gap by up to 0.3 eV. The comparison between the DFT,

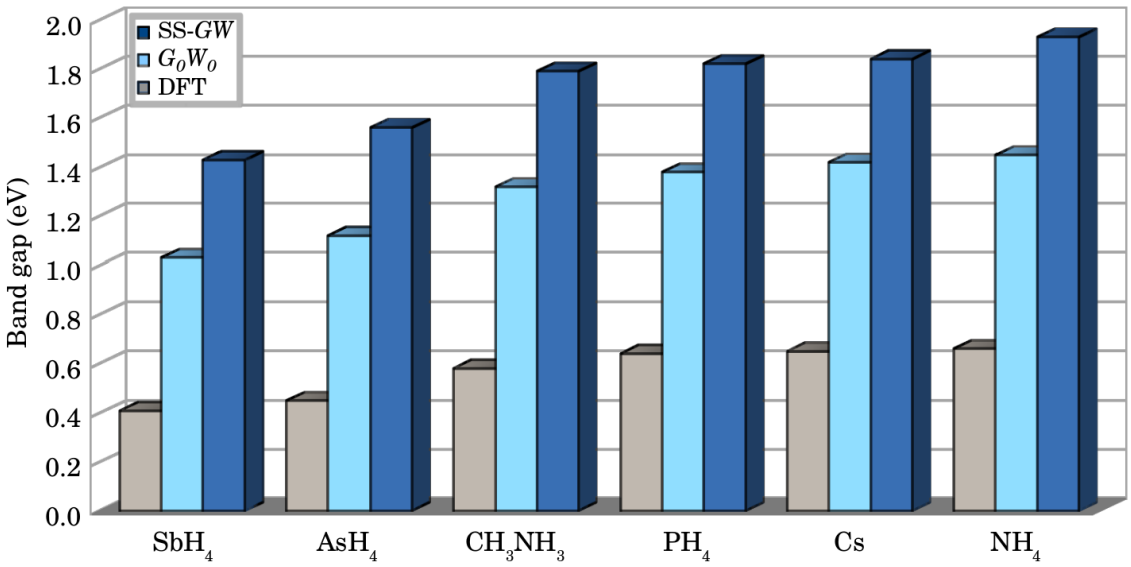


Figure 6.3: Comparison between the DFT/LDA (grey boxes), $G_0W_0$ (light blue boxes) and SS-*GW* (dark blue boxes) band gaps including spin-orbit coupling for $NH_4PbI_3$, $PH_4PbI_3$, $AsH_4PbI_3$, $SbH_4PbI_3$, $CH_3NH_3PbI_3$ and $CsPbI_3$.

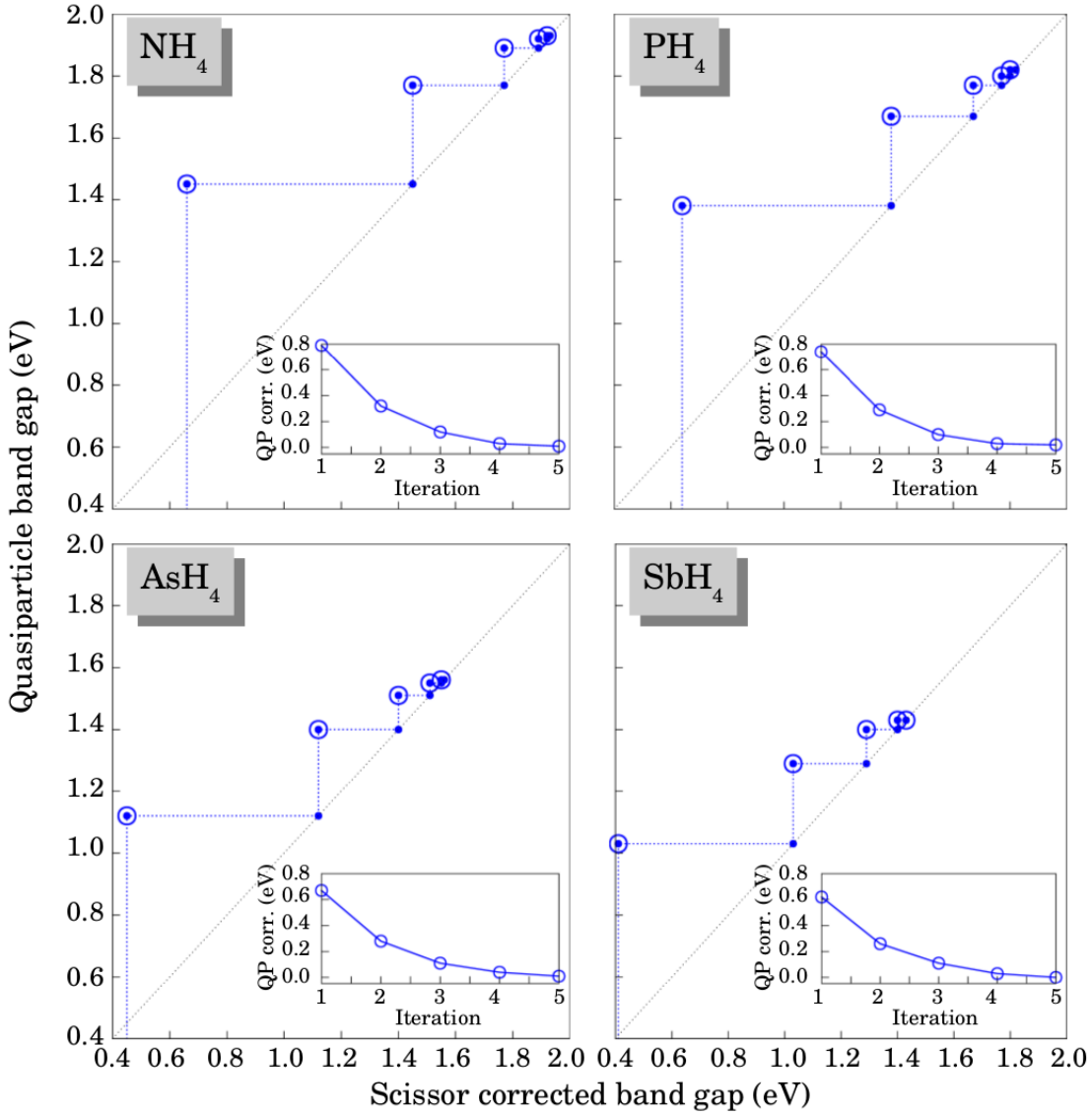


Figure 6.4: Comparison between the band gaps obtained at every stage of the SS-*GW* calculations for $NH_4PbI_3$, $PH_4PbI_3$, $AsH_4PbI_3$ and $SbH_4PbI_3$. The insets in each graph show the convergence of the quasiparticle correction with respect to each iteration.

$G_0W_0$ and SS-*GW* band gaps obtained for $AsH_4PbI_3$, $SbH_4PbI_3$, $NH_4PbI_3$, $PH_4PbI_3$, $CsPbI_3$ and the optimised crystal structure of $CH_3NH_3PbI_3$ shows that the band gaps follow the same trend irrespective of the computational methodology. Table 6.5 summarises the final $G_0W_0$ and SS-*GW* band gaps for all four hypothetical structures. In the same table we include $G_0W_0$ and SS-*GW* band gaps calculated for $CH_3NH_3PbI_3$ (using the optimised crystal structure) and $CsPbI_3$ as well as experimental band gaps where available. The results shown in Table 6.5 confirm the wide range of the band gaps accessible by changing the cation components of the perovskite structure.

| | $NH_4PbI_3$ | $PH_4PbI_3$ | $AsH_4PbI_3$ | $SbH_4PbI_3$ | $CsPbI_3$ | $CH_3NH_3PbI_3$ |
|---|---|---|---|---|---|---|
| DFT | 0.66 | 0.64 | 0.45 | 0.41 | 0.65 | 0.58 |
| $G_0W_0$ | 1.45 | 1.38 | 1.12 | 1.03 | 1.42 | 1.32 |
| SS-*GW* | 1.93 | 1.82 | 1.56 | 1.43 | 1.84 | 1.79 |
| Experiment | | | | | 1.67 [145]<br>1.73 [200] | 1.62-1.64 [169] |

Table 6.5: DFT, $G_0W_0$ and SS-*GW* band gaps calculated for $NH_4PbI_3$, $PH_4PbI_3$, $AsH_4PbI_3$, $SbH_4PbI_3$, $CsPbI_3$ and $CH_3NH_3PbI_3$ and experimental optical gaps where available. The calculations for $CH_3NH_3PbI_3$ are performed for the structurally optimised unit cell. All values are reported in units of eV.

The SS-*GW* band gaps calculated for the structurally optimised $CH_3NH_3PbI_3$ and $CsPbI_3$ are overestimating the experimental band gaps on average by 0.15 eV. As it was shown for the case of $CH_3NH_3PbI_3$ in Chapter 4 this difference is explained by the small differences between the experimental and relaxed crystal structures. Given this observation, we could expect a similar effect for the SS-*GW* band gaps of $NH_4PbI_3$, $PH_4PbI_3$, $AsH_4PbI_3$ and $SbH_4PbI_3$.

Figure 6.5 shows a plot of the maximum attainable efficiency of a hetero-junction solar cell as a function of the band gap of the light absorber for five values of the loss-in-potential, as shown in Eq. 1.11 described in Chapter 1. The efficiencies are calculated assuming a fill factor of 75% and IPCE of 90%. To give context, Ref. [37] reports a planar hetero-junction solar cell implementing $CH_3NH_3PbI_3$ with an efficiency of 19.3%, fill factor of 75%, a loss-in-potential of approximately 0.4 eV and a band gap of 1.55 eV. This is marked on Figure 6.5 by the red dotted line, intersecting the efficiency plot for 0.4 eV loss-in-potential at just over 20%. The blue vertical dotted lines in Figure 6.5 mark the calculated band gaps for $NH_4PbI_3$, $PH_4PbI_3$, $AsH_4PbI_3$, $SbH_4PbI_3$, $CsPbI_3$ and $CH_3NH_3PbI_3$. In Figure 6.5 all calculated band gaps are red-shifted by 0.15 eV, in order to anticipate the possible band gap overestimation due to structural relaxations.

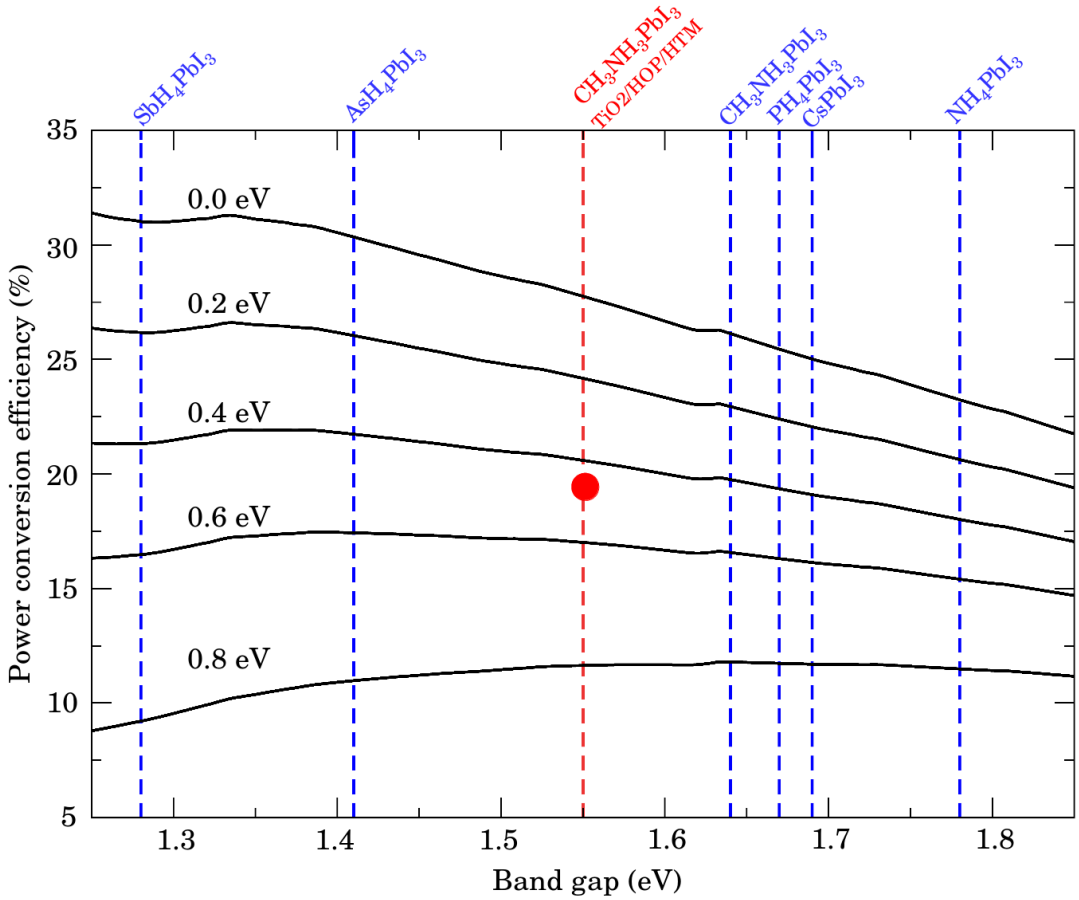


Figure 6.5: Ideal efficiency of solar cells as a function of band gap for five values of the loss in potential: 0.0, 0.2, 0.4, 0.6 and 0.8 eV. The plot marks the ideal efficiency corresponding to the band gap of each of the 6 perovskite structures discussed in Table 6.5. The maximum attainable efficiency is calculated as detailed in Chapter 1 using a fill factor of 73%. The blue dotted lines mark the band gaps of each of the four structure, red-shifted by 0.15 eV. The red dotted line marks the band gaps measured in Ref [37], reporting 19.3% (marked on the plot by the red disk) for the $TiO_2$/HOP/HTM solar cell.

While for high values of the loss-in-potential (0.6, 0.8 eV) the maximum attainable efficiency is shown to improve only marginally for $AsH_4PbI_3$ and $SbH_4PbI_3$, for the ideal case of a vanishing loss-in potential we calculate an increase in the efficiency of up to 20% when $CH_3NH_3PbI_3$ is replaced by $AsH_4PbI_3$ and $SbH_4PbI_3$. This ideal case can be seen as an upper limit for the efficiency that can be obtained for solar cells employing these perovskite materials.

## 6.3 Summary

In this chapter we analysed four hypothetical perovskite structures identified as most promising for photovoltaic applications. From the analyses of the band structures and the projected densities of states we confirmed that the electronic properties of these hypothetical perovskites are influenced primarily by the geometry of the Pb-I perovskite network enclosing the cation. Calculations of the effective masses also confirmed the expected trend predicted by the Platonic model: the larger the cation the smaller the electron and hole effective masses.

We have shown that the band gap trend identified in Chapter 5 is maintained also for their $G_0W_0$ quasiparticle band gaps, showing a band gap tunability over 0.4 eV. Furthermore, by employing the SS-*GW* procedure presented in Chapter 4 we obtained a quasiparticle band gap increase by of almost 0.3 eV in each case, in agreement with observations made for $CH_3NH_3PbI_3$. Moreover, an analysis of the maximum theoretical efficiencies of hetero-junction solar cell employing these perovskite structures using the band gaps predicted from the SS-*GW* procedure shows that $AsH_4PbI_3$ and $SbH_4PbI_3$ may improve the upper limit for the power conversion efficiency by up to 20%.

The results shown in this chapter are supportive of the predictions made by the Platonic model in Chapter 5. However, all of the results obtained assume that all the geometrically optimised structures are stable against structural distortions. While all the structures are fully relaxed, we have pointed out that for example, in the case of $NH_4PbI_3$ structural relaxations are dependent on the geometry of the starting point. Even if a structural geometry which corresponds to a local minimum of the total energy landscape can be identified (as it was done for the case of $AsH_4PbI_3$ in Figure 5.16), confirming the thermodynamic stability of that particular structure is a much more challenging task.

Moreover, the synthesis of these materials is not expected to be straightforward given the safety risks associated particularly with the cation components (the neutral $AsH_3$ and $SbH_3$ gases are toxic, and $SbH_3$ in gas phase is unstable and flammable). Rare experimental reports of $AsH_4^+$ and $SbH_4^+$ cations [226] as well as data on the $AsH_4I$ salt [221] can be found in literature, however no such compounds are purchasable from distributors such as Sigma Aldrich [227]. Despite these possible setbacks, the analysis presented in the last three chapters is a validation the concept of band gap tuning of a perovskite material via the size of the cation.

Further work should assess the other possible crystal structures of these hypothetical materials and their stability in various thermodynamic conditions. This task would require a systematic screening of possible structures, perhaps using random structure searching algorithms [228]. Moreover, an analysis of the thermodynamic phase diagram of these materials would require a thorough understanding of their vibrational properties. These challenging tasks will, however, not be addressed in this thesis. Further exploration of the perovskite materials landscape should also be extended to other halogen and metal atoms in order to achieve a complete screening of the materials properties accessible within this metal-halide perovskite family.

# Chapter 7

# The $A_2B_3$ metal chalcogenides (A = Sb, Bi; B = S, Se): An overview of recent literature

Records of the existence of stibnite ($Sb_2S_3$) date back to ancient times. Stibnite powders were used in Ancient Egypt as a popular eye make up among Egyptian queens or even as skin medicine in Ancient Greece [229]. Stibnite is a naturally occurring mineral, appearing as a collection of black-metallic rod-like crystals. Figure 2.3a depicts a large stibnite crystal currently on display at the Natural History museum in London.

Metal chalcogenides based on Sb and Bi have increased in popularity in the last decade, being linked with the discovery of novel topological insulators [230] as well as thermoelectric applications [231]. In solar cell applications, stibnite has been implemented as a semiconductor sensitiser in SSSCs due to its optimum band gap for optical absorption (1.7 eV) and high absorption coefficient in the visible range ($10^5$ $cm^{-1}$) [232]. Solar cells implementing stibnite recently achieved a record of 7.5% efficiency [233]. Computational studies of the hetero-junction between $TiO_2$ and stibnite, antimonselite and bismuthinite pointed out that solar cells implementing antimonselite may lead to an improvement in the power conversion efficiency due to its smaller band gap of 1.2 eV and favourable band alignment to $TiO_2$ [20]. Since this report, the popularity of antimonselite sensitised solar cells has been increasing [31, 234], with

Figure 7.1: Large stibnite crystal on display at the Natural History Museum in London.

a current efficiency record of 3.7% [32]. Furthermore, solar cells using sensitisers with a graded composition of stibnite and antimonselite, $Sb_2Se_xS_{3-x}$ have also been reported. The efficiency of this configuration was shown to be superior to devices employing pure stibnite and antimonselite solar cells [235].

According to Ref. [236] $A_2B_3$ metal chalcogenides can be classified based on their crystal structures at room temperature. The diagram sketched in Figure 7.2 depicts all possible combinations between Sb and Bi and S, Se, Te. Ref. [236] points out that the lighter $Sb_2S_3$, $Sb_2Se_3$ and $Bi_2S_3$ are low band gap insulators and have an orthorhombic crystal structure, while the heavier $Bi_2Se_3$, $Sb_2Te_3$ and $Bi_2Te_3$ are topological insulators and stabilise in a rhombohedral structure under ambient temperature and pressure [236]. As it will emerge from the following discussions, $Bi_2Se_3$ also crystallises in an orthorhombic (semiconducting) phase which is isostructural with $Sb_2S_3$, $Sb_2Se_3$ and $Bi_2S_3$. All four $A_2B_3$ semiconductors, with A = Sb, Bi and B = S, Se, exhibit similar electronic and optical properties, as well as optimum band gaps for optical absorption [237].

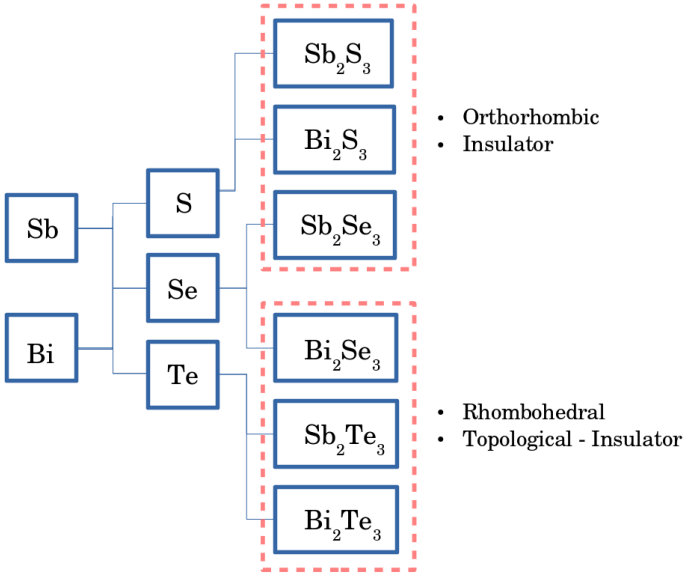


Figure 7.2: Schematic classification of the possible $A_2B_3$ (A = Sb, Bi and B = S, Se, Te), as suggested by Ref. [236]. The pink dotted squares mark the group of structures which are orthorhombic and rhombohedral at room temperature.

Given these observations, this second part of the thesis sets out to investigate the electronic properties of this group of four $A_2B_3$ metal chalcogenides. In this chapter, we aim to provide context to this discussion by summarising some of the most recent experimental and computational studies reported in literature. The majority of the literature review presented in this chapter will be focused on stibnite, with reports on antimonselite, bismuthinite guanajuatite also summarised where available. While these four materials have been investigated in relation to a variety of applications, in the following we will primarily focus on summarising the properties which are relevant for photovoltaic applications.

## 7.1 Structure and synthesis

All four minerals specified above crystallise in an orthorhombic structure. The unit cell of the $A_2B_3$ crystals contain 20 atoms, arranged according to the *Pnma* 62 symmetry group. The crystal structure consists of parallel one-dimensional ribbons, each containing two formula units: $(A_4B_6)_n$. Figure 7.3a shows a polyhedral representation

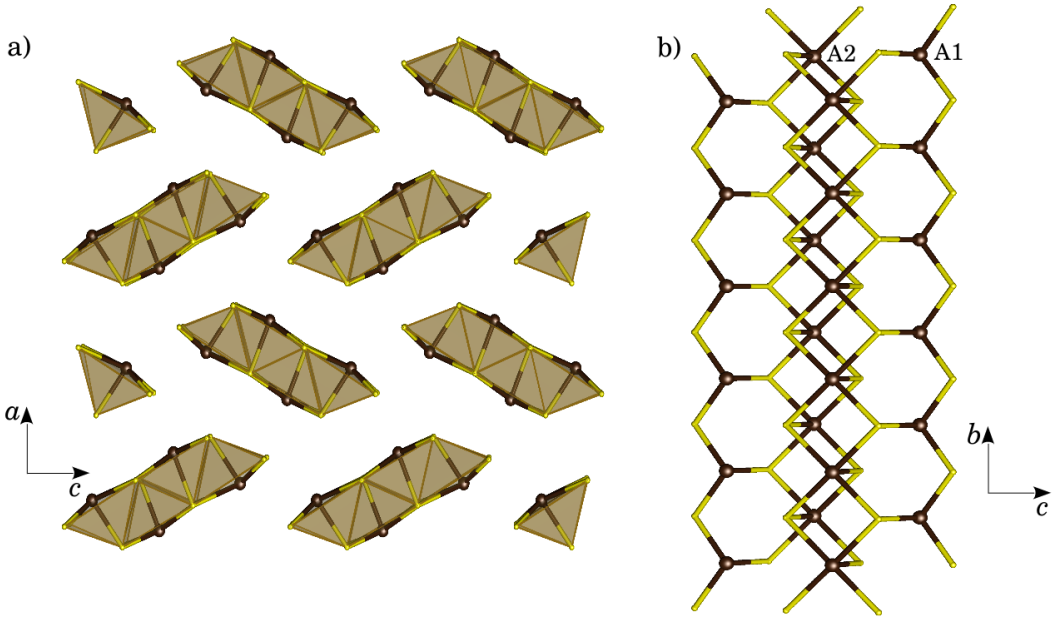


Figure 7.3: a) Polyhedral model of the bulk orthorhombic $A_2B_3$ structure, as viewed along the *b* axis. b) Side view of the single $A_4B_6$ infinite ribbon. The 3 and 5-fold coordinated atoms are marked by A1 and A2.

of the bulk $A_2B_3$ structure. As it is highlighted by the polyhedral model, the ribbons are separated from each other within the bulk structure and interact via weak van der Waals forces [237]. Figure 7.3b shows a side-view of an $A_4B_6$ ribbon. Within this single ribbon we can distinguish two inequivalent metal atoms: a three-fold coordinated atom (A1) and a five-fold coordinated atom (A2) [Figure 7.3b].

High pressure studies of stibnite, bismuthinite and antimonselite show that the orthorhombic structures do not undergo significant changes for pressures up to at least 50 GPa. In this range of pressures the highest compressibility is observed for the *a* and *c* lattice parameters perpendicular to the direction of the ribbon [238, 238–240]. Above 50 GPa antimonselite transitions to a bcc phase [239] while bismuthinite becomes structurally disordered [239]. $Bi_2Se_3$ crystallises at room temperature and pressure in a rhombohedral structure. Upon increasing the temperature and pressure to (1023 K and 12 GPa or 1073 K and 6.5 GPa), it undergoes a phase transition to an orthorhombic phase, isostructural to stibnite, bismuthinite and antimonselite [241]. A recently published study of $Bi_2Se_3$ phase transitions shows that this

orthorhombic phase can also be stabilised at ambient temperature and pressure [241]. Ref. [241] shows that upon increasing pressure rhombohedral $Bi_2Se_3$ becomes body-centred tetragonal at 25 GPa. This phase relaxes at ambient temperature and pressure conditions transforming first into an amorphous structure, and finally into an orthorhombic *Pnma* structure which remains stable for up to 90 days [241]. More details on the phase diagrams of high pressure phases of these metal chalcogenides can be found in Refs. [238–241].

Besides its natural occurrence in mineral form (Figure 7.3a), stibnite can be synthesised using a variety of deposition techniques such as electrodeposition, chemical bath deposition or chemical vapour deposition [242–245]. Chemically deposited stibnite thin films are generally amorphous [243]. In order to obtain crystalline structures, the amorphous films are annealed until a phase transition is observed, above 225° C [243]. Depending on the annealing time and annealing temperatures the degree of crystallinity of the film, as well as their physical properties may vary [246]. Similar deposition techniques can also be used for antimonselite [244, 247] and bismuthinite [248, 249].

## 7.2 Electronic and optical properties: insight from experimental and computational studies

### 7.2.1 Experimental studies

The measured optical band gaps of stibnite, antimonselite and bismuthinite are as follows: 1.42-1.78 eV for stibnite [243, 250–253], 1-1.55 eV for antimonselite [247, 250, 254] and 1.38-1.58 for bismuthinite [249, 251, 255, 256]. The spread in the measured values can be attributed to different preparation conditions, yielding different degrees of polycrystallinity (even amorphous samples in some cases) and also stoichiometry. In addition, all these compounds exhibit closely lying direct and indirect transitions

thereby complicating the assignment of the nature of the optical gap. Upon analysis of the recent literature, some examples can be found that point out the variations of the band gaps with the experimental conditions [246, 257, 258].

Ref [246] demonstrates the sensitivity of the measured band gap of stibnite to the annealing temperature of the deposited thin films. As it was discussed in the previous section, $Sb_2S_3$ undergoes a structural phase transition from amorphous to crystalline around 225° C. This transition is captured by Ref. [246] showing the decrease of the optical band gap for thin films annealed at increasing temperatures. The optical band gap stabilises for samples annealed at temperatures over 250° C, but shows a variability of approximately 0.5 eV over the entire amorphous to crystalline transition. Ref. [257] points out the sensitivity of the optical band gap to the Sb:S ratio used in the deposition process. While XRD spectra confirm that the final reaction product is crystalline $Sb_2S_3$, the optical band gap for different Sb:S ratios (3:7, 4:6, 5:5, 6:4) is found to vary 1.9 to 2.3 eV [257]. Furthermore, Ref. [258] shows an increase in the band gap of $Sb_2S_3$ thin films from 1.7 to 2.5 eV with the decrease in the thickness of the films from 600 to 120 nm. Ref. [258] points out that the average crystallite size decreases with the decrease in the thickness of the films from 71 to 49 nm and relate the increase in the band gap to quantum confinement effects.

Continuous band gap tunability is reported in Ref. [259] in solid solutions of $Sb_2Se_xS_{3-x}$ nanotubes over the full range of concentrations ($x = 0$ to 3). The size of the nanotubes is large comparative to the size of a single ribbon (20 nm thick, and 400 nm wide), suggesting that their electronic properties should not be affected by quantum confinement effects. The band gaps obtained are continuously tuned from 1.18 to 1.63 eV for decreasing concentrations of Se [259]. Figure 7.4a shows the optical absorption spectra of $Sb_2Se_xS_{3-x}$ for increasing concentrations of Se, taken at room temperature.

Ref. [260] reports a weak excitonic peak for bismuthinite, observed from absorp-

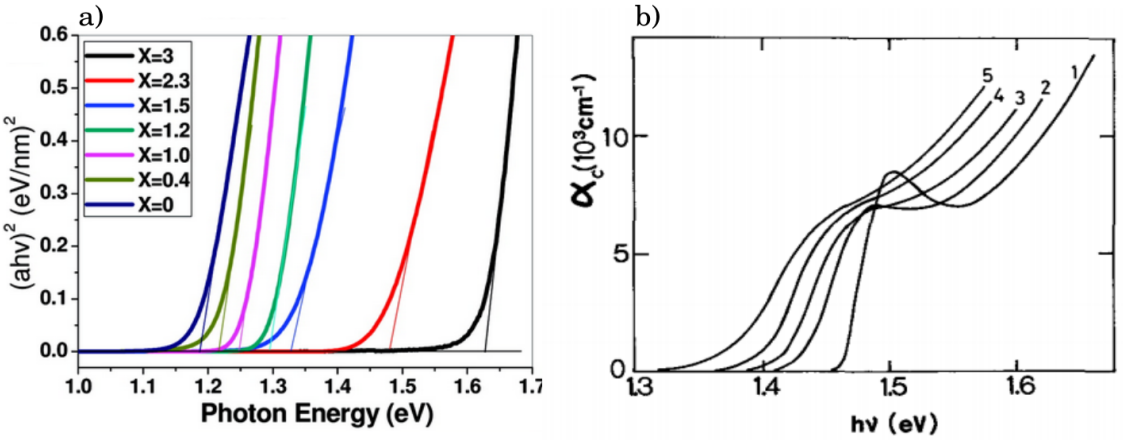


Figure 7.4: a) Optical absorption spectra for solid solutions of $Sb_2Se_xS_{3-x}$ nanotubes for several concentrations of Se shown in the legend. This plot was taken from Ref. [259] with permission. b) Optical absorption spectra obtained for $Bi_2S_3$ at the following temperatures: 29 K (curve 1), 137 K (curve 2), 173 K (curve 3), 214 K (curve 4) and 269 K (curve 5). The figure was taken from Ref. [260] with permission.

tion spectra measured at increasing temperatures. A small exciton binding energy of 28 meV was estimated. This would explain the absence of excitonic features in optical absorption spectra measured at room temperature [260]. The emergence of the excitonic peak in optical absorption spectra is clearly depicted in Figure 7.4b, where spectra obtained at 29, 137, 173, 214 and 269 K are shown [260]. Moreover, Ref. [260] reports an optical band gap of 1.52 eV at 29 K, and 1.44 eV at room temperature.

Various nanostructured forms of the $A_2B_3$ structures are also explored. For example, Refs. [231, 261, 262] report nanowires stibnite antimonselite and bismuthinite. Nanowires of stibnite appear to have enhanced ferroelectric and piezoelectric properties as compared to their bulk counterparts [231] and are being considered for thermoelectric applications. The smallest thickness reported so far is of 1.6 nm for bismuthinite nanowires, and corresponds to the transverse size of only two ribbons [261]. However structural details for these nanoribbons are yet to be confirmed.

### 7.2.2 Computational studies

There are several density functional theory studies on this group of semiconductors, largely focusing on the bulk electronic properties [20, 237, 263–270], but also on the

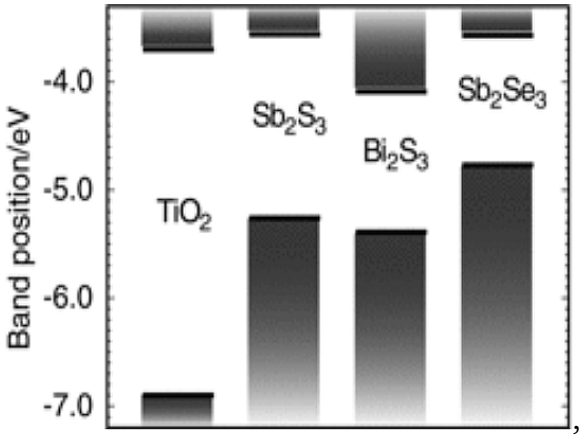


Figure 7.5: Alignment of the band structures of stibnite, antimonselite and bismuthinite to $TiO_2$ as calculated from DFT. The figure was taken from Ref. [20] with permission.

structural and elastic properties if these materials [264, 271].

The band gaps calculated within DFT for the bulk structures show some variability among different publications: 1.18-1.55 eV (stibnite) [20, 237, 263–268], 0.79-1.14 eV (antimonselite) [237, 264–267], 1.32-1.67 eV (bismuthinite) [237, 268, 269] and 0.8-1.1 (guanajuatite) [270]. The character of the band gap (direct vs indirect) is also not fully clarified in literature. We speculate that these differences could be due to the use of different exchange-correlation functionals (LDA vs GGA) or possibly due to using slightly different crystal structures. Despite these variations, the overall consensus among computational studies reported so far is that these four materials exhibit very similar electronic structures.

This observation is further explored in Ref. [20] where the hetero-junctions of stibnite, antimonselite and bismuthinite with $TiO_2$ are analysed by calculating the band alignments from DFT [20]. As shown in Figure 7.5, the valence and conduction band edges of stibnite and antimonselite align with the band structure of $TiO_2$ in a type-II hetero-junction, favourable for the injection of photogenerated electrons [20]. By contrast, the alignment of $TiO_2$ to $Bi_2S_3$ is found to not be favourable for photovoltaics, given that the conduction band minimum of $Bi_2S_3$ is found at a lower energy level than the conduction band minimum of $TiO_2$, forming a type-I hetero-junction [20].

To the best of our knowledge, two publications report the *GW* quasiparticle band gap

of stibnite and antimonselite [265, 266], obtaining values of 1.67 eV and 1.21 eV respectively [265, 266], in good agreement with experiments. However, Refs. [265, 266] do not give details regarding the computational setup of their *GW* calculations.

The analyses of the partial densities of states show similar features for all four structures [264, 267]. The top of the valence band is dominated by the chalcogen 3(4)$p$ states, with a small contribution from the Sb(Bi) 5(6)$p$ and $s$ electrons. The bottom of the conduction band is dominated by the Sb(Bi) 5(6)$p$ states, with a smaller contribution from the chalcogen $p$ electrons [264, 267, 272]. The electron and hole effective masses of $Sb_2S_3$ are calculated from the DFT/GGA band structure along the Γ - S $(0.5, 0.5, 0)$ direction, obtaining $m_h^* = 1.843$ and $m_e^* = 1.035$ a.u. respectively [272]. Moreover, Ref. [272] the Wannier exciton binding energy for $Sb_2S_3$ is estimated using the calculated effective masses and $\varepsilon_0 = 11$ for the dielectric constant [272], obtaining an excitonic binding energy of less than 0.1 eV [272]. This result has not yet been verified experimentally or within electronic structure calculations within within the Bethe-Salpeter formalism.

First principles studies stibnite, antimonselite and bismuthinite nanoribbons are focused primarily on the quantum confinement effect and the band gap dependence on the dimensions of the nanostructures [265, 268]. Ref. [268] reports a comparison between the band gaps of bulk stibnite and bismuthinite, infinite nanoribbons and finite nanoribbons. The DFT band gaps calculated for the bulk and infinite nanoribbons have similar values in both cases (they differ by up to 0.1 eV) [268]. By contrast the band gaps of the finite nanoribbons decrease as expected with the ribbon length [268], for both stibnite and bismuthinite. The band gap decreases in both cases by up to 0.6-0.7 eV as the nanoribbon length increases from 1 to 7 nm. Interestingly, the quasiparticle corrections for the band gaps of the finite bismuthinite nanoribbons as calculated within ΔSCF are of the order of 1.2 eV [268], while bulk quasiparticle corrections for bismuthinite are of 0.3 eV [212]. A similar DFT study of the band gap dependence on nanoribbon length is shown in Ref [265] for stibnite

and antimonselite. The DFT results are in agreement with the calculations reported by Ref. [268]. However, Ref. [265] finds that the *GW* quasiparticle corrections for the bulk and nanoribbon case only differ by up to 0.2 eV. There are no further details on the computational setup of the *GW* calculations performed in Ref. [265], therefore it is difficult to comment on the discrepancy in the results shown in Refs [265, 268].

## 7.3 Summary

In this chapter we have summarised some of the recent literature discussing the structural, electronic and optical properties of $A_2B_3$ metal chalcogenides, with A = Sb, Bi and B = S, Se. These four isostructural semiconductors exhibit similar electronic properties (small band gaps within 1.1-1.8 eV) and represent good candidates for photovoltaic applications. While there are many experimental reports detailing their electronic structure, clarifications are required regarding the value and the character of their band gaps. Indeed, experimental studies have shown a great deal of variability for the optical band gaps with respect to the preparation methods.

In principle, computational modelling should provide clarity in the discussion of the electronic structure. However, density functional theory studies reported so far exhibit similar variations of the band gaps across different publications. In this context, there is a need for detailed and reproducible calculations of the electronic structure of these four metal chalcogenide semiconductors based on quasiparticle techniques. In the next chapter, we will present a detailed study of the quasiparticle band structure of stibnite, bismuthinite, antimonselite and guanajuatite. The study will focus on the sensitivity of the band gaps with respect to structural parameters, inclusion of semicore *d* states and spin orbit coupling.

# Chapter 8

# Electronic properties of light sensitisers of the $A_2B_3$ metal chalcogenide semiconductors (A = Sb, Bi; B = S, Se)

In this chapter we analyse the electronic properties of four metal chalcogenide semiconductors of the stibnite family, $A_2B_3$ (A = Sb, Bi; B = S, Se). We study the structural and electronic properties of all four materials within the DFT and the $G_0W_0$ method. We put an emphasis on the impact of the semicore electrons and the spin-orbit coupling in a similar manner as it was done for the case of $CH_3NH_3PbI_3$ and related perovskites in Chapters 4 and 6. The main difference between the study of Chapters 4 and 6 and the approach presented here is that the spin-orbit coupling effect on the band gap is introduced as a scissor correction of the quasiparticle band gap, and not taken into account in the $G_0W_0$ calculation.

Furthermore, we report a systematic and reproducible study of the quasiparticle band gaps of all four semiconductors, and investigate the sensitivity of the quasiparticle corrections to the structural parameters. Indeed, we find that the quasiparticle band gaps may change by up to 0.3 eV when either experimental or structurally optimised lattice parameters and atomic positions are used in the calculations. This effect explains the variation of the band gap values reported in literature and discussed in Chapter 7.

Finally we relate the calculated band gaps with the ideal Shockley-Queisser limit for the photovoltaic efficiency, and find that all four structures are promising candidates for photovoltaic applications.

## 8.1 Crystal structure

### 8.1.1 Structural relaxations

All four semiconductors of the $A_2B_3$ type, with A = Sb, Bi and Bi = S, Se crystallise in an orthorhombic lattice. The crystal symmetry follows the operations of the *Pnma* 62 space group [237]. All four crystal lattices have unit cells containing 20 atoms. As discussed in Chapter 7 and highlighted in Figure 8.1, the crystal structure appears as a bundle of parallel quasi one-dimensional ribbons, separated along the $a$ and $c$ directions.

We perform structural optimisations within DFT/LDA for all four structures, using the XRD data reported in Refs [273–276] and collected in Ref. [237] as a starting point.

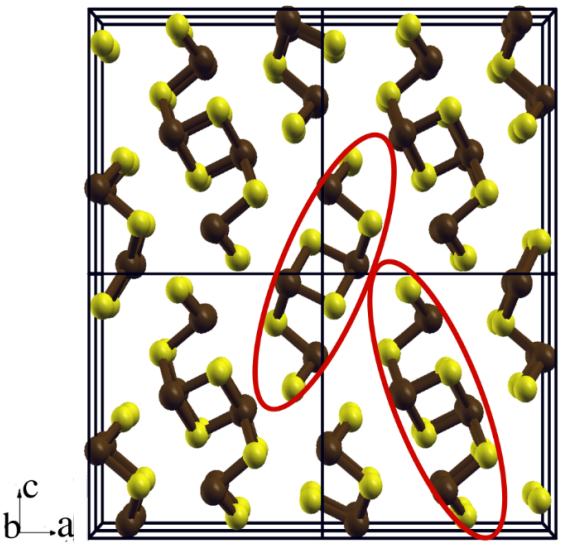


Figure 8.1: Ball-and-stick model of $A_2B_3$ semiconducting metal chalcogenides of the stibnite family, with A standing for Sb or Bi (brown) and B for S or Se (yellow). The two inequivalent $(A_4B_6)_n$ ribbons in the unit cell are highlighted in red, and the perspective view is along the directions of the ribbons.

| | $a$ | | $b$ | | $c$ | |
|---|---|---|---|---|---|---|
| | | | Experiment | | | |
| $Sb_2S_3$ | 11.311[a] | | 3.836[a] | | 11.229[a] | |
| $Sb_2Se_3$ | 11.794[b] | | 3.986[b] | | 11.648[b] | |
| $Bi_2S_3$ | 11.305[c] | | 3.981[c] | | 11.147[c] | |
| $Bi_2Se_3$ | 11.830[d] | | 4.090[d] | | 11.620[d] | |
| | | | Calculations without semicore | | | |
| $Sb_2S_3$ | 11.036 | (-2.4 %) | 3.795 | (-1.1 %) | 10.753 | (-4.2 %) |
| $Sb_2Se_3$ | 11.609 | (-1.6 %) | 3.952 | (-0.9 %) | 11.213 | (-3.7 %) |
| $Bi_2S_3$ | 11.227 | (-0.7 %) | 3.999 | (0.5 %) | 11.001 | (-1.3 %) |
| $Bi_2Se_3$ | 11.767 | (-0.5 %) | 4.141 | (1.3 %) | 11.491 | (-1.1 %) |
| | | | Calculations with semicore | | | |
| $Sb_2S_3$ | 11.087 | (-2.0 %) | 3.838 | (0.1 %) | 10.834 | (-3.5 %) |
| $Sb_2Se_3$ | 11.646 | (-1.3 %) | 3.989 | (0.1 %) | 11.287 | (-3.1 %) |
| $Bi_2S_3$ | 11.030 | (-2.4 %) | 3.949 | (-0.8 %) | 10.853 | (-2.6 %) |
| $Bi_2Se_3$ | 11.609 | (-1.9 %) | 4.099 | (0.2 %) | 11.374 | (-2.1 %) |

[a] Ref. 273, [b] Ref. 274,
[c] Ref. 275, [d] Ref. 276.

Table 8.1: Comparison between the calculated DFT/LDA lattice parameters of stibnite, antimonselite, bismuthinite, and guanajuatite and experiment (all values are given in Å). The percentile deviation from experiment is indicated in each case.

For both Sb and Bi we explore the influence of semicore electrons on the structural optimisation, and perform these calculations using the following valence configurations in their pseudopotentials: Sb ($4s^2 4p^3$ or $3d^{10} 4s^2 4p^3$) and Bi ($5s^2 5p^3$ or $4d^{10} 5s^2 5p^3$). In the case of S and Se only pseudopotentials without semicore electrons are used: S ($3s^2 3p^4$) and Se ($4s^2 4p^4$). In total we perform 8 structural relaxations for all compounds.

Table 8.1 shows the comparison between the experimental and our optimised lattice parameters for all four structures obtained from calculations with and without semicore $d$ electrons included in the valence configuration of Sb and Bi, respectively. As expected, the use of the local density approximation leads to a general underestima-

tion of the experimental parameters. Interestingly, while such underestimation does not exceed 1.1% along the direction of the $(A_4B_6)_n$ ribbons ($b$ parameter in Table 8.1), the deviation can reach up to 4.2% in the direction perpendicular to the ribbons ($a$ and $c$ parameters in Table 8.1). We tentatively assign this behaviour to the fact that the inter-ribbon forces are likely to include non-negligible van der Waals components and hence are not described correctly within the LDA.

Upon using the van der Waals functional of Ref. [277], the lattice parameters overestimate the experimental values by up to 6.9% along the directions perpendicular to the ribbons, while along the ribbons the calculated parameters are in agreement with experiment (within 0.3%). This observation is in line with calculations in graphite and boron nitride reported in literature [278]. These results indicate that for semiconductors of the stibnite family the inclusion of van der Waals forces as described by the functional of Ref. [277] does not improve the agreement of the calculated structural parameters with experiment.

In order to take into account the differences between calculated and experimental lattice parameters, in this chapter we describe electronic structure calculations performed either for the DFT/LDA structures (with and without semicore) or the experimental structures.

### 8.1.2 Cohesive energies

In order to have a quantitative assessment of the inter-ribbon and intra-ribbon interactions, we calculate their respective cohesive energies. The intra-ribbon cohesive energy is calculated as the difference between the total energy of one ribbon and the total energies of its constituent atoms. The inter-ribbon cohesive energy is evaluated as the difference between the total energy of the unit cell and twice the total energy of one ribbon in isolation.

Inspection of the calculated cohesive energies supports the possibility that the inter-

| | $Sb_2S_3$ | $Sb_2Se_3$ | $Bi_2S_3$ | $Bi_2Se_3$ |
|---|---|---|---|---|
| Intra-ribbon | 0.2 | 0.2 | 0.3 | 0.3 |
| Inter-ribbon | 3.9 | 3.5 | 3.6 | 3.3 |

Table 8.2: Comparison between the inter-ribbon and intra-ribbon cohesive energy for all four compounds. All values are reported in units of eV/atom.

ribbon interactions include a van der Waals component. From Table 8.2 we can see that the intra-ribbon cohesive energy is smaller than the inter-ribbon cohesive energy by an order of magnitude in all four cases.

## 8.2 Electronic properties

### 8.2.1 DFT/LDA band structures

Figure 8.2 shows the DFT/LDA band structures calculated using experimental lattice parameters and without semicore electrons along the $Z-\Gamma-X$ and the $Y-\Gamma$ segments of the Brillouin zone. The top of the valence band is found to be predominantly of S-3$p$ or Se-4$p$ character, while the bottom of the conduction band comprises of Sb-5$p$ or Bi-6$p$ states, consistent with previous calculations [237, 263].

The band structures shown in Figure 8.2 exhibit several extrema in the proximity of the fundamental gap, making the direct and indirect transitions almost degenerate. Table 8.3 shows that the energy separation between direct and indirect DFT/LDA band gaps falls within 0.15 eV in all cases. Interestingly, there is a discrepancy in the difference between the indirect and direct gaps when experimental or optimised lattice parameters are used in the DFT/LDA calculations. The largest difference in this sense is in the case of $Bi_2Se_3$ where there is a 0.14 eV difference between the minimum direct band gap and the indirect band gap when the electronic structure is calculated for the experimental crystal structure. When optimised lattice parameters and atomic positions are used in the same calculation, the difference between the minimum di-

rect band gap and the indirect band gap is 0.04 eV. Moreover, the band gap calculated for the experimental crystal structure is larger than the band gap calculated for the optimised crystal structure in all of the analysed cases. This observation could explain the variability in the DFT band gaps reported in literature for these compounds, as discussed in Chapter 7.

The data in the Table 8.3 suggests, however, that in these compounds the direct transition will most likely dominate over the indirect one, apart from a very narrow onset of 0.1-0.2 eV. This observation is consistent with experimental evidence showing a weak absorption onset just below the threshold for direct absorption [243, 253]. Therefore, for photovoltaics applications, stibnite, antimonselite, bismuthinite and guanajuatite

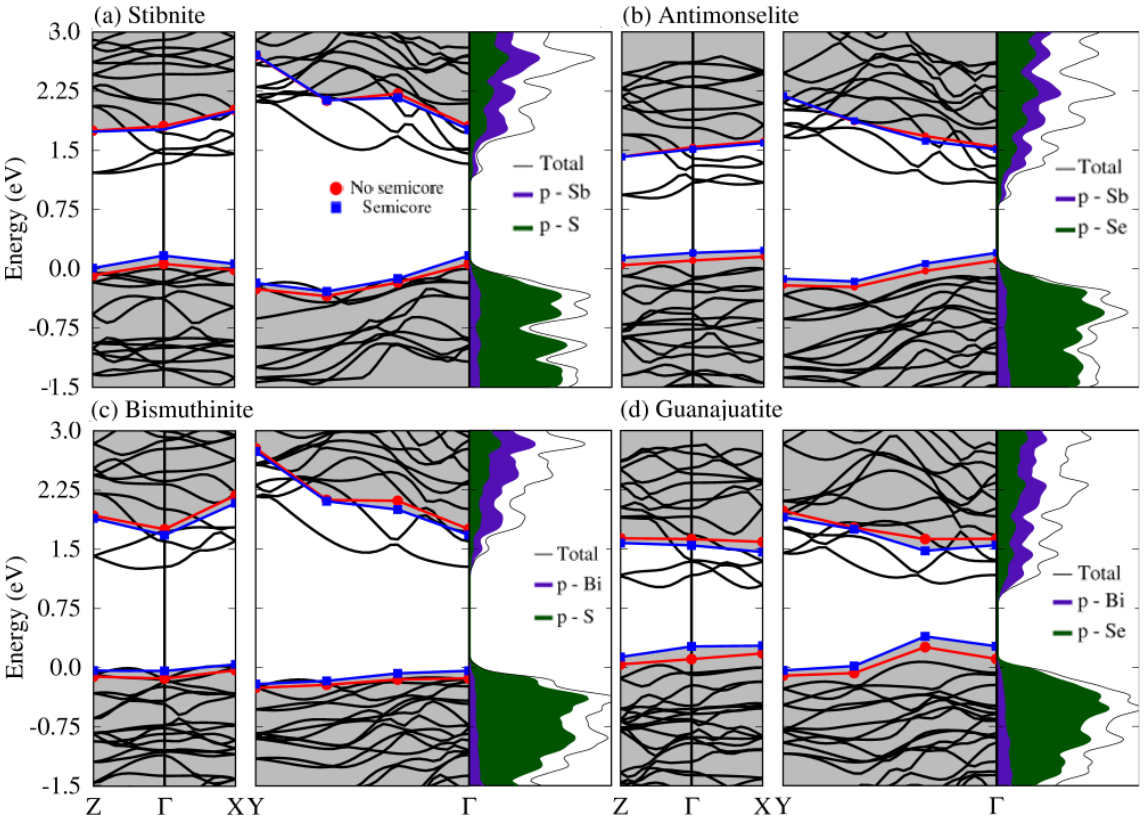


Figure 8.2: Band structures of (a) stibnite, (b) antimonselite, (c) bismuthinite, and (d) guanajuatite calculated using DFT/LDA experimental lattice parameters and without semicore electrons (black solid lines), as well as corresponding density of states (DOS, black dashed lines). The contributions to the DOS from the *p* states of S and Se (Sb and Bi) are indicated by the green (blue) shaded areas in each case. The *GW* quasiparticle energies of the band extrema at high-symmetry points are also shown, with blue squares and red circles indicating calculations with and without semicore electrons respectively. The connecting lines are a guide to the eye. The coordinates of the high-symmetry points in reciprocal lattice units are as follows: Z (0,0,0.5), X (0.5,0,0), Y(0,0.5,0).

| | Mimimum gap | | Direct gap | |
|---|---|---|---|---|
| | w semicore | w/o semicore | w semicore | w/o semicore |
| | Experimental parameters | | | |
| $Sb_2S_3$ | 1.19 | 1.21 | 1.25 | 1.27 |
| $Sb_3Se_3$ | 0.84 | 0.86 | 0.84 | 0.86 |
| $Bi_2S_3$ | 1.25 | 1.24 | 1.28 | 1.27 |
| $Bi_2Se_3$ | 0.85 | 0.86 | 0.99 | 0.99 |
| | Optimised parameters | | | |
| $Sb_2S_3$ | 1.06 | 1.12 | 1.06 | 1.15 |
| $Sb_3Se_3$ | 0.75 | 0.79 | 0.71 | 0.78 |
| $Bi_2S_3$ | 1.08 | 1.11 | 1.16 | 1.16 |
| $Bi_2Se_3$ | 0.77 | 0.76 | 0.81 | 0.79 |

Table 8.3: Comparison between the minimum band gaps and the direct band gaps of stibnite, antimonselite, bismuthinite, and guanajuatite, as obtained from DFT/LDA. We show results from calculations using both the experimental and the optimised lattice parameters (with and without semicore) lattice parameters. All values are in units of eV.

can effectively be considered as "quasi-direct gap" semiconductors.

### 8.2.2 Quasiparticle corrections

Figure 8.2 shows that *GW* quasiparticle corrections lead to a moderate increase of the band gaps in all cases, while generally preserving the shape of the band extrema. From this figure we deduce that a simple scissor operator should be able to capture the most important effects of the *GW* corrections.

A detailed analysis of the quasiparticle corrections at the high-symmetry points Γ, $X$ and $Z$ is given in Figure 8.2 and Table 8.4. In Figure 8.3 we show the quasiparticle corrections as a function of the corresponding Kohn-Sham eigenvalues around the band extrema. In the cases of stibnite and antimonselite we observe that in the calculations with semicore electrons the valence bands are slightly up-shifted (by about 0.1 eV) as compared to calculations without semicore, while the corrections to the conduction band are essentially the same. In the cases of bismuthinite and guanajuatite the effect of the semicore is to shift the valence bands up and the conduction bands down

| | Optimised parameters | | | | Expt. parameters | | | |
|---|---|---|---|---|---|---|---|---|
| | LDA | | GW | | LDA | | GW | |
| | w/o S | S | w/o S | S | w/o S | S | w/o S | S |
| | | | | Stibnite | | | | |
| $\Gamma_v$ | 0.00 | 0.00 | 0.10 | 0.20 | 0.00 | 0.00 | 0.06 | 0.17 |
| $\Gamma_c$ | 1.15 | 1.11 | 1.58 | 1.52 | 1.33 | 1.29 | 1.81 | 1.77 |
| $X_v$ | -0.05 | -0.03 | -0.03 | 0.09 | 0.00 | -0.01 | -0.02 | 0.06 |
| $X_c$ | 1.40 | 1.39 | 1.90 | 1.88 | 1.46 | 1.43 | 2.01 | 1.99 |
| $Z_v$ | -0.16 | -0.14 | -0.14 | -0.04 | -0.06 | -0.06 | -0.08 | 0.01 |
| $Z_c$ | 1.17 | 1.17 | 1.65 | 1.65 | 1.22 | 1.20 | 1.75 | 1.74 |
| | | | | Antimonselite | | | | |
| $\Gamma_v$ | -0.12 | -0.12 | 0.07 | 0.18 | -0.11 | -0.11 | 0.11 | 0.20 |
| $\Gamma_c$ | 0.97 | 0.91 | 1.40 | 1.32 | 1.09 | 1.07 | 1.54 | 1.52 |
| $X_v$ | 0.00 | 0.00 | 0.19 | 0.29 | 0.00 | 0.00 | 0.15 | 0.23 |
| $X_c$ | 1.05 | 1.00 | 1.53 | 1.46 | 1.10 | 1.08 | 1.62 | 1.60 |
| $Z_v$ | -0.23 | -0.24 | -0.06 | 0.02 | -0.09 | -0.09 | 0.04 | 0.14 |
| $Z_c$ | 0.92 | 0.91 | 1.37 | 1.35 | 0.94 | 0.93 | 1.42 | 1.42 |
| | | | | Bismuthinite | | | | |
| $\Gamma_v$ | -0.10 | -0.04 | -0.04 | 0.08 | -0.14 | -0.12 | -0.14 | -0.04 |
| $\Gamma_c$ | 1.14 | 1.14 | 1.57 | 1.48 | 1.28 | 1.30 | 1.76 | 1.68 |
| $X_v$ | 0.00 | 0.00 | 0.02 | 0.09 | 0.00 | 0.00 | -0.03 | 0.04 |
| $X_c$ | 1.50 | 1.67 | 2.04 | 2.09 | 1.61 | 1.63 | 2.18 | 2.09 |
| $Z_v$ | -0.15 | -0.11 | -0.13 | -0.04 | -0.08 | -0.07 | -0.11 | -0.04 |
| $Z_c$ | 1.43 | 1.51 | 1.89 | 1.93 | 1.41 | 1.45 | 1.93 | 1.89 |
| | | | | Guanajuatite | | | | |
| $\Gamma_v$ | -0.02 | -0.02 | 0.18 | 0.30 | -0.07 | -0.04 | 0.11 | 0.26 |
| $\Gamma_c$ | 0.95 | 0.89 | 1.39 | 1.24 | 1.17 | 1.16 | 1.63 | 1.54 |
| $X_v$ | 0.00 | 0.00 | 0.19 | 0.28 | 0.00 | 0.00 | 0.18 | 0.27 |
| $X_c$ | 1.07 | 1.18 | 1.61 | 1.58 | 1.04 | 1.06 | 1.59 | 1.45 |
| $Z_v$ | -0.24 | -0.19 | -0.06 | 0.05 | -0.14 | -0.12 | 0.04 | 0.12 |
| $Z_c$ | 1.17 | 1.25 | 1.63 | 1.65 | 1.16 | 1.18 | 1.64 | 1.57 |

Table 8.4: Quasiparticle energies of stibnite, antimonselite, bismuthinite and guanajuatite at the high-symmetry points $\Gamma$, $X$, $Z$ vs. the corresponding DFT/LDA eigenvalues. We report both sets of results obtained using optimised or experimental lattice parameters. The columns labelled "S" and "w/o S" indicate calculations with and without semicore electrons, respectively. For each high-symmetry point we consider the energies at the valence band top (e.g. $\Gamma_v$) and the conduction band bottom (e.g. $\Gamma_c$). All values are in units of eV.

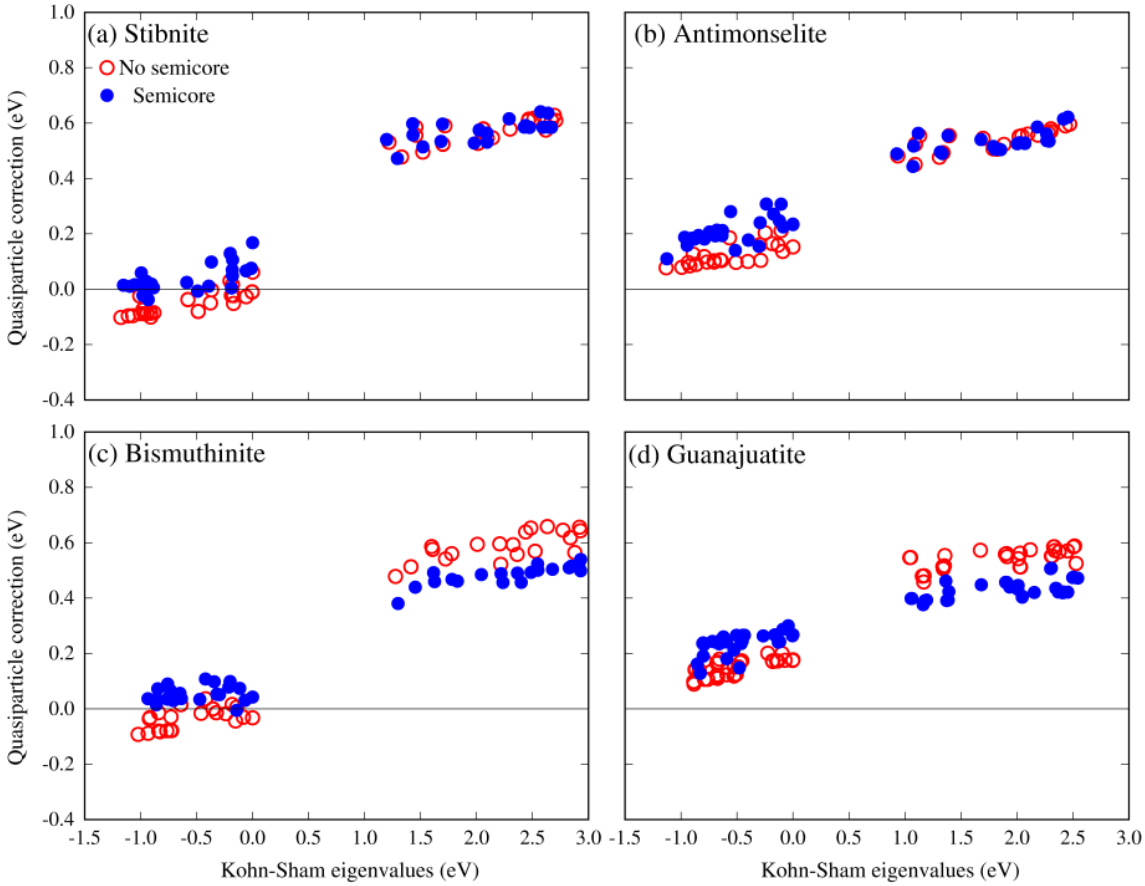


Figure 8.3: Quasiparticle corrections as a function of the corresponding DFT/LDA eigenvalues for (a) stibnite, (b) antimonselite, (c) bismuthinite, and (d) guanajuatite. Only eigenvalues at the high-symmetry points Γ, $X$ and $Z$ are considered. Blue disks and red circles indicate calculations with and without semicore electrons, respectively. All calculations were performed using experimental lattice parameters.

by a similar amount (∼0.1 eV). As a result of these small changes, the quasiparticle corrections to the band gaps calculated with or without semicore electrons can differ by up to 0.2 eV (Table 8.4).

Semicore electrons appear to slightly reduce the quasiparticle corrections as compared to calculations without the semicore. Similarly to the case of $CH_3NH_3PbI_3$, the semicore $d$ states introduce additional contributions to $\Sigma_x$ and $\Sigma_c$. Of these contributions, the change in the correlation self energy is small upon inclusion of semicore $d$ states, due to the large energy separation between semicore states and conduction states. For the exchange self energy the contribution of the $d$ states does not contain the energy denominators but it is sensitive to the overlap between band edge states and semicore states. This can be observed in Figure 8.4 where we can see how the inclusion of

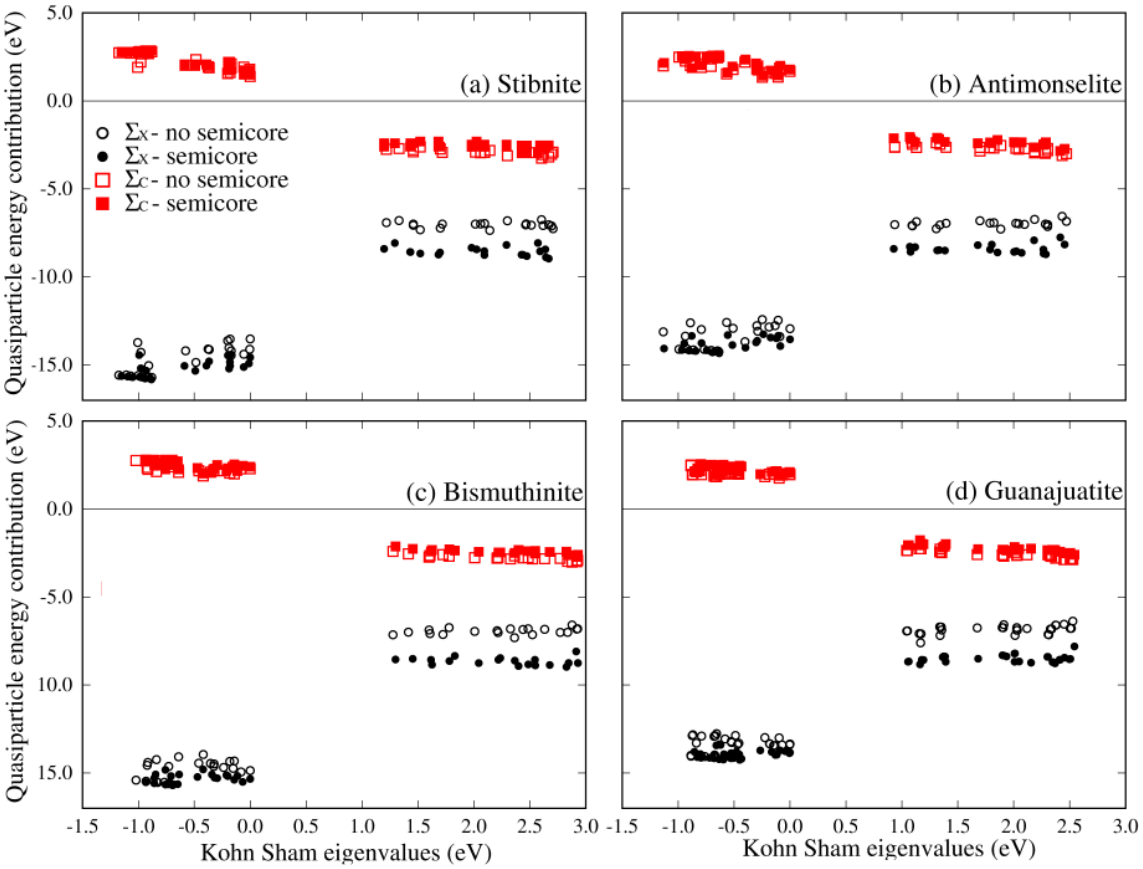


Figure 8.4: Exchange (black disks and circles) and correlation (red filled and empty squares) self energy contributions to the quasiparticle corrections vs DFT/LDA eigenvalues for (a) stibnite, (b) antimonselite, (c) bismuthinite and (d) guanajuatite. Only eigenvalues at the high symmetry points Γ, $X$ and $Z$ are considered. Filled and empty symbols indicate calculations with and without semicore states respectively. All calculations were performed using experimental lattice parameters.

semicore electrons affects each the exchange and correlation self energy.

Table 8.4 reports the DFT/LDA eigenvalues and the corresponding quasiparticle corrections for the valence band top and conduction band bottom at the high symmetry points Γ, $X$ and $Z$. From this table we see that the LDA band gaps at these points are sensitive to the choice of lattice parameters and this sensitivity is reflected in the corresponding quasiparticle energies. Calculations performed using optimised lattice parameters or experimental parameters can differ by up to 0.3 eV. This observation may explain the lack of consensus between previous computational investigations of the band structures of these compounds [20, 237, 264, 266].

Taken together the sensitivity of the quasiparticle energies to the presence of semicore

electrons and to the choice lattice parameters leads to non-negligible variations in the calculated band gaps. Given that the quasiparticle calculations performed using the experimental lattice parameters yield band gaps closer to the experimental values, for the rest of this chapter we will focus on calculations using the experimental lattice parameters including semicore *d* electrons for Sb and Bi. We consider these choices yield our best estimates for the quasiparticle energies of these compounds.

### 8.2.3 Relativistic corrections

We calculate the relativistic corrections within DFT/LDA for all four structures using the experimental structure. In Figure 8.5 we show a comparison of the band structure of $Sb_2S_3$ and $Bi_2S_3$ calculated with and without the inclusion of relativistic spin-orbit corrections. From Figure 8.5 we can see that the effect of spin-orbit coupling is, as expected, larger in the case of $Bi_2S_3$ than in the case of $Sb_2S_3$. More importantly, from Figure 8.5 we can see that the band structures obtained including spin-orbit coupling maintain a similar topology of the valence band edges. This observation allows us to include the contribution from relativistic effects to the final quasiparticle band gaps as rigid scissor corrections.

The corrections to the band edges at the high-symmetry points Γ, *X* and *Z* are reported in Table 8.5 In all four semiconductors the inclusion of spin-orbit coupling does not alter the top of the valence band. This is consistent with the observation that the states at the valence band top are predominantly associated with S or Se *p* states. On the other hand the bottom of the conduction bands are of Bi of Sb *p* character, hence a spin-orbit splitting is observed in this case (Figure 8.5). As expected, the spin-orbit coupling effect is very small in the case of $Sb_2S_3$ and $Sb_2Se_3$, lowering the conduction band minima by less than 0.1 eV. In the case of $Bi_2S_3$ and $Bi_2Se_3$ the spin orbit coupling lowers the band gap by 0.3-0.4 eV.

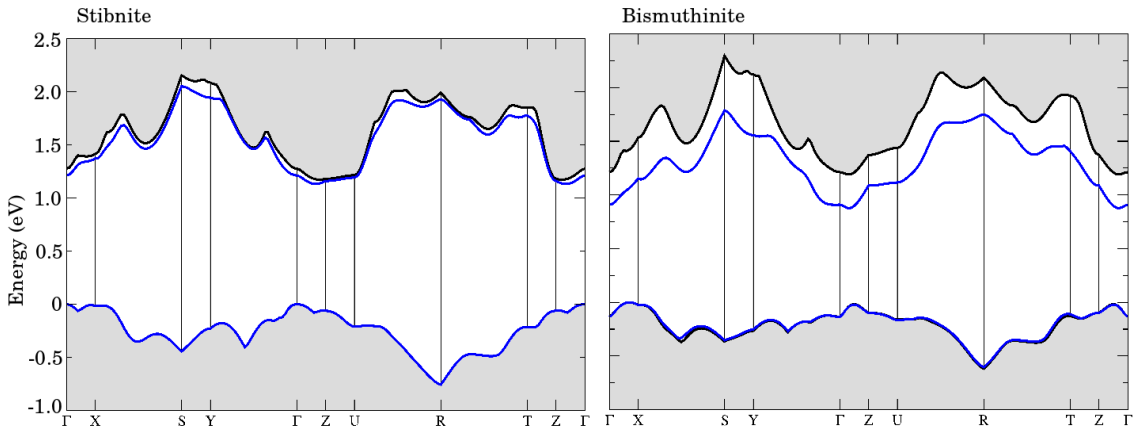


Figure 8.5: Comparison between the DFT/LDA valence and conduction band edges of stibnite and bismuthinite with (blue lines) and without (black lines) spin-orbit coupling, calculated for the experimental lattice parameters. The path for which the band structure is calculated includes the following high symmetry points (in reciprocal lattice units): X (0.5,0,0), S (0.5,0.5,0), Y (0,0.5,0), Z (0,0,0.5), T (0,0.5,0.5), U (0.5,0,0.5), R (0.5,0.5,0.5). The grey shading covers the features of the valence and conduction bands above the band edges.

| | $Sb_2S_3$ | | $Sb_2Se_3$ | | $Bi_2S_3$ | | $Bi_2Se_3$ | |
|---|---|---|---|---|---|---|---|---|
| | SR | SOC | SR | SOC | SR | SOC | SR | SOC |
| $\Gamma_v$ | 0.00 | 0.00 | -0.11 | 0.00 | -0.12 | -0.02 | -0.04 | -0.01 |
| $\Gamma_c$ | 1.29 | -0.06 | 1.07 | -0.05 | 1.30 | -0.32 | 1.16 | -0.38 |
| $X_v$ | -0.01 | 0.00 | 0.00 | 0.00 | 0.00 | -0.02 | 0.00 | -0.02 |
| $X_c$ | 1.43 | -0.04 | 1.08 | -0.03 | 1.63 | -0.40 | 1.06 | -0.27 |
| $Z_v$ | -0.06 | 0.00 | 0.09 | 0.00 | -0.07 | -0.02 | -0.12 | -0.01 |
| $Z_c$ | 1.20 | -0.02 | 0.93 | -0.02 | 1.45 | -0.31 | 1.18 | -0.28 |

Table 8.5: Relativistic corrections calculated for stibnite, antimonselite, bismuthinite and guanajuatite at high-symmetry points. The column labelled "SR" indicates the scalar relativistic values of the band edges, while the column labelled "SOC" reports the corresponding relativistic corrections. All calculations are performed using the experimental structures and including semicore $d$ states. All values are in units of eV.

### 8.2.4 Band gaps

Table 8.6 reports the quasiparticle band gaps calculated using the experimental structures, including semicore electrons and relativistic corrections. The band gaps are obtained by considering the band extrema at Γ, $X$ and $Z$ and we give both the fundamental gap and the direct gap. While in antimonselite and bismuthinite the calculated minimum band gap is indirect, and the difference between direct and indirect gaps is

| | Previous | Present |
|---|---|---|
| | DFT | |
| $Sb_2S_3$ | 1.55[a], 1.76[b], 1.3[c], 1.18[d], 1.22[e] | 1.23 |
| $Sb_2Se_3$ | 1.14[a], 0.99[d], 0.79[k], 0.89[e] | 1.13 (0.91) |
| $Bi_2S_3$ | 1.47[a], 1.32[n], 1.63[n], 1.45[n], 1.67[n] | 1.12 (1.00) |
| $Bi_2Se_3$ | 0.9[a], 1.1[r] | 0.83 |
| | *GW* | |
| $Sb_2S_3$ | 1.67[e] | 1.54 |
| $Sb_2Se_3$ | 1.21[k] | 1.27 (1.17) |
| $Bi_2S_3$ | | 1.42 (1.34) |
| $Bi_2Se_3$ | | 0.91 |
| | Experiment | |
| $Sb_2S_3$ | 1.73[f], 1.42-1.65[g], 1.78[h], 1.7[i], 1.74[j] | |
| $Sb_2Se_3$ | 1.55[l], 1.2[i], 1.0 - 1.2[m] | |
| $Bi_2S_3$ | 1.4[o], 1.38[p], 1.58[q,j] | |
| $Bi_2Se_3$ | | |

[a] Ref. 237, [b] Ref. 263, [c] Ref. 20, [d] Ref. 264, [e] Ref. 265, [f] Ref. 243, [g] Ref. 252, [h] Ref. 253, [i] Ref. 250, [j] Ref. 251,[k] Ref. 266, [l] Ref. 247, [m] Ref. 254, [n] Ref. 269, [o] Ref. 255, [p] Ref. 256, [q] Ref. 249, [r] Ref. 270

Table 8.6: Comparison between calculated and measured band gaps of stibnite, antimonselite, bismuthinite, and guanajuatite. We report the direct band gaps calculated within DFT (Kohn-Sham gaps) and *GW* (quasiparticle gaps), and the measured optical gaps. The values in parenthesis indicate the calculated indirect band gaps in each case. All band gaps are in eV. The direct gaps are reported for Γ ($Sb_2S_3$ and $Bi_2S_3$), $X$ ($Bi_2Se_3$), and $Z$ ($Sb_2Se_3$). Our calculations include semicore electrons and were performed using the experimental lattice parameters.

within 0.1 eV, in guanajuatite and stibnite the fundamental gap is direct. These results suggest that all four compounds can be considered "quasi-direct" gap semiconductors for practical photovoltaic applications. The calculated direct gaps are 1.54 eV (stibnite), 1.27 eV (antimonselite), 1.42 eV (bismuthinite) and 0.91 eV (guanajuatite). As shown in Table 8.6 these values are in line with previous *GW* calculations where available [265, 266], and also close to measured optical gaps.

Figure 8.6 provides a schematic view of our final calculated band gaps (*GW*+SOC) compared to the Kohn Sham band gaps (DFT/LDA + SOC) and experiment. The comparison with experimental data is not straightforward since the experimental literature

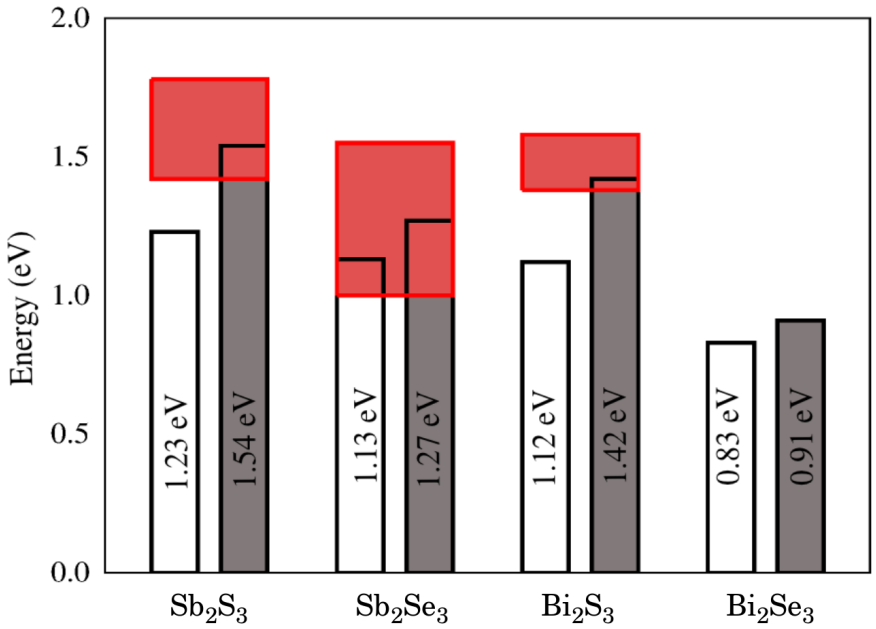


Figure 8.6: Schematic summary of the band gaps of stibnite, antimonselite, bismuthinite and guanajuatite: Kohn-Sham gaps (empty rectangles) and GW gaps (filled rectangles) including relativistic corrections. The band gaps were obtained by including semicore electrons and using experimental lattice parameters. The red rectangles indicate the range of experimental optical gaps shown in Table 8.6.

appears to only report optical gaps, as seen in Table 8.5, while our calculations refer to quasiparticle gaps and do not include excitonic effects. The agreement between our calculated quasiparticle gaps and the measured optical gaps can be seen *a posteriori* as an indication that the excitonic shifts are small in this class of semiconductors. This is in agreement with Ref. [260] where the exciton binding energy of $Bi_2S_3$ was estimated at 28 meV.

Taking the calculated quasiparticle band gaps as representative of the optical gaps, the four semiconductors considered here lie in the range of the optimal Shockley-Queisser performance. In Figure 8.7 we show an analysis of the maximum attainable efficiency of semiconductor-sensitised solar cells based on stibnite, antimonselite, bismuthinite and guanajuatite as performed in Chapter 6 for the case of the hypothetical perovskites [17]. Here, we calculate the maximum attainable efficiency by taking into account five values of the loss-in-potential: 0.0, 0.2, 0.4, 0.6 and 0.9 eV, using a fill factor of 65% and an IPCE of 80%. In Figure 8.7 we also show the theoretical effi-

ciencies calculated for the experimental band gaps for $Sb_2S_3$ and $Sb_2Se_3$ as reported in Ref [233] and Ref [32] respectively. The values for the fill factor and IPCE are chosen to match those of the best performing $Sb_2S_3$ cell, reported in Ref. [233], with an efficiency of 7.5% and a 0.9 eV loss in potential. According to our calculations, the maximum attainable efficiency for these parameters and corresponding experimental band gap is of 10%. The red dotted line on the left hand side is marked to highlight the best performing SSSC employing antimonselite. In this case, we calculate a maximum attainable efficiency of approximately 6%, while the reported value is of 3.7% [32] (with a smaller fill factor of 47%).

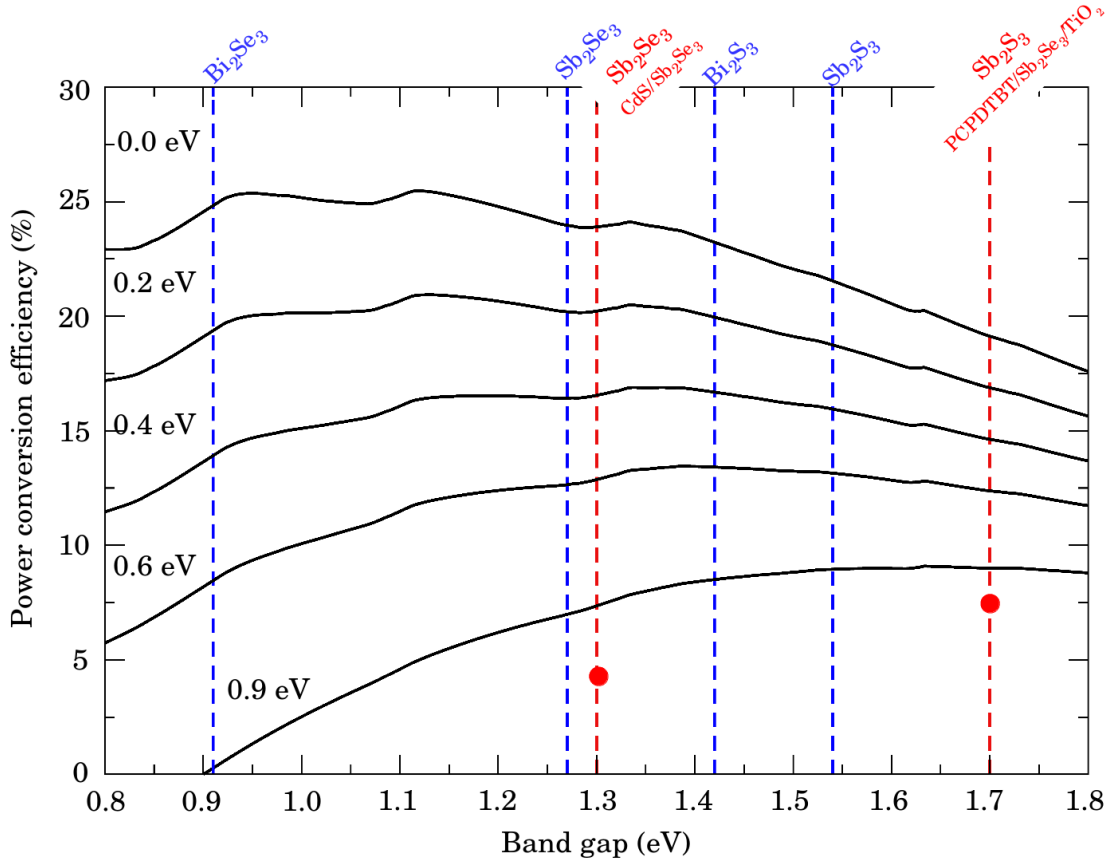


Figure 8.7: Ideal efficiencies of nanostructured solar cells based on semiconductors of the stibnite family. The theoretical efficiencies as a function of the band gap energy (black solid curves) are calculated as detailed in Chapter 1 and Ref. [17] for five values of the loss-in-potential of 0.0, 0.2, 0.4, 0.6 and 0.9 eV, a fill factor of 65%, and IPCE of 80%. The blue dotted lines mark the *GW* calculated band gaps for stibnite, antimonselite, bismuthinite and guanajuatite. The red dotted lines mark the experimental band gaps calculated in Ref. [233] (stibnite) and [32] (antimonselite). The hetero-junction employed in the stibnite and antimonselite solar cells are marked in red writing above the plot. The red disks mark the power conversion efficiencies reported in Refs [32, 233] respectively.

From the calculated theoretical efficiencies, we note that for large values of the loss-in-potential stibnite is indeed the best choice for light absorbing material, due to its optimum band gap. However, as the loss-in-potential decreases the theoretical efficiency improves substantially as the band gap of the light sensitiser decreases. For example, in the ideal case of a vanishing loss-in-potential the power conversion efficiency improves by up to 16% if stibnite is replaced by guanajuatite, and by up to 13% if antimonselite and bismuthinite is used instead. These results suggest that antimonselite, bismuthinite and guanajuatite could also be promising candidates for light absorbers in SSSCs.

## 8.3 Summary

In this chapter we reported a systematic study of quasiparticle band structures of the four isostructural metal chalcogenides: $Sb_2S_3$, $Sb_2Se_3$, $Bi_2S_3$ and $Bi_2Se_3$ within the *GW* approximation. We have shown that the inclusion of semicore electrons in the calculations is found to modify the band gaps by up to 0.2 eV and the choice of experimental versus optimised lattice parameters can lead to differences in the band gap of up to 0.3 eV. These findings indicate that some caution should be used in discussing theoretical band gaps of these materials and in comparing with experiment. Furthermore, relativistic effects were found to lower the conduction bands of all four materials. Spin-orbit coupling effects were found important in $Bi_2S_3$ and $Bi_2Se_3$, where they reduce the band gaps by 0.3-0.4 eV, while they essentially negligible in $Sb_2S_3$ and $Sb_2Se_3$.

Our calculations indicated that all four compounds have direct band gaps, barring indirect transitions marginally below the direct gap. The calculated band gaps are 1.54 eV ($Sb_2S_3$), 1.27 eV ($Sb_2Se_3$), 1.42 eV ($Bi_2S_3$) and 0.91 eV ($Bi_2Se_3$). These values fall within the range of measured optical gaps, although a considerable scatter exists among experimental data, possibly due to different preparation conditions.

We estimated the ultimate performance of solar cells based on these compounds as light sensitisers using Eq. 1.11. While, Refs. [20, 28] have shown that bismuthinite does not work as a semiconductor sensitiser for $TiO_2$, owing to the incorrect energy level alignment at the interface, it cannot be excluded that other electron conductors would form a type-II hetero-junction with these four semiconductors. Based on the estimated maximum maximum attainable efficiency we showed that by increasing the fill factor and the open-circuit voltage, the efficiency of existing solar cell devices based on stibnite and antimonselite can be improved significantly. Furthermore, we showed that if the loss-in-potential could be reduced, antimonselite, bismuthinite and guanajuatite sensitisers could yield efficiencies exceeding those of stibnite by more than 16%.

Further work is required to understand the recombination mechanisms in solar cells employing metal chalcogenide light sensitisers. Recombination rate in stibnite was shown to be influenced by the thickness of the light absorbing layer and impact significantly the solar cell performance [279]. Furthermore, future calculations should address the optical absorption spectra of these compounds within the Bethe-Salpeter approach, in order to establish whether excitonic effects are as small as our data appear to suggest. Moreover, excitonic effects are likely to enhance as the dimensionality of the structure is reduced, which is possible in the context of these semiconductors. Synthesis of individual nanoribbons of these metal chalcogenides should be achievable due to their weak van der Waals like bonding, potentially through liquid-phase exfoliation techniques, which have become increasingly popular in recent years [280].

# Chapter 9

# Conclusions

## 9.1 Summary

Research behind development of novel photovoltaic devices is extremely complex and involves a thorough understanding of the materials components from their fundamental physical properties all the way to device engineering. At the fundamental level first principles modelling can contribute to these efforts through two principal pathways: by improving the understanding of existing materials and by assisting materials discovery. In this thesis, we have used computational methods to analyse two promising groups of light sensitising materials: hybrid organic-inorganic metal-halide perovskites, and metal chalcogenides of the stibnite family.

Hybrid inorganic-organic perovskites have shown unprecedented progress in just four years, and have polarised the attention of the photovoltaics research community. The success of these materials has been due in large part to their remarkable electronic and optical properties: high absorption in the visible range and long electron and hole diffusion lengths. While the hybrid organic-inorganic solar cells have had an already successful start, it is obvious that there is potential for significant improvement. In this context a better understanding of the fundamental physical properties of the champion

material $CH_3NH_3PbI_3$ is a priority.

In this thesis we have focused on the structural and electronic properties of $CH_3NH_3PbI_3$ and related Pb-I perovskites, and have dedicated three chapters to the analysis of our results. The first study discussed in Chapter 4 was aimed at analysing the electronic structure of $CH_3NH_3PbI_3$ within the density functional theory and the *GW* method. We identified the sensitivity of electronic structure calculations to factors such as relativistic spin-orbit coupling effects, the inclusion of semicore electrons, and the correct description of the crystal structure. Furthermore, we have devised a simple self-consistent scissor *GW* method, which led to a calculated band gap of $CH_3NH_3PbI_3$ in good agreement with experiment.

In Chapter 5 we performed a more systematic analysis of the interplay between the the geometry of the inorganic Pb-I network and the electronic structure, identifying two Pb-I-Pb bond angles (apical and equatorial) as the principal descriptor of the orthorhombic perovskite unit cell. We constructed orthorhombic Pb-I perovskite structures by uniformly varying these two bond angles, and calculated the band gaps of each of these ideal systems. Finally, we obtained a map of band gaps as a function of the two bond angles. Within this approach, we identified that the increase in the Pb-I-Pb bond angles determines a decrease of the band gap. Furthermore, by exploring a range of cations, we showed that the Pb-I-Pb bond angles and the band gaps can be tuned due to the steric size of this cation. In this context, we highlighted $AsH_4PbI_3$ and $SbH_4PbI_3$ as two possible new perovskite structures with the highest potential for applications as light sensitisers.

In Chapter 6 we used the method established in Chapter 4 to study the electronic properties of $AsH_4PbI_3$ and $SbH_4PbI_3$. Moreover, we extended this study to the two other pnictogen cations $NH_4PbI_3$ and $PH_4PbI_3$ in order to verify whether the trend obtained in Chapter 5 is robust. Using the band gaps calculated within SS-*GW* we estimated the maximum attainable efficiency attainable from implementing these semiconductor

into photovoltaic devices, as detailed in Chapter 1. We obtained that $SbH_4PbI_3$ could increase the power conversion efficiency by up to 8% in the ideal limit of a vanishing loss-in-potential.

The second part of this thesis was focused on the metal-chalcogenides of the stibnite family: stibnite, antimonselite, bismuthinite and guanajuatite. These materials have shown promise as semiconductor sensitisers in photovoltaic applications, however experimental and computational studies of the electronic and optical properties of these materials showed significant variability in the reported band gaps. In Chapter 8 we performed a study of the electronic and optical properties of this group of materials within density functional theory and the *GW* method, in a similar way as in Chapter 4. We analysed the sensitivity of the calculated band gaps to relativistic spin-orbit coupling effects, semicore electrons and changes in the crystal structure. Finally, we analysed the calculated band gaps in the context of the maximum attainable theoretical efficiency for a solar cell, in the same spirit as the approach used in Ref [17]. We concluded that all four metal-chalcogenides would be promising light sensitisers in photovoltaic applications.

## 9.2 Outlook

Currently there are several open questions involving hybrid organic-inorganic perovskites which are actively investigated: the problem of the current-voltage hysteresis of HOPSCs, understanding the mechanisms of recombination and charge transfer in hybrid organic-inorganic perovskites as well as their excitonic properties. Tackling these problems within a first principles approach should involve a thorough analysis of the excitonic properties and the effect of electron-phonon interaction of hybrid organic-inorganic perovskites. Furthermore, there is an urgent requirement for a targeted first principles materials design strategy, focusing on the replacement of the toxic Pb element in metal-halide perovskites.

Nanostructured stibnite, antimonselite, bismuthinite and guanajuatite are becoming attractive due to their natural quasi-one dimensional crystal structure. However, the electronic and optical properties of these metal-chalcogenide nanoribbons are yet to be fully understood. In this context, knowledge acquired from the study of the electronic structure of bulk metal-chalcogenides should be used as a starting point for the analysis of the structural, electronic and excitonic properties of these nanomaterials.

These open questions certainly constitute a challenging set of tasks for the study of these novel semiconductors. However, approaching these problems from first principles opens an exciting perspective, not just towards the understanding of the unique physical properties of these materials, but also towards the design and discovery of novel materials. We hope that the work presented in this thesis has demonstrated this potential and that our results constitute a step forward, as well as a reliable starting point for future research of these fascinating compounds.

# Appendix

# Computational details

## A.1 Computational setup for Chapter 4

### A.1.1 DFT calculations

#### Pseudopotentials

For C, N and H we use non-relativistic norm conserving von Barth-Car [281] pseudopotentials from the `Quantum ESPRESSO` pseudopotential library. For Pb and I we generate two sets of Troullier-Martins [104] norm-conserving, fully relativistic pseudopotentials using the `ld1.x` pseudopotential generation tool of the `Quantum ESPRESSO` suite. We consider the following valence configurations: Pb without ($6s^2 6p^2$) or with semicore states ($5d^{10} 6s^2 6p^2$), I without ($5s^2 5p^5$) or with semicore states ($4d^{10} 5s^2 5p^5$).

#### Convergence tests

The total energy is converged within 6 meV/atom using a plane waves kinetic energy cutoff of 100 Ry for the calculations without I-4$d$ semicore electrons. In order to

achieve the same level of convergence in the presence of I-4*d* states we employ a cutoff of 150 Ry. Self-consistent calculations are performed using a $6\times6\times6$ Γ-centred Brillouin zone grid, comprising of 112 irreducible points. The non-collinear spin-orbit coupling calculations show vanishing magnetisation in convergence tests. Therefore, all subsequent calculations are performed with vanishing magnetisation in order to limit computational effort.

### A.1.2 *GW* calculations

#### Plasmon pole approximation

In order to check whether the plasmon-pole approximation is adequate for $CH_3NH_3PbI_3$ we check the sensitivity of the calculated band gap to the plasmon pole parameter $\omega_p$. To this aim we perform $G_0W_0$ calculations using $\omega_p = 7,\ 14,\ 20,\ 27$ and 34 eV. The corresponding variation of the gap is found to be at most of 10 meV, suggesting that the dynamical screening is correctly described. These tests correspond to scalar-relativistic calculations in the absence of semicore electrons, using 240 unoccupied states, kinetic energy cutoffs of 136 eV and 54 eV for the exchange and correlation parts of the self energy, respectively, and an unshifted $2\times2\times2$ Brillouin zone grid.

#### Brillouin zone sampling

We test the convergence of the quasiparticle band gap with respect to the sampling of the Brillouin zone used in the convolution of $G$ and $W$ by comparing the band gaps obtained using unshifted $2\times2\times2$, $3\times3\times3$ and $4\times4\times4$ meshes (with 8, 14 and 26 irreducible **k**-points respectively). The band gap is found to change by less than 10 meV throughout. These tests were carried out using the same parameters as reported in the previous paragraph.

**Unoccupied states**

Since the planewaves kinetic energy cutoff for the polarisability and the number of unoccupied states depend on whether we include semicore *d* states in our calculations, we study the convergence for all four combinations of pseudopotentials for Pb and I. For completeness we carry out these tests for both scalar-relativistic and fully-relativistic calculations. In total we consider 8 scenarios, as shown in Figure A.1.

In order to determine optimal cutoff parameters we perform convergence tests for both $\Sigma_x$ and $\Sigma_c$ separately. We found that a cutoff of 408 eV is sufficient to achieve convergence for $\Sigma_x$ in all cases.

In the case of $\Sigma_c$ we test the convergence of the band gap with the number of empty states, for polarisability cutoffs ranging from 14 to 82 eV for all cases, and using an exchange cutoff of 136 eV in all cases. We define an energy cutoff for the unoccupied states using the highest energy state at Γ, relative to the valence band top. As a reference, the rightmost data points in Figure A.1a and c correspond to 1000 bands in total.

In the case of the fully relativistic calculations the number of bands that need to be evaluated doubles with respect to the scalar relativistic calculations. This can be seen in Figure A.1a and c where 1000 states correspond to a cutoff of 30 eV and 55 eV in the fully relativistic and scalar relativistic cases respectively. However, from Figure A.1 we can see that the scalar and fully relativistic curves follow very similar trends. This is expected given that the same pseudopotentials are used for both sets of calculations. By comparing the convergence trends in the scalar and fully relativistic cases we estimate that the fully-relativistic gaps calculated for the right-most points in Figure A.1c are converged within less than 0.1 eV in all cases.

**Polarisability cutoff**

The convergence of the band gap with respect to the polarisability cutoff is shown in

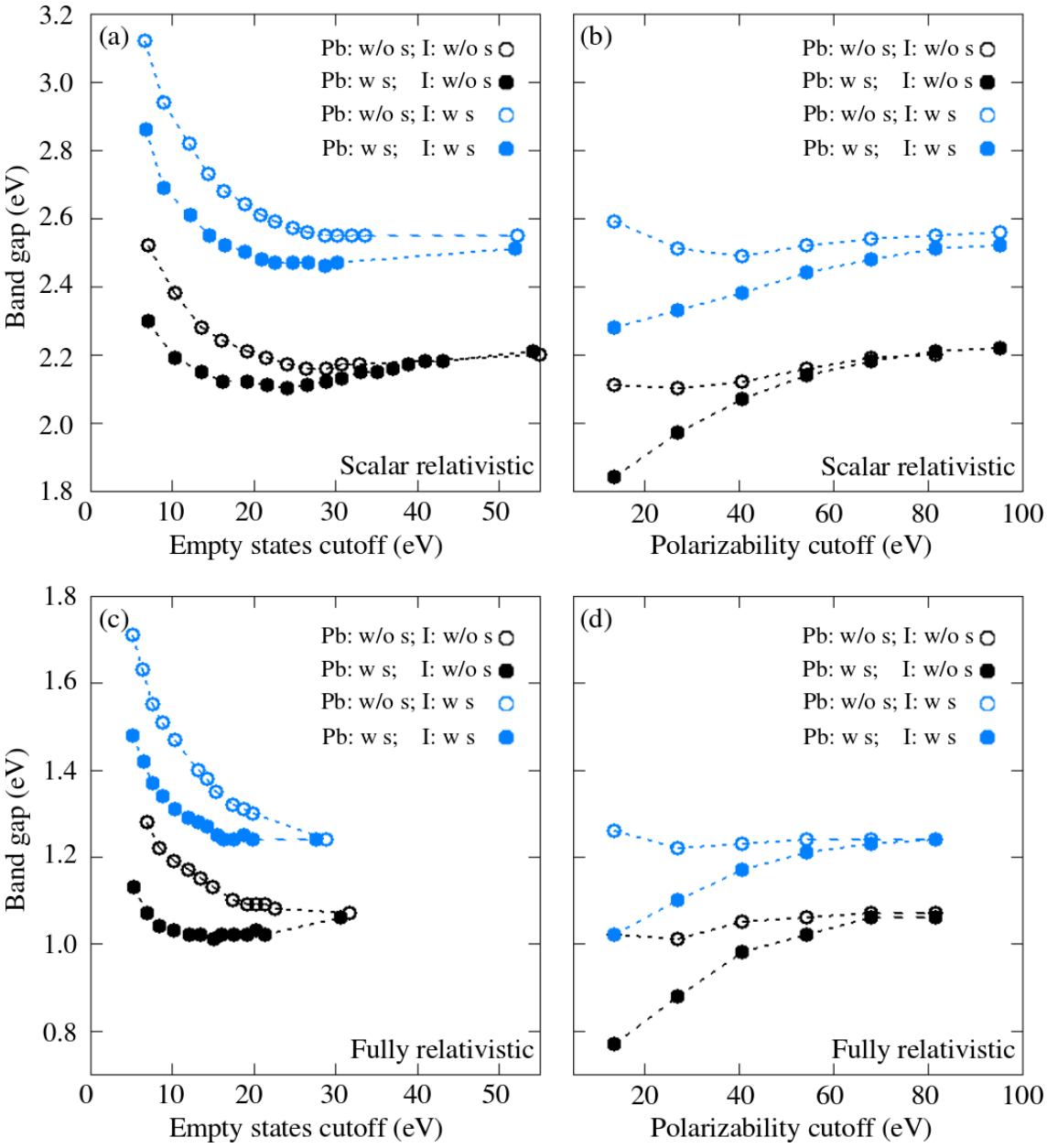


Figure A.1: Convergence of the quasiparticle band gap of $CH_3NH_3PbI_3$ with respect to the energy cutoff for unoccupied states [(a) and (c)], and with respect to the plane wave kinetic cutoff for the polarisability [(b) and (d)]. Panels (a) and (b) refer to scalar relativistic calculations while (c) and (d) are for fully relativistic band gaps. In each panel we show results for all four combinations of pseudopotentials considered here: Pb and I without semicore states ('w/o s', black empty circles), Pb without semicore ('w s') and I without semicore (black filled circles), Pb without semicore and I with semicore states (blue empty circles), Pb and I with semicore states (blue filled circles). These data correspond to a $2 \times 2 \times 2$ Γ-centred Brillouin zone mesh, and a 136 plane wave cutoff for the exchange self energy. The planewaves cutoff for the polarisability in panels (a) and (c) is set to 82 eV, and the number of total bands in (b) and (d) is set to 1000.

Figure A.1b and d. The calculations are performed using 1000 bands in all cases. In order to contain the computational effort we tested cutoffs up to 95 eV in the scalar relativistic case and 82 eV in the fully relativistic case. In all cases considered the quasiparticle band gaps appear converged when using a polarisability cutoff of 82 eV.

It is worth noting at this point that for all convergence tests performed in this study the target quantity is the band gap, which is known to converge much faster with the energy cutoff parameters than the absolute quasiparticle energies. For band alignment studies, for example, further convergence tests would be required to ensure accuracy [91].

Based on these convergence tests the final calculation parameters are set as follows:

- Exchange cutoff: 408 eV,
- KS plane wave cutoff: 408 eV,
- Polarisability cutoff: 82 eV,
- Number of bands: 1000,
- Brillouin zone sampling: unshifted $2 \times 2 \times 2$ grid,
- Plasmon-pole parameter: 27 eV.

## A.2 Computational setup for Chapter 5

### A.2.1 DFT calculations

#### Pseudopotentials

For Pb and I we use scalar relativistic and fully relativistic ultrasoft pseudopotentials including non-linear core correction found on in the `Quantum ESPRESSO` library, both for calculations without and with spin-orbit coupling. For Pb we use the $5d^{10}6s^26p^2$ valence configuration, while for I we use a $5s^25p^5$ valence configuration. For all atomic

components except Sb, Rb and Cs we use ultrasoft pseudopotentials from the `Quantum ESPRESSO` library, while for Sb, Rb and Cs we use norm-conserving pseudopotentials.

#### Convergence

The electron wave functions and the charge density are expanded in planewaves basis sets with energy cutoffs of 40 Ry and 200 Ry respectively. Structural optimisations are performed by sampling the Brillouin zone using uniform and unshifted 4×4×4 meshes. Electronic structure calculations are performed using a 6×6×6 Brillouin zone grid. All structural optimisations are initialised using the crystallographic data for $CH_3NH_3PbI_3$ reported in Ref. [146]. The initial coordinates for the molecular cations are chosen so that the centre of mass is located in the middle of the cuboctahedral cavity, and the orientation of the four inequivalent cations in one unit cell follows the symmetry properties of the *Pnma* space group.

## A.3 Computational setup for Chapter 6

#### Pseudopotentials

For Pb and I we use the norm-conserving pseudopotentials with semicore generated for the calculations described in Chapter 4. Norm conserving pseudopotentials from the `Quantum ESPRESSO` library are used for H, N, P, As, Sb and Cs.

#### Convergence

All DFT and *GW* calculations performed in this chapter use the same calculation parameters as in Chapter 4.

## A.4 Computational setup for Chapter 8

### A.4.1 DFT calculations

#### Pseudopotentials

For calculations without spin-orbit coupling we use Troullier-Martins norm-conserving scalar-relativistic pseudopotentials generated using the `FHI98` code [103]. In the case of S(Se) the $3s^2 3p^4$ ($4s^2 4p^4$) electrons are included in the valence as usual. For Sb and Bi we generate two sets of pseudopotentials, one set with 5 electrons in the valence, i.e., $5s^2 5p^3$ and $6s^2 6p^3$ respectively, and one set with the semicore $4^{10}$ and $5d^{10}$ electrons included respectively.

For fully relativistic calculations we generate a set of fully relativistic norm-conserving pseudopotentials including semicore $d$ states for Sb and Bi using the `ld1.x` program of the `Quantum ESPRESSO` package.

#### Convergence

The electronic wave functions are expanded in plane-wave basis sets with kinetic energy cutoffs of 70 Ry ($Sb_2Se_3$, $Bi_2Se_3$) and 90 Ry ($Sb_2S_3$ and $Bi_2S_3$) for the calculations without semicore states and 100 Ry ($Bi_2S_3$, $Bi_2Se_3$) and 130 Ry ($Sb_2S_3$, $Sb_2Se_3$) when semicore states are included. In each case considered the selected cutoff yields a total energy converged to within 2 meV/atom. Fully relativistic pseudopotentials use the same cutoffs as those obtained for the scalar-relativistic pseudopotentials with semicore.

All self-consistent calculations are carried out using a $8\times8\times8$ Brillouin zone mesh centred at $\Gamma$, corresponding to 170 irreducible points for $Sb_2S_3$ and $Bi_2S_3$ and 260 points for $Sb_2Se_3$ and $Bi_2Se_3$. The non-collinear spin-orbit coupling calculations show vanishing magnetisation in convergence tests, and for this reason subsequent calculations

are performed with vanishing starting magnetisation. Full geometry optimisations of lattice parameters and atomic positions in each case are performed both with and without semicore *d* states using a $4 \times 8 \times 4$ Γ-centred Brillouin zone mesh.

### A.4.2 *GW* calculations

All *GW* calculations are performed using the `SaX` code [89].

#### Exchange cutoff parameters

For the exchange self energy we use a (over-converged) kinetic cutoff of 75 Ry for calculations without semicore and 100 Ry for calculations with semicore.

#### Plasmon pole parameters

The energy dependence of the correlation contribution $\Sigma_c$ arising from the dynamically screened Coulomb interaction is described via the Godby-Needs plasmon-pole model. We use a plasmon energy of 1 Ry for all materials, similar to the energy of the peaks in the calculated electron energy loss spectra.

#### Number of bands

In Figure A.2a we show the convergence of the band gap with respect to the energy of the highest unoccupied state included in the polarisability. Based on the trend shown in this figure we find that all calculations are converged for a total number of 320 bands.

#### Polarisability cutoff

For the correlation contribution we perform convergence tests by calculating the band gap at various kinetic energy cutoffs up to 7 Ry for the polarisability. Figure A.2a shows that the band gap is converged within 0.05 eV already for a cutoff of 5 Ry. The dependence of the band gap on the polarisability cutoff shows the same trend for

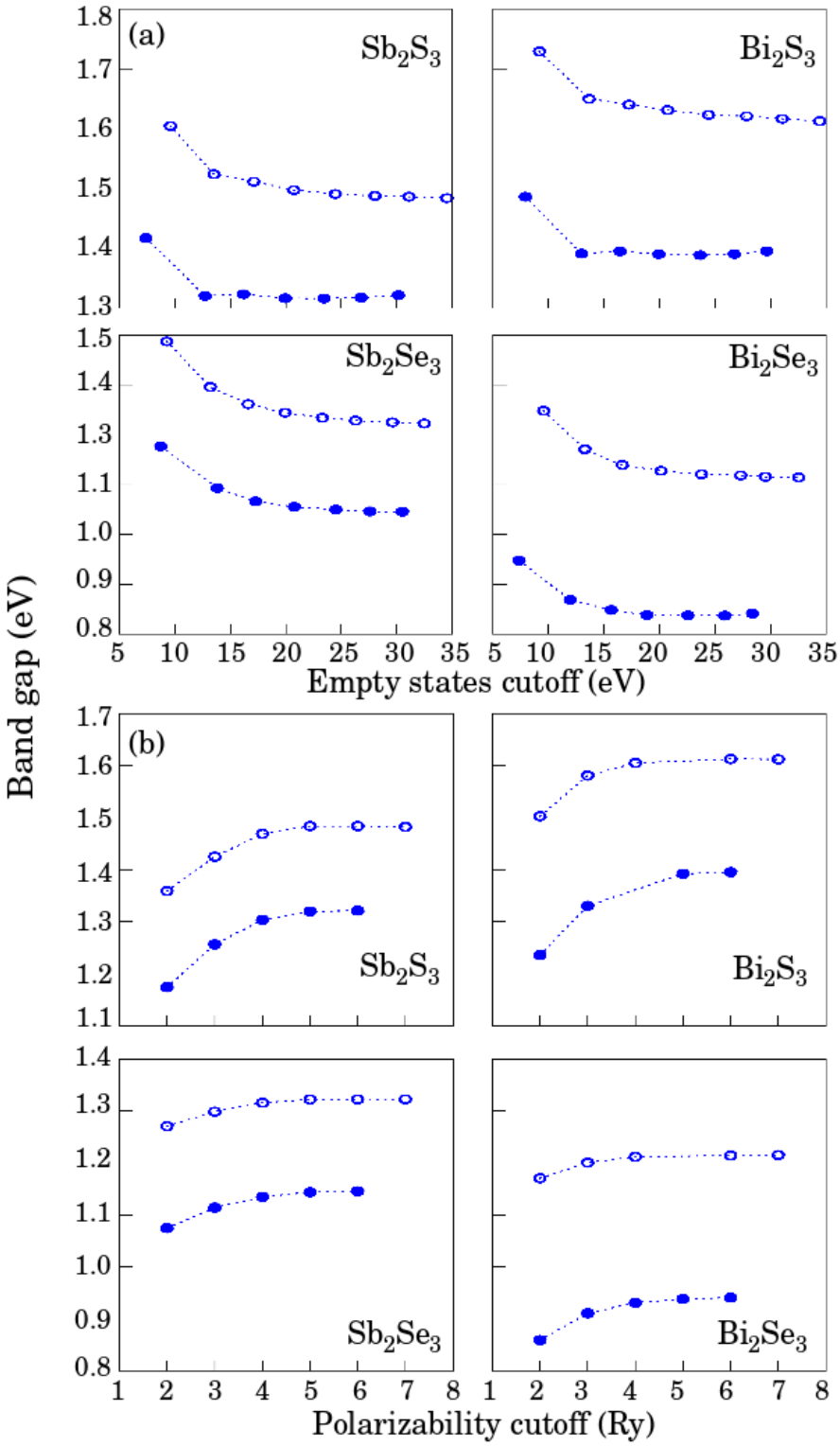


Figure A.2: Convergence tests for the quasiparticle band gaps of all four structures with respect to (a) the empty states cutoff and (b) polarisability cutoff. The calculations without semicore are represented by the empty blue circles and the calculations with semicore are represented by the filled blue disks. All calculations were performed using optimised lattice parameters

calculations with and without semicore states. This is consistent with the expectation that the effect of semicore states in $\Sigma_c$ should be small [210].

Based on these convergence tests we use the following parameters for the *GW* calculation on all four $A_2B_3$ structures:

- Exchange cutoff: 70 Ry (no semicore), 100 Ry (semicore),
- KS plane wave cutoff: same as the kinetic cutoff in DFT,
- Polarisability cutoff: 7.0 Ry,
- Number of bands: 320,
- **k**-point grid: $2 \times 6 \times 2$ $\Gamma$ centred,
- Plasmon-pole parameter: 1 Ry.

All figures depicting structural models and wave function plots were rendered with VESTA [282], except for Figure 8.1 which was rendered using XCrysden [283]

# References


[1] Elliot, L. Lord Stern: I should have been fiercer in climate change review. The Guardian online; posted January 23, 2014.

[2] Elliot, L. Davos 2015: climate change makes a comeback. The Guardian online; posted January 21, 2015.

[3] Ragoussi, M.-E. & Torres, T. New generation solar cells: concepts, trends and perspectives. *Chem. Commun.* (2015).

[4] Best research-cell efficiencies. `http://www.nrel.gov/ncpv` (2014).

[5] Green, M. A., Emery, K., Hishikawa, Y., Warta, W. & Dunlop, E. D. Solar cell efficiency tables (version 44). *Progress in Photovoltaics: Research and Applications* **22**, 701 (2014).

[6] O'Regan, B. & Grätzel, M. High-efficiency solar cell based on dye sensitized colloidal $TiO_2$ films. *Nature* **353**, 737–740 (1991).

[7] Grätzel, M. Recent advances in sensitized mesoscopic solar cells. *Acc. Chem. Res.* **42**, 1788 (2009).

[8] Grätzel, M. Conversion of sunlight to electric power by nanocrystalline dye-sensitized solar cells. *J. Photochem. Photobiol. A: Chemistry* **164**, 3 (2004).

[9] Mathew, S. *et al.* Dye-sensitized solar cells with 13% efficiency achieved through the molecular engineering of porphyrin sensitizers. *Nature. Chem.* **6**, 242 (2014).

[10] Hodes, G. Comparison of dye- and semiconductor sensitized porous nanocrystalline liquid junction solar cells. *J. Phys. Chem. C* **112**, 17778 (2008).

[11] Grätzel, M. The light and shade of perovskite solar cells. *Nature Mater.* **13**, 838 (2014).

[12] Snaith, H. J. Perovskites: The emergence of a new era for low-cost, high-efficiency solar cells. *J. Phys. Chem. Lett.* **4**, 3623 (2013).

[13] Park, N.-G. Perovskite solar cells: an emerging photovoltaic technology. *Materials Today* **365**, 1 (2014).

[14] Green, M., Ho-Baillie, A. & Snaith, H. J. The emergence of perovskite solar cells. *Nature Photonics* **8**, 506 (2014).

[15] Nelson, J. *The Physics of Solar Cells* (Imperial College Press, 2003), 1 edn.

[16] Shockley, W. & Queisser, H. J. Detailed balance limit of efficiency of p-n junction solar cells. *J. Appl. Phys.* **32**, 510 (1961).

[17] Snaith, H. J. Estimating the maximum attainable efficiency in dye-sensitized solar cells. *Adv. Func. Mater.* **20**, 13–19 (2010).

[18] Reference solar spectral irradiance: Air Mass 1.5. `http://rredc.nrel.gov/solar/spectra/am1.5`.

[19] Hardin, B., Snaith, H. J. & McGehee, M. D. The renaissance of dye-sensitized solar cells. *Nature Phot.* **6**, 162 (2012).

[20] Patrick, C. E. & Giustino, F. Structural and electronic properties of semiconductor-sensitized solar cells interfaces. *Adv. Funct. Mater.* **21**, 4663 (2011).

[21] Hodes, G. & Cahen, D. All solid-state, semiconductor sensitized nanoporous solar cells. *Acc. Chem. Res.* **45**, 705 (2012).

[22] Chang, J. A. *et al.* High performance nanostructured inorganic-organic heterojunction solar cells. *Nano Lett.* **10**, 2609 (2010).

[23] Chang, J. A. *et al.* Panchromatic photon-harvesting by hole-conducting materials in inorganic-organic heterojunction sensitized-solar cell through the formation of nanostructured electron channels. *Nano Lett.* **4**, 1863 (2012).

[24] Rath, A. K. *et al.* Solution-processed inorganic bulk nano-heterojunctions and their application to solar cells. *Nature Photonics* **6**, 529 (2012).

[25] Guijarro, N. *et al.* Toward antimony selenide sensitized solar cells: efficient charge photogeneration at spiro-OMeTAD/Sb2Se3/Metal Oxide heterojunctions. *J. Phys. Chem. Lett* **3**, 1351 (2012).

[26] Fukumoto, T. *et al.* Effect of interfacial engineering in solid-state nanostructured $Sb_2S_3$ heterojunction solar cells. *Adv. Energ. Mater.* **3**, 29 (2012).

[27] Choi, H. *et al.* Cesium-doped methylammonium lead iodide perovskite light absorber for hybrid solar cells. *Nano Energy* **117**, 80 (2014).

[28] Lutz, T. *et al.* Thermal decomposition of solution processable metal xanthates on mesoporous titanium dioxide films: a new route to quantum-dot sensitised heterojunctions. *Phys. Chem. Chem. Phys.* **14**, 16192 – 16196 (2012).

[29] Choi, Y. C. *et al.* $Sb_2Se_3$ sensitized inorganic-organic heterojunction solar cells fabricated using a single-source precursor. *Angew. Chem.* **126**, 1353 (2013).

[30] Tuyen Ngo, T. *et al.* Electrodeposition of antimony selenide thin films and application in semiconductor sensitized solar cells. *Appl. Mater. Interfaces* **6**, 2836 (2014).

[31] Zhou, Y. *et al.* Solution-processed antimony selenide heterojunction solar cells. *Adv. Energ. Mater.* **4** (2014).

[32] Leng, M. *et al.* Selenization of $Sb_2Se_3$ absorber layer: An efficient step to improve device performance of $CdS/Sb_2Se_3$ solar cells. *Appl. Phys. Lett.* **105**, 083905 (2014).

[33] Kojima, A., Teshima, K., Shirai, Y. & Miyasaka, T. Novel photoelectrochemical cell with mesoscopic electrodes sensitized by lead-halide compounds (11). *Proc. 214th ECS Meeting* (2006).

[34] Kojima, A., Teshima, K., Shirai, Y. & T., M. Organometal halide perovskites as visible-light sensitizers for photovoltaic cells. *J. Am. Chem. Soc.* **131**, 6050 (2009).

[35] Kim, H.-S. *et al.* Lead iodide perovskite sensitized all-solid-state submicron thin film mesoscopic solar cell with efficiency exceeding 9%. *Sci. Rep.* **2**, 591 (2012).

[36] Lee, M. M., Teuscher, J., Miyasaka, T., Myrakami, T. N. & Snaith, H. J. Efficient hybrid solar cells based on meso-superstructured organometal halide perovskites. *Science* **338**, 643 (2012).

[37] Zhou, H. *et al.* Interface engineering of highly efficient perovskite solar cells. *Science* **345**, 542 (2014).

[38] Heo, J. H. *et al.* Efficient inorganic-organic hybrid heterojunction solar cells containing perovskite compound and polymeric hole-conductors. *Nature Photonics* **7**, 486 (2013).

[39] Burschka, J. *et al.* Sequential deposition as a route to high-performance perovskite-sensitized solar cells. *Nature* **499**, 316 (2013).

[40] Eperon, G. E., Burlakov, V. M., Goriely, A. & Snaith, H. J. Neutral color semitransparent microstructured perovskite solar cells. *ACS Nano* **8**, 591 (2014).

[41] Roldan-Carmona, C. *et al.* High efficiency single-junction semitransparent solar cells. *Energ. Env. Sci.* **7**, 2968 (2014).

[42] Docampo, P., Ball, J. M., Darwich, M., Eperon, G. E. & Snaith, H. J. Efficient organometal trihalide perovskite planar-heterojunction solar cells on flexible polymer substrates. *Nature Commun.* **4**, 2761 (2013).

[43] Kumar, M. H. *et al.* Flexible, low-temperature solution processed ZnO-based solar cells. *Chem. Commun.* **49**, 11089 (2013).

[44] You, J. *et al.* Low-temperature solution-processed perovskite solar cells with high efficiency and flexibility. *ACS Nano* **8**, 1674 (2014).

[45] Roldan-Carmona, C. *et al.* Flexible high efficiency solar cells. *Energ. Env. Sci.* **7**, 994 (2014).

[46] Noh, J. H., Im, S. H., Heo, T. N., J. H. end Mandal & Seok, S. I. Chemical management for colorful, efficient and stable inorganic-organic hybrid nanostructured solar cells. *Nano Lett.* **13**, 1764 (2013).

[47] Kulkarni, S. A. *et al.* Band-gap tuning of lead halide perovskites using a sequential deposition process. *J. Mater. Chem. A* **2**, 9221 (2014).

[48] Liu, D. & Kelly, T. L. Perovskite solar cells with a planar heterojunction structure prepared using room-temperature solution processing techniques. *Nature. Photon.* **8**, 133 (2014).

[49] Stranks, S. D. *et al.* Electron-hole diffusion length exceeding 1 micrometer in an organometal trihbalide perovskite absorber. *Science* **342**, 341 (2013).

[50] Xing, G. *et al.* Long range balanced electron-and hole-transport lengths in organic-inorganic $CH_3NH_3PbI_3$. *Science* **342**, 344 (2013).

[51] Etgar, L. *et al.* Mesoscopic $CH_3NH_3PbI_3/TiO_2$ heterojunction solar cells. *J. Am. Chem. Soc.* **134**, 17396 (2012).

[52] Mei, A. *et al.* A hole-conductor free, fully printable mesoscopic perovskite solar cell with high stability. *Science* **345**, 295 (2014).

[53] Heo, J. H. *et al.* Efficient inorganic-organic hybrid heterojunction solar cells containing perovskite compound and polymer hole conductors. *Nature Photon.* **7**, 486 (2014).

[54] Liu, M., Johnston, M. B. & Snaith, H. J. Efficient planar heterojunction perovskite solar cells by vapour deposition. *Nature* **501**, 395 (2013).

[55] Malinkiewicz, O. *et al.* Perovskite solar cells employing organic charge-transport layers. *Nature Photon.* **8**, 128 (2014).

[56] Martin, R. M. *Electronic structure: basic theory and practical methods* (Cambridge University Press, 2004).

[57] Giustino, F. *Materials modelling using density functional theory* (Oxford University Press, 2014).

[58] Payne, M. C., Teter, M. P., Allan, D. C., Arias, T. A. & Joannopoulos, J. D. Iterative minimization techniques for *ab initio* total energy calculations, molecular dynamics and conjugate gradients. *Rev. Mod. Phys.* **64** (1992).

[59] Hedin, K. & Lundqvist, S. Effects of electron-electron and electron-phonon interactions on the one-electron states of solids. *Solid State Physics* **23**, 1 (1969).

[60] Hedin, L. New method for calculating the one-particle Green's function with application to the electron-gas problem. *Phys. Rev.* **139**, A796 (1965).

[61] Strinati, G. Applications of the Green's functions methods to the study of the optical properties of semiconductors. *Riv. del Nuovo Cimento* **11** (1988).

[62] Onida, G., Reining, L. & Rubio, A. Electronic excitations: density-functional versus many-body Green's function approaches. *Rev. Mod. Phys.* **74**, 601–659 (2002).

[63] Aryasetiawan, F. & Gunnarsson, O. The *GW* method. *Rep. Prog. Phys.* **61**, 237 (1998).

[64] Aulbur, W. G., Jönsson, L. & Wilkins, J. W. Quasiparticle calculations in solids. *Solid State Physics* **54**, 1–218 (2000).

[65] Hybertsen, M. S. & Louie, S. G. Electron correlation in semiconductors and insulators: Band gaps and quasiparticle energies. *Phys. Rev. B* **34**, 5390 (1986).

[66] Giustino, F., Cohen, M. L. & Louie, S. G. *GW* method with the self-consistent Sternheimer equation. *Phys. Rev. B* **81**, 115105 (2010).

[67] Inkson, J. C. *Many body theory of solids* (Springer, 1984).

[68] Hohenberg, P. & Kohn, W. Inhomogeneous Electron Gas. *Phys. Rev.* **136**, B864 (1964).

[69] Wang, Y. A. & Carter, E. A. Orbital-free kinetic energy density functional theory. *Prog. Theor. Chem. Phys.* **5**, 117 (2002).

[70] Kohn, W. & Sham, L. J. Self-consistent equations including exchange and correlation effects. *Phys. Rev.* **140**, A1133 (1965).

[71] Jackson, J. D. *Classical electrodynamics* (Wiley, 1998).

[72] Fock, V. Näherungsmethode zur lösung des quantumechanischen metkörperproblems. *Zeitschrift für Physik* **61**, 126 (1930).

[73] Ceperley, D. M. & Alder, B. J. Ground state of the electron gas by a stochastic method. *Phys. Rev. Lett.* **45**, 566 (1980).

[74] Perdew, J. P. & Zunger, A. Self-interaction correction to density-functional approximations for many-electrons systems. *Phys. Rev. B* **23**, 5048 (1981).

[75] Slater, J. C. A simplification of the Hartree-Fock method. *Phys. Rev.* **81**, 385 (1981).

[76] Ashcroft, N. W. & Mermin, N. D. *Solid state physics* (Hartcourt College, 1976).

[77] Pedew, J. P., Burke, K. & Wang, Y. Generalized gradient approximation for the exchange-correlation hole of a many-electron system. *Phys. Rev. B* **54**, 16533 (1996).

[78] Dal Corso, A., Pasquarello, A., Baldereschi, A. & Car, R. Generalized-gradient approximations to density functional theory: A comparative study for atoms and solids. *Phys. Rev. B* **53**, 1180 (1996).

[79] Messiah, A. *Quantum Mechanics*, vol. II (Dover Publications, Inc., 1999).

[80] Thomas, L. H. The motion of the spinning electron. *Nature* **117**, 554 (1926).

[81] Dirac, P. A. M. The quantum theory of the electron. *Proceedings of the Royal Society of London A* **117**, 610 (1926).

[82] von Barth, U. & Hedin, L. A local exchange-correlation potential for the spin polarized case: I. *J. Phys. C: Solid State Phys.* **5**, 1629 (1972).

[83] Kübler, J., Hock, K.-H., Sticht, J. & Williams, A. R. Density functional theory of noncollinear magnetism. *J. Phys. F: Metal Phys.* **18**, 469 (1988).

[84] Sham, L. J. & Schlüter, M. Density-Functional Theory of the Energy Gap. *Phys. Rev. Lett.* **51**, 1888 (1983).

[85] Tran, F. & Blaha, P. Accurate band gaps of semiconductors and insulators with a semilocal exchange-correlation potential. *Phys. Rev. Lett.* **102**, 226401 (2009).

[86] Heyd, J., Peralta, J. E., Scuseria, G. E. & Martin, R. L. Energy band gaps and lattice parameters evaluated with the Heyd-Scuseria-Ernzerhof screened hybrid functional. *J. Chem. Phys.* **123**, 174101 (2005).

[87] Adler, S. L. Quantum theory of the dielectric constant in real solids. *Phys. Rev.* **126**, 413–420 (1962).

[88] Wiser, N. Dielectric constant with local field effects included. *Phys. Rev.* **129**, 62–69 (1963).

[89] Martin-Samos, L. & Bussi, G. SaX: An open source package for electronic-structure and optical-properties calculations in the GW approximations. *Comp. Phys. Commun.* **180**, 1416 (2009).

[90] van Schilfgaarde, M., Kotani, T. & Faleev, S. Quasiparticle Self-Consistent GW Theory. *Phys. Rev. Lett.* **96**, 226402 (2006).

[91] Patrick, C. E. & Giustino, F. GW quasiparticle bandgaps of anatase $TiO_2$ starting from DFT + U. *J. Phys. Condens. Matter* **24**, 202201 (2012).

[92] Kioupakis, E., Zhang, P., Cohen, M. L. & Louie, S. G. GW quasiparticle corrections to the LDA+U GGA+U electronic structure of bcc hydrogen. *Phys. Rev. B* **77**, 155114 (2008).

[93] Fuchs, F., Furthmüller, J., Bechstedt, F., Shishkin, M. & Kresse, G. Quasiparticle band structure based on a generalized Kohn-Sham scheme. *Phys. Rev. B* **76**, 115109 (2007).

[94] Bruneval, F. & Marques, M. A. L. Benchmarking the Starting Points of the GW Approximation for Molecules. *J. Chem. Theory. Comput.* **9**, 324 (2013).

[95] Caruso, F., Rinke, P., Ren, X., Scheffler, M. & Rubio, A. Unified description of ground and excited states of finite systems: The self-consistent GW approach. *Phys. Rev. B* **86**, 081102 (2012).

[96] Caruso, F., Rinke, P., Ren, X., Rubio, A. & Scheffler, M. Self-consistent GW: All-electron implementation with localized basis functions. *Phys. Rev. B* **88**, 075105 (2013).

[97] Filip, M. R. & Giustino, F. GW quasiparticle band gap of the hybrid organic-

inorganic perovskite CH3NH3PbI3: Effect of spin-orbit interaction, semicore electrons, and self-consistency. *Phys. Rev. B* **90**, 245145 (2014).

[98] Sakuma, R., Friedrich, C., Miyake, T., Blügel, S. & Aryasetiawan, F. GW calculations including spin-orbit coupling: Application to Hg chalchogenides. *Phys. Rev. B* **84**, 085144 (2011).

[99] Aryasetiawan, F. & Biermann, S. Generalized Hedin's equations for quantum many-body systems with spin-dependent interactions. *Phys. Rev. Lett.* **100**, 116402 (2008).

[100] Aryasetiawan, F. & Biermann, S. Generalized Hedin equations and $\sigma G \sigma W$ approximation for quantum many-body systems with spin-dependent interactions. *J. Phys. Condens. Matter* **21**, 064232 (2009).

[101] Gianozzi, P. *et al.* QUANTUM ESPRESSO: a modular and open-source software project for quantum simulations of materials. *J. Phys.: Condens. Matter.* **21** (2009).

[102] Marini, A., Hogan, C., Grüning, M. & Varsano, D. Yambo: an ab initio tool for excited state calculations. *Comp. Phys. Commun.* **180**, 1392 (2009).

[103] Fuchs, M. & Scheffler, M. Ab initio pseudopotentials for electronic structure calculations of poly-atomic systems using density functional theory. *Comp. Phys. Commun.* **119**, 67 (1999).

[104] Troullier, N. & Martins, J. L. Efficient pseudopotentials for plane-wave calculations. *Phys. Rev. B* **43**, 1993 (1991).

[105] Vanderbilt, D. Soft self-consistent pseudopotentials in a generalized eigenvalue formalism. *Phys. Rev. B* **41**, 7892 (1990).

[106] Laasonen, K., Pasquarello, A., Car, R., Lee, C. & Vanderbilt, D. Car-Parinello

molecular dynamics with Vanderbilt ultrasoft pseudopotentials. *Phys. Rev. B* **47**, 10142 (1993).

[107] Oliveira, M. J. T. & Nogueira, F. Generating relativistic pseudopotentials with explicit incorporation of semicore states using APE, the Atomic Pseudopotentials Engine. *Comp. Phys. Commun.* **178**, 524 (2008).

[108] Koelling, D. D. & Harmon, B. N. A technique for relativistic spin-polarised calculations. *J. Phys. C: Solid State Phys.* **10**, 3107 (1977).

[109] Cuadrado, R. & Cerdá, J. I. Fully relativistic pseudopotential formalism under an atomic orbital basis: spin-orbit splittings and magnetic anisotropies. *J. Phys. Condens. Matter.* **24**, 086005 (2012).

[110] Bachelet, G. B., Hammann, D. R. & Schlüter, M. Pseudopotentials that work: From H to Pu. *Phys. Rev. B* **26**, 4199 (1982).

[111] Louie, S. G., Froyen, S. & Cohen, M. L. Nonlinear ionic pseudopotentials in spin-density-functional calculations. *Phys. Rev. B* **26**, 1738 (1982).

[112] Svane, A. Hartree-Fock band structure calculations with the linear muffin-tin-orbital method: Application to C, Si, Ge, and $\alpha$-Sn. *Phys. Rev. B* **55**, 5496 (1987).

[113] Kang, W. & Hybertsen, M. Enhanced static approximation to the electron self-energy operator for efficient calculation of quasiparticle energies. *Phys. Rev. B* **82**, 195108 (2010).

[114] Godby, R. W. & Needs, R. J. Metal-insulator transition in Kohn-Sham theory and quasiparticle theory. *Phys. Rev. Lett.* **62**, 1169 (1989).

[115] Kazim, S., Nazeeruddin, M. K., Grätzel, M. & Ahmad, S. Perovskite as light harverster: A game changer in photovoltaics. *Angew. Chem. Int. Ed.* **53**, 2 (2014).

[116] Goldschmidt, V. M. Die Gesetze der Krystallochemie. *Die Naturwissenschaften* **21**, 477 (1926).

[117] Gao, P., Grätzel, M. & Nazeerudding, M. K. Organohalide lead perovskites for photovoltaic applications. *Energ. Environ. Sci.* **7**, 2448 (2014).

[118] Müller, K. A. & Kod, T. W. *Properties of perovskites and other oxides* (World Scientific, 2010).

[119] Grindberg, I. *et al.* Perovskite oxides for visible-light-absorbing ferroelectric and photovoltaic materials. *Nature* **503**, 509 (2013).

[120] Glazer, A. M. The classification of tilted octahedra in perovskites. *Acta. Cryst. B* **28**, 3384 (1972).

[121] Glazer, A. M. Simple ways of determining perovskite structures. *Acta. Cryst. A* **31**, 756 (1975).

[122] Woodward, P. M. Octahedral tilting of Perovskites. I Geometrical considerations. *Acta Cryst. B* **53**, 32 (1997).

[123] Megaw, H. D. Changes in polycrystalline barium-strontium titanate at its transition temperature. *Nature* **157**, 20 (1946).

[124] Howard, C. J. & Stokes, H. T. Structures and phase transitions in perovsites - a group theoretical approach. *Acta Cryst. A* **61**, 93 (2005).

[125] Howard, C. J. & Stokes, H. T. Group-theoretical analysis of octrahedral tilting in perovskites. *Acta Cryst. B* **54**, 782 (1998).

[126] Mitzi, D. B. *Progress in inorganic chemistry* (John Wiley & Sons, Inc, 1999).

[127] Jones, A. P., Wall, F. & Williams, C. T. *Rare earth minerals: Chemistry, origin and ore deposis* (Springer, 1996).

[128] Mitzi, D. B., Chondroudis, K. & Kagan, C. R. Organic-inorganic electronics. *IBM J. Res. & Dev.* **45** (2001).

[129] Bedlyvi, D. & Mereiter, K. The structures of potassium lead triiodide dihydrate and ammonium lead triiodide dihydrate. *Acta Cryst. B* **36**, 782 (1980).

[130] Im, J.-H., Lee, C.-R., Lee, J.-W., Park, S.-W. & Park, N.-G. 6.5% efficient perovskite quantu-dot-sensitized solar cell. *Nanoscale* **3**, 4088 (2011).

[131] Ku, Z., Rong, Y., Xu, M., Liu, T. & Han, H. Full printable processed mesoscopic $CH_3NH_3PbI_3/TiO_2$ heterojunction solar cells with carbon counter electrode. *Sci. Rep.* **3**, 3132 (2013).

[132] Eperon, G. E., Burlakov, V. M., Goriely, A. & Snaith, H. J. Morphological control for high-performance, solution-processed planar heterojunction solar cells. *Adv. Func. Mater.* **24**, 151 (2014).

[133] Conings, B. *et al.* Perovskite-based hybrid solar cells exceeding 10% efficiency with high reproducibility using a thin film sandwich approach. *Adv. Mater.* **26**, 2041 (2014).

[134] Wojciechowski, K., Saliba, M., Leijtens, T., Abate, A. & Snaith, H. J. Sub-150 degree C processed meso-superstructured perovskite solar cells with enhanced efficiency. *Energ. Environ. Sci.* **7**, 1142 (2014).

[135] Liang, K., Mitzi, D. B. & Prikas, M. T. Synthesis and characterization of organic-inorganic perovskite thin films prepared using a versatile two-step dipping technique. *Chem. Mater.* **10** (1998).

[136] Mitzi, D. B. Thin-film deposition of organicâĹŠinorganic hybrid materials. *Chem. Mater.* **13**, 3283 (2001).

[137] Pellet, N. *et al.* Mixed-organic-cationic perovskite photovoltaics for enhanced solar-light harvesting. *Angew. Chem.* **53**, 3151 (2014).

[138] Mitzi, D. B., Prikas, M. T. & Chondroudis, K. Thin film deposition of organic-inorganic hybrid materials using a single source thermal ablation technique. *Chem. Mater.* **11**, 542 (1999).

[139] Hao, F., Stoumpos, C. C., Liu, Z., Chang, R. P. H. & Kanatzidis, M. G. Controllable perovskite crystallization as a gas-solid interface for hole-conductor-free solar cells with steady power conversion efficiency over 10%. *J. Am. Chem. Soc.* **136**, 16411 (2014).

[140] Chen, Q. *et al.* Planar heterojunction perovskite solar cells via vapor-assisted solution process. *J. Am. Chem. Soc.* **136**, 622 (2014).

[141] Sum, T. C. & Mathews, N. Advancements in perovskite solar cells: photophysics behind the photovoltaics. *Energ. Environ. Sci.* **7**, 2518 (2014).

[142] Papavassiliou, G. C. Three- and low-dimensional inorganic semiconductors. *Prog. Solid State Chem.* **25**, 125 (1997).

[143] Vincent, B. R., Robertson, K. N., Cameron, T. S. & Knop, O. Alkylammonium lead halides. Part 1. Isolated $PbI_6$ - ions in $(CH_3NH_3)_4PbI_62H_2O$. *Can. J. Chem.* **65** (1987).

[144] Poglitsch, A. & Weber, D. Dynamic disorder in methylammoniumtrihalogeno-plumbates (II) observed by millimeter-wave spectroscopy. *J. Chem. Phys.* **87**, 6373 (1987).

[145] Stoumpos, C. C., Malliakas, C. D. & Kanatzidis, M. G. Semiconducting tin and lead iodide perovskites with organic cations: phase transitions, high mobilities, and near-infrared photoluminescent properties. *Inorg. Chem.* **52**, 9019 (2013).

[146] Baikie, T. *et al.* Synthesis and crystal chemistry of the hybrid perovskite $(CH_3NH_3PbI_3)$ for solid-state sensitized solar applications. *J. Chem. Mater. A* **1**, 5628 (2013).

[147] Onoda-Yamamuro, N., Matsuo, T. & Suga, H. Calorimetric and IR spectroscopic studies of phase transitions in methylammonium trihalogenoplumbates (II). *J. Phys. Chem. Solids* **51**, 1383 (1990).

[148] Kawamura, Y., Mashiyama, H. & Hasebe, K. Structural study of cubic-tetragonal transition of CH3NH3PbI3. *J. Phys. Soc. Jpn.* **71**, 1694 (2002).

[149] Onoda-Yamamuro, N., Matsuo, T. & Suga, H. Dielectric study of $CH_3NH_3PbX_3$ (X = Cl, Br, I). *J. Phys. Chem. Solids* **53**, 935 (1992).

[150] Wasylishen, R. E., Knop, O. & Macdonald, J. B. Cation rotatio in methylammonium lead halides. *Solid State Commun.* **56**, 581 (1985).

[151] Weber, D. $CH_3NH_3PbX_3$ ein Pb(II)-System mit kubischer Perowskitstruktur. *Z. Naturforsch., B: Anorg. Chem., Org. Chem.* **33**, 1443 (1978).

[152] Mashiyama, H., Kurihara, Y. & Azetsu, T. Disordered cubic perovskite structure of $CH_3NH_3PbX_3$ (X = Cl, Br, I). *J. Kor. Phys. Soc.* **32**, S156 (1998).

[153] Zheng, F., Tekenaka, H., Wang, F., Zoocher, N. Z. & Rappe, A. M. First-principles calculation of bulk photovoltaic effect in $CH_3NH_3PbI_3$ and $CH_3NH_3PbI_{3-x}Cl_x$. *arxiv:1410.3389* (2014).

[154] Mosconi, E., Amat, A., Nazeeruddin, M. K., Grätzel, M. & De Angelis, F. First-principles modeling of mixed halide organometal perovskite of photovoltaic applications. *J. Phys. Chem. C* 117 (2013).

[155] Filippetti, A., Delugas, P. & Mattoni, A. Methylammonium lead-iodide perovskite: recombination and photoconversion pf an inorganic semiconductor within a hybrid body. *J. Phys. Chem. C* **43**, 24843 (2014).

[156] Geng, W., Zhang, L., Zhang, Y.-N., Lau, W.-M. & Liu, L.-M. First-principles study of lead-iodide perovskite tetragonal and orthorhombic phases for photovoltaics. *J. Phys. Chem. C* **34**, 19565 (2014).

[157] Wang, Y. *et al.* Density functional theory analysis of structural and electronic properties of orthorhombic perovskite $CH_3NH_3PbI_3$. *Phys. Chem. Chem. Phys.* **16**, 1424 (2013).

[158] Filip, M. R., Eperon, G., Snaith, H. J. & Giustino, F. Steric engineering of metal-halide perovskites with tunable optical band gaps. *Nat. Commun.* **5**, 6747 (2014).

[159] Frost, J. M., Butler, K. T. & Walsh, A. Molecular ferroelectric contributions to anomalous hysteresis in hybrid perovskite solar cells. *Appl. Phys. Lett.* **2**, 081506 (2014).

[160] Frost, J. M. *et al.* Atomistic origins of high-performance in hybrid halide perovskite solar cells. *Nano Lett.* **5**, 2584 (2014).

[161] Carignano, M. A., Kachmar, A. & Hutter, J. Thermal effects on $CH_3NH_3PbI_3$ perovskite from ab-initio molecular dynamics simulations. *arxiv:1409.6842v2* (2014).

[162] Quarti, C. *et al.* The Raman spectrum of the $CH_3NH_3PbI_3$ hybrid perovskite: interplay of theory and experiment. *J. Phys. Chem. Lett.* **5**, 279 (2014).

[163] Grancini, G. *et al.* The impact of crystallization processes on the structural and optical properties of hybrid perovskite films for photovoltaics. *J. Phys. Chem. Lett., in press* (2014).

[164] Koutselas, I. B., Doucasse, L. & Papavassiliou, G. C. Electronic properties of three- and two- dimensional semiconductiong materials with Pb halide and Sn halide units. *J. Phys.: Condens. Matter. B* **8**, 1217 (1996).

[165] Hirasawa, M., Ishihara, T., Goto, T., Uchida, K. & Miura, N. Magnetoabsorbtion of the lowest exciton in perovskite-type compound $CH_3NH_3PbI_3$. *Physica B* **201**, 427 (1994).

[166] Tanaka, K. *et al.* Comparative study on the excitons in lead-halide based perovskite-type crystals $CH_3NH_3PbI_3$. *Solid State Commun.* **127**, 619 (2003).

[167] Ishihara, T. Optical properties of PbI-based perovskite structures. *J. Lumin.* **60**, 269 (1994).

[168] Sun, S. *et al.* The origin of high efficiency in low-temperature solution-processable bilayer organometal halide hybrid solar cells. *Energ. Environ. Sci.* **7**, 399 (2014).

[169] D'Innocenzo, V. *et al.* Excitons versus free charges in organo-lead tri-halide perovskites. *Nature Commun.* **5**, 3586 (2014).

[170] Yamada, Y., Nakamura, T., Endo, M., Wakamiya, A. & Kanemitsu, Y. Photoelectronic responses in solution-processed perovskite $CH_3NH_3PbI_3$ solar cells studied by photoluminescence and absorbtion spectroscopy. *IEEE J. Photov.* (2014).

[171] Yu, P. & M., C. *Fundamentals of semiconductors* (Springer, 2010), 4th edn.

[172] Lin, Q., Armin, A., Nagiri, R. C. R., Burn, P. L. & Meredith, P. Electro-optics of perovskite solar cells. *Nature Photon.* (2014).

[173] Miyata, A. *et al.* Direct Measurement of the Exciton Binding Energy and Effective Masses for Charge carriers in an Organic-Inorganic Tri-halide Perovskite. *Nature Physics* (2015).

[174] Wehrenfennig, C., Eperon, G. E., Johnston, M. B., Snaith, H. J. & Herz, L. M. High charge carrier mobilities and lifetimes in organolead trihalide perovskites. *Adv. Mater.* **26**, 1584 (2014).

[175] Marchioro, A. *et al.* Unravelling the mechanism of photoinduced charge transfer processes in lead iodide perovskite solar cells. *Nature Photon.* **8**, 250 (2014).

[176] Oga, H., Saeki, A., Ogomi, Y., Hayase, S. & Seki, S. Improved understanding

of the electronic and energetic landscapes of perovskite solar cells: High local charge carrier mobility, reduced recombination and extreme shallow traps. *J. Am. Chem. Soc.* **136**, 13818 (2014).

[177] Deschler, F. *et al.* High photoluminescence efficiency and optically pumped lasing in solution-processed mixed halide perovskite semiconductors. *J. Phys. Chem. Lett.* **5**, 1421 (2014).

[178] Xing, G. *et al.* Low-temperature solution-processed wavelength-tunable perovskites for lasing. *Nature Mater.* **13**, 476 (2014).

[179] Stranks, S. D. *et al.* Recombination kinetics in organic-inorganic perovskites: excitons, free charge and subgap states. *Phys. Rev. Applied* **2**, 034007 (2014).

[180] Edri, E. *et al.* Elucidating the charge carrier separation and working mechanisms of $CH_3NH_3Pb_{1-x}Cl_x$. *Nature Commun.* **5**, 3461 (2014).

[181] Bergmann, V. W. *et al.* Real-space observation of unbalanced charge distribution inside a perovskite-sensitized solar cell. *Nature Commun.* (2014).

[182] Papavassiliou, G. C. *Mol. Cryst. Liq. Cryst. Sci. Technol. Sect.* **286**, 231 (1996).

[183] Umebayashi, T., Asai, K., Kondo, T. & Nakao, A. Electronic structures of lead iodide based low-dimensional crystals. *Phys. Rev. B* **67**, 155405 (2003).

[184] Menéndez-Proupin, E., Palacios, P., Wahnón, P. & Conesa, J. C. Self-consistent relativistic band structure of the $CH_3NH_3PbI_3$ perovskite. *Phys. Rev. B* **90**, 045207 (2014).

[185] Chang, Y. H., Park, C. H. & Matsuishi, K. First-principles study of the structural and the electronic properties of the lead-halide-based inorganic-organic perovskites $(CH_3NH_3)PbX_3$ and $CsPbX_3$ (X = Cl, Br, I). *J. Kor. Phys. Soc.* **44**, 89 (2004).

[186] Even, J., Pedesseau, L., Jancu, J.-M. & Katan, C. Importance of spin-orbit cou-

pling in hybrid organic/inorganic perovskites for photovoltaic applications. *J. Phys. Chem. Lett.* **4**, 2999 (2013).

[187] Giorgi, G., Fujisawa, J.-I., Segawa, H. & Yamashita, K. Small photocarrier effective masses featuring ambipolar transport in methylammoniumlead iodide perovskite: A density functional theory analysis. *J. Phys. Chem. Lett.* **4**, 4213 (2013).

[188] Lang, L., Yang, J.-H., Liu, H.-R., Xiang, H. J. & Gong, X. G. First-principles study on the electronic and optical properties of cubic $ABX_3$ halide perovskites. *Phys. Lett. A* **378**, 290 (2014).

[189] Even, J., Pedesseau, L., Jancu, J. M. & Katan, C. DFT and kp modelling of the phase transitions of lead and tin halide perovskites for photovoltaic cells. *Phys. Status Solidi (RRL)* **8**, 31 (2014).

[190] Brivio, F., Walker, A. B. & Walsh, A. Structural and electronic properties of hybrid perovskites for high-efficiency thin-film photovoltaics from first-principles. *Appl. Phys. Lett.* **1**, 042111 (2013).

[191] Umari, P., Mosconi, E. & De Angelis, F. Relativistic GW calculations on $CH_3NH_3Pb_3$ and $CH_3NH_3SnI_3$ perovskites for solar cell applications. *Sci. Rep.* **4**, 4467 (2014).

[192] Brivio, F., Butler, K. T., Walsh, A. & van Schilfgaarde, M. Relativistic quasiparticle self-consistent electronic structure of hybrid halide perovskite photovoltaic absorbers. *Phys. Rev. B* **89**, 155204 (2014).

[193] Lindblad, R. *et al.* Electronic structure of $TiO_2/CH_3NH_3PbI_3$ perovskite solar cell interfaces. *J. Phys. Chem. Lett.* **5**, 648 (2014).

[194] Amat, A. *et al.* Cation-induced band-gap tuning in organohalide perovskites: interplay of spin-orbit coupling and octahedra tilting. *Nano Lett.* **14**, 3508 (2014).

[195] Zhu, X., Su, H., Marcus, R. A. & Michel-Beyerle, M. E. Computed and experimental absorbtion spectra of the perovskite $CH_3NH_3PbI_3$. *J. Phys. Chem. Lett.* **5**, 3061 (2014).

[196] Nanguneri, R. & Parkhill, J. Relaxation between bright optical Wannier excitons in perovskite solar absorbers $CH_3NH_3PbI_3$. *arxiv:1411.1110v1* (2014).

[197] Mosconi, E., Ronca, E. & De Angelis, F. First-principles investigation of the TiO2/organohalide perovskites interface: the role of interfacial chlorine. *J. Phys. Chem. Lett.* **5**, 2619 (2014).

[198] Roiati, V. *et al.* Stark effect in Perovskite/$TiO_2$ solar cells: evidence of local interfacial order. *Nano Lett.* **14**, 2168 (2014).

[199] Knutson, J., Martin, J. D. & Mitzi, D. B. Tuning the band gap in hybrid tin iodide perovskite semiconductors using structural templating. *Inorg. Chem.* **44**, 4699 (2005).

[200] Eperon, G. E. *et al.* Formamidinium lead trihalide: a broadly tunable perovskite heterojunction solar cells. *Energ. Env. Sci.* **7**, 982 (2014).

[201] Hao, F., Stoumpos, C. C., Chan, R. P. H. & Kanatzidis, M. G. Anomalous band gap behavior in mixed Sn and Pb perovskites enables broadening of the absorbtion spectrum in solar cells. *J. Am. Chem. Soc.* **136**, 8094 (2014).

[202] Gao, X. & Daw, M. S. Investigation of band inversion in (Pb, Sn)Te alloys using *ab initio* calculations. *Phys. Rev. B.* **77**, 033103 (2008).

[203] Mosconi, E., Umari, P. & De Angelis, F. Electronic and optical properties of mixed Sn-Pb organohalide perovskites: a first principles investigation. *J. Mater. Chem. A* **Advance Article** (2015).

[204] Kitazawa, N., Watanabe, Y. & Nakamura, Y. Optical properties of $CH_3NH_3PbX_3$ (X = halogen) and their mixed halides. *J. Mater. Sci.* **37**, 3585 (2002).

[205] Abrusci, A. *et al.* High-performance perovskite-polymer hybrid solar cells via electronic coupling with fullerene monolayers. *Nano Lett.* **13**, 3124 (2013).

[206] Ball, J. M., Lee, M. M., Hey, A. & Snaith, H. J. Low-temperature processed meso-superstructured to thin film solar cells. *6* 1739 (2013).

[207] Chiarella, F. *et al.* Combined experimental and theoretical investigation of optical, structural and electronic properties of $CH_3NH_3SnX_3$ thin films (X = Cl, Br). *Phys. Rev. B.* **77**, 045129 (2008).

[208] Borriello, I., Cantele, G. & Ninno, D. Ab initio investigation of hybrid organic-inorganic perovskite based on tin halides. *Phys. Rev. B* **77**, 235214 (2008).

[209] Trots, D. M. & Myagkota, S. V. High-temperature structural evolution of caesium and rubidium triodoplumbates. *J. Phys. Chem. Solids* **69**, 2520 (2008).

[210] Rohlfing, M., Krüger, P. & Pollmann, J. Quasiparticle band structure of CdS. *Phys. Rev. Lett.* **75**, 3489 (1995).

[211] Tiago, M. L., Ismail-Beigi, S. & Louie, S. G. Effect of semicore orbitals on the electronic band gaps of Si, Ge and GaAs within the GW approximation. *Phys. Rev. B* **69**, 125212 (2004).

[212] Filip, M. R., Patrick, C. E. & Giustino, F. GW quasiparticle band structures of stibnite, antimonselite, bismuthinite, and guanajuatite. *Phys. Rev. B* **87**, 205125 (2013).

[213] Schultz, P. *et al.* Interface energetics in organo-metal halide perovskite-based photovoltaic cells. *Energ. Environ. Sci.* **7**, 1377 (2014).

[214] Schultz, P. *et al.* Electronic Level Alignment in Inverted Organometal Perovskite Solar Cells. *Adv. Mater. Interfaces* **2** (2015).

[215] Goldstein, H., Poole, C. & Safko, J. *Classical Mechanics* (Addison Wesley, 2002), 3rd edn.

[216] Slater, J. C. & Koster, G. F. Simplified LCAO theory for the periodic potential problem. *Phys. Rev. B* **94**, 1498 (1954).

[217] Souza, I., Iniguez, J. & Vanderbilt, D. First-principles approach to insulators in finite electric fields. *Phys. Rev. Lett.* **89**, 117602 (2002).

[218] Umari, P. & Pasquarello, A. Ab initio molecular dynamics in a finite homogeneous electric field. *Phys. Rev. Lett.* **89**, 157602 (2002).

[219] Shannon, R. D. Revised effective ionic radii and systematic studies of interatomic distances in halides and chalchogenides. *Acta. Cryst. A* **32**, 751 (1976).

[220] Tanaka, K. *et al.* Electronic and excitonic structures of inorganic-organic perovskite-type quantum well crystal. *J. Appl. Phys. Part 1* **44**, 5923 (2005).

[221] Durig, J. R., Pate, C. B. & Li, Y. S. Far-infrared and Raman spectra of arsonium iodide. *J. Chem. Phys.* **54**, 1033 (1971).

[222] Baroni, S., De Gironcoli, S., Dal Corso, A. & Gianozzi, P. Phonons and related crystal properties from density functional perturbation theory. *Rev. Mod. Phys.* **73**, 515 (2001).

[223] Blöchl, P. E., Jepsen, O. & Andersen, O. K. Improved tetrahedron method for Brillouin-zone integrations. *Phys. Rev. B* **49**, 16223 (1994).

[224] Fan, L.-Q. & Wu, J. H. $NH_4PbI_3$. *Acta Cryst. E* **63**, 189 (2007).

[225] Meloni, S. *et al.* Valence and conduction bands engineering in halide perovskites for solar cell applications. *arxiv:1412.3659* (2014).

[226] Minkwitz, R., Kornath, A., Sawodny, W. & Härtner, H. Über die Darstellung der Pniktogeniumsalze $AsH_4^+SbF_6^-$, $AsH_4^+AsF_6^-$, $SbH_4^+SbF_6^-$. *Z. Anorg. Allg. Chem.* **620**, 753 (1994).

[227] `http://www.sigmaaldrich.com/united-kingdom.html`.

[228] Pickard, C. J. & Needs, R. J. Ab initio random structure searching. *J. of Phys. Condens. Matter.* **23**, 053201 (2011).

[229] Hansell, C. All manner of antimony. *Nature Chem.* **7** (2015).

[230] Zhang, H., Liu, C. X., Qi, X. L., Fang, Z. & Zhang, S.-C. Topological insulators in $Bi_2Se_3$, $Bi_2Te_3$ and $Sb_2Te_3$ with a single Dirac cone on the surface. *Nature Physics* **5**, 438 – 442 (2009).

[231] Mehta, R. J. *et al.* High electrical conductivity antimony selenide nanocrystalsa and assemblies. *Nano. Lett.* **10**, 4417 (2010).

[232] Rhee, J. H., Chung, C.-C. & Diau, E. W.-G. A perspective of mesoscopic solar cells based on metal chalcogenide quantum dots and organometal-halide perovskites. *NPG Asia Materials* **5**, e68 (2013).

[233] Choi, Y. C., Lee, D. U., Noh, J. H., Kim, E. K. & Seok, S. I. Highly improved $Sb_2S_3$ sensitized-inorganic-organic heterojunction solar cells and quantification of traps by deep-level transient spectroscopy. *Adv. Func. Mater* **24**, 3587 (2014).

[234] Choi, Y. C. *et al.* $Sb_2Se_3$-sensitized inorganic-organic heterojunction solar cells fabricated using a single-source precursor. *Angew. Chem.* **53**, 1329 (2014).

[235] Choi, Y. C. *et al.* Efficient inorganic-organic heterojunction solar cells employing $Sb_2(S_x/Se_{1-x})_3$ graded-composition sensitizers. *Adv. Energ. Mater.* **4** (2014).

[236] Efthimiopoulos, I. *et al.* $Sb_2Se_3$ under pressure. *Sci. Rep* **3** (2013).

[237] Caracas, R. & Gonze, X. First principles of the electronic properties of $A_2B_3$ minerals, with A=Bi,Sb and B=S,Se. *Phys. Chem. Minerals* **32**, 295–300 (2005).

[238] Lundegaard, L. F., Miletich, R., Balic-Zunic, T. & Makovicky, E. Equation of state and crystal structure of $Sb_2S_3$ between 0 and 10 GPa. *Phys. Chem. Minerals* **30**, 463 (2003).

[239] Efthimiopoulos, I. *et al.* High-pressure studies of $Bi_2Se_3$. *J. Phys. Chem. A* **118**, 1713 (2014).

[240] Lundegaard, L. F., Makovicky, E., Boffa-Ballaran, T. & Balic-Zunic, T. Crystal structure and cation lond electron pair activity of $Bi_2S_3$ between 0 and 10 GPa. *Phys. Chem. Minerals* **32**, 578 (2005).

[241] Zhao, J. *et al.* High-pressure phase transitions, amorphization and crystallization behaviors in $Bi_2Se_3$. *J. Phys: Condens. Matter* **25**, 125602 (2013).

[242] Bhosale, C. H., Uplane, M. D., Patil, P. S. & Lockhande, C. D. Preparation and properties of sprayed antimony trisulphide films. *Thin Solid Films* **248**, 137 (1994).

[243] Versavel, M. Y. & Haber, J. A. Structural and optical properties of amorphous and crystalline antimony sulphide thin-films. *Thin Solid Films* **515**, 7171–7176 (2007).

[244] Lokhande, C. D. *et al.* XRD, SEM, AFM, HRTEM, EDAX and RBS studies of chemically deposited Sb2S3 and Sb2Se3 thin films. *Appl. Surf. Sci.* **193**, 1 – 10 (2002).

[245] Maghraoui-Meherzi, H., Ben Nasr, T., Kamoun, N. & Dachraoui, M. Structural, morphology and optical properties of chemically deposited Sb2S3 thin films. *Physica B* **405**, 3101 (2010).

[246] Perales, F., Lifante, G., Agullo-Rueda, F. & de la Heras, C. Optical and structural properties in the amorphous to polycrystalline transition in Sb2S3 thin films. *J. Phys. D: Appl. Phys.* **40**, 2440 (2007).

[247] Torane, A. P., Rajpure, K. Y. & Bhosale, C. H. Preparation and characterization of electrodeposited $Sb_2Se_3$ thin films. *Mater. Chem. Phys.* **61**, 219 – 222 (1999).

[248] Rincon, M. E., Sanchez, M., George, P. J., Sanchez, A. & Nair, P. K. Comparison

of the properties of bismuth sulfide thin films prepared by thermal evaporation and chemical bath deposition. *J. Solid State Chem.* **136**, 167 (1998).

[249] Mahmoud, S., Eid, A. H. & Omar, H. Optical characteristics of bismuth sulfide ($Bi_2S_3$) thin films. *Fizika A* **3**, 111–120 (1997).

[250] Black, J., Conwell, E. N., Sigle, L. & Spencer, C. W. Electrical and optical properties of some $M_2N_3$ semiconductors. *J. Phys. Chem. Solids* **2**, 240–251 (1957).

[251] Yesugade, N. S., Lokhande, C. D. & Bhosale, C. H. Structural and optical properties of electrodeposited $Bi_2S_3$, $Sb_2S_3$ and $As_2S_3$ thin films. *Thin Solid Films* **263**, 145–149 (1995).

[252] Mahanty, S., Merino, J. M. & León, M. Preparation and optical studies on flash evaporated $Sb_2S_3$ thin films. *J. Vac. Sci. Technol. A* **15**, 3060 (1997).

[253] El Zawawi, I. K., Abdel-Moez, A., Terra, F. S. & Mounir, M. Substrate temperature effect on the optical and electrical properties of antimony trisulfide thin films. *Thin Solid Films* **324**, 300–304 (1998).

[254] Rodriguez-Lazcano, Y., Pena, Y., Nair, M. T. S. & Nair, P. K. Polycrystalline thin films of antimony selenide via chemical bath deposition and post deposition treatments. *Thin Solid Films* **493**, 77–82 (2005).

[255] Gildart, L., Kline, J. M. & Mattox, D. M. Some semiconducting properties of bismuth trisulphide. *J. Phys. Chem. Sol.* **18**, 286–289 (1961).

[256] Lukose, J. & Pradeep, B. Electrical and optical properties of bismuth sulphide [$Bi_2S_3$] thin films prepared by reactive evaporation. *Sol. State. Comm.* **78**, 535–538 (1991).

[257] Rajpure, K. Y. & Bhosale, C. H. Effect of composition on the structural, optical and electrical properties of sprayed $Sb_2S_3$ thin films prepared from non-aqueous medium. *J. Phys. Chem. Solids* **61**, 561 (2000).

[258] Haj Lakhdar, M., Ouni, B. & Amlouk, M. Thickness effect on the structural and optical constants of stibnite thin films prepared by sulfidation annealing of antimony films. *Optik* **125**, 2295 (2014).

[259] Deng, Z., Mansuripur, M. & Muscat, A. J. Simple colloidal synthesis of single-crystal Sb-Se-S nanotubes with composition dependent band gap energy in the near-infrared. *Nano. Lett.* **9**, 2015 (2009).

[260] Cantatero, A., Martinez-Pastor, J. & Segura, A. Excitonic absorbtion and Urbach's tail in bismuth sulfide single crystals. *Appl. Phys. A* **42**, 125 (1988).

[261] Cademartiri, L. *et al.* Large-scale synthesis of Ultrathin Bi2S3 necklace nanowires. *Angew. Chem. Int. Ed.* **47**, 3814 (2008).

[262] Malakooti, R., Cademartiri, L., Migliori, A. & Ozin, G. A. Ultrathin Sb2S3 nanowires and nanoplatelets. *J. Mater. Chem* **18**, 66–69 (2008).

[263] Ben Nasr, T., Maghraoui-Meherzi, H., Ben Abdallah, H. & Bennaceur, R. Electronic structure and optial properties of $Sb_2S_3$ crystal. *Physica B* **406**, 287–292 (2011).

[264] Koc, H., Mamedov, A. M., Deligoz, E. & Ozisik, H. First principles prediction of elastic, electronic, and optical properties of $Sb_2S_3$ and $Sb_2Se_3$ compounds. *Sol. State. Sci.* **14**, 1211–1220 (2012).

[265] Vadapoo, R., Krishnan, S., Yilmaz, H. & Marin, C. Electronic structure of Antimony Selenide ($Sb_2Se_3$) from GW calculations. *Phys. Status Solidi B* **248**, 700–705 (2011).

[266] Vadapoo, R., Krishnan, S., Yilmaz, H. & Marin, C. Electronic structure of Antimony Selenide ($Sb_2Se_3$) from GW calculations. *Phys. Status Solidi B* **248**, 700–705 (2011).

[267] Carey, J. J., Allen, J. P., Scanlon, D. O. & Watson, G. W. The electronic structure

of the antimony chalchogenide series: Prospects for optoelectronic aplications. *J. Solid State Chem.* **213**, 116 (2014).

[268] Calzia, V., Molloci, G., Bongiovanni, G. & Mattoni, A. Electronic properties of quantum confinement in $Bi_2S_3$ ribbon-like structures. *J. Phys. Chem. C* **117**, 21923 (2013).

[269] Sharma, Y. *et al.* Electronic structure, optical properties and Compton profiles of $Bi_2S_3$ and $Bi_2Se_3$. *Sol. State Sci.* **14**, 241–249 (2012).

[270] Sharma, Y. & Srivastava, P. First principles study of electronic and optical properties of $Bi_2Se_3$ in its trigonal and orthorhombic phase. *AIP Conf. Proc.* **1249**, 183 (2010).

[271] Liu, Y., Chua, K. T. E., Sum, T. C. & Gan, C. K. First-principles study of the lattice dynamics of $Sb_2S_3$. *Phys. Chem. Chem. Phys.* **16**, 345 (2014).

[272] Validžić, I. L. *et al.* Structural analysis, electronic and optical properties of the synthesized $Sb_2S_3$ nanowires with small band gap. *Semicond. Sci. Technol.* **29**, 035007 (2014).

[273] Bayliss, P. & Nowacki, W. Refinement of the crystal strucuture of stibnite, $Sb_2S_3$. *Z Kristall* **135**, 308–315 (1972).

[274] Voutsas, G. P., Papazoglou, A. G. & Rentzeperis, P. J. *Z Kristall* **171**, 261–268 (1985).

[275] Kanishcheva, A. S., Mikhailov, Y. N. & Trippel, A. F. *Izv. Akad. Nauk. SSSR. Neorganicheskie Mater.* **17**, 1972–1975 (1981).

[276] Atabaeva, E. Y., Mashkov, S. A. & Popova, S. V. *Sov. Phys. Crystallogr.* **18**, 173–174 (1973).

[277] Dion, M., Rydberg, H., Langreth, D. C. & Ludqvist, B. I. Van der Waals density functional for general geometries. *Phys. Rev. Lett.* **92**, 246401 (2004).

[278] Langreth, D. C. *et al.* Van der Waals Density Functional Theory with Applications. *Int. J. Quant. Chem.* **101**, 599 (2005).

[279] Darga, A. *et al.* On charge carrier recombination of $Sb_2S_3$ and its implication for the performance of solar cells. *J. Phys. Chem. C* **117**, 20525 (2014).

[280] Coleman, J. N. *et al.* Two-Dimensional Nanosheets Produced by Liquid Exfoliation of Layered Materials. *Science* **331**, 568–571 (2011).

[281] von Barth, U. & Car, R. (unpublished).

[282] Momma, K. & Izumi, F. VESTA: A three-dimensional visualization system for electronic and structural analysis. *J. Appl. Cryst.* **41**, 653 (2008).

[283] Kokalj, A. *Comp. Mater. Sci.* **28**, 155 (2003).

# Acknowledgements

The research projects I have been involved in during the past three and half years in Oxford have been the most exciting learning experiences, and for that I have to express my gratitude to my supervisor, Prof. Feliciano Giustino. I have to thank him for dedicating so much of his time to our almost daily discussions, and for clearly understanding my strengths and weaknesses and helping me grow as a scientist. His mentorship, constant support and encouragement, his honest advice and enthusiasm towards my work are in no small measure responsible for the successful completion of this thesis. I have to also thank him for supporting my passion for teaching, and giving me the opportunity to run the classes for his Predictions of Materials Properties lecture. Learning how to teach your own research topic is an extremely fun and rewarding experience.

I would like to acknowledge Prof. Peter Haynes, at Imperial College London for introducing me to the topic of computational modelling in 2010 and for encouraging me to apply to this DPhil. Furthermore, I would like to acknowledge our collaborators in the Department of Physics, Giles Eperon and Prof. Henry Snaith for their pro-active discussions and valuable experimental contribution to the work shown in Chapter 5.

I have to thank Chris Patrick for patiently helping me through the learning curve at the start of this DPhil, for always being positive and friendly and not least for introducing me to my favourite Tuesday night passtime - the Oxford Millenium Orchestra. A huge thank to all my friends in the Giustino group and in the MML for creating such great day to day atmosphere. I have to thank here my former office mates and shopping buddies, Charlotte and Natalie and my current office mates Tim, Harry, Henry and Davide (and former colleague Hannes) for tolerating me and my messy desk, particularly during the last couple of months of writing this thesis. Even with all the time we spend with each other in and out of the office, we surely do not seem to be bored of our little group: Carla, Fabio, George, Henry, Keian, Kun, Marios, Miguel and Tim. From coffee times, lunches and cakes to our regular pub outings and delicious culinary experiments - you guys are great!

I am incredibly greatful for all the unconditional support I have always received from my family. I have to say, I think I always wanted to have a PhD just because my big brother had one. So thank you to Lucian, for setting such a great example for me, and for always being there for me whenever I needed him. My parents have always been the biggest supporters for both my brother and I, and no ambitions were unreachable for us in their eyes. Most importantly, they have been my first and best teachers and foremost role models in everything I do. Everything I am today I owe to them, thank you! Finally, I must thank my husband, Tony, for being so supportive and and patient with me during this DPhil, and for making me always look forward to our exciting adventures together.

# List of published papers

1. Filip, M. R., Eperon, G. E., Snaith, H. J. and Giustino, F., Steric engineering of metal-halide perovskites with tunable optical band gaps, *Nature Communications* 5, 5757 (2014).

2. Filip, M. R. and Giustino, F., *GW* quasiparticle band gap of the hybrid organic-inorganic perovskite $CH_3NH_3PbI_3$: Effect of spin-orbit interaction, semicore electrons and self-consistency, *Physical Review B*, 90 (24), 245145 (2014).

3. Filip, M. R., Patrick, C. E. and Giustino, F., *GW* quasiparticle band structure of stibnite, antimonselite, bismuthinite and guanajuatite, *Physical Review B*, 87 (20), 2015125 (2013).